The processing, microstructure, properties and performance of abradable environmental barrier coatings

By Alex Lynam

Supervisor: Prof Tanvir Hussain

Co-supervisors: Assistant Prof Fang Xu, Dr Acacio Rincon Romero

Department of Mechanical, Materials and Manufacturing

Faculty of Engineering

30th September 2024

Contents

List of Abbreviations

APS	Atmospheric plasma spray
BSAS	Barium strontium alumino-silicate
BSE	Backscattered electron
CIF	Crystallographic information file
CMAS	Calcium magnesium alumino-silicate
CMC	Ceramic matrix composite
CT	Computed tomography
CTE	Coefficient of thermal expansion
CVD	Chemical vapour deposition
DSC	Differential scanning calorimetry
EBC	Environmental barrier coating
EBSD	Electron backscatter diffraction
EDX	Energy dispersive X-ray spectroscopy
HPT	High pressure turbine
HV	Vickers hardness
HVOF	High velocity oxy-fuel
LPT	Low pressure turbine
OEM	Original equipment manufacturer
PE	Polyester
PVD	Physical vapour deposition
RE	Rare earth
SE	Secondary electron
SEM	Scanning electron microscope
SPS	Suspension plasma spray
TBC	Thermal barrier coating
TET	Turbine entry temperature
TGA	Thermogravimetric analysis
TGO	Thermally grown oxide
VLPPS	Very low-pressure plasma spray
XRD	X-ray diffraction

YbDS	Ytterbium disilicate
YbMS	Ytterbium monosilicate
YSZ	Yttria stabilised zirconia

Table of Figures

List of Tables

Acknowledgments

I would like to thank the Engineering and Physical Sciences Research Council and Roll-Royce Plc for funding my research. I am incredibly grateful for the support of my supervision team over the course of this project, the guidance provided by Prof Tanvir Hussain, Assistant Prof Fang Xu and Dr Acacio Rincon Romero has proven invaluable. A special thank you to Dr Rincon Romero, who's day-to-day support and insight has help make me into the scientist I am today.

The experiments and characterisation conducted in this thesis would not have been possible without help of the Materials Engineering and Nanoscale and Microscale Research Centre technician team. I particularly appreciate the help of John Kirk without who none of the thermal spray experiments would have been possible.

It has been a pleasure working with the Coatings and Surface Engineering Centre of Excellence team for the last four years, and I would like to thank all my colleagues for their sharing knowledge and friendship with me.

Outside of the university, my family and friends have always been there when I needed them and have supported me throughout this journey.

Finally, and most importantly, my deepest love and gratitude to my partner, Dr Joanna Yorke. You believed in me when I doubted myself and your love, compassion and encouragement has got me through my most challenging moments.

Abstract

Ceramic coatings find application in a variety of fields, ranging from biomedical implants to high temperature coatings for aerospace engines. Of all the coating techniques and processes, plasma spray has proven to be one of the most versatile and reliable. For instance, plasma sprayed ceramic coatings are found throughout modern aerospace gas turbines engines. Within the hottest sections of these turbines, ceramics are beginning to replace metallic superalloys in a variety of components. These ceramics face unique difficulties when operating in such extreme environments and require protective coatings, known as environmental barrier coatings (EBCs). Abradable EBCs are used to reduce clearances between blades and casings, increasing the overall efficiency of the turbine, however, research into the processing and performance of such coatings is limited. In this context, the aim of this thesis will be to study the processing and performance of plasma sprayed abradable EBCs for use in the latest generation of gas turbine engines.

Initially, a parametric study was undertaken to demonstrate how processing parameters using an atmospheric plasma spraying (APS) torch affect the phase composition, microstructure and basic mechanical properties of the EBC. EBCs were deposited using a ytterbium disilicate ($Yb_2Si_2O_7$ or YbDS) powder and 4 sets of spray parameters, varying the spray power from 12 to 24 kW. The phases present in these coatings were quantified using x-ray diffraction with Rietveld refinement, and the level of porosity was measured. Using this data, the relationship between processing parameters and phase composition and microstructure was examined. Using the optimum process parameter window determined in this work, abradable EBCs were deposited using polyester (PE) feedstock additions as a pore forming phase. Two different PE levels were added and compared to the coating containing no PE. This created abradable EBCs with three distinct porosity levels. The mechanical performance and resistance to corrosion by species and environments found in gas turbine hot sections was analysed in the subsequent studies.

Research into the mechanical performance of abradable EBCs is limited. The aim of this subsequent work was to better understand the relationship between microstructure and erosion and wear performance in abradable EBCs. The abradable EBCs were characterised in numerous ways; the porosity was quantified, the thermal conductivity was measured, the

superficial hardness and erosion resistance were measured, and finally, the coatings were subjected to a rig test designed to simulate in-service cutting mechanisms against a ceramic tipped turbine blade. This showed that increasing the level of porosity via increasing the amount of pore forming phase in the feedstock, led to reduced erosion resistance and improved cutting by a turbine blade.

Finally, the performance of the abradable EBCs, when exposed to corrosive environments typically found within the hot section of gas turbines, was investigated. The first part of this of this study was to better understand how porous abradable EBCs perform when exposed to molten calcium magnesium alumino-silicates (CMAS), one of the key challenges facing current EBC design and how this exposure affects the mechanical properties of the abradable coatings. The abradable EBCs were exposed to CMAS at high temperatures for 0.5 hr, 4 hrs and 100 hrs. This showed that increasing the overall level of porosity had minimal impact on the degree of CMAS infiltration and mechanism of corrosion, and CMAS loading, and exposure time had the largest impact on the penetration depth. Reaction with the CMAS occurred by a dissolution-precipitation mechanism, with a reprecipitated ytterbium disilicate phase and Yb-apatite ($Ca_2Yb_8(SiO_4)_6O_2$) crystals noted as the only reaction products. After 100 hrs CMAS exposure, the erosion resistance of the coatings was investigated. For all the coatings, ductile failure was the main erosion mechanism. The change in phase composition and microstructure after CMAS exposure led to an increase in erosion resistance for all the coatings.

The second part of this study was to better understand how abradable coatings perform when exposed to steam, and combined steam and CMAS to try and replicate, on a laboratory scale, the extreme environments experienced by EBCs in service. The coatings were exposed to steam and combined steam and CMAS at 1350 °C for 100 hrs. The results show that increasing the overall level of porosity had minimal impact on the degree of steam or CMAS interaction. Exposure to steam caused the formation of a thin ytterbium monosilicate (Yb_2SiO_5 or YbMS) reaction layer. After the combined exposure, the CMAS infiltration depth was higher than that observed in standalone CMAS exposure. Also, an increased amount of Yb-apatite formation was observed within with YbMS reaction layer, and an ytterbium aluminium garnet ($Yb_3Al_5O_{12}$ or YbAG) phase was also observed.

Importantly, neither long term exposure to steam nor CMAS corrosion at high temperature led to failure of the abradable EBC.

The work presented in this thesis provides the foundations for further work into abradable EBCs, both in terms of processing and performance, as the potential efficiency gains that can be realised by their implementation within gas turbines are significant. Also, this work drives towards more realistic testing of EBCs, attempting to replicate the extreme environment and corrosive species they will encounter in gas turbine hot sections more closely.

List of publications presented in this thesis

A. Lynam, A. Rincon Romero, F. Xu, G.J. Brewster, G. Pattinson, T. Hussain, Atmospheric plasma spraying of ytterbium disilicate for abradable and environmental barrier coatings: A story of processing-microstructure relationships, Ceramics International, Volume 49, Issue 13, 2023, Pages 22232-22243, https://doi.org/10.1016/j.ceramint.2023.04.053

A. Lynam, A. Rincon Romero, F. Xu, A. Baillieu, M. Marshall, G.J. Brewster, G. Pattinson, T. Hussain, An investigation into the erosion and wear mechanisms observed in abradable ytterbium disilicate environmental barrier coatings, Journal of the European Ceramic Society, Volume 44, Issue 12, 2024, Pages 7310-7327, https://doi.org/10.1016/j.jeurceramsoc.2024.05.008.

A. Lynam, A. Rincon Romero, B. Zhang, S. Lokachari, F. Xu, G. Pattinson, G.J. Brewster and T. Hussain, Abradable ytterbium disilicate environmental barrier coatings: A story of CMAS and combined CMAS-erosion performance. Manuscript submitted for publication.

A. Lynam, A. Rincon Romero, B. Zhang, E.B. Owusu, F. Xu, G. Pattinson, G.J. Brewster and T. Hussain, Abradable ytterbium disilicate environmental barrier coatings: A study of steam, CMAS and combined steam-CMAS corrosion. Manuscript submitted for publication.

List of publications related to this thesis

A. Lynam, A. Rincon Romero, R.G. Wellman and T. Hussain, Thermal Spraying of Ultra-High Temperature Ceramics: A Review on Processing Routes and Performance, Journal of Thermal Spray Technology, Volume 31, Issue 4, 2022, Pages 745–779, https://doi.org/10.1007/s11666-022-01381-5

Chapter 1: Introduction

1.1. Gas Turbines

For decades, gas turbines have been ubiquitous within aerospace, powering the vast majority of aircraft flying today. Their development has significantly shaped the evolution of modern aviation, enabling faster, more efficient air travel. Piston-engine aircraft dominated aviation from its beginnings with the Wright brothers' flight in 1903 up until the end of World War II, however, they had limitations in terms of speed, altitude performance, and efficiency. As a result, gas turbine engines gradually replaced them, allowing for the development of faster, higher-flying, and more powerful aircraft. Although specific designs can vary, the underlying principle of their operation remains the same: "*Suck, squeeze, bang and blow*". Initially, air enters the turbine and is compressed by a series of rotating blades, to a high pressure, atomised fuel is then injected into the compressed air, and the mixture is subsequently ignited in the combustion chamber. Combustion produces a high temperature, high pressure gas, which, as it expands, drives the high-pressure turbine (HPT), in turn driving the compressor. Finally, the remaining energy in the hot gas stream is used to drive another turbine-compressor set (low-pressure turbine or LPT) and then it is expanded and accelerated through the nozzle which provides thrust. The highest temperatures within the gas turbine are found in the hot section, which comprises the combustor and the HPT vanes, blades and shrouds. The temperature between the combustor and the HPT is known as the turbine entry temperature (TET) and is a measure of how hot the exhaust gases are as they leave the combustion chamber and enter the turbine. In modern gas turbine and any increase in TET directly correlates to an increase in the thermal efficiency of the gas turbine. Given this, the materials required for hot section components need to be able to operate in an extreme environment. Historically, and even in the majority of gas turbine engines found on-wing today, nickel (Ni) based superalloys have proven to be up to the task. Even as the TET has exceeded the melting point of these superalloys, the use of low thermal conductivity ceramic coatings applied to the surface, known as a thermal barrier coating (TBC), has maintained safe operating conditions for the metallic superalloy components [1]. A schematic of a gas turbine with some TBC coated hot section components is shown in Figure 1. But as further thermal efficiency gains are sought, and more fuel-efficient aircraft are designed, the TET in the latest generation gas turbines can be up to 1500 °C, beyond the

capability of even these superalloy based systems [2]. Thus, even more sophisticated material solutions are required.

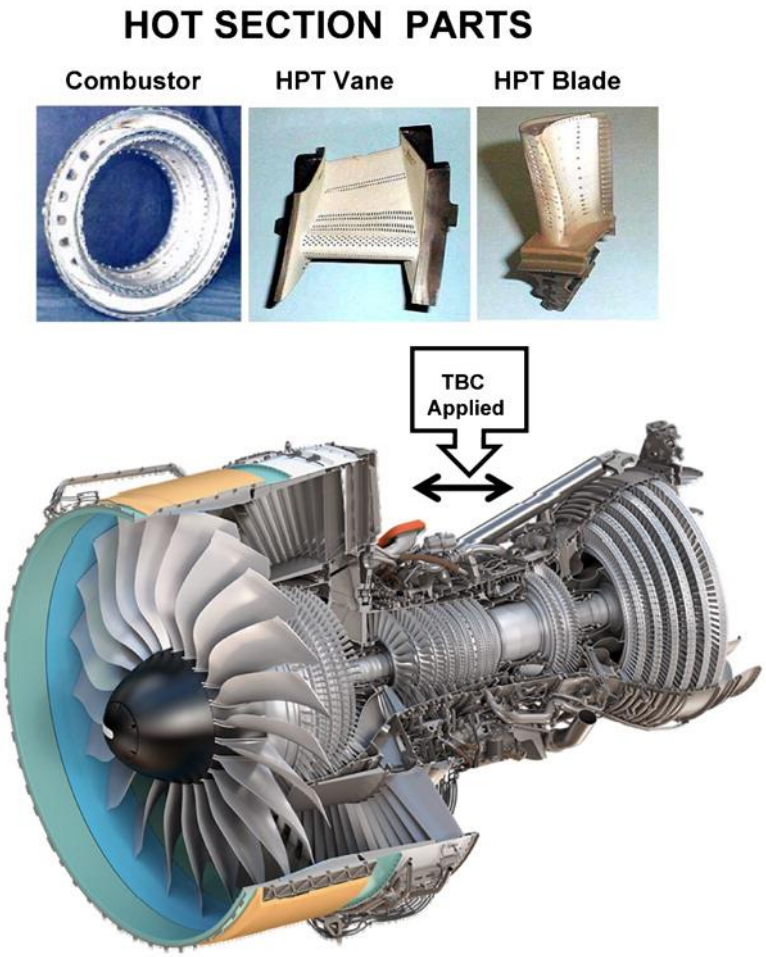

Figure 1. A schematic of a gas turbine engine and examples of some coated hot section components and their location within the turbine [3].

One such solution is the use of ceramic matrix composites (CMCs), specifically silicon carbide (SiC) CMCs. SiC CMCs are made up of SiC fibres surrounded by a SiC matrix and exhibit excellent high-temperature properties and have a higher strength-to-weight ratio relative to the Ni-based superalloys [1, 2, 4]. Despite apparent suitability for the next generation of hot section components, SiC CMCs are not without drawbacks. The most pressing of which is their susceptibility to oxidation-recession in water vapour containing environments, which is a by-product of the combustion process. In dry air, SiC will oxidise forming a protective silica scale, preventing further oxidation. In the presence of water vapour, this protective scale will react, forming a gaseous product, exposing the SiC beneath to oxidation and leading to rapid recession of the material [5]. Hot section components are

also vulnerable to corrosion by molten ash and sand, ingested into the turbine. As with the Ni-based superalloys, ceramic coatings have been developed to protect the CMCs and ensure their safe operation. These coatings are known as environmental barrier coatings (EBCs), and due to its similar coefficient of thermal expansion (CTE) relative to SiC and phase stability at high-temperature, ytterbium disilicate ($Yb_2Si_2O_7$ or YbDS) is one of the most promising EBC materials [4, 5], these requirements are outlined in Figure 2. In fact, manufacturers are already producing gas turbine engines containing SiC CMC components protected with EBCs, the General Electric GE9X contains CMC HPT shroud and nozzles as well as combustor linings, while the CFM Internation LEAP contains CMC turbine shrouds [6, 7]. Nevertheless, in 2017, an EBC failure on a CMC shroud in the LEAP engine led to overhaul of 8 in-service engines and a potential cost of €50 million to CFM International [8], demonstrating the need for robust research and development of the CMC/EBC system.

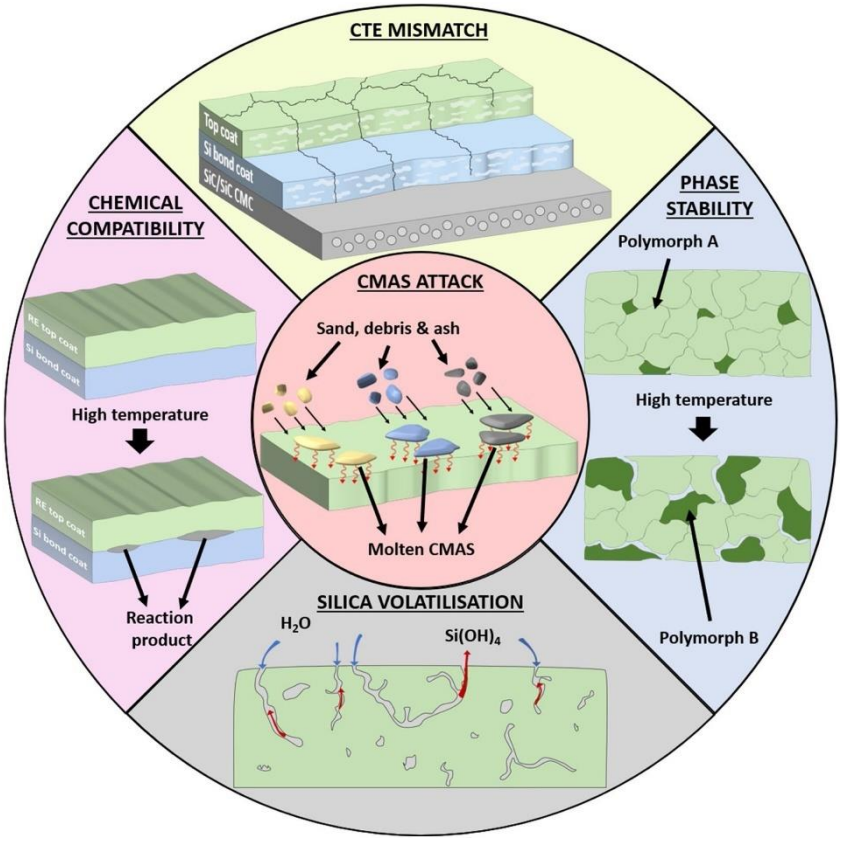

Figure 2. A schematic showing the main requirements required of an EBC [9].

1.2. Thermal spray

While many of the materials properties are determined by the bulk, the surface also plays an important role in determining the use and lifespan of the material. Surface engineering allows modification of the mechanical, chemical, electronic, corrosion resistant and wear resistant properties of a materials surface ensuring the material is robust for the environment in which it will be used. Surface engineering processes include mechanical (shot blasting, peening), surface transformation (heat treatment), surface composition changes (thermochemical processes such as nitriding) and coating (where a new material is deposited on top of the substrate) [10].

Thermal spraying is one form of surface engineering in which coatings are deposited on to a substrate. In the most basic terms, thermal spraying uses a gun to melt the coating material or feedstock and accelerate it towards the component, where the molten particles impact, solidify and a coating is built up. Thermal spraying techniques can be categorised into four main sub-groups. These are plasma spraying, flame spraying (including high velocity oxy-fuel or HVOF, detonation and warm spraying), wire arc spraying and cold spraying [11]. Plasma and wire arc spraying use electrical means to heat the feedstock material to a molten or semi-molten state, whereas flame spraying uses a chemical method. The molten/semi-molten feedstock particles are then accelerated towards the substrate inside a jet or flame. Upon impact with the substrate the particles deform to create a splat which adheres to the surface of the substrate. As the spraying process continues, these splats solidify and build up layer by layer to form the coating [11]. While the cold spray process is classed as a thermal spray technique, it is a solid-state process that relies on high kinetic energy. In cold spraying the feedstock is accelerated in a compressed gas stream, causing plastic deformation and bonding upon impact with the substrate. The process takes place at temperatures below that of the melting point of the feedstock as opposed to the other thermal spray processes where a heat source is used to melt the feedstock [11]. Figure 3 shows the particle temperatures and velocities associated with various thermal spraying techniques. Various feedstock materials can be employed in the thermal spray process including ceramics, metals and metal alloys, polymers and composites. These feedstocks can also take various forms including powder, wire, liquid and suspension.

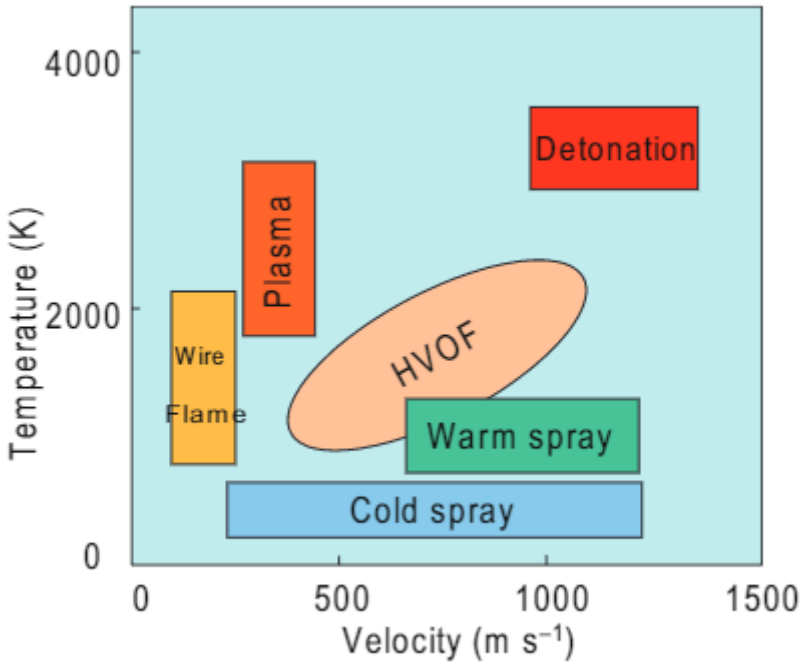

Figure 3. Comparison of various thermal spray processes in terms of particle temperature and velocity [12].

Compared to other surface coating techniques widely employed in aerospace applications, such as physical vapour deposition (PVD) and chemical vapour deposition (CVD) thermal spray processes are typically able to deposit thicker coatings (thermal spray coatings can be of the millimetre order) at quicker deposition rates and are significantly cheaper [10]. However, this does not mean thermal spraying processes are without drawbacks, the magnitude of which is largely determined by the thermal spray process being employed. Due to the high temperatures of the feedstock material during the spraying process, it can interact with the surrounding atmosphere in-flight, forming oxides, which will inevitably be present in the microstructure of the coating. The presence of oxide impurities within a coating can be controlled by spraying in a controlled atmosphere or vacuum; however, this adds significant cost to the process [13]. Porosity is inherent in virtually all thermal spray coatings and, depending on the application requirement of the coating can be beneficial or detrimental. Pores within the coating can be formed by one or a combination of the following mechanisms: solidification shrinkage, gas entrapment and/or the presence of unmolten particles within the coating [14]. Residual stresses within the coating can lead to defects such as cracking or delamination. As the coating is deposited, thermal cycling, thermal shock effects, and solidification shrinkage create residual stresses between the

coating and substrate. As the coating process continues and further layers are deposited, these residual stresses are superimposed until the bond strength or cohesive strength is potentially exceeded [11].

Arguably the most versatile thermal spray process is atmospheric plasma spraying (APS). APS uses a radio frequency or, more commonly, direct current arcs between a pair of electrodes to ionise process gases, creating a plasma jet. As these unstable plasma ions reform into their gaseous states, a large amount of thermal energy is released, creating extremely high temperatures, up to 14,000 K, within the plasma jet. Process gases typically used in APS are argon (Ar), hydrogen (H_2), nitrogen (N_2), helium (He) or a combination thereof. Feedstock particles are injected into the gas stream, where particle velocities can be between 20 and 500 mm/s depending on the size of the particle [11]. The extreme temperatures associated with APS mean a wide variety of feedstock materials, including refractory ceramics, can be readily melted. The relatively high particle velocity and high jet temperatures mean APS can produce coatings with low levels of porosity, high densities and good bond strengths relatively cheaply [13]. It is thanks to this versatility that APS coatings are employed throughout gas turbines and are widely used to deposit the range of ceramic coatings used to protect hot section components [15].

1.3. Abradable coatings

Aircraft gas turbines are exposed to extreme temperatures, high pressures, and corrosive environments; hence a variety of coatings are used throughout the turbine. TBCs and EBCs are used to protect components from the extreme environments found in the hottest sections of the turbine, corrosion, oxidation and wear resistant coatings are also employed in various forms throughout the turbine. Coatings are also used for clearance control, these are known as abradable coatings. Abradable coatings are a type of thermal spray coating that are employed on engine casing walls and allow clearances between rotating components such as fins and blades to be minimised, leading to an increase in efficiency and a reduction in fuel consumption [16]. By reducing the clearances between rotating components, efficiency gains within gas turbines can be realised. In fact, in a HPT, reducing the blade tip clearance by 25 µm could lead to a 0.1 % reduction in specific fuel consumption and a 1 °C reduction in exhaust gas temperature [17]. Furthermore, when using an abradable seal coating in the HPT, power and efficiency gains of over 3 % for the

HPT stage can be achieved when compared to a design without such coatings and the inherent larger blade tip clearance [18].

Abradable coatings are designed in such a way that when the rotating component strikes them, they will easily wear away rather than damaging the blade, thus creating a seal between the two. Ideally, abradable coatings will, when cut, produce brittle fracture failure, leaving behind a smooth, uniform wear track and without any damage to the blade [19]. Any undesirable failure mechanisms in the abradable coating or wear to the blade could lead to oversizing (an increase in the blade tip clearance) or even catastrophic failure of the system [19]. Good cutting is achieved by creating a porous coating (usually through the addition of a fugitive polymer), sometimes with the addition of dislocators and/or solid lubricants such as hexagonal boron nitride (hBN), graphite or bentonite. A wide range of metallic and ceramic materials are used for abradable coatings, usually selected based on their temperature capability. Figure 4 demonstrates the range of operating temperatures appropriate for each abradable coating and blade material.

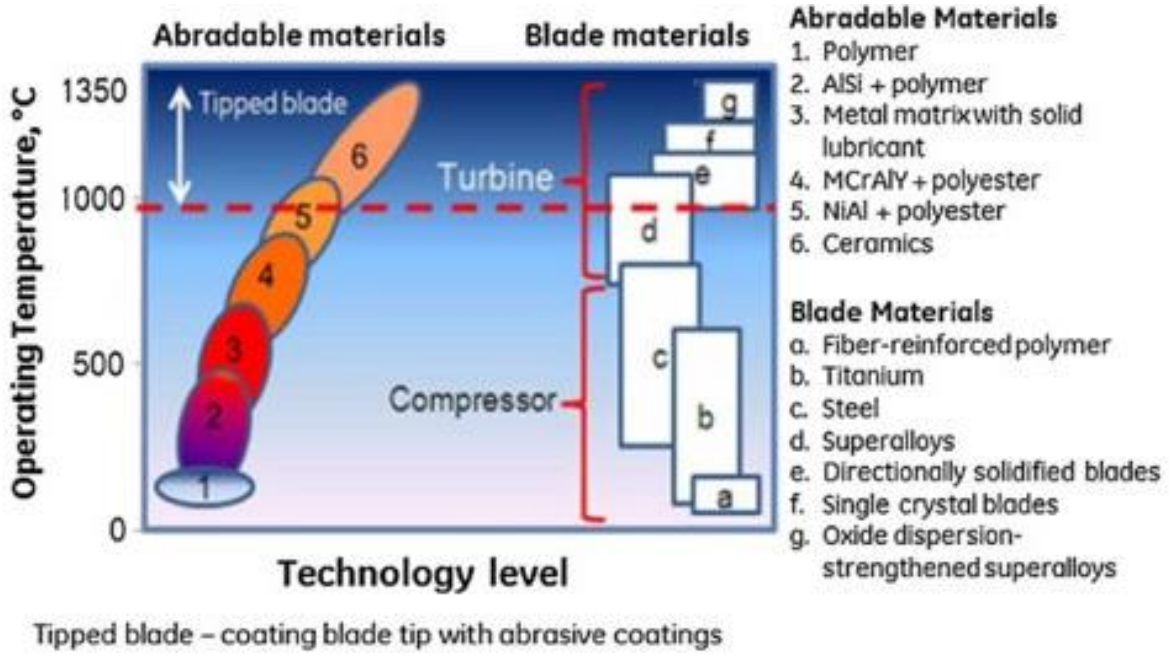

Figure 4. The relationship between operating temperature and abradable coating/blade material technology level [15].

In the fan and compressor stages, aluminium-silicon (Al-Si) based alloys are widely used. As the temperature increases in the latter regions of the compressor Ni-based alloys and

MCrAlY which has base metal (M) of Ni or Cobalt (Co) combined with chromium (Cr), aluminum (Al), and Yttrium (Y) are preferred. Ceramics are used exclusively in the hot section, with yttria stabilised zirconia (YSZ) and magnesia alumina spinel the most common materials. However, as the TET increases and the operating temperature of the abradable coating increases, attention has turned to YbDS based abradable coatings. Due to the inherent hardness of ceramic abradable coatings, harder than conventional turbine blade materials, abrasive coatings must be applied to the blade tip, to prevent blade wear and promote good cutting of the abradable. Due to its high hardness and thermal stability cubic boron nitride (cBN) is the current blade tip material of choice.

1.4. Thesis Structure

This thesis is submitted in a Thesis by Publication format whereby:

- Chapter 1 introduces the context behind the thesis, with an overview of gas turbines, thermal spraying and abradable coatings.
- Chapter 2 provides an extensive literature review of the areas of research contained within this thesis. First, a review of the testing of abradable coatings, primarily ceramic coatings, in gas turbines is presented. Secondly, the current state of EBC research is critically interrogated, including materials, steam corrosion, CMAS corrosion and mechanical and tribological properties. This section ends with a summary of the current landscape and gaps in the literature are given and finally the aims and objectives of the thesis are also presented.
- Chapter 3 provides detail on the experimental methods used throughout this thesis, details of which were not captured in the published work.
- Chapter 4 is an experimental study whereby a variety of APS spray parameters are used to produce YbDS coatings. Scanning electron microscopy (SEM), x-ray diffraction (XRD) and porosity analysis are used to characterise the coatings. Using the optimised spray parameters, abradable YbDS coatings with three porosity levels are produced by addition of PE pore former to the feedstock. These abradable EBCs where then further characterised again using SEM, XRD and porosity analysis.
- Chapter 5 examines the erosion and wear performance of the abradable YbDS coatings produced in the previous chapter. The wear of the coatings was tested

using a specially designed rig at the University of Sheffield, which allows for replication of in-service blade incursion conditions.

- Chapter 6 studies the interaction between the abradable YbDS coatings and molten CMAS. The effects of porosity level on the infiltration of CMAS and exposure time were investigated. The microstructural and compositional changes were characterised. Finally, the erosion resistance of the abradable coatings after CMAS exposure was tested and compared to their as-sprayed counterparts.
- Chapter 7 assess the performance of the abradable YbDS coatings when exposed to high temperature water vapour. The effects of porosity level on the corrosion resistance were investigated, and the microstructural and compositional changes were characterised. Additionally, subsequent tests were carried out whereby the coatings were subjected to both molten CMAS and high temperature water vapour simultaneously. Again, the effects of porosity level on the corrosion resistance were investigated and the microstructural and compositional changes were characterised.
- Chapter 8 summarises the published experimental works, outlines the conclusions and its contribution to the scientific field. It also provides suggestions for future work within the field that could advance upon the foundations laid within this thesis.

Chapter 2: Literature review

This chapter presents a critical appraisal of the current state-of-the-art, preceding the experimental work conducted in this thesis. Initially, a review of ceramic abradable coatings, their properties and performance are presented, however much of this literature is focussed on abradable TBCs (minimal public domain work has thus far been undertaken concerning abradable EBCs). This is followed by a short history of EBC development, in terms of material selection and the deposition of EBCs. Next, a detailed review of the performance of EBCs is offered, including the main corrosion mechanisms faced by EBCs in-service, namely steam and CMAS corrosion, as well as mechanical and tribological performance. Finally, a summary of the gaps in literature regarding abradable EBCs is outlined.

2.1. Abradable ceramic coatings

While much of the published research into abradable coatings has focused on metallic or metallic/ceramic composite coatings, these are not appropriate for use at the extreme temperatures found in the hot section of a gas turbine. In the lowest temperature sections of the turbine, the fan and low-pressure compressor stages, Al-Si containing a pore former such as polyester (PE) or solid lubricant (hBN or graphite) have been widely researched [20-32] as well as Ni based coatings containing graphite [24, 33-36]. As temperatures increase in the high-pressure compressor, MCrAlY based coatings are employed, again containing PE, hBN or bentonite [37-42]. Finally, in the hottest section of the gas turbine, where temperatures are above 750 °C, ceramic abradable coatings are required, such coatings were being investigated as early as the 1980's [43]. This has been largely based on TBC materials, designed to protect Ni-based superalloy components. Typically, TBCs are made from zirconia (ZrO_2) stabilised with a rare earth oxide, usually yttria (Y_2O_3) to form yttria stabilised zirconia (YSZ), however other rare earth oxides have also been employed, such as dysprosia (Dy_2O_3) and ytterbia (Yb_2O_3), forming dysprosia stabilised zirconia (DySZ) and ytterbia stabilised zirconia (YbSZ) respectively. As with metallic abradable coatings, additions of PE and/or hBN are typically made to abradable TBCs [44-54]. Another abradable TBC material that has been explored is magnesia alumina spinel, due to its higher temperature capabilities relative to YSZ [55-57]. However, as the TET increases further and the demand for SiC CMCs in gas turbine hot sections increases, new abradable materials will

need to be developed. Researchers have started to explore abradable EBCs, including barium strontium alumino-silicate (BaO-SrO-Al_2O_3-SiO_2 or BSAS) [58] and YbDS [59-62], again typically with additions of PE or hBN to the feedstock. On top of this, patents are also starting to materialise, indicating gas turbine manufacturers are investing significant effort into the research of abradable EBCs outside of the public domain [63, 64].

2.1.1. Measurement of abradability

Given the complexity of the blade-abradable rub interaction, numerous test methodologies have been developed to quantify the abradability of the coating materials. The simplest of these is surface hardness testing. This is done using the Rockwell superficial scale, whereby a small load (typically 15, 30 or 45 kgf) is applied to a diamond (N) or ball (Y) indenter. Better abradability has typically been linked with lower hardness [16, 65]. The next technique in terms of complexity is erosion testing, specifically the GE E50TF121CL erosion test [16, 66]. In this test, the abradable coating is held at 20° and at a distance of 100 mm relative to an air-jet. 600 g of alumina are then fed through the air-jet, eroding the surface of the abradable coating. The maximum depth of the erosion pit is measured, and the erosion rate can be calculated, this is defined as the time taken for 25.4 µm of the coating to be eroded, is described by the unit s/mil and is known as the GE erosion number. While the abradable coatings must be resistant to damage by foreign bodies it must also wear easily against the blade, not causing any damage. Given this, a range of 2-5.5 s/mil) is considered suitable for abradable coatings [16, 55].

Finally, the wear of abradable coatings can be quantified using, using either pin-on-disk tribometers or specially designed abradable test rigs. While tribometers are widely used to quantify the wear and friction of two surfaces in contact, even going as far as to represent harsh environmental conditions, such as high temperature and the presence of corrosive species, when testing abradable-blade rub interactions they are somewhat limited. This is due to the extreme speeds at which the blade is moving, that no tribometer could replicate. Because of this, specific test rigs have been designed, more closely representing the in-service conditions the abradable coating and blade tip would face. One such rig has been designed by Oerlikon Metco. The rig features a high velocity flame which can heat ceramic abradable coatings to 1200 °C, can accommodate real or dummy turbine blades rotating on a spindle that can achieve tip velocities of up to 500 m/s, a stepper motor moves the

abradable coating towards the rotating blade at an incursion rate of up to 2000 µm/s, somewhat replicating the conditions hot section abradable coatings will be exposed to [67, 68], the rig itself is shown in Figure 5. A similar rig has been designed at the University of Sheffield, this rig operates in much the same manner, but without heating, and is equipped with two stroboscopic imaging systems allowing images of the blade, both front-on and side-on, to be captured after each rotation if the spindle allowing the change in blade profile to be monitored during the test [27, 29, 30].

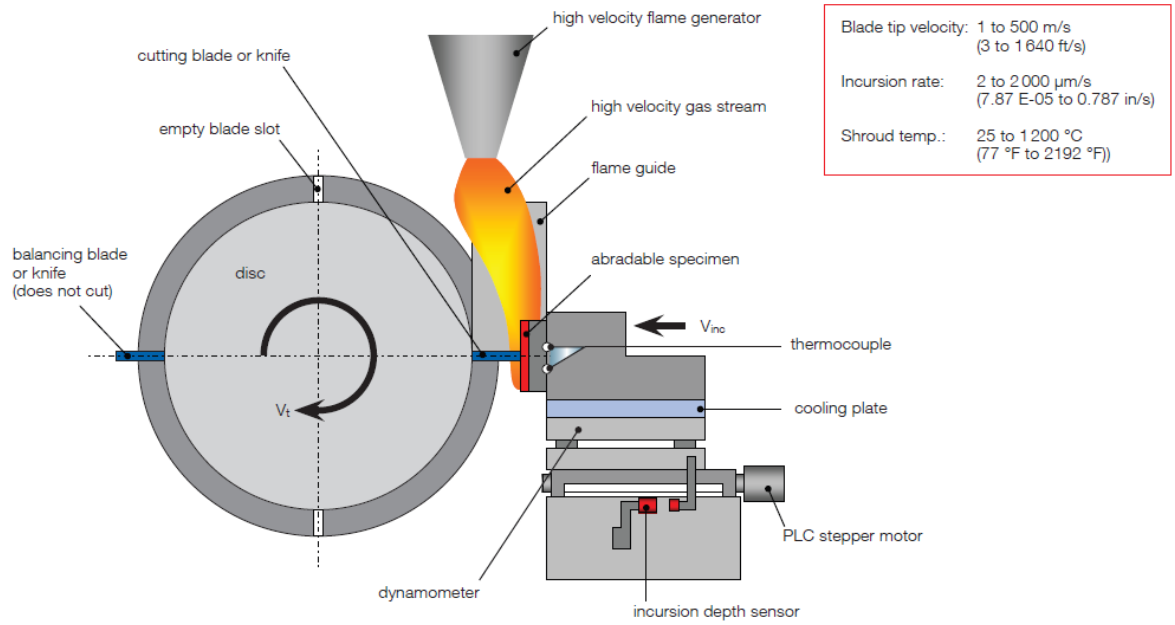

Figure 5. Schematic diagram of the Oerlikon Metco abradable test rig [67, 68].

2.1.2. Abradable ceramic coating properties

The properties that are required for abradable ceramic coatings for use in the hot section can prove complex when it comes to their manufacture. Firstly, they must exhibit good bonding and adhesion to the substrate, even under thermal cycling at extreme temperatures and offer suitable thermal/environmental protection to the substrate. On top of this, the coating must be able to withstand erosion by any particles that are ingested by the turbine but at the same time it must be able to be cut efficiently by the turbine blade. To understand how coatings can be cut effectively it is important to understand the mechanisms at play.

The wear mechanisms observed in abradable coatings (from analysis of parts that had been in service) was first described by Borel et al. [19]. Three main mechanisms were identified: cutting, adhesion and deformation. Cutting is similar to a turning process, where the blade tip acts as the cutting tool, and material is removed in a brittle manner, even in ductile material, and is the most efficient mechanism [19]. Adhesion and deformation were noted as being undesirable mechanisms. Adhesion involves the transfer of the abradable material to the blade or vice versa and is associated with overheating of the system and the creation of an undesirable hard transfer layer. Deformation can refer to either the plastic flow of the abradable material on the surface or a compaction/densification of the porosity in the radial direction. Compaction is particularly detrimental as the densification of the abradable means it is less likely to give way during future blade impacts [19, 23].

For abradable ceramic coatings, the ideal cutting mechanism has been described by Sporer, et al. [47] and is shown in Figure 6. As the blade impacts the coating, elastic energy is transferred to the coating surface particles, and they are pushed away from the blade incursion (particles i and ii in Figure 6), the stored elastic energy from this interaction then pushes the particles back towards the surface (particles iii and iv) where, if the elastic energy is high enough to overcome the bond strength between particles within the coating, it will be released as debris (particle vi).

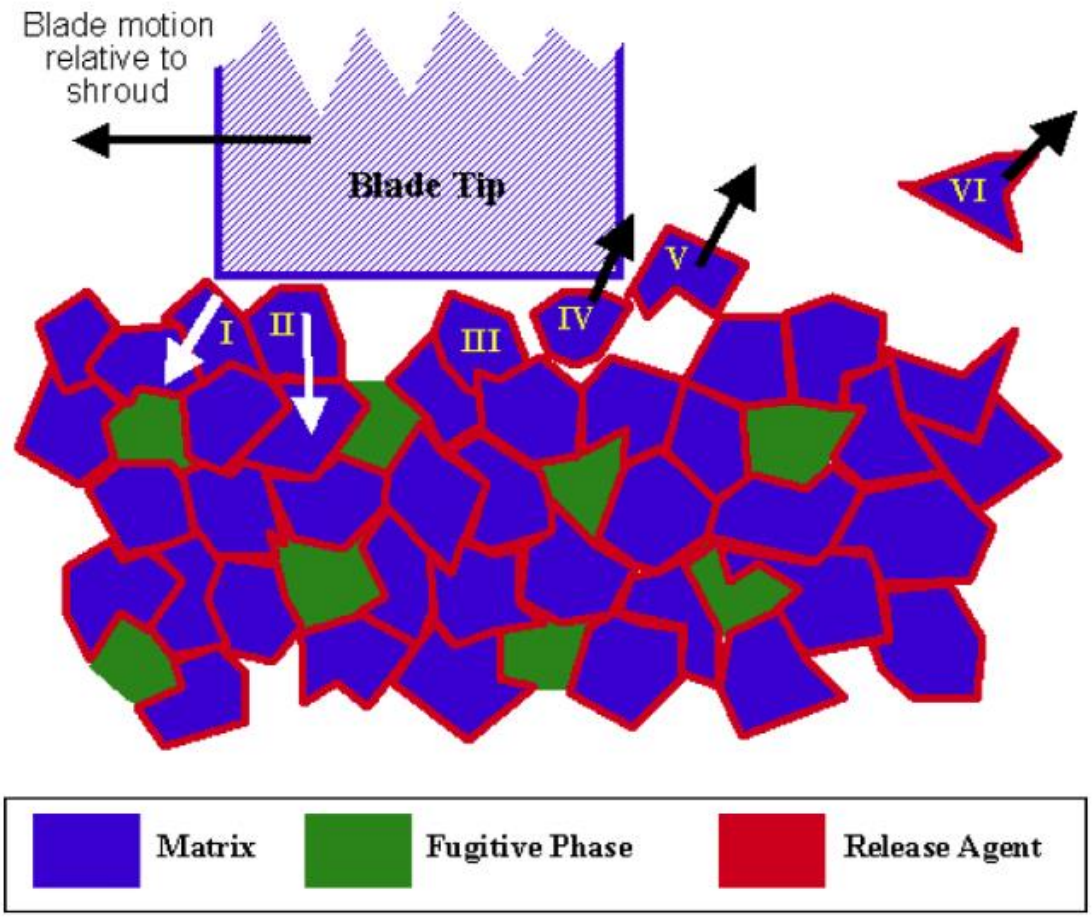

Figure 6. Schematic showing the ideal cutting mechanism of an abradable ceramic coating (blue), containing a fugitive pore forming phase (green) and a dislocator phase (red) [47, 69].

To improve the cutting of the abradable ceramic coating, it follows that the energy required for particle detachment must be reduced, this can be achieved through control of the coating microstructure via the feedstock material and the parameters used during deposition. It is generally understood that increased levels of porosity lead to improved cutting of the abradable coating [16, 65]. To achieve this, fugitive phases, typically PE which is burnt out during subsequent heat treatment leaving large pores behind, are added to the feedstocks of abradable TBCs [44-47, 49, 51] and EBCs [58-60, 62]. In fact, Tejero Martin, et al. [59] found that including ~1.5 wt.% PE to the feedstock of a YbDS EBC increased the porosity from 2.4 % to 21.3 % when the coatings were deposited using the same plasma spray torch. Similarly, Guo, et al. [58] added 4 and 8 wt.% PE to a BSAS abradable EBC and found the porosity increased from 6.0, 11.9 and 29.3 for BSAS, BSAS + 4 wt.% PE and BSAS + 8 wt.% PE coatings respectively. As well as increasing porosity the addition of the PE was

also found to reduce the superficial hardness of the abradable EBCs. As the PE was increased, the hardness was reduced from 90.0 HR45Y, to 69.0 HR45Y and 57.7 HR45Y. Additionally, dislocator/solid lubricant phases have also been added to the feedstocks, hBN [44, 46, 53, 61], lanthanum phosphate ($LaPO_4$) [50, 54] and even MAX phases, specifically Ti_3AlC_2 [70] and Ti_3SiC_2 [54], have all been added to abradable TBCs/EBCs to alter the wear performance of the coatings. Specifically, hBN additions were found to reduce the superficial hardness of abradable YbDS EBCs [61]. An addition of 15 wt.% hBN was found to reduce the hardness of the abradable EBC from 83.5 HR45Y to 68.0 HR45Y.

The other way by which abradable coating microstructure and properties can be controlled is through the careful selection of spray parameters used in the deposition process. Abradable ceramic coatings are universally deposited using APS, and control of the ionising arc current, process gases and their respective flow rates, the stand-off distance (distance from torch exit to substrate) and a host of other parameters is imperative when considering optimised abradable coating microstructures, and as such process parameters have been explored by many researchers. By altering the arc current between 380, 450 and 625 A to create low, medium and high power deposition conditions, Sporer, et al. [46] found that the properties of abradable YSZ could be drastically altered. As the spray power was increased, the particle velocity and temperatures that were measured in-flight also increased. Subsequently, the porosity measured in the deposited coatings was found to have an inverse relationship with the spray power, decreasing as the spray power increased. The erosion resistance (GE erosion number) of the coatings was also found to increase as the spray power increased, with the erosion resistance of the abradable coatings being a good indicator of their abradability.

This is in agreement with subsequent work, whereby the effect of arc current, Ar and H_2 flow rate and stand-off distance were systematically changed between high and low values when depositing abradable YSZ coatings [49]. Increasing the arc current was found to decrease the number and size of the pores, reducing the stand-off distance and increasing the Ar flow rate was also found to decrease the number and size of the pores. Reducing the arc current, H2 flow and increasing the stand-off distance were found to reduce the erosion resistance of the YSZ abradable coatings. Interestingly, changing the spray parameters did not illicit any changes in the superficial hardness (HR15Y) of the abradable coatings. A

similar study has also been conducted on abradable magnesia alumina spinel TBCs [55]. In this study, arc current, Ar flow rate, stand-off distance and feedstock powder feed rate were changed between low medium and high levels and in-flight particle characteristics, and a variety of coating properties were recorded. Generally, hardness and porosity of the abradable coatings showed an inverse correlation and were primarily impacted by Ar flow rate and arc current, whereby increases to either would result in decreased porosity and increased hardness.

More recently, similar studies have begun to emerge regarding abradable EBCs. Xu, et al. [62] considered the effect of arc current on PE containing YbDS coatings. Three abradable EBCs were deposited using arc currents of 300, 400 and 500 A. The subsequent coatings had porosity 35.5 %, 28.4 % and 23.3 % respectively, and the microstructures are shown in Figure 7. While hardness ranged from 77.9 HR15Y for the coating deposited at 300 A, to 82.5 HR15Y for the abradable coating deposited at 500 A.

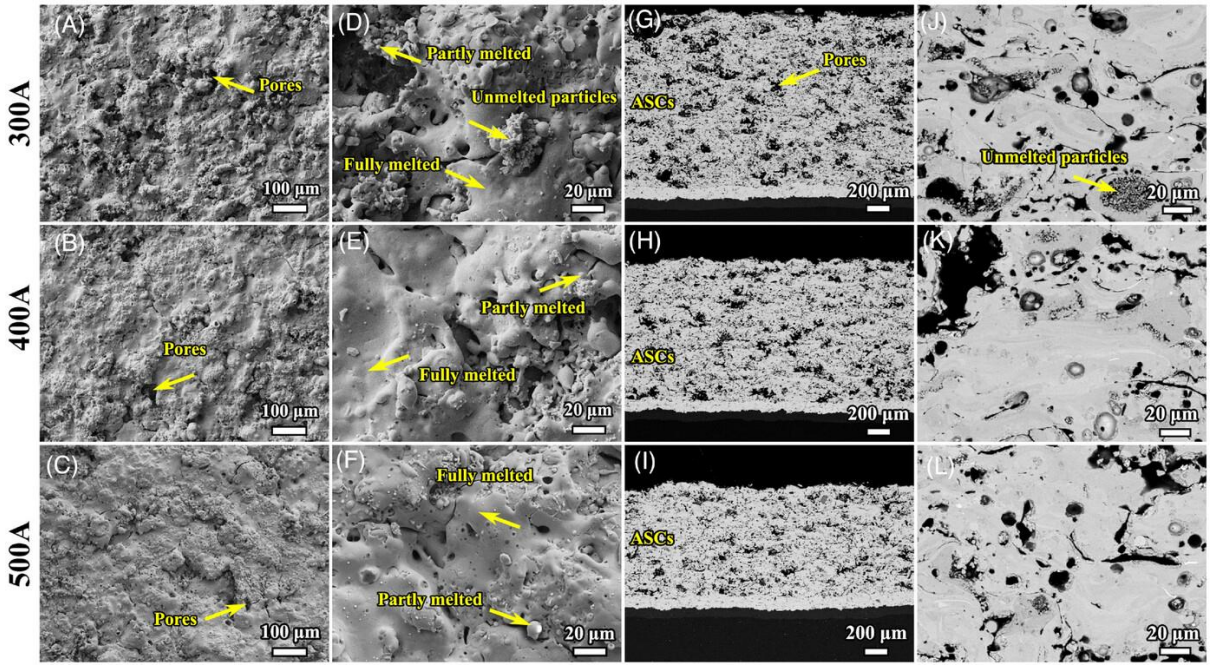

Figure 7. Microstructures of abradable YbDS EBCs, deposited using three different arc current parameters. Where a-c) shows low-magnification and d-f) high-magnification surface morphologies, g-i) low-magnification and j-l) high-magnification cross-section morphologies [62].

2.1.3. Abradable ceramic coating wear testing

Beyond measuring the hardness and erosion resistance of abradable ceramic coatings, the most effective way to quantify the abradability is through tribological testing, using either pin-on-disk tribometers or specially designed abradable test rigs. Much of the contemporary testing of ceramic abradable coatings has been conducted using Oerlikon Metco's abradable test rig [67]. In some of the first testing using this rig, a variety of TBC materials were analysed [44]. A commercially available abradable YSZ was compared to novel DySZ and YbSZ coatings. All the coatings contained 5 wt.% PE addition were produced using APS and subjected to a variety of tests to characterise their abradable performance. The YSZ, DySZ and YbSZ abradable coatings were found to have porosity levels of 26.6, 29.3 and 39.6 vol.%, respectively, superficial hardness values of 92, 89 and 85 HR15N, respectively and GE erosion numbers of 0.89, 2.17 and 1.33 s/mil, respectively. The coatings were tested on the abradable test rig at a temperature of 1100 °C, incursion rates of 5 and 500 µm/s, and blade tip speeds of 250 and 410 m/s, an intermediate condition of 50 µm/s incursion rate and 350 m/s blade tip speed was also tested. The abradable coatings were tested against Inconel 718 blades with a cBN abrasive tip. Under all the conditions, the YSZ abradable coating showed slight blade wear, while the DySZ and YbSZ abradable coatings showed a combination of blade wear and material transfer from the abradable coating to the blade. Nevertheless, the authors concluded that all the coatings were comparable and could be easily cut by the cBN tipped blades. Good cutting of other abradable ceramic TBC materials against cBN tipped blades has also subsequently been reported in further studies using the same abradable test rig [47, 48], in fact, it has been shown the efficient cutting of abradable TBC materials by cBN tipped blade is largely dependent on the overall porosity level of the abradable coating [47]. Sporer, et al. [47] examined the YSZ abradable coatings with porosity levels of 13, 21 and 27 % under the same conditions as described previously. Regardless of the test conditions, the 13 % porosity coating showed severe blade wear and material transfer onto the abradable coating. While the two more porous coatings cut well under all conditions.

While the cutting of ceramic abradable coatings with cBN tipped blades can be efficient, the use of these tipped blades presents two problems. [47] The first of these is limited oxidation resistance of cBN above 900 °C, meaning that while the blades may cut effectively during initial start-up rubs, over time their performance will reduce when used in the HPT.

Secondly, the use of tipped blades and time and costs in the production process, so the use of un-tipped metallic blades would be preferred. To examine this, a subsequent study was conducted on the same rig, using the same test parameters and similar coatings, this time examining the cutting of abradable coatings by un-tipped Inconel 718 blades [45, 46]. YSZ and DySZ abradable coatings with porosity levels of 24 and 30 %, respectively, were tested along with another YSZ abradable coating, this time containing 43 % porosity. Against the un-tipped blade, the 24 % porosity YSZ coating did not provide suitable abradability; under all the tested conditions severe coating rupture, blade wear and transfer of the blade material to the abradable coating were observed. However, when the porosity was increased to 43 %, the coating was found to cut well under all conditions, all of the worn surfaces of the YSZ abradable coatings are shown in Figure 8. The DySZ abradable coating exhibited good cutting at high blade tip speeds; however, when this was reduced, significant transfer of the blade material onto the abradable coating was seen.

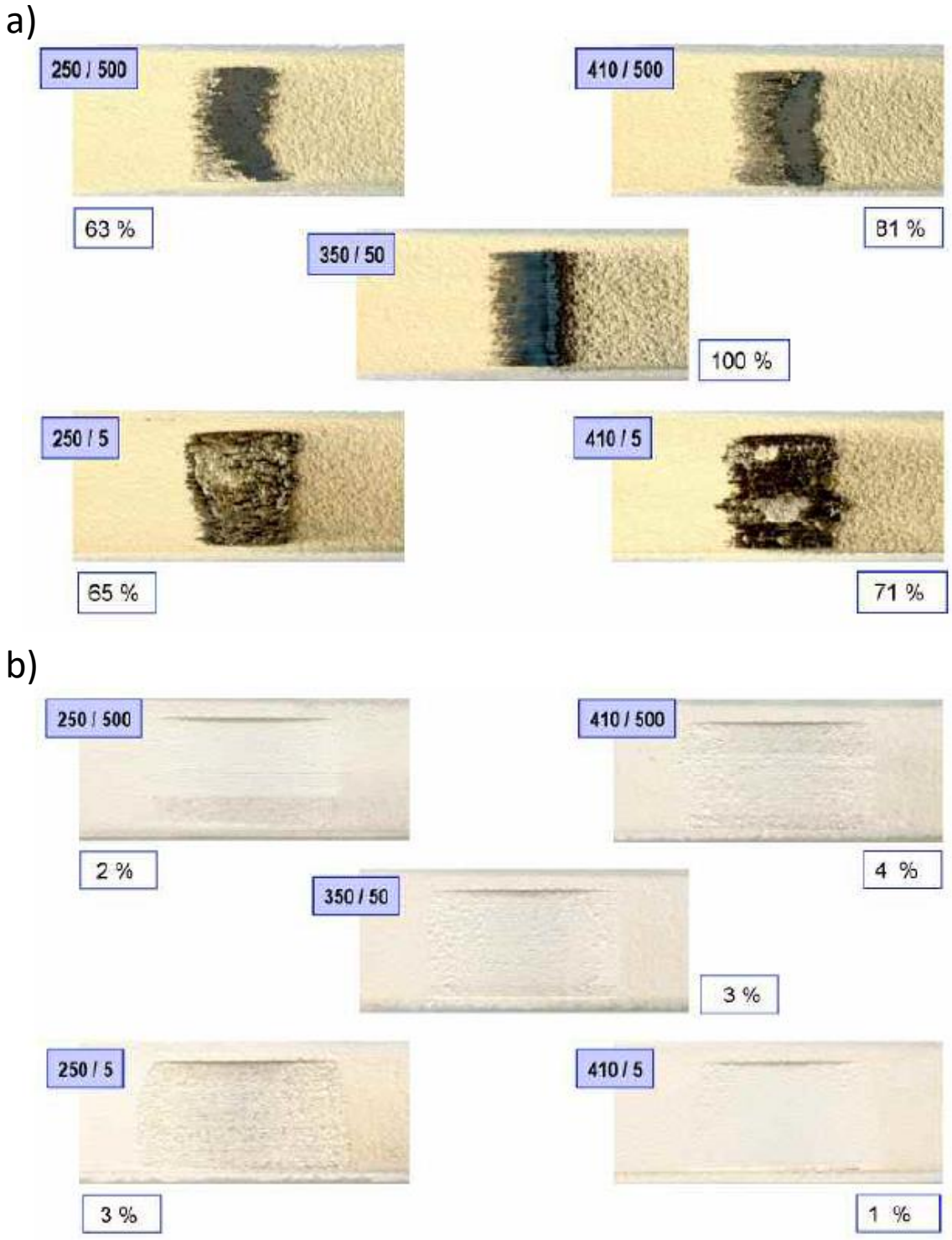

Figure 8. YSZ coatings after testing on the abradable test rig against un-tipped Inconel 718 blades, with the test conditions shown in the blue boxes and blade wear as a percentage of total incursion depth shown in the white boxes. The YSZ abradable coating with 24 % porosity, which cut poorly, with coating rupture and blade transfer visible, is shown in a), while b) shows the coating with 43 % porosity, which cut well under all conditions [45].

The authors used the results of this testing to create the wear maps shown in Figure 9; however, reference to the material of the abradable coating was made, only to the overall porosity level [45, 47, 67].

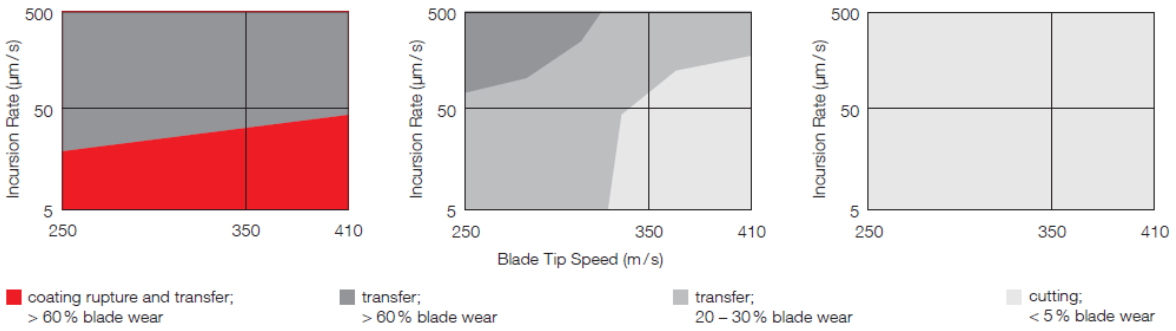

Figure 9. Wear maps of the ceramic abradable coatings with different porosity levels, showing the affect incursion rate and blade tip speed have on the wear mechanism when rubbed against un-tipped Inconel 718 blades [47, 67].

Finally, the same authors made a direct comparison between both un-tipped and cBN tipped Inconel 718 blades and abradable YSZ coatings [45]. This time, two YSZ coatings containing a blend of hBN and PE were prepared using APS. One YSZ abradable coating had a porosity of 15 %, a hardness of 95 HR15Y and a GE erosion number of 3.20 s/mil. The second YSZ abradable coating contained a porosity of 31 %, a hardness of 85 HR15Y and a GE erosion number of 0.73 s/mil. The harder, less porous coating was tested against the cBN tipped blades, while the softer, more porous coating was tested against the un-tipped Inconel 718 blades. For this series of tests, the temperature was reduced to 850 °C, the incursion rate was fixed at 50 µm/s and blade tip speeds of 250, 350 and 410 m/s were used. Against the cBN tipped blade, the harder YSZ coating cut well under all conditions, while against the un-tipped blade, the softer YSZ coating's wear mechanism was dependant on the blade tip speed. At 250 m/s and 350 m/s, severe blade material transfer was observed, while at 410 m/s, blade wear was reduced; however, coating rupture was prominent. This series of work using the Oerlikon Metco abradable test rig has shown that while abradable ceramic TBC materials can be cut well with cBN tipped blades, the effectiveness of un-tipped blades is very much dependent on the coating microstructure and the parameters under which the coating is being worn.

While YSZ is a widely used TBC material, its operation above 1200 °C is limited. More recently, research has focused on magnesia-alumina-spinel TBCs, and abradable TBCs for use at higher temperatures. Steinke, et al. [55] tested a variety of magnesia-alumina-spinel abradable coatings deposited by varying APS spray parameters, also using the Oerlikon Metco abradable test rig. Generally speaking, the abradable coatings with the lowest hardness (~HV400) and highest porosity (>20 %) cut well while the harder (>600HV) and less porous (>15 %) coatings exhibited high blade wear. Rolls-Royce has also tested magnesia-alumina-spinel abradable coatings against cBN tipped blades using the Oerlikon Metco abradable test rig [56]. Despite limited information regarding the test conditions and results, the authors suggested that the coating cut well with minimal wear to the blade.

While the study of abradable TBC materials is somewhat mature, research into abradable EBCs, especially when considering wear/abradability performance is limited. In one of the only studies on such coatings, Guo, et al. [58] tested BSAS EBCs containing 4 wt.% and 8 wt.% PE against untipped DD6 single crystal superalloy blades. An uncoated SiC CMC was also tested as a control. The rig, at the Beijing General Research Institute of Mining and Metallurgy, was similar to the setups described previously. Parameters of blade tip speed of 450 m/s, temperature of 1100 °C, incursion rate of 30 µm/s, and fixed incursion feed depth of 380 µm were used. To quantify the abradability, the blade wear as a percentage of total incursion depth was calculated. Higher values for this parameter indicate minimal cutting of the abradable and severe blade wear, while low values indicate good cutting behaviour and minimal blade wear. For the uncoated CMC this value was 86.1 % and material transfer from the blade was observed on the surface of the CMC. The abradable coating containing 4 wt.% PE reduced this figure to 69.2 %, and the 8 wt.% PE coating reduced this even further to 22.4 %. This value is still relatively high, and the worn surfaces of the CMC and abradable EBCs, shown in Figure 10, exhibit signs of material transfer and poor cutting.

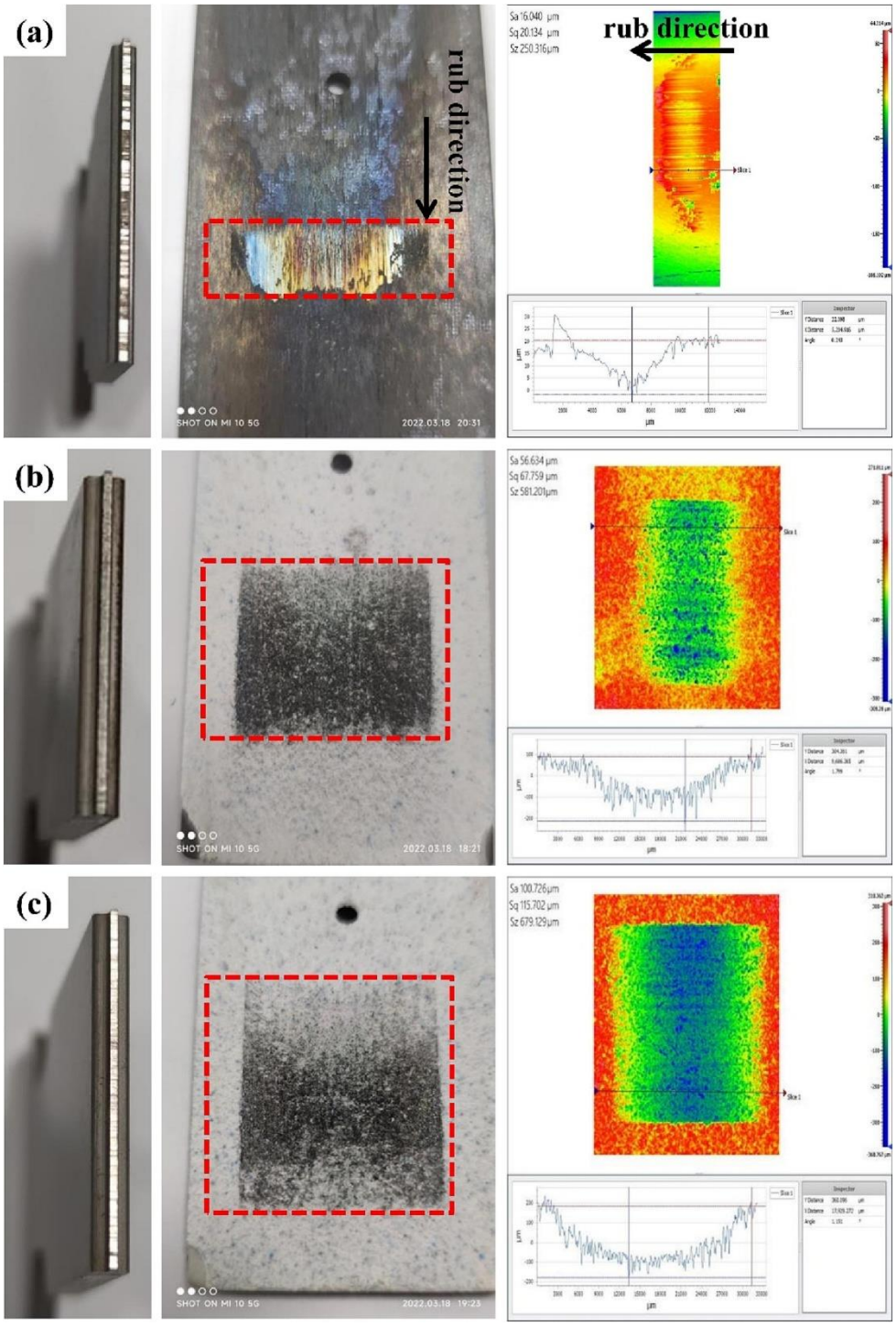

Figure 10. Abradable rig test results of a) uncoated SiC CMC, b) BSAS abradable EBC containing 4 wt.% PE and c) BSAS abradable EBC containing 8 wt.% PE [58]. Images indicate (from left to right) the dummy blade tip, the worn surface of the abradable coating, and the topography of wear scars.

2.2. Environmental barrier coatings

While abradable coatings are typically designed to be highly porous, the design considerations for EBCs are significantly different. They must provide a gas-tight seal above the SiC CMC components, protecting them from the extreme environments and corrosive species found in gas turbine hot sections. The CMCs themselves are advantageous when compared to Ni-based superalloys due to their superior high temperature strength and strength-to -weight ratio relative to Ni-based superalloys (as can be seen in Figure 11), their implementation is not straightforward [2]. The primary concern being the recession of the SiC by steam corrosion. While in the presence of air at high temperature, SiC will form a protective SiO_2 scale, limiting further oxidation of the SiC [71]. If water vapour (a combustion product found in the gas turbine) is introduced into the environment, this will react with SiO_2, leading to recession of the ceramic, as per Equation 1 [72].

$$SiO_2 + 2H_2O\ (g) \rightarrow Si(OH)_4\ (g) \quad \text{(Equation 1)}$$

Under typical turbine operating conditions, it has been estimated that recession could be as high as 1 µm/h under normal turbine operating conditions [73, 74], an unacceptable number considering the components would be expected to withstand 30,000 hours of service without maintenance [9]. To combat this, protective EBCs have had to be developed.

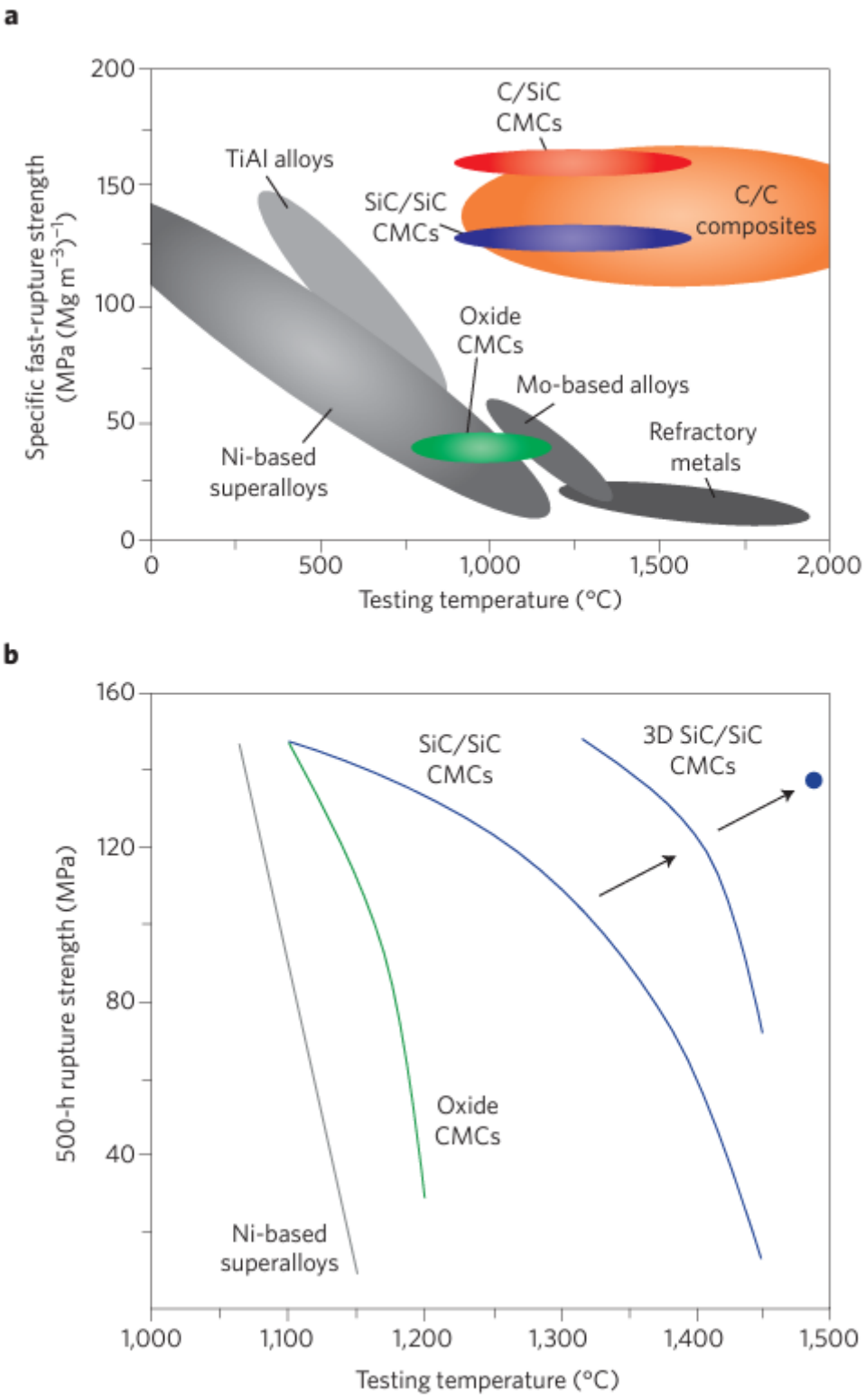

Figure 11. High-temperature mechanical properties of various materials where a) shows the specific fast-rupture strength as a function of the temperature of various metals and composites while b) shows the 500-hour rupture strength as a function of temperature of Ni-

based superalloys, oxide CMCs and various SiC/SiC CMCs. The point on the right is the 300-hour rupture strength [2].

As well as resistance to silica volatilisation, the EBC must also exhibit a coefficient of thermal expansion (CTE) similar to that of the CMC, SiC itself has a CTE of 4.5-5.5 $\times 10^{-6}$ °C [4]. Due to the repetitive heating to extreme temperature and then cooling the CMC system will undergo, a large difference in CTE will lead to a build-up of thermally induced stresses and eventually cracking and failure of the EBC. The first generation of EBCs, produced in the 1990s, were based on mullite [75]. While it exhibited a CTE similar to that of SiC, (5-6 $\times 10^{-6}$ °C [4]), at temperatures above 1000 °C metastable amorphous mullite, which itself formed during the rapid cooling associated with plasma spray deposition, crystallised and formed cracks in the coating [76]. Mullite was also found to have a high silica activity when exposed to high temperature water vapour [77].

With this in mind, EBCs must also show phase stability across the working temperature range, as any phase changes will also be accompanied by an associated volume change, which could also lead to cracking of the coating, as seen with mullite EBCs. The next iteration of EBCs was based around BSAS, which had lower silica activity in water vapour than mullite, as well as a CTE of 4-5 x10^{-6} °C [4]. Above 1400 °C, a reaction occurs between BSAS and silica formed from oxidation of the Si bond coat used to improve adhesion between the EBC and CMC [78]. This reaction formed a glass phase that was molten at 1300 °C and could be blown away by the high velocity gas in the turbine, leading to rapid recession of the EBC. Interfacial porosity was also formed due to the BSAS-silica reaction, leading to spallation of the coating. This limited the use of BSAS EBCs to environments where the temperature did not exceed 1300 °C. This discovery led to a further requirement for EBCs, chemical compatibility with the bond coat and substrate.

Given the now more well-defined requirements for EBCs, in the late 1990s and early 2000s, NASA embarked on the Ultraefficient Engine Technology Program (UEET) to develop EBCs that could withstand temperatures of ~1500 °C and sustain ~1300 °C EBC/substrate temperatures for thousands of hours [4]. Initially, due to their low silica activity in water vapour, rare earth monosilicates (RE_2SiO_5 where RE is rare earth) were investigated, specifically the program identified ytterbium monosilicate (Yb_2SiO_5 or YbMS) as a candidate

for EBCs. However, despite excellent resistance to silica volatilisation and phase stability, the CTE of YbMS (7.1-7.4 x10^{-6} °C [79]) proved problematic and led to through cracking during thermal cycling in the presence of water vapour [80]. Subsequently, attention turned to ytterbium disilicate ($Yb_2Si_2O_7$ or YbDS), which despite showing higher silica activity than YbMS, had a CTE very similar to that of SiC (3.6-4.5 x10^{-6} °C [81, 82]). Unlike other rare earth disilicates, YbDS does not undergo phase changes, presenting a single polymorph over the operating temperature range. As such YbDS has become the material of choice in the current generation of EBCs.

2.2.1. Plasma spraying of environmental barrier coatings

Due to the success of thermal spray processes, particularly APS, in reliably applying TBCs to gas turbines, this technique has also been widely adopted for the deposition of EBCs as well. Despite this, plasma spraying of EBCs, specifically YbDS EBCs, is not without drawbacks. This is largely due to the extreme temperatures found within the plasma, inducing phase changes within the feedstock material. During the APS process, YbDS was found to transform into YbMS. Richards et al. [83] proposed this was due to the higher vapour pressure of the Si bearing species leading to its preferential volatilisation at elevated temperatures above ~1000 °C, resulting in the formation of YbMS. Between 1300 and 2500 °C the vapour pressure of the Si bearing species was ~10^6 times larger than the vapour pressure of the Yb bearing species [83]. On top of this, the extreme cooling rates experienced by the molten particles as they impinge the substrate leads to the formation of metastable and amorphous phases. This means rare earth silicate EBCs typically require post-spray heat treatment to form fully crystalline coatings. To this end, many studies have been undertaken regarding the optimisation of YbDS deposition.

In an effort to reduce the cooling rates experienced by the molten particles, EBCs have been deposited on to substrates that are held at high temperature within a furnace during the deposition process. Work by Richards, et al. [83] found that when deposited onto substrates heated to 1200 °C, as-sprayed YbDS coatings showed almost no amorphous phase content. Despite this, a metastable YbMS phase (P21/c) was detected, upon post spray heat treatment at 1300 °C for 20 hrs, this phase had transformed into the stable I2/a phase. This work was expanded by Huang, et al. [84], who investigated the effect of deposition temperature on the phase composition and microstructure of YbDS EBCs. Substrates were

heated to 500, 900, 1000 and 1100 °C and YbDS coatings were deposited. The degree of crystallinity increased from 34.4 % for the 500 °C coatings to 94.8 % for the 1100 °C samples. Contrary to this, the YbMS secondary phase content increased with substrate temperature, from 40.3 wt.% to 60.5 wt.% for the 500 and 1100 °C samples respectively. Interestingly, a bimodal porosity distribution was observed in all the coatings, regardless of substrate temperature. For the 500 °C coatings a low porosity region was formed towards the coating-substrate interface. While for the 900, 1000 and 1100 °C coatings, a high porosity region was formed towards the interface, and a lower porosity region towards the surface. As the substrate temperature increased, the thickness of this low porosity region decreased. Despite the benefits in terms of phase crystallinity, depositing EBCs on to furnace heated substrates is unlikely to be feasible when considering component scale spraying.

The influence of the process parameters used during plasma spray deposition is also understood to be key in determining the phase composition and microstructure of YbDS EBCs. Richards, et al [83] changed the spray power by systematically varying the arc current and the secondary process gas (in this case H_2) flow. As the spray power increased, so did the amount of precipitated YbMS phase, increasing from ~9 vol.% for a coating deposited using 10.6 kW to ~24 vol.% for the 13.3 kW coating. Increasing the spray power also led to increased splat aspect ratios, indicating higher particle temperatures and velocities, as well as increasing the microcrack density. This was followed by a similar study by Garcia et al. [85] whereby YbDS EBCs were also deposited with varied spray powers by adjustment of the secondary process gas (H_2) flow. Gas flows of 3, 4.5, 6 and 9 SLM were used, resulting in spray powers of 30.7, 32.0, 34.2 and 36.4 kW respectively. This time, inflight measurements of the particle velocity and temperature were taken using a Tecnar DPV 2000 diagnostic sensor. While the particle velocity remained stable, between 165 and 169 m/s, regardless of spray power, an increase in particle temperature with increasing spray power was observed, with the particle temperatures being measured at 1768, 1955, 1966 and 2058 °C, respectively for the increasing spray powers. Increasing spray power led to an increase in silica volatilisation and the formation of a secondary YbMS phase, which also led to the CTE of the coating increasing. The coating deposited at the lowest spray power exhibited high porosity (14 %), while porosity for the coatings deposited at the higher powers were all low

(2, 3 and 4 % respectively). The microstructures and XRD patterns of the coatings produced using the lowest and highest spray powers are shown in Figure 12.

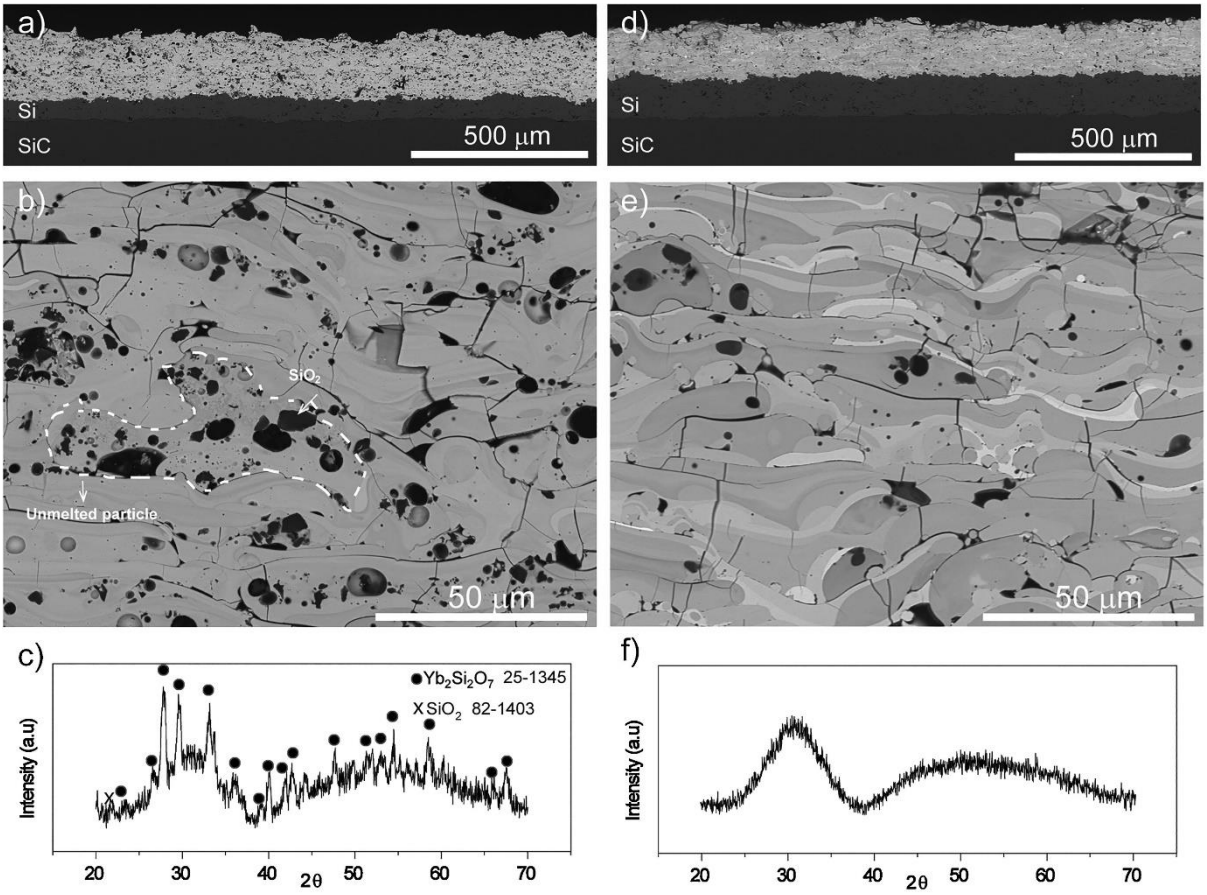

Figure 12. Microstructures of the YbDS EBCs deposited onto SiC substrates with an Si bond coat produced using a low and high spray power [85]. Where a) and b) show the microstructure and c) shows the XRD pattern of the coating produced using low power, while d) and e) show the microstructure and f) shows the XRD pattern of the coating produced using high power. The higher degree of porosity is visible in the microstructure while the increased level of crystallinity can be seen in XRD pattern of the coating produced using low power.

The findings of this study were largely confirmed by subsequent studies [86, 87]. Following a similar methodology, Chen, et al. [88] used three discrete spray parameter configurations to deposit YbDS EBCs under low, medium and high enthalpy conditions achieved by reducing the Ar/H_2 flow ratio. Again, increasing the enthalpy was found to increase particle temperatures in-flight (1962, 2156 and 2330 °C for the low, medium and high enthalpy conditions respectively), increase the YbMS phase content in the deposited coatings (32.8,

41.2 and 65.3 vol.%) and increase the CTE of the coatings (5.01 x10^{-6} °C for the low enthalpy condition and 6.37 x10^{-6} °C for the high enthalpy). Another similar study was conducted by Li, et al. [89], whereby YbDS EBCs were deposited using spray powers of 36.0, 39.0, 42.3 and 45.5 kW. As the spray power increased, the degree of crystallinity in the as-sprayed coatings decreased. Similarly, after heat treatment, the amount of YbMS was found to be much higher in the coatings deposited using the highest spray powers. Interestingly, the spray power was found to have a minimal impact on the porosity of the coatings, with all the coatings presenting a porosity of between 4 and 5 %. While the spray power, and therefore particle temperature, has been shown to be instrumental in the phase composition and microstructure of APS YbDS EBCs, the effect of particle velocity has also been investigated. Vaßen, et al. [90] created high velocity plasma conditions by increasing the primary process gas (Ar) flow and reducing the diameter of the torch exit nozzle. For the high velocity conditions, the as-sprayed coatings contained 4 wt.% YbMS, with ~95% crystallinity. While the conventional APS conditions contained 5 wt.% YbMS and 50 wt.% or less crystallinity. Despite the low YbMS phase content and high degree of crystallinity, the high velocity coatings had a porous microstructure (>15 %), unsuitable for use as an gas-tight EBC. The same authors also deposited YbDS using very low-pressure plasma spray (VLPPS), in a controlled atmosphere [91, 92]. This technique produced a highly crystalline (2 wt.% amorphous content) EBC with minimal YbMS secondary phase (5 wt.%). A dense microstructure with 3.6 % porosity that was free from cracks was also achieved. This was attributed to the ability to maintain the substrate temperature at 1000 °C prior to spraying and the use of the plasma flame to reduce the post-deposition cooling rate however the economics and size limitations of the controlled atmosphere chamber would likely prevent this technique from becoming widely adopted in industry.

In an attempt to reduce the occurrence of the secondary YbMS during APS, modified YbDS feedstocks have also been investigated. This involves using a silica rich feedstock to counteract the silica volatilisation from YbDS during the spray process. Garcia, et al. [85] used a feedstock powder containing 27.8 mol.% Yb_2O_3 and 72.2 mol.% SiO_2 (with YbDS containing 33.3 mol.% Yb_2O_3 and 66.6 mol.% SiO_2) and found that by controlling the spray power, a coating containing 99 mol.% YbDS could be achieved. Conversely, the same authors leveraged this phenomenon in the opposite direction, taking advantage of the

inherent silica volatilisation to deliberately produce a mixed phase, composite coating containing 53 vol.% YbDS and 47 vol.% YbMS from a YbDS feedstock [93]. Upon heat treatment, the coating was found to have crack healing properties, due to the transformation of metastable YbDS and YbMS phases. A variety of Yb silicate compositions were deposited by Zhu, et al. [94] who also found that silica rich feedstocks could lead to reduced YbMS phase content in the EBC, however, this did result in increased coating porosity. Highly crystalline YbDS EBCs have also been achieved through the use of suspension [95, 96] and solution precursor feedstocks [97].

2.2.2. Steam corrosion of environmental barrier coatings

The primary role of EBCs is to provide a gas tight seal, protecting the CMC component from the harsh environment found within the turbine hot section which could lead to recession and failure. Because of this, the research effort in YbDS EBCs has largely been focused on their performance in the presence of high temperature, flowing water vapour. Several studies have investigated the effects of high temperature steam corrosion on YbDS, both sintered pellets [98-100] and plasma sprayed coatings [60, 96, 101-106]. Typically, in the presence of high temperature water vapour, YbDS will form a gaseous silicon hydroxide, leaving behind a porous YbMS scale, as shown in Equation 2.

$$Yb_2Si_2O_7 + 2H_2O\ (g) \rightarrow Yb_2SiO_5 + Si(OH)_4\ (g) \quad \text{(Equation 2)}$$

Despite undergoing a similar corrosion process, the recession rates of YbDS are much lower than SiC, and the remaining YbMS layer still offers a level of protection. A schematic demonstrating this mechanism is shown in Figure 13. Instead of YbMS formation, some researchers have reported YbDS enrichment of the surface [60, 105]. Typically, YbDS EBCs are applied by APS; however, as previously explained, this leads to some silica volatilisation, leading to a mixed Yb-silicate phase composition. It is this YbMS, formed during the deposition process, that is depleted during high temperature water vapour exposure, forming a YbDS rich surface layer. This mechanism has tentatively been attributed to alumina impurities present, usually occurring from the furnace tubes used for the steam exposure test [60, 105]. In fact, the presence of alumina, either within the coating or as an impurity from the furnace has been shown to be beneficial and preventing silica volatilisation. The reaction with YbMS has been shown to form a protective ytterbium

aluminium garnet ($Yb_3Al_5O_{12}$ or YbAG) layer on the surface of the coating, thus preventing the YbMS rich reaction layer from forming [60, 105]. Paksoy, et al. [98] have shown that YbAG is very effective at preventing steam corrosion of YbDS based EBCs, eliminating the volatilisation of silica during high temperature steam exposure [99].

Another challenge affecting EBC systems at high temperatures is the growth of a silica layer, known as a thermally grown oxide (TGO), on the interface between the coating and Si bond coat. Diffusion of oxidisers through the EBC during high temperature exposure can lead to the formation of the TGO. While formed and stable at high temperature, this silica layer undergoes a phase transformation from β-cristobalite to α-cristobalite at ~220 °C upon cooling. Associated with this phase change is a volume shrinkage of ~4.5 %, which can lead to crack formation and spallation of the EBC at the EBC-bond coat interface. The process of TGO formation is also shown in Figure 13 [80, 101] [107].

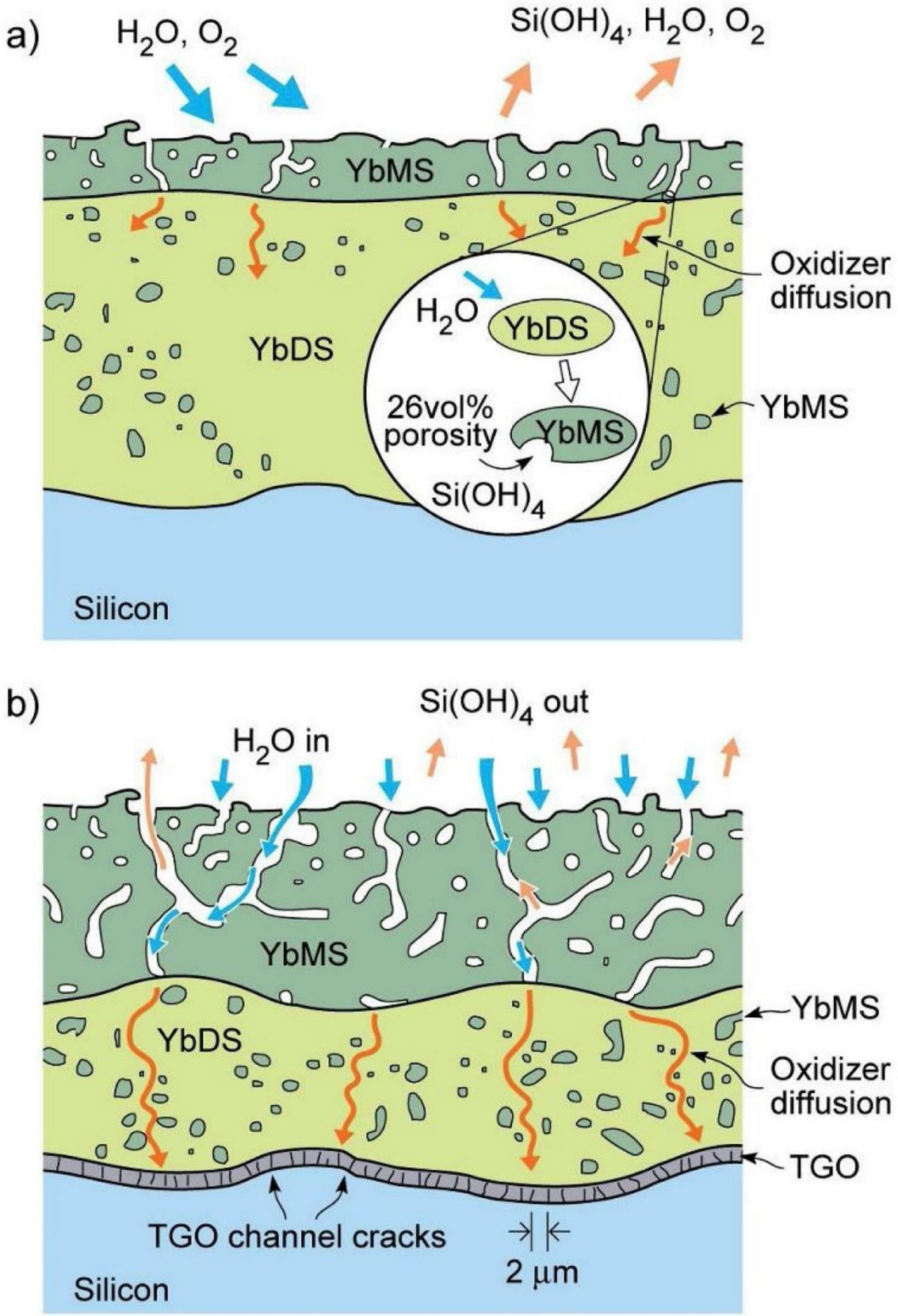

Figure 13. Schematic showing the a) early stage and b) late stage of silica volatilisation and bond coat TGO formation of a YbDS EBC exposed to high temperature steam [101].

Despite the amount of research that has gone into this topic, there is no clearly defined protocol to enable direct comparison of results. This is due to variations in methods of sample production, the process parameters used within these methods, the microstructure and phase composition of the tested samples and testing setups and conditions. Typically, these rigs feature a furnace in which samples are held at high temperature; this can either be isothermal or cycling between low and high temperature, a separate furnace to generate steam and a compressed air line to generate the high velocity steam. A summary of various YbDS high temperature steam exposure testing is shown in Table 1. The preparation method (coating or sintered pellet) is reported, as well as the test conditions, phase composition and porosity (if known) before the test. The phase composition after the test is also reported, along with, where data was available, the volatilisation (mass loss per unit surface area) or the volatilisation rate.

Early work on the steam corrosion testing of EBC materials showed that YbMS showed lower silica activity, thus offering better protection than YbDS [4, 108], however, much of this work was conducted using sintered pellets as opposed to thermal spray coatings. When YbMS was applied as a coating, mud cracking, due to thermomechanical incompatibility of the systems, led to the formation of diffusion/volatilisation pathways through the coating, leading to rapid oxidisation of the bond coat and fracturing of the TGO during thermal cycling and delamination of the coating [107]. Subsequently much work on the steam corrosion of EBCs has focused on YbDS, deposited using APS. While differences in materials and testing protocol remain, some studies are worth highlighting. When considering sintered YbDS pellets, Ridley and Opila [100] determined the silica volatilisation showed parabolic kinetics, with volatilisation increasing with exposure time and temperature. The rate of volatilisation was slowed by the formation of a YbMS reaction layer which, at high temperatures (>1300 °C) and steam velocities (>100 m/s), densified, acting as a barrier to gas transport. The effects of steam velocity was also investigated by Owusu, et al. [96]; however, in this case, increased steam velocities (5 m/s vs. 1 m/s) were found to increase the rate of recession due to an erosion phenomena. The added porosity of abradable EBCs was considered by Tejero Martin, et al. [60], who observed the formation of a protective YbAG layer rather than silica volatilisation. A YbDS-enriched layer was formed towards the

surface of the coatings; the thickness of this layer increased for the more porous abradable EBCs.

Table 1. Summary of the processing and testing conditions of various YbDS EBCs exposed to high temperature water vapour. The maximum volatilisation and/or volatilisation rate is shown where data was available.

Deposition method	**Testing conditions**	**Phase composition**	**Porosity**	**Phase composition (after high temperature steam exposure)**	**Recession**	**Recession rate**	**Reference**
Hot pressing at 1500 °C and 27.6 MPa in vacuum	Temperature: 1500 °C. Flow velocity: 4.4 cm/s. Composition: 50 %H_2O/10 % O_2. Testing up to 100 hrs	YbDS, trace YbMS	-	YbDS, trace YbMS, trace $Yb_3Al_5O_{12}$	-0.2 to -0.4 mg/cm^2 after 100 hrs	-	[4]
Cold pressing + sintering at 1600 °C	Temperature: 1500 °C. Flow velocity: 0.046 cm/s. Composition: 30 %H_2O/70 % O_2. Testing up to 100 hrs	-	-	-	-	-0.75 mg/cm^{2}h	[108]

Cold pressing + sintering at 1400 - 1600 °C	Temperature: 1500 °C. Flow velocity: 13 cm/s. Composition: 30 % H_2O/70 % air, 0.3 bar steam pressure. Testing up to 310 hrs	>99 wt.% YbDS	<5 %	-	-0.616 mg/cm^2 after 310 hrs	-	[109]
Spark plasma sintering at 1550 °C and 65 MPa	Temperature: 1200 °C. Flow velocity: up to 242 m/s. Composition: 1 atm steam pressure. Testing up to 250 hrs	>97 % YbDS	4 %	YbDS, YbMS, Yb_2O_3, $Yb_3Al_5O_{12}$	-	-0.008 mg^2/cm^4h	[100]
	Temperature: 1300 °C. Flow velocity: up to 242 m/s. Composition: 1 atm steam pressure. Testing up to 250 hrs					-0.022 mg^2/cm^4h	
	Temperature: 1400 °C. Flow velocity: up to 242 m/s. Composition: 1 atm					-0.042 mg^2/cm^4h	

	steam pressure. Testing up to 250 hrs						
Cold pressing + sintering at 1450 °C	Temperature: 1350 °C. Flow velocity: 19 cm/min. Composition: 5 % H_2O/95 % air. Testing up to 40 hrs	YbDS	7 %	52 % YbDS, 47 % YbMS	-12.6 mg/cm^2 after 40 hrs	-	[98]
		YbDS, 3 wt.% Al_2O_3 and trace $Yb_3Al_5O_{12}$	0 %	95 % YbDS, 5 % $Yb_3Al_5O_{12}$	0 mg/cm^2 after 40 hrs	-	
APS on Si bond coat and SiC CMC substrate	Temperature: 1350 °C. Flow velocity: 100 m/s. Composition: 5 % H_2O/95 % argon. Testing up to 750 hrs	YbDS, YbMS	-	YbDS, YbMS, $Yb_3Al_5O_{12}$	0.3 % weight gain after 750 hrs	-	[110]
APS on Si bond coat and SiC substrate	Temperature: 1316 °C. Flow velocity: 4.4 cm/s. Composition: 90 % H_2O/10 % O_2. Testing up to 2000 hrs	YbDS, YbMS	-	YbDS, YbMS	-	-	[101]

APS on Si bond coat and SiC substrate	Temperature: 1425 °C. Flow velocity: 15 cm/s. Composition: 100 % H_2O. Testing up to 100 hrs	54 wt.% YbDS, 46 wt.% YbMS	5.3 %	>99 wt.% YbDS	-0.71 mg/cm^2 after 100 hrs	-	[105, 106]
APS on Si bond coat and SiC substrate	Temperature: 1200 °C. Flow velocity: 100 m/s. Composition: 0.15 atm steam pressure. Testing up to 200 hrs	62 wt.% YbDS, 38 wt.% YbMS	2 %	32 wt.% YbDS, 68 wt.% YbMS	-	-	[111]
APS on Si bond coat and SiC substrate	Temperature: 1400 °C. Flow velocity: 90 m/s. Composition: 0.19 atm steam pressure. Testing up to 200 hrs	70 wt.% YbDS, 30 wt.% YbMS	7 %	5 wt.% YbDS, 95 wt.% YbMS	-0.3 mg/cm^2 after 200 hrs	-	[112]
APS on Si bond coat and SiC substrate	Temperature: 1316 °C. Flow velocity: 4.4 cm/s. Composition: 90 % H_2O/10 % O_2. Testing up to 2000 hrs	74 wt.% YbDS, 26 wt.% YbMS	-	30 wt.% YbDS, 70 wt.% YbMS	-	-	[104]

APS free-standing coatings	Temperature: 1350 °C. Flow velocity: 100 mm/s. Composition: 90 % H_20/10 % O_2. Testing up to 96 hrs	71 wt.% YbDS, 29 wt.% YbMS	2.4 %	86 wt.% YbDS, 8 wt.% YbMS, 7 wt.% $Yb_3Al_5O_{12}$	-	-	[60]
	Temperature: 1400 °C. Flow velocity: 100 mm/s. Composition: 90 % H_20/10 % O_2. Testing up to 96 hrs			79 wt.% YbDS, 4 wt.% YbMS, 17 wt.% $Yb_3Al_5O_{12}$			
	Temperature: 1350 °C. Flow velocity: 100 mm/s. Composition: 90 % H_20/10 % O_2. Testing up to 96 hrs	70 wt.% YbDS, 30 wt.% YbMS	21.3 %	87 wt.% YbDS, 13 wt.% YbMS	-	-	
	Temperature: 1400 °C. Flow velocity: 100 mm/s. Composition: 90 % H_20/10 % O_2. Testing up to 96 hrs			85 wt.% YbDS, 13 wt.% YbMS, 2 wt.% $Yb_3Al_5O_{12}$			
APS free-standing coating	Temperature: 1400 °C. Flow velocity: 2.5 x 10^4 m/s. Composition: 90 %	YbDS	-	YbDS, YbMS, $Yb_3Al_5O_{12}$	-	-	[103]

	H_20/10 % O_2. Testing up to 200 hrs						
SPS on Si bond coat and SiC substrate	Temperature: 1400 °C. Flow velocity: 1 m/s. Composition: 90 % H_20/10 % O_2. Testing up to 96 hrs	86 wt.% YbDS, 14 wt.% YbMS	11 %	27 wt.% YbDS, 73 wt.% YbMS	-0.045 mg/cm^2 after 96 hrs	-	[96]
	Temperature: 1400 °C. Flow velocity: 5 m/s. Composition: 90 % H_20/10 % O_2. Testing up to 96 hrs			56 wt.% YbDS, 44 wt.% YbMS	-22 mg/cm^2 after 96 hrs	-	

2.2.3. CMAS corrosion of environmental barrier coatings

While providing protection from steam recession is imperative, EBCs also need to be resistant to attack molten corrosive species such as CMAS. CMAS is an umbrella term for combinations of CaO, MgO, Al_2O_3 and SiO_2 originating from airborne sand or ash ingested by the turbine, which then, due to the operating temperatures of the turbine (>1200 °C), melts and adheres to the EBC surface [113-116]. Typical CMAS build-up on gas turbine components is shown in Figure 14. Perhaps the most infamous example is the eruption of the Icelandic volcano Eyjafjallajökull, which grounded air travel in 2010 due to the potential damage the ash cloud could cause. Researchers have studied the interaction between a variety of CMAS compositions with YbDS (both sintered pellets and thermal spray coatings) under a variety of fluxes, exposure times and temperatures [117].

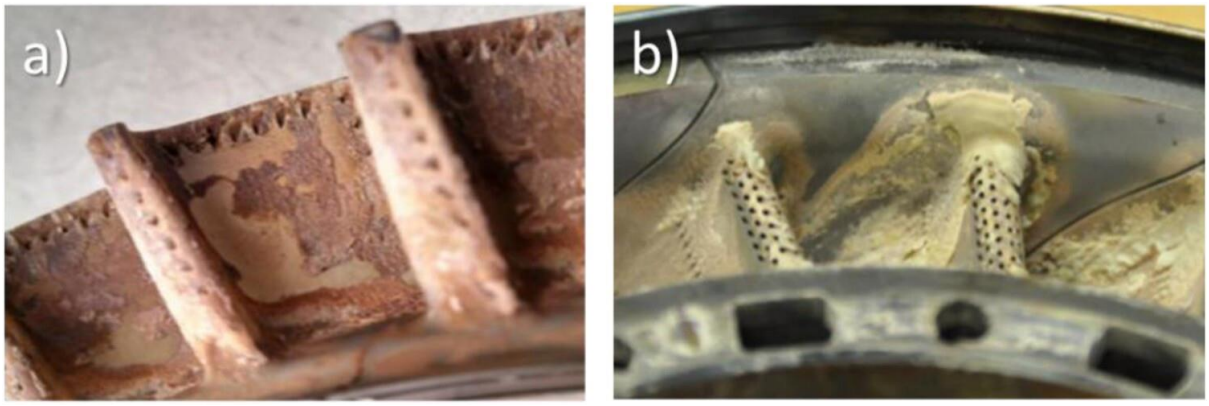

Figure 14. Typical CMAS build-up on a) blade and b) vane [118].

When observing sintered YbDS pellets, a minimal reaction between YbDS and CMAS has typically been described with penetration of the CMAS into the sintered body driven largely by grain boundary diffusion [115, 119-121]. However, when considering plasma sprayed coatings, the picture becomes more complex. A dissolution and reprecipitation process between YbDS and the CMAS melt is understood to be the primary corrosion mechanism [122]. Thermal spray coatings are also likely to contain at least some degree of porosity, through which CMAS may penetrate [59]. In addition, silica (SiO_2) volatilisation caused by the chemistry and temperature of the plasma during coating deposition leads to a mixed phase coating of YbDS and YbMS. Unlike YbDS, YbMS will tend to react with molten CMAS, given a high enough concentration of CaO in the melt, to form a ytterbium oxyapatite ($Ca_2Yb_8(SiO_4)_6O_2$ labelled Yb-apatite henceforth). The higher reactivity of YbMS can be

explained by the theory of optical basicity, as described by Nieto et al. [118] and Padture et al. [123]. The reactivity between an oxide glass and crystalline oxide will increase as the difference in optical basicity between the two increases. As YbMS has a larger optical basicity difference to CMAS than YbDS, YbMS is seen to be more reactive and hence more likely to form Yb-apatite. The formation of Yb-apatite is also dependant on the Ca:Si ratio of the CMAS itself [124]. At low Ca:Si ratios, below a certain threshold dependant on composition and temperature, Yb-apatite is unlikely to form, instead the dissolution of the Yb-silicates is driven by the solubility limit within the melt, with recession of the Yb-silicate only ceasing when this value is reached. At high Ca:Si ratios, Yb-apatite will form, consuming CaO from the melt, reducing the Ca:Si ratio until equilibrium is reached and the reaction stops.

In one of the first studies investigating the interaction of CMAS with plasma sprayed EBCs, Zhao et al. [125] showed that both YbDS and YbMS coatings were dissolved by molten CMAS and precipitated the same Yb-apatite phase. While in the YbMS coating this apatite phase formed a dense layer at the reaction front and the YbDS coating formed a porous, discontinuous Yb-apatite layer. Yb-apatite crystals precipitated preferentially around YbMS rich splats, formed during APS deposition of YbDS EBCs. Due to the lamellar structure of the splats, the formation of the Yb-apatite penetrated deep into the coating, leaving behind peninsulas of unreacted YbDS.

When examining the effect CaO content of CMAS, Zhou, et al. [126] found that the reaction between CMAS and YbDS rich or YbMS rich EBCs was dependent on the CaO concentration. When exposed to CaO rich CMAS (33 mol% CaO) both coatings formed a dense reaction layer, preventing further CMAS infiltration. While in the presence of CaO lean CMAS (19 mol% CaO), only reprecipitated YbDS crystals were observed, and CMAS rapidly infiltrated through grain boundaries. Zhong, et al. [127] demonstrated that relative to YbMS rich coatings, YbDS coatings showed an inability to prevent CMAS induced recession of the EBC. While a Yb-apatite phase was produced, it was porous and did not prevent further CMAS infiltration. While the reaction of YbDS and CMAS consumed CaO from the melt, it also produced a similar amount of SiO_2. Hence, the dissolution precipitation process continues until all the CaO in the CMAS melt is consumed. A porous apatite layer that was unable to prevent CMAS infiltration was also observed by Liu et al. [128]. After 50 hours of exposure

at 1350 °C and 25 hours at 1400 °C, this led to residual CMAS on the surface of the (thermally grown oxide) TGO, causing the accelerated failure of the EBC system.

While EBCs typically exhibit low levels of porosity, abradable EBCs are porous by design; this makes the infiltration of CMAS a much bigger problem. Tejero Martin et al. [59] showed that abradable EBCs were completely infiltrated with CMAS after 48 hrs exposure but that the high porosity of the abradable coatings may be useful for accommodating the strains associated with CMAS infiltration and reaction. Also of interest, especially when projecting conditions experienced by EBCs in service, is the combined effects of CMAS and other degradation mechanisms. Harder et al. [129] found that in the presence of CMAS and steam, TGO growth could be suppressed, while exposure to CMAS has been found to increase the erosion resistance of EBCs when tested simultaneously [130, 131].

Similarly to high temperature steam testing of YbDS EBCs, comparisons of the CMAS testing of such coatings are also difficult due to differences in sample preparation, CMAS composition, exposure times and temperatures. While much of the research into CMAS corrosion of YbDS EBCs has focused on sintered pellets, work has also been done to characterise the effects on thermal spray coatings. Nevertheless, a summary of experimental CMAS corrosion testing of YbDS EBCs is presented in Table 2, where the processing/deposition methods, CMAS compositions, test conditions and observed corrosion mechanisms are shown.

Table 2. Summary of YbDS EBC CMAS testing, showing processing/deposition methods, CMAS compositions, test conditions and observed corrosion mechanisms.

Deposition Method	CMAS composition	Test conditions	Corrosion mechanism	Reference
Cold pressed and sintered at 1500 °C	33 mol.% CaO-9 mol.% MgO-13 mol.% Al_2O_3-45 mol.% SiO_2	0.314 g/cm^2 at 1400 °C for 10 hrs in flowing steam	Dissolution of YbDS and formation of a porous reaction zone	[114]
Cold pressed and sintered at 1300 °C	33 mol.% CaO-9 mol.% MgO-13 mol.% Al_2O_3-45 mol.% SiO_2	35 mg/cm^2 at 1300 °C for 1 min - 96 hrs in air	CMAS penetration along grain boundaries, slow dissolution of YbDS	[115]
APS on to mullite, Si, SiC CMC substrate	33 mol.% CaO-9 mol.% MgO-13 mol.% Al_2O_3-45 mol.% SiO_2	36 mg/cm^2 at 1300 °C for 1 min - 96 hrs in air	CMAS interaction with YbDS led to changes in lattice spacing, alterations of the ambient temperature stresses, and large cracks in the CMAS that extend through the topcoat	[132]
APS on to mullite, Si, SiC substrate	33 mol.% CaO-9 mol.% MgO-13 mol.% Al_2O_3-45 mol.% SiO_2	30-35 mg CMAS pellet at 1300 °C for 1 min - 250 hrs in air	Inward diffusion of Ca, dissolution of YbDS, preferential formation of discontinuous Yb-apatite at YbMS splats	[125]

Spark plasma sintering at 1600 °C and 75 MPa	39.2 mol.% CaO-5.2 mol.% MgO-4.1 mol.% Al_2O_3-51.5 mol.% SiO_2	15 mg/cm^2 at 1500 °C for 1 - 24 hrs in air	CMAS penetration along grain boundaries-causing blister crack damage, slow dissolution of YbDS and precipitation of Yb-apatite	[121]
YbDS powder mixed with CMAS powder at 50:50 mol.%	30.67 mol.% CaO-8.25 mol.% MgO-12.81 mol.% Al_2O_3-48.27 mol.% SiO_2	YbDS and CMAS powder blend heated to 1200, 1300 and 1400 °C for 1 hr in air	Dissolution of YbDS and precipitation of Yb-apatite, as the CaO content of the CMAS reduced YbDS became the main reaction product	[119]
	24.82 mol.% CaO-9.08 mol.% MgO-14.24 mol.% Al_2O_3-51.86 mol.% SiO_2			
	6.74 mol.% CaO-8.89 mol.% MgO-14.23 mol.% Al_2O_3-70.14 mol.% SiO_2			
Hot pressed at 1550 °C and 30 MPa	33 mol.% CaO-9 mol.% MgO-13 mol.% Al_2O_3-45 mol.% SiO_2	30 mg/cm^2 at 1300 and 1500 °C for 50 hrs in air	At 1300 °C dissolution of YbDS and precipitation of Yb-apatite, at 1500 °C vigorous penetration of CMAS and formation of blister cracks	[133]
Spark plasma sintered YbDS containing 0, 10, 20 and 30 vol.% YbMS	33 mol.% CaO-9 mol.% MgO-13 mol.% Al_2O_3-45 mol.% SiO_2	35-45 mg/cm^2 at 1300 °C for 1 - 200 hrs in air	Dissolution of YbDS and precipitation of Yb-apatite, YbMS fractions over 20 vol.% showed improved resistance to CMAS due to	[134]

	21 mol.% CaO-9 mol.% MgO-13 mol.% Al_2O_3-57 mol.% SiO_2		increased Yb-apatite formation, a higher degree of CMAS infiltration was observed in the higher CaO CMAS	
PS-PVD on to SiC substrate	23.3 mol.% CaO-6.4 mol.% MgO-3.1 mol.% Al_2O_3-62.5 mol.% SiO_2-4.1 mol.% Na_2O-0.5 mol.% K_2O-0.04 mol.% Fe_2O_3	29 mg/cm^2 at 1300 °C for 1 - 10 hrs and 1400 °C for 1 hr in air	Coatings exposed at 1300 °C for 10 hrs and 1400 °C for 1 hr were fully infiltrated by CMAS. Dissolution of YbDS followed by precipitation of cyclosilicate, silicocarnotite, and YbDS at 1300 °C and YbDS at 1400 °C enabled CMAS to effectively infiltrate top coats	[135]
Hot pressed at 1500 °C	23.3 mol.% CaO-6.4 mol.% MgO-3.1 mol.% Al_2O_3-62.5 mol.% SiO_2-4.1 mol.% Na_2O-0.5 mol.% K_2O-0.04 mol.% Fe_2O_3	35 mg/cm^2 at 1200, 1300, 1400 and 1500 °C for 1 - 50 hrs in air	Dissolution and reprecipitation of YbDS and grain boundary penetration of CMAS at higher temperatures	[120]
Hot pressed at 1500 °C and 50 MPa	38 mol.% CaO- 5 mol.% MgO-4 mol.% Al_2O_3-50 mol.% SiO_2-1 mol.% Na_2O-1 mol.% K_2O-1 mol.% Fe_2O_3	20 mg/cm^2 at 1400 °C for 8 hrs in air	Dissolution of YbDS and precipitation of Yb-apatite	[136]

APS free-standing coatings	35 mol.% CaO-10 mol.% MgO-7 mol.% Al_2O_3-48 mol.% SiO_2	15 mg/cm^2 at 1350 °C for 1 and 48 hrs in air	Porous abradable EBCs show increased infiltration of CMAS through inter-splat pores after 1 hr, preferential dissolution of YbMS to form Yb-apatite, after 48 hrs all coatings completely infiltrated with CMAS	[59]
APS free-standing coatings	33 mol.% CaO-10 mol.% MgO-13 mol.% Al_2O_3-44 mol.% SiO_2	35 mg/cm^2 at 1400 °C for 25 and 50 hrs in air	Dissolution of YbDS and precipitation of a loose corrosion layer of precipitated Yb-apatite	[127]
APS YbMS top coat on YbDS and Si interlayers and SiC substrate	33 mol.% CaO-10 mol.% MgO-13 mol.% Al_2O_3-44 mol.% SiO_2	35 mg/cm^2 at 1300, 1350 and 1400 °C for 25 and 50 hrs in air	Dissolution of YbMS top coat and precipitation of Yb-garnet and Yb-apatite phases, precipitation of coarse Yb-apatite crystals in YbDS interlayer	[128]
Spark plasma sintered at 1700 °C and 75 MPa	39.2 mol.% CaO-5.2 mol.% MgO-4.1 mol.% Al_2O_3-51.5 mol.% SiO_2	15 mg/cm^2 at 1500 °C for 2 hrs in air, water quenched	CMAS penetration along grain boundaries and dissolution of YbDS, secondary-phase inclusions at grain boundaries (YBMS and Yb2O3) are filled with Yb-containing CMAS glass and distributed throughout the EBC	[137, 138]
APS on to Si bond coat and SiC substrate	30.67 mol.% CaO-8.25 mol.% MgO-12.81 mol.% Al_2O_3-48.27 mol.% SiO_2	2 mg/cm^2 at 1316 °C for 300 hrs in flowing steam	CMAS reduced TGO thickness, lower CaO content CMAS resulted in thinnest oxide	[129]

	24.82 mol.% CaO-9.08 mol.% MgO-114.24 mol.% Al_2O_3-51.86 mol.% SiO_2		however CMAS exposure led to premature coating delamination	
APS on to Si bond coat and SiC substrate	33 mol.% CaO-9 mol.% MgO-13 mol.% Al_2O_3-45 mol.% SiO_2	20 mg/cm^2 at 1300 °C for 25 and 50 hrs in air	CaO rich CMAS precipitated Yb-apatite, while CaO lean CMAS penetrated grain boundaries with limited reaction	[126]
	19 mol.% CaO-8 mol.% MgO-15 mol.% Al_2O_3-58 mol.% SiO_2			
APS on to Si bond coat and SiC substrate	30.67 mol.% CaO-8.25 mol.% MgO-12.81 mol.% Al_2O_3-48.27 mol.% SiO_2	2 and 4 mg/cm^2 at 1316 °C for 4 hrs in air	Dissolution of YbDS and precipitation of Yb-apatite, erosion resistance increased with CMAS loading	[131]

2.3. Gaps in literature

While current generation of YbDS EBCs can be considered somewhat mature as a research topic, the same cannot be said for abradable EBCs. Given the drastic differences in properties required of an EBC compared to an abradable coating, significant gaps in literature exist when considering the development of abradable EBCs.

While studies into the deposition of EBCs have been conducted, abradable EBCs require completely different microstructures and properties. The processing of EBCs has been tailored towards producing coatings with minimal porosity, to provide a gas-tight seal protecting the SiC CMC component. The opposite is true of abradable coatings, which are designed to be highly porous, new feedstocks and deposition conditions will need to be understood to optimise the required microstructural features such as porosity and phase composition.

How the increased level of porosity affects the resistance of the abradable EBC to corrosive species such as molten CMAS and water vapour will also need to be studied. While the performance of EBCs have been examined, the porosity of an abradable EBC will likely lead to a high degree of penetration of these corrosive species. In order for the lifetimes of abradable EBCs to be adequate it is crucial to understand what mechanisms and reactions lead to corrosion of the coatings and how severe this corrosion is. The laboratory testing of EBCs also needs improvement, typical thermo-chemical testing is isothermal and usually features only one corrosive species, while much of the limited mechanical testing has been performed at room temperature. Abradable EBCs will be required to operate in extreme environments, featuring many potentially damaging species, and undergoing many thermal cycles to extremely high temperatures. New testing regimes, featuring combined corrosion and thermal cycling should be developed to better represent the in-service conditions found with the gas turbine.

A balance between abradability and durability needs to be established. Abradable EBCs need to be soft enough to be easily cut be a turbine blade, yet hard enough to resist erosion by foreign bodies ingested by the turbine. Representative testing of the blade-abradable coating interactions using abradable test rigs are also yet to be studied, these are crucial for understanding and developing abradable EBCs.

2.4. Aims and objectives

The aim of this thesis was to investigate the processing-microstructure-performance relationships of abradable YbDS EBCs. To achieve this, abradable YbDS EBCs were deposited using APS under a variety of conditions. The resultant coatings were subsequently characterised using a variety of analytical techniques, such as scanning electron microscopy (SEM), X-ray diffraction (XRD) and porosity measurement. Once the deposition parameters had been optimised, coatings were produced and subjected to a variety of performance tests. The erosion and wear of the abradable EBCs was examined using specially designed test rigs. While abradable coatings have been used in gas turbines for decades, publicly accessible research into ceramic abradable coatings, especially abradable EBCs, is minimal. Finally, the resistance of the abradable EBCs to a variety of corrosive species commonly encountered under normal operation was investigated. These included exposure to high temperature steam and calcium-magnesium-alumino-silicates (CMAS). Combined corrosion and corrosion-wear studies were also conducted to observe any effects of combined degradation mechanisms on the abradable EBCs. Many researchers have conducted steam and CMAS corrosion studies of EBCs however, what is less well understood, is the effect the increased porosity levels of an abradable coating have on the protective requirements of an EBC. While most of these previous studies have investigated one corrosion mechanism in isolation, what is more representative of in-service conditions, is a combination of degradation mechanisms taking place simultaneously. Given this, four key objectives were defined as the goals for this thesis:

- To deposit abradable EBCs with a variety of porosity levels using APS and to subsequently understand the relationship between processing, microstructure, phase composition and performance (both mechanical and corrosion). The spray parameters affecting the temperature and velocity of the feedstock particles in flight will be systematically adjusted, and the effect on porosity and microhardness examined.
- To understand how the porosity level of an abradable coating effects the wear and mechanics under blade tip rub conditions, in an effort to optimise performance and efficiency. This will be achieved by producing abradable EBCs with three distinct

porosity levels and investigating their comparative abradbaility using a specially designed test rig.

- To understand how the porosity level of an abradable coating effects the high temperature steam and CMAS corrosion resistance. Resistance to these corrosive species is instrumental for EBC longevity in service. The abradable EBCs will be exposed to high temperature, isothermal corrosion tests, whereby the corrosion mechanisms and resulting changes in the coatings will be analysed to understand its suitability for use in HPT sections.
- To understand how combined corrosive test methodologies, more closely related to in-service conditions create synergies and/or discordant effects which have previously been understudied. The abradable EBCs will be exposed to high temperature, isothermal combined corrosion tests and any changes in corrosion mechanism and coating composition and microstructure will be characterised and compared to the results of isolated steam and CMAS exposure.

Chapter 3: Experimental methods

This chapter covers the principles and theories behind the experimental and characterisation techniques used throughout this work. More detailed explanation of specific parameters, measurements and materials are given in the materials and methods section of each chapter individually.

3.1. Coating deposition

The Praxair SG-100 plasma spray torch (Praxair Surface Technology, USA) is a high-performance thermal spray system used to apply coatings to materials by projecting molten particles at high velocities onto a substrate. It operates on the principle of plasma spraying, which is part of the thermal spray family. A combination of gases, in this case argon and hydrogen flow through the torch. A high-voltage electrical arc is struck between a cathode (tungsten) and an anode (copper) inside the torch. This arc ionizes the gas, transforming it into a high-temperature plasma. The coating material, in the form of fine powder, is fed into the plasma jet radially. The powder particles are accelerated, heated and melted as they travel through the plasma jet. The velocity and temperature depend on the gas mixture, arc current, and other operating parameters. The high-velocity molten particles are projected onto the substrate. When they hit the surface, they flatten and cool rapidly, forming a coating layer. This process is repeated as more particles accumulate to create a dense, well-adhered coating. The torch is controlled by a six-axis robot, operating in a raster pattern.

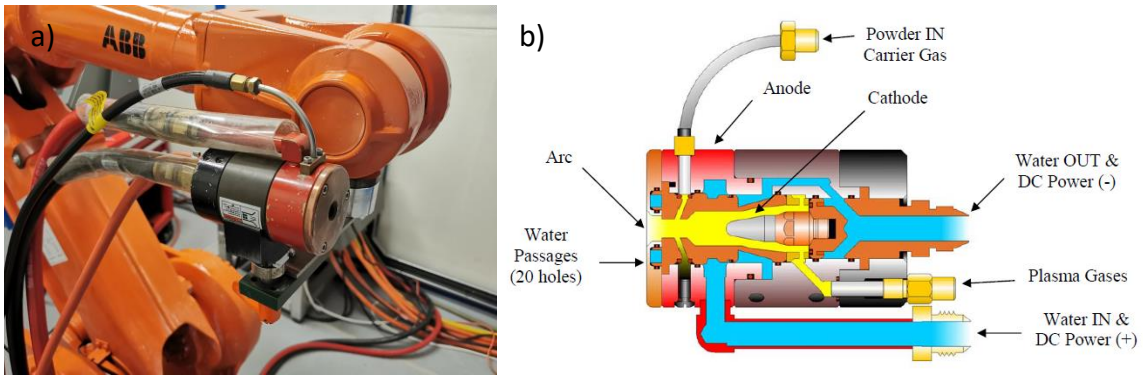

Figure 15. Images of the Praxair SG-100 plasma spray torch used throughout this work, where a) shows the torch mounted on the six-axis robot, and b) shows a diagram of the torch internal design [139].

The SG-100 torch uses an array of anode and cathode designs and geometries depending on the material to be deposited. Throughout this study the torch was fitted with a 02083-175 anode, 02083-120 cathode and a 03083-112 gas injector (all Praxair Surface Technology, USA), these are shown in Figure 16. These designs are known as sub-sonic configurations and are specially designed for the deposition of ceramic materials. The sub-sonic refers to the particle velocity achieved during the deposition process, slower particle velocities mean the feedstock powder spends longer in the plasma, which helps to fully melt ceramic materials which may have relatively high melting points.

a)

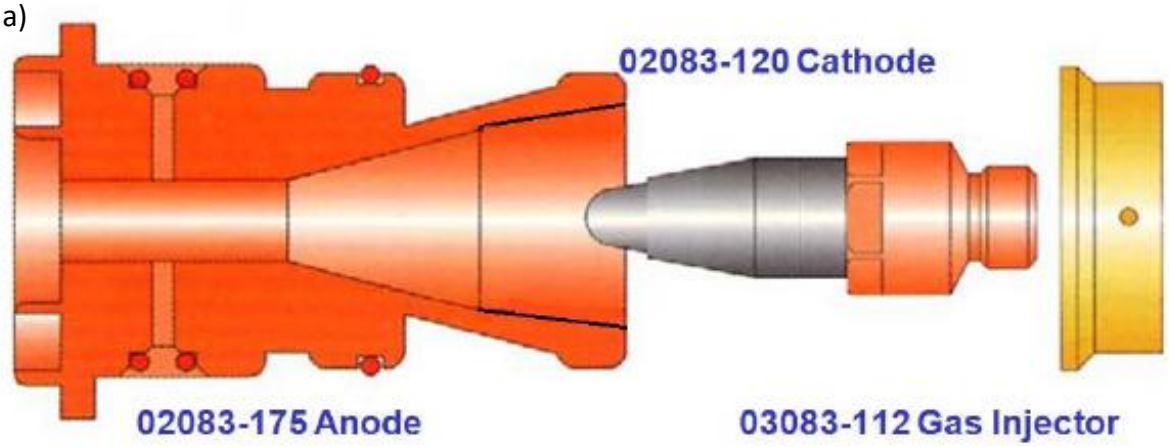
02083-120 Cathode
02083-175 Anode
03083-112 Gas Injector

b)

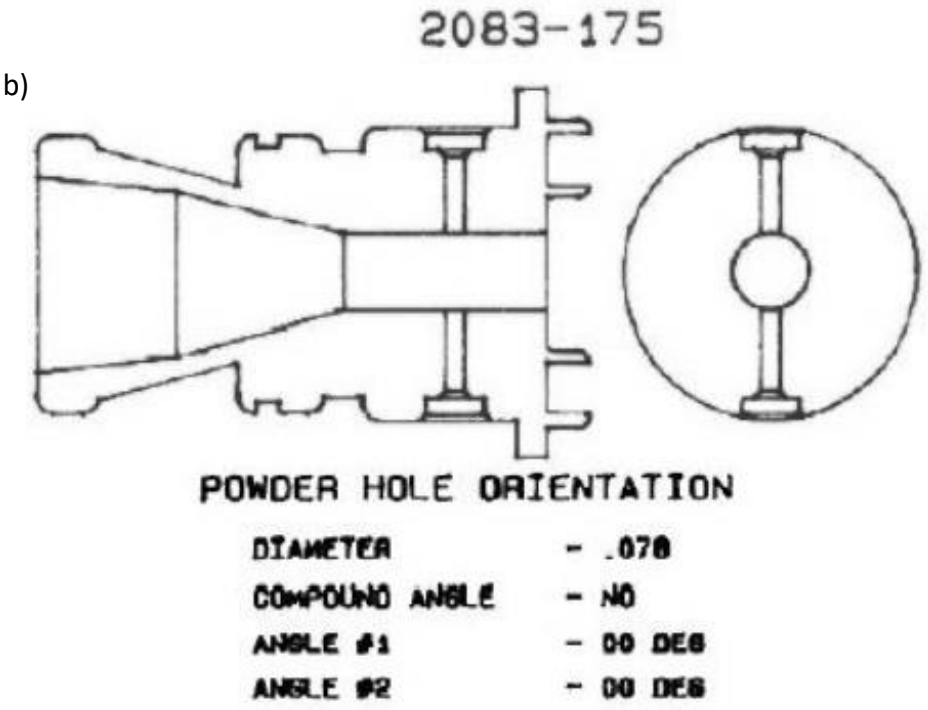
2083-175
POWDER HOLE ORIENTATION
DIAMETER - .070
COMPOUND ANGLE - NO
ANGLE #1 - 00 DEG
ANGLE #2 - 00 DEG

c)

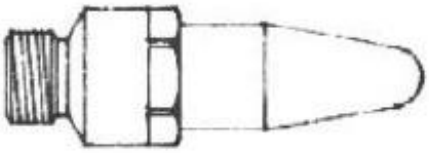
2083-120
80KW MACH I
40KW SUBSONIC

d)

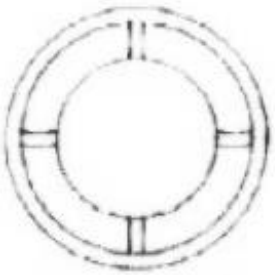
3083-112
SUBSONIC
LAMINAR FLOW

Figure 16. Schematics of the a) electrode and gas injector configuration, b) anode, c) cathode and d) gas injector used in this study [139]. For reference, the anode is ~70 mm was length, while the cathode is ~50 mm in length.

The feedstock powder is fed using a Praxair 1264 powder feeder (Praxair Surface Technology, USA). The powder is stored in a sealed and heated hopper. An inert carrier gas, in this case nitrogen, enters the feeder and helps transport the powder to the plasma spray torch. The hopper contains a rotating feed disc with evenly spaced holes that hold an amount of powder. As the disc rotates, it picks up powder from the hopper in these slots. The rotation of the wheel ensures that the powder is delivered consistently to the outlet. As the powder-filled pockets pass over the gas inlet, the carrier gas picks up the powder and transports it out of the feeder through a feed tube to the torch. The pressure and flow rate of the carrier gas and rotational speed of the feed disc are controlled to ensure stable powder flow to the torch. Powders used for APS coatings typically have a size range of 45 – 125 µm.

The substrates used in this thesis are shown in Figure 17. They are 25 mm diameter reaction bonded SiC disc (JAI Engineering, UK) used in Chapter 4 and 6, stainless steel test plates 50 x 50 mm and 5 mm thick, designed to be fixed into the abradable test rig used in Chapter 5 and graphite plate (GPE Scientific Ltd., UK), 60 mm x 20 mm x 5 mm thickness, were used to create the free-standing coatings in Chapters 6 and 7. The substrates were mounted on a clamping rail, with built in compressed air lines, to control substrate temperature during heating, shown in Figure 18. To reduce any batch-to-batch variation all the coatings analysed within this work were deposited in a single spray run after the initial parametric study presented in Chapter 4.

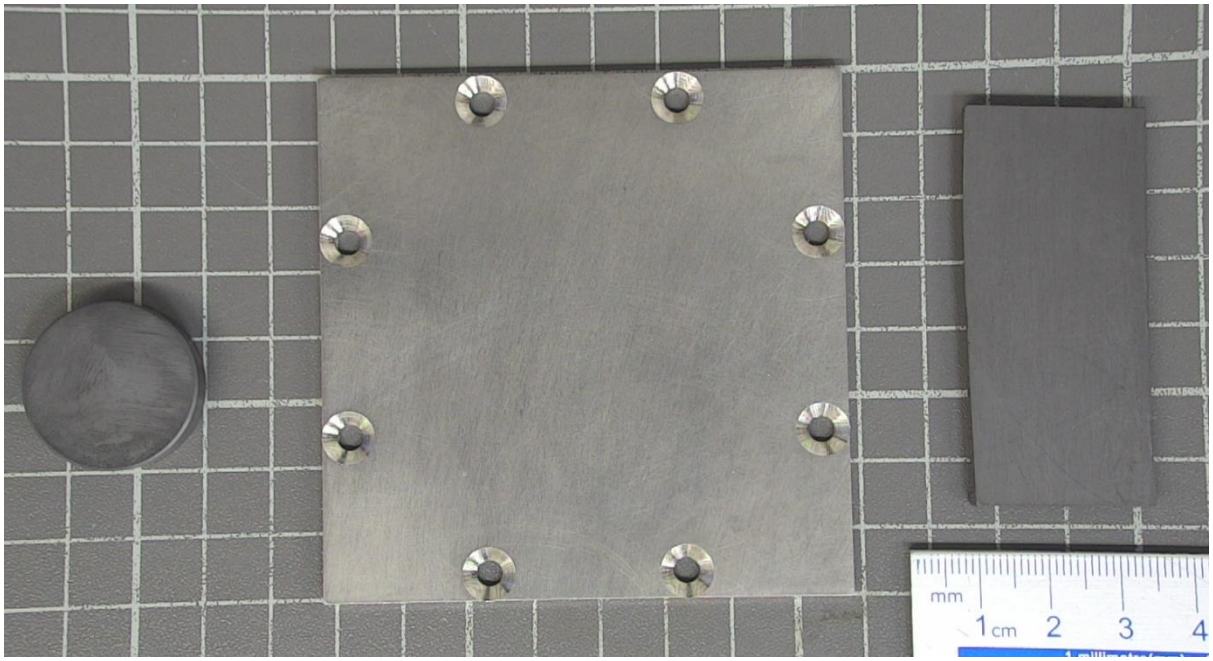

Figure 17. The substrates used throughout this thesis, 25 mm diameter reaction bonded SiC disc, stainless steel test plates 50 x 50 mm and 5 mm thick, designed to be fixed into the abradable test rig and graphite plate (GPE Scientific Ltd., UK), 60 mm x 20 mm x 5 mm thickness are shown from left to right.

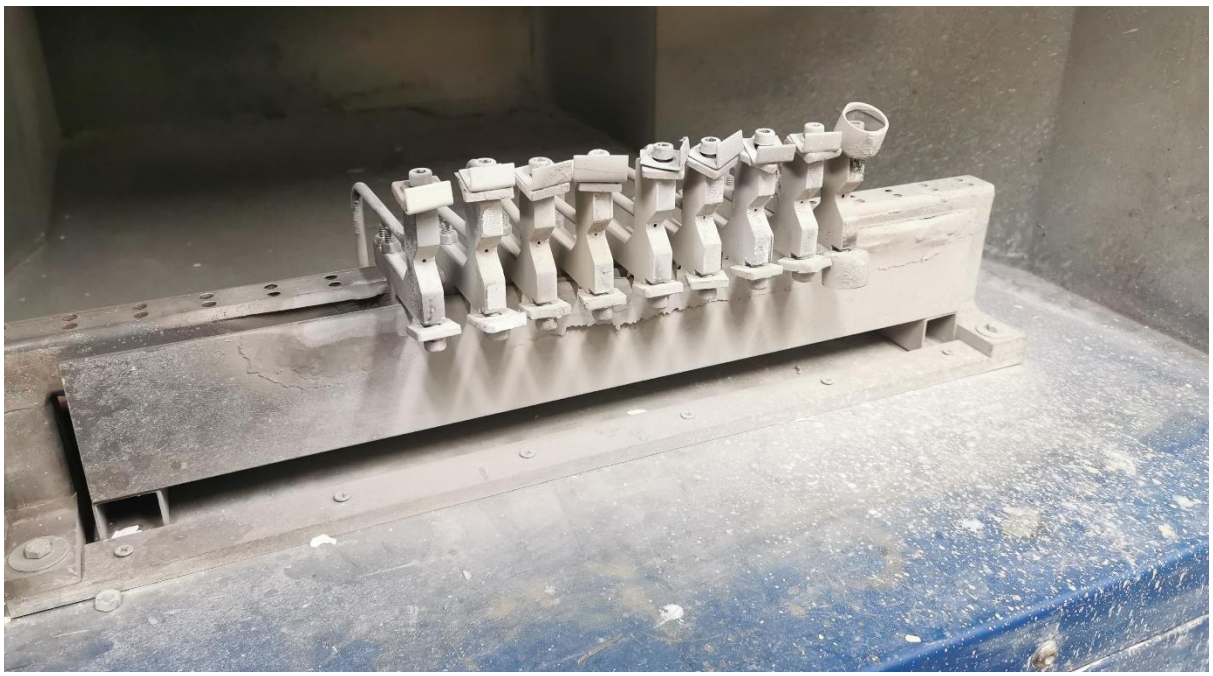

Figure 18. The substrate clamps and integrated cooling channels. For reference, the beam to which the clamps are mounted is 100 mm in length.

3.2. Characterisation

3.2.1. X-ray diffraction

X-ray Diffraction (XRD) is a technique used to study the atomic structure of crystalline materials. When a beam of monochromatic X-rays strikes a crystalline sample, the X-rays are scattered in specific directions. This scattering occurs because the crystal's atoms cause the X-rays to interfere constructively or destructively, depending on their spacing and arrangement, a schematic of the basic principles of XRD is shown in Figure 19. The relationship between the wavelength of the X-rays and the angles at which they are diffracted is described by Bragg's Law:

$$n\lambda = 2d\sin\theta \quad \text{(Equation 3)}$$

Where:

- n is an integer, often referred to as the order of the reflection
- λ is the wavelength of the X-rays
- d is the lattice spacing
- θ is the angle of incidence

By measuring the angles and intensities of the diffracted X-rays, XRD can determine the crystal structure, lattice parameters, and atomic spacing. The resulting diffraction pattern (a series of peaks) is unique to the material's structure, allowing identification of phases, crystallinity, and sometimes even stresses or defects in the material.

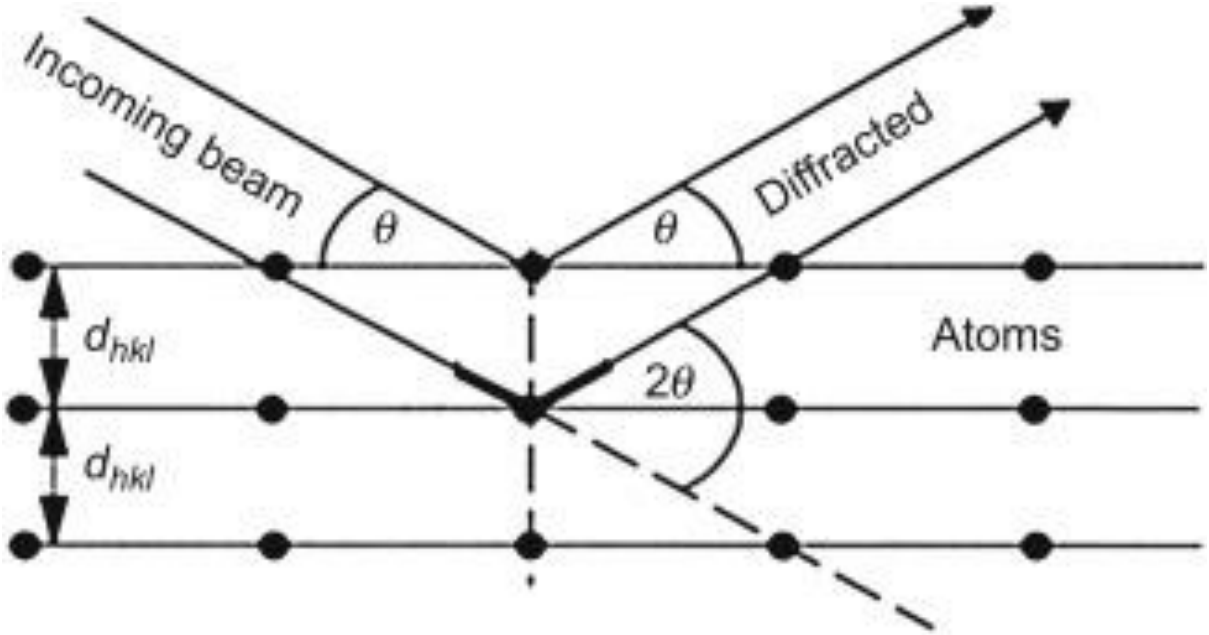

Figure 19. Schematic showing the diffraction of incident X-rays in XRD [140].

Rietveld refinement focuses on fitting a model of a crystal structure to a collected diffraction pattern, enabling the quantification of different phases present in a material. This model includes parameters such as atomic positions, thermal vibrations, and unit cell dimensions of the phases present in the material, obtained from crystallographic information files (CIF). The observed diffraction pattern is compared with the calculated pattern derived from the initial model. The refinement involves adjusting model parameters iteratively to minimize the difference between the observed and calculated patterns. This is done using least-squares fitting techniques. The key parameters that are refined include lattice parameters (depending on the crystal structure of the phase) and peak shape parameters. The peak shape is influenced by the crystallite size (smaller crystallite sizes lead to broader peaks due to increased strain and reduced coherence length) and the microstrain (distortions in the crystal lattice can cause peak broadening). A pseudo-Voigt function (combination of Lorentzian and Gaussian functions) was used to refine the contribution of these characteristics.

Throughout this work XRD was conducted using a D8 Advance (Bruker, UK) with Bragg-Brentano geometry from 10 to 80° 2θ, using Cu Kα radiation (0.154 nm wavelength), a 0.02° step size and 0.2 s per step using Bragg-Brentano geometry. Phase identification in the coatings was completed using EVA software (Bruker, UK) supported by data from the PDF-2

database (ICDD-PDF). Phase quantification (in wt. % according to Hill and Howard [141]) was performed using Rietveld refinement in TOPAS V5 (Bruker, UK) with reference to the guidelines outlined by McCusker et al. [142]. Rather than measuring a sample without any broadening effects, the instrumental broadening was accounted for by employing a fundamental parameters approach whereby the details of the experimental set-up (radiation source, slits, detector, etc.) are used for instrumental function calculations [143]. For all the phases observed, standard structures were taken from the Crystallography Open Database and used in the refinements.

3.2.2. Scanning electron microscopy

A Scanning Electron Microscope (SEM) works by directing a focused beam of high-energy electrons onto the surface of a sample. These electrons interact with the atoms in the sample, generating signals like secondary electrons, backscattered electrons, and X-rays. The SEM detects these signals to create detailed, high-resolution images of the sample's surface topography, texture, and composition. A schematic of a typical SEM and its detectors is shown in Figure 20.

Topographical images are produced using a secondary electron (SE) detector. This works by collecting low-energy electrons that are emitted from the surface of the sample when it is hit by the primary electron beam. These secondary electrons are generated very close to the surface, making them ideal for capturing fine details and topographical information. The SE detector is often positioned to the side of the sample, and it attracts the secondary electrons using an electric field. Because secondary electrons provide high surface sensitivity, the resulting images offer excellent detail and depth, revealing the texture and fine features of the sample’s surface.

A backscattered electron (BSE) detector works by capturing high-energy electrons that are scattered back from the sample after interacting with the primary electron beam and is used to provide compositional images of the sample. These backscattered electrons originate from deeper within the sample and have higher energy compared to secondary electrons. The BSE detector is typically placed above the sample to detect these electrons. Since the intensity of backscattered electrons depends on the atomic number of the elements in the sample, the BSE detector can provide compositional contrast, elements with

higher atomic numbers appear brighter, while those with lower atomic numbers appear darker in the resulting image.

Energy Dispersive X-ray Spectroscopy (EDX or EDS) works by detecting the characteristic X-rays emitted from a sample when it is bombarded by the electron beam. When the electron beam hits the atoms in the sample, it can displace inner-shell electrons. Electrons from higher energy levels then drop down to fill these vacancies, releasing energy in the form of X-rays. The energy of these X-rays is specific to the elements in the sample. An EDX detector measures the energy of these X-rays, allowing the system to identify the elements present in the sample and their relative concentrations, providing elemental composition and chemical analysis.

Throughout this work, SEM analysis was conducted using a FEI XL30 (Phillips FEI, Netherlands) operated in secondary electron (SE) and backscattered electron (BSE) modes, using an accelerating voltage of 20 kV, spot size of 5 nm and working distance of 10 mm. The SEM was equipped with energy-dispersive x-ray spectroscopy (EDX) (Oxford Instruments, UK) which was used to perform elemental analysis. Identification of possible phases was achieved by comparing the elemental stoichiometry of the phase, identified previously by XRD, to the composition of the feature analysed using EDX.

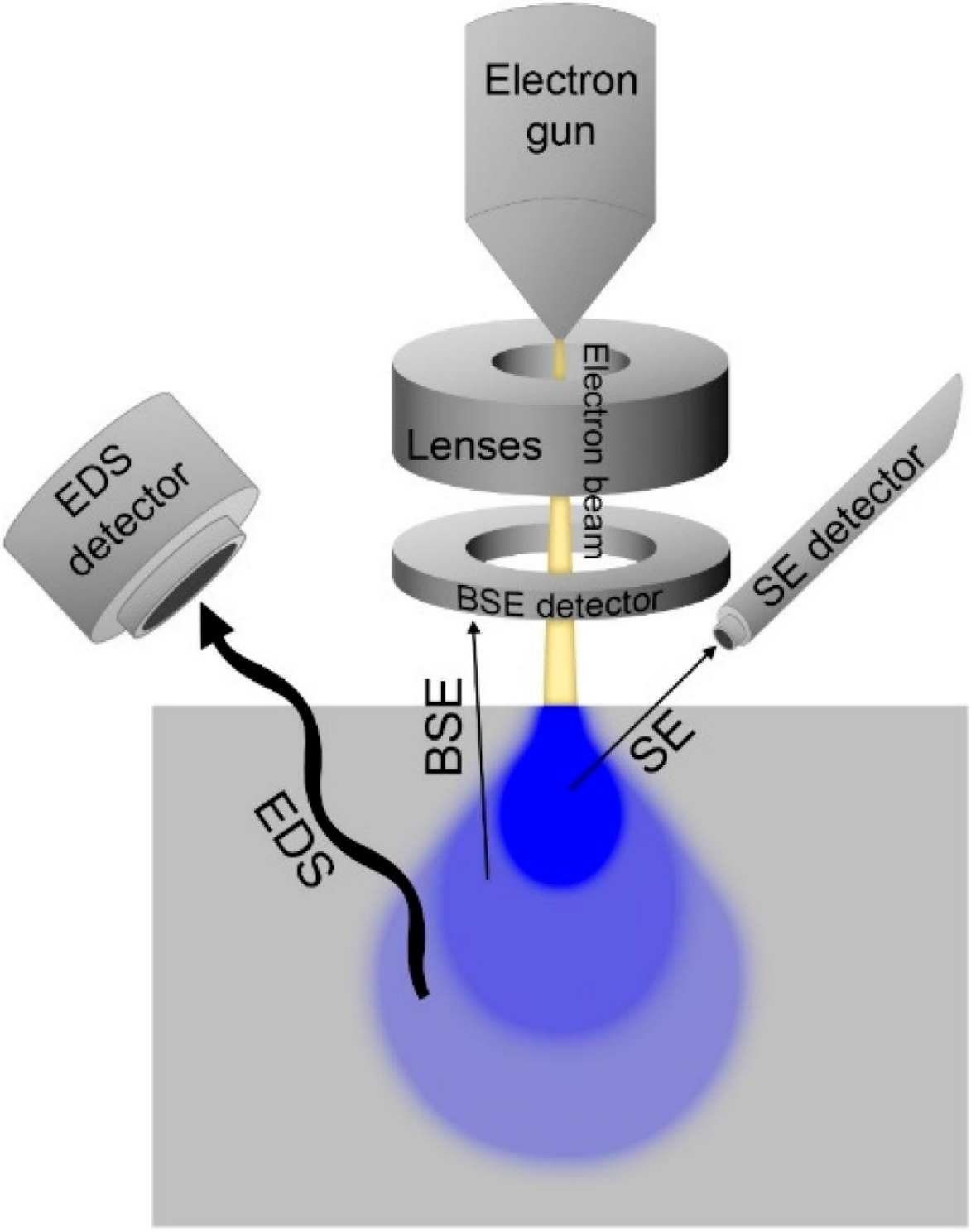

Figure 20. Schematic of an SEM, with the SE, BSE and EDX detectors and respective interaction volumes shown [144].

3.2.3. Electron backscatter diffraction

Electron Backscatter Diffraction (EBSD) is a microstructural analysis technique used primarily in a SEM to determine the crystallographic orientation, grain size, and phase distribution of materials. As with other SEM techniques, a focused electron beam from the SEM is directed onto the surface of a crystalline material held at a shallow angle (typically 70°). Some of the high-energy electrons are scattered back from the surface. As they interact with the crystal lattice, they can generate diffraction patterns. These patterns are known as Kikuchi bands, which are characteristic of the crystal structure and orientation. A detector captures these patterns, the detector itself is made up of a phosphor screen, which is highly sensitive to capture the weak signal of the backscattered electrons, and a charge-coupled camera, which captures the light signal emitted by the phosphor screen and converts it to a digital image. Software analyses the resulting data using information from the CIF of the phases within the sample and produces maps showing the location and orientation of the phases within the material. A typical EBSD configuration is shown in Figure 21.

In this work EBSD analysis was conducted using a JEOL 7100F field emission gun SEM (JEOL, Japan) using a spot size of 4 and a working distance of 10 mm. The SEM was equipped with energy dispersive X-ray spectroscopy (EDS, X-max 150, Oxford Instruments, UK) and electron backscatter diffraction (Oxford Instruments, UK) detectors. EBSD was used with an accelerating voltage of 15 kV on the ~ 70° tiled specimen. EBSD data acquisition was performed at a step size of 0.0285 µm. Crystallographic information files (CIF) were used to identify the suspected phases present in the coatings. AZtec Crystal (Oxford Instruments, UK) was used to analyse the EBSD data.

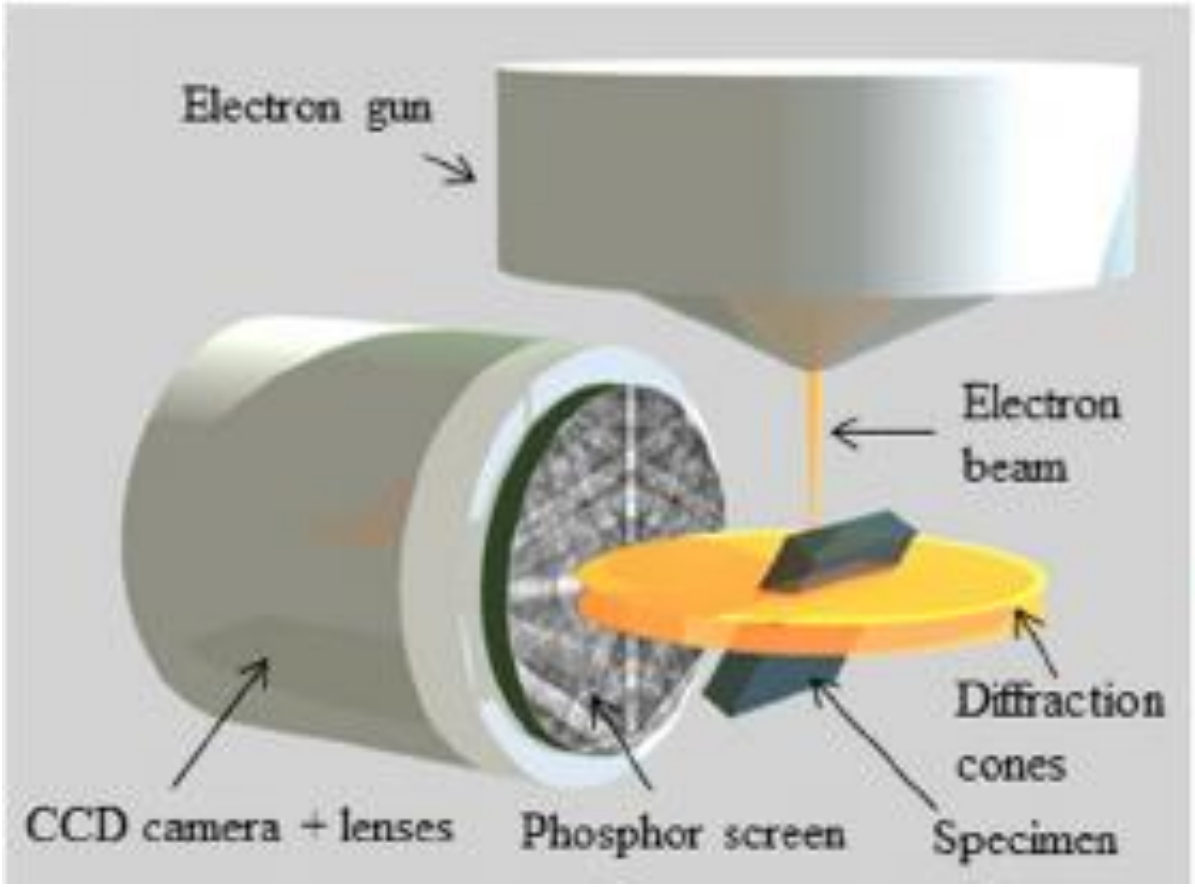

Figure 21. Schematic showing EBSD detection geometry and a typical EBSD detector [145].

3.2.4. X-ray computed tomography

X-ray Computed Tomography (CT) is a non-destructive imaging technique that creates detailed 3D images of an object's internal structure. An X-ray source emits a beam of X-rays that passes through the sample being examined. As the X-rays penetrate the object, some are absorbed while others pass through depending on the materials density and composition. A detector captures the X-rays that emerge from the other side. The X-ray source and detector rotate around the object, capturing multiple 2D images (slices) from different angles. These slices are processed using algorithms to reconstruct them into a 3D model of the samples internal structure.

3.2.5. Thermal conductivity

Laser Flash Analysis (LFA) is a technique used to measure the thermal properties of materials, particularly their thermal diffusivity, specific heat, and thermal conductivity. A short pulse of laser light is directed onto the surface of the sample. The sample is coated in graphite to improve the absorption of the laser energy. The laser heats the surface very

quickly (in microseconds). As the heated surface of the sample begins to cool, the heat diffuses through the material. The opposite side of the sample is monitored with an infrared detector to measure the temperature change over time. The temperature rise on the unheated side is recorded as a function of time. The resulting data is then analysed to calculate thermal diffusivity using mathematical models based on Fourier's law of heat conduction. This value can then be used to calculate the thermal conductivity of the sample using the following equation:

$$k = \alpha \rho C_P \quad \text{(Equation 4)}$$

Where:

- k is thermal conductivity
- α is thermal diffusivity
- ρ is density
- C_P is specific heat capacity

The specific heat capacity can be calculated from the constituent oxides using the Neumann-Kopp rule [146] (whereby the value for the bulk material is a weighted sum of its constituents).

3.3. Mechanical properties testing

3.3.1. Hardness

Hardness testing enables quantification of a materials strength and ductility. Vickers hardness is a method of measuring a material's hardness by determining its resistance to indentation. In the Vickers test, a diamond-shaped pyramid indenter with a square base is pressed into the material's surface under a specific load. The size of the indentation is measured, and the Vickers Hardness Number (HV) is calculated using the applied load and the surface area of the indentation. The formula used is:

$$HV = \frac{2F \sin\frac{136}{2}}{d^2} \quad \text{(Equation 5)}$$

where:

- F is the applied force

- d is the diagonal length of the indentation

Rockwell Superficial Hardness is a variation of the Rockwell hardness test used for soft or thin materials with small indentations. It follows the same principle as the standard Rockwell test, whereby an indenter is pressed into the material under a specific minor load, followed by a major load. In the superficial test, lighter loads (usually 15, 30, or 45 kgf) are used compared to the standard Rockwell test. The hardness value is determined based on the depth of penetration of the indenter after applying both loads, given by:

$$HR = N - (d/D) \quad \text{(Equation 6)}$$

Where:

- HR is the Rockwell hardness value
- N is the load applied (in kgf)
- d is the depth of the indentation (in mm)
- D is a geometric factor depending on the scale and indenter used

The different scales use different indenter materials and geometries, the most commonly used are the N scale which uses a diamond cone with a 120° angle and the Y scale which uses a ¼" diameter steel ball.

The microhardness of the coatings was assessed in Chapter 4 while the superficial hardness was assessed in Chapter 5.

3.3.2. Abradable test rig

The abradability of the coatings produced in this thesis was examined using an abradable test rig at University of Sheffield. In this rig the cutting of an abradable coating by a turbine blade is simulated. In this rig, two blades, one that cuts the abradable and one dummy blade (positioned 180° from the test blade) to ensure balance during rotation, are mounted on a high frequency grinding spindle (GMN Paul Müller Industrie GmbH, Germany). The speed at which the spindle rotates controls the tip speed of the blade, a maximum blade tip speed of 200 m/s can be achieved. This is far higher than can be achieved with typical ball/pin-on-disc tribometers and is designed to replicate the blade speeds found in gas turbines. The abradable coating itself is deposited onto a steel backing plate which is mounted on a motorised single-axis movable stage, which moves the abradable into the cutting blade at a

defined speed or incursion rate, incursion rates from 0.02 – 2000 µm/s can be achieved. The stage is connected to a dynamometer which measures the magnitude of the forces (normal and tangential to the wear direction) exerted on the abradable coating. The test is completed when a desired incursion depth is reached. A schematic of the rig is presented in Figure 22. While the test rig itself is not actively heated, the temperature on the surface of the abradable is measured using a single wavelength pyrometer (OptoSigma, Japan) pointing at the centre of the wear scar. The pyrometer has a spectral response at 2.3 µm. Images of the blade, both front-on and side-on, are captured during the test to allow the change in blade profile to be monitored. This is achieved using two stroboscopic imaging systems (Gardasoft, UK) whereby LEDs are used to illuminate the blade, a light gate is used to trigger the camera and images of the blade are captured after a certain delay every rotation [29, 30].

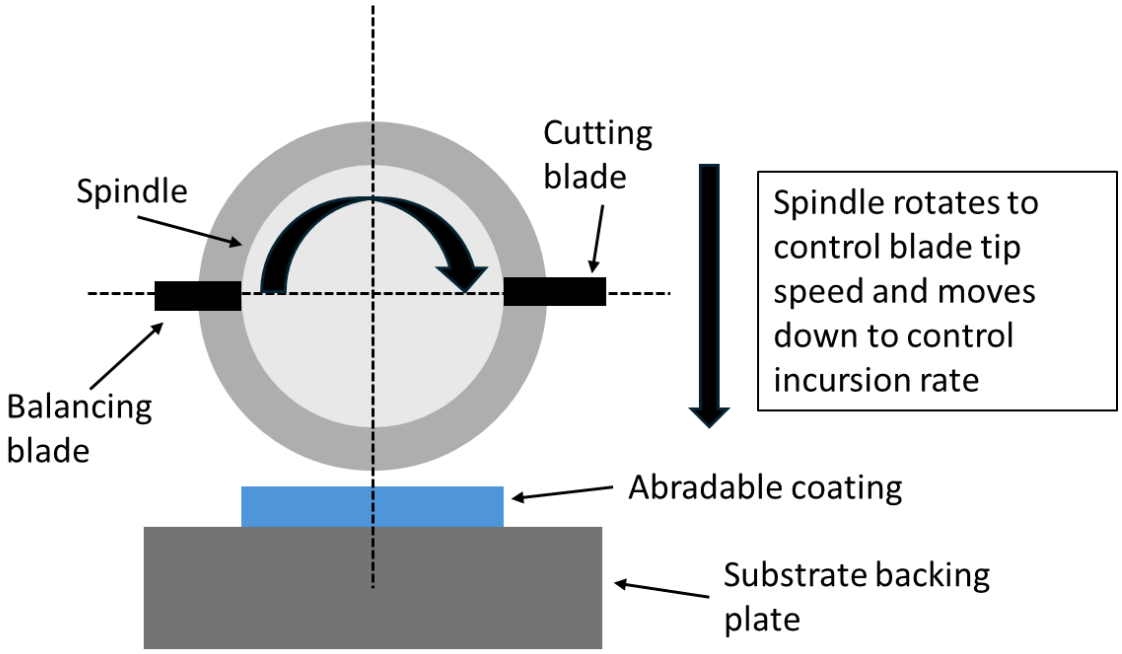

Figure 22. A schematic of the abradability test rig at the University of Sheffield, with the key components labelled [25].

3.4. Corrosion testing

3.4.1. CMAS testing

CMAS powder with a nominal composition of 35 CaO – 10 MgO – 7 Al_2O_3 – 48 SiO_2 mol. % (Oerlikon Metco AG, Switzerland) was used throughout this thesis, giving a Ca:Si ratio of

0.73. The melting point of the CMAS powder was obtained using direct scanning calorimetry, this was found to be 1217 °C, this is shown in Figure 23.

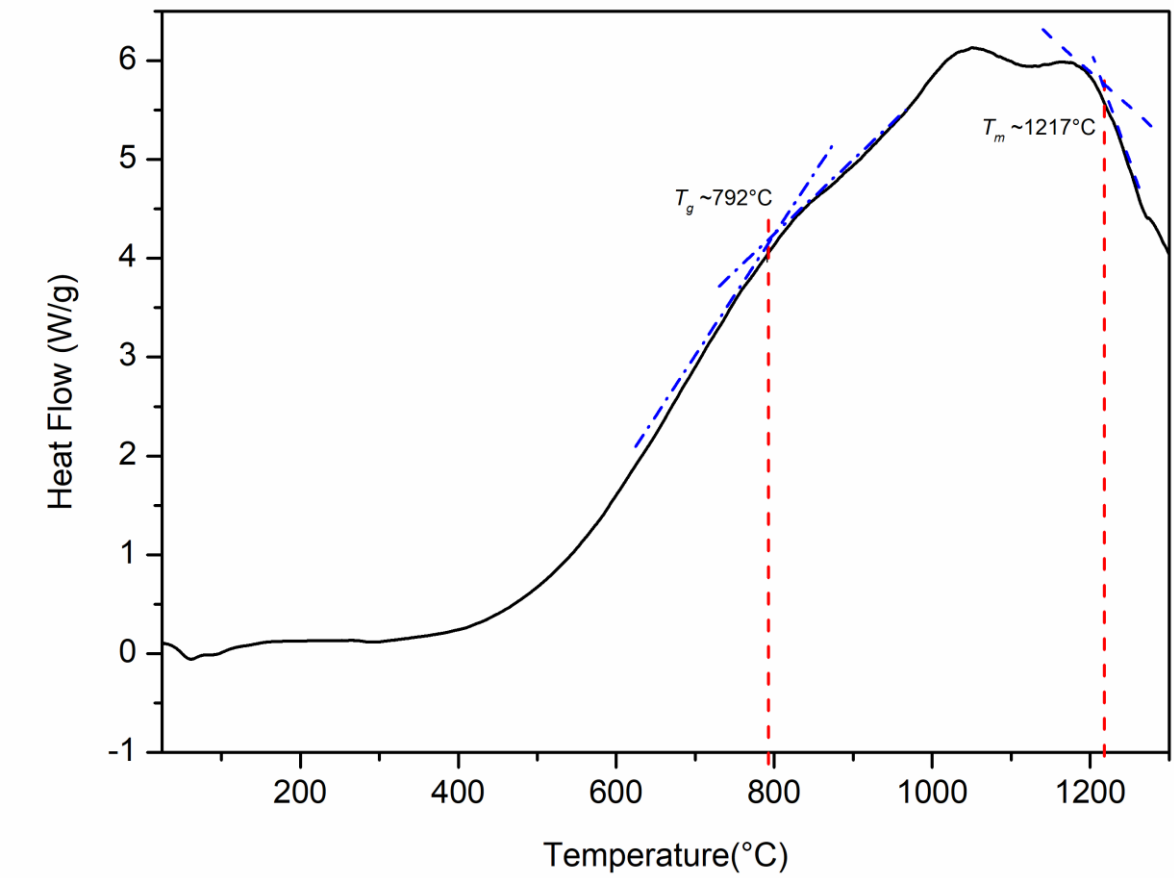

Figure 23. DSC results of the CMAS used throughout this thesis, with the glass transition and melting temperatures shown (analysis conducted previously by Centre of Excellence in Coatings & Surface Engineering group at the University of Nottingham).

To apply the CMAS to the coating surface, the CMAS powder was mixed with deionised water at a 1:9 ratio by weight and mixed using a magnetic stirrer to ensure homogeneity. The CMAS slurry was applied via an airbrush to YbDS coatings at a stand-off distance of 150 mm. The coatings had been placed on a hotplate at ~100 °C to promote the evaporation of water from the CMAS slurry. The process of applying a layer of CMAS slurry and drying was repeated until a mass representing the desired concentration had been applied to the surface of the samples. A schematic of the airbrush, hot plate and stirrer are shown in Figure 24. Subsequently the CMAS coated samples were heated in a box furnace (Elite Thermal Systems, Uk) to the desired temperature, for the desired duration.

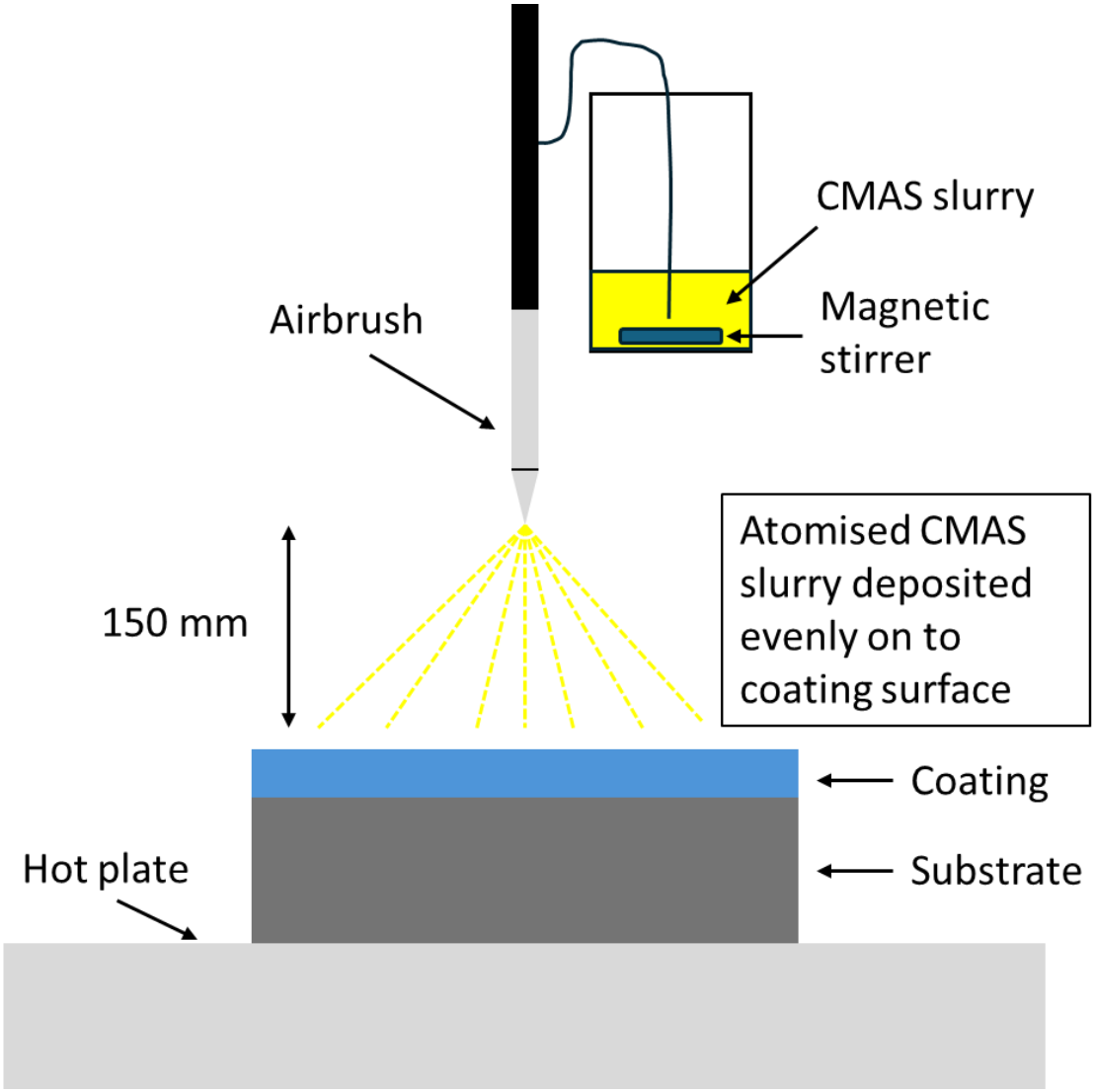

Figure 24. A schematic of the CMAS application process, showing a coated sample on a hot plate, CMAS slurry, the magnetic stirrer and the airbrush.

3.4.2. Steam testing

To examine the effects of steam exposure on the coatings an isothermal steam test was conducted. A steam rig consisting of two interconnected tube furnaces (Elite Thermal Systems Ltd., UK), mass flow controller (Omega Engineering Inc, UK), 120S peristaltic pump (Watson-Marlow Ltd., UK) and co-axial zirconia tubes (Almath Crucibles Ltd., UK) was employed for the testing. The first furnace was used to produce the steam by boiling deionised water and was set to 400 °C. The second furnace was used to heat the abradable EBCs to 1350 °C at a rate of 2.5 °C/min. The samples sat in the middle of a 25 mm diameter by 750 mm long zirconia tube placed in the centre of the furnace, this tube was placed in an alumina tube with a 52 mm diameter. The other end of the furnace was kept open to

maintain atmospheric pressure. Once this temperature was reached, the pump was turned on, flowing at 5 ml/min and the steam was mixed with compressed air, itself flowing at 0.8 SLM. The steam and air flow created an atmosphere of 90 vol.% H_2O/10 vol.% air with a gas velocity of 1 m/s. A smaller zirconia tube (7 mm diameter by 400 mm length) was used to transport the air-steam mixture to the hot zone of the furnace, the samples were places 100 mm away from the outlet of this steam injector tube. The use of the zirconia tubes prevented any alumina contamination which would promote YbAG formation within the coatings. A schematic of this rig is shown in Figure 25.

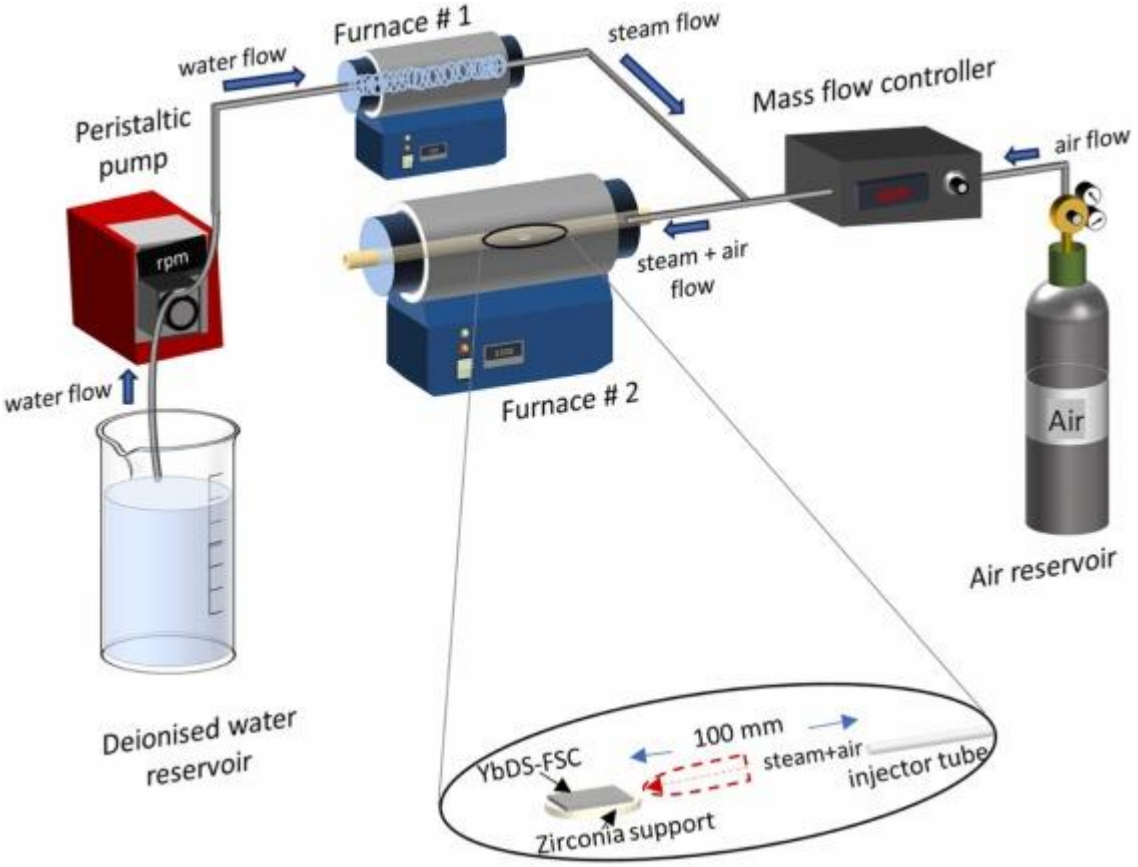

Figure 25. Schematic showing the high temperature steam rig used in this study [60, 96].

Chapter 4: Atmospheric plasma spraying of ytterbium disilicate for abradable and environmental barrier coatings: A story of processing-microstructure relationships

This chapter is reproduced from the paper:

A. Lynam, A. Rincon Romero, F. Xu, G.J. Brewster, G. Pattinson, T. Hussain, Atmospheric plasma spraying of ytterbium disilicate for abradable and environmental barrier coatings: A story of processing-microstructure relationships, Ceramics International, Volume 49, Issue 13, 2023, Pages 22232-22243, https://doi.org/10.1016/j.ceramint.2023.04.053

Abstract

Environmental barrier coatings (EBCs) are required to protect SiC based composites in high temperature, steam containing combustion environments found in the latest generation of high efficiency gas turbine aeroengines. Ytterbium disilicate (YbDS) has shown promise as an environmental barrier coating, showing excellent phase stability at high temperatures and a coefficient of thermal expansion close to that of SiC however its performance is dependent on the conditions under which the coating was deposited. In this work, a parametric study was undertaken to demonstrate how processing parameters using a widely used Praxair SG-100 atmospheric plasma spraying (APS) torch affect the phase composition, microstructure and mechanical properties of ytterbium disilicate. Ytterbium disilicate coatings were deposited using 4 sets of spray parameters, varying the spray power from 12 to 24 kW. The phases present in these coatings were quantified using x-ray diffraction with Rietveld refinement, and the level of porosity was measured. Using this data, the relationship between processing parameters and phase composition and microstructure was examined. Using the optimum process parameter window determined in this work, abradable YbDS coatings were deposited using polyester feedstock additions as a pore forming phase. Two different polyester levels were added to create coatings with two different porosity levels.

4.1. Introduction

As performance and efficiency gains in gas turbines are constantly sought, the temperatures under which Ni-based superalloys must operate are approaching their limit. Thermal barrier coatings (TBCs) have allowed turbine inlet temperatures of ~1500°C, improving thrust outputs, thermal efficiency and reducing harmful emissions [2]. Even with the use of TBCs, the in-service temperature such components are exposed to is now approaching the melting point of the Ni alloys, so it is clear that new material solutions must be sought. One such solution is using SiC/SiC ceramic matrix composites (CMCs). CMCs show excellent high temperature mechanical properties, have a temperature limit ~200 °C higher than Ni based superalloys and have a lower density than their metallic counterparts (improving thrust to weight ratios) [147]. Nevertheless, SiC/SiC CMCs are not without drawbacks. At high temperatures in oxidising environments, SiC will form a protective SiO_2 layer however in the presence of steam, as found in gas turbines, the usually protective SiO_2 will form volatile silicon hydroxide ($Si(OH)_4$), resulting in a recession of SiC [72].

Naturally, SiC-based CMCs must be protected from such environments; one approach to do this is through coating the CMC, known as an environmental barrier coating (EBC). Similar to how thermal barrier coatings have been employed to protect nickel superalloys from high temperatures, EBCs can be used to protect CMCs from steam recession. To be effective, the EBC must have; low silicon volatilisation, a coefficient of thermal expansion (CTE) similar to that of the CMC, chemical compatibility with the CMC and phase stability over the range of operating temperatures [148]. For over 30 years, silicates have been investigated for use as EBCs due to their combination of properties and the ease with which they can be deposited using thermal spray techniques, primarily atmospheric plasma spraying (APS) [93, 107]. More recently, rare-earth silicates, specifically ytterbium monosilicate (Yb_2SiO_5 or YbMS) and ytterbium disilicate ($Yb_2Si_2O_7$ or YbDS), are considered state-of-the-art due to their low CTE (7.5 x10^{-6} K^{-1}, measured over a range of 473–1673 K and 4.1 x10^{-6} K^{-1}, measured over a range of 303–1873 K respectively), excellent phase stability and the fact they present a single polymorph over the operating temperature range, while YbMS may provide better protection against steam recession, the CTE mismatch means YbDS is preferred for EBCs [4, 82, 149, 150].

Beyond higher operating temperatures, another practical way in which the efficiency of gas turbines can be increased is to reduce leakages that occur during the compression and turbine stages. This can be achieved by reducing the clearances between the moving parts within the turbine, for example, between the blades and the casing. Due to the high operating temperatures within the turbine, the blades will expand and contact the casing if the clearance is too low, high loads and large vibrations could also lead the blade to impact the casing. To get around this, abradable seal coatings can be employed. Such coatings are soft enough to be worn away by the turbine blade tip (without damaging the tip itself), allowing for tighter clearances to be used, limiting leakages and increasing efficiency, whilst still (in the case of an abradable EBC) providing protection of the CMC substrate from steam recession. Abradable seals are typically made up of a matrix phase to which pore forming phases (e.g. polyester) and/or solid lubricants (e.g. hBN or $LaPO_4$) are added to provide abradability [16, 59]. While research into abradable EBCs is still in its infancy, studies have been conducted into a hBN containing YbDS APS deposited EBCs, and within industry patents regarding polyester and solid lubricant containing EBCs have been granted [61, 63, 64].

Many studies have been undertaken regarding the optimisation of YbDS deposition [85, 91, 107, 111]. In particular, Richards et al. [83] used a Praxair SG-100, a widely used plasma spray torch similar to the type used in this study, to obtain a dense YbDS coating with relatively low YbMS phase content while exploring a range of spray parameters. In order to obtain a crystalline coating, the spray was conducted inside a furnace, a setup up not feasible for high volume coating production. Despite this, the requirements of an abradable coating are vastly different to that of an EBC. To prevent the ingress of steam, EBCs must provide a gas-tight seal over the CMC substrate, whereas porosity is inherent in abradable coatings. While Qin et al. [61] have investigated the wear resistance of hBN containing YbDS abradable coatings and Tejero-Martin et al. [59] have determined the resistance of abradable YbDS coatings to CMAS attack, no fundamental study has been conducted on the deposition of abradable YbDS coatings. If abradable EBCs are to be considered for the next generation of gas turbines, their deposition needs to be better understood. The aim of this study was to determine an optimum deposition condition for an abradable YbDS system maximising the level of porosity. Bearing this in mind, a parametric investigation was

undertaken to optimise a YbDS coating deposited by APS. The effect of spray power and stand-off distance were investigated, the phase composition, microstructure and level of porosity were characterised for all the coatings. Finally, polyester acting as a pore former, was added to the feedstock and these coatings characterised.

4.2. Materials and methods

4.2.1. Materials

EBC and abradable EBC systems were deposited using APS. The coating system is comprised of a reaction bonded SiC substrate (JAI Engineers, UK), an intermediate Si bond layer and YbDS as a protective top layer. Commercially available Si (Metco 4810) and YbDS (Metco 6157) (both Oerlikon Metco AG, Switzerland) were used as feedstocks for the respective layers. The Si powder had a nominal size range of 15-75 µm and contained < 1.5 wt. % SiO_2 and a balance of Si. The YbDS powder had a nominal size range of 11-90 µm, contained a maximum of 5 vol. % of unreacted Yb_2O_3 and YbMS. Prior to spraying, the powders were treated at 80 °C for 12 hours using a box furnace (Elite Thermal Systems, UK) to remove any moisture. Finally, Metco 600NS (Oerlikon Metco AG, Switzerland), a polyester (PE) powder, was mixed with the YbDS powder at 1.5 and 4.5 wt. %. The pore former was a crystalline aromatic polyester powder with a nominal size range of 45-125 µm. The mixture was homogenised using a Labram acoustic mixer (Resodyn Acoustic Mixers, USA).

Reaction bonded SiC discs with a diameter of 25 mm and thickness of 10 mm, were used as the substrates. These were grit blasted using a blast cleaner (Guyson, UK) with SiC (220 mesh) particles at a pressure of 9 bar. After grit blasting the surface roughness (R_a) of the SiC discs was found to be 3.1 ± 0.1 µm (average of 3 grit blasted discs). Following surface preparation, the substrates were sonicated in industrial methylated spirit (IMS) using a FB-505 ultrasound probe (Fischer Scientific, UK) in pulse mode (1 s pulse every 2 s) at 60% amplitude. Finally, the substrates were dried using compressed air.

4.2.2. Coating Deposition

An SG-100 plasma spray system (Praxair Surface Technology, USA) was used to deposit the coatings. The spray gun was fitted with a 02083-175 anode, 02083-120 cathode and a 03083-112 gas injector. Ar was used as the primary gas, and H_2 was used as the secondary gas.

The Si bond coat was deposited using a spray power of 27 kW, a current of 600 A, primary gas (Ar) pressure of 85 psi (equivalent to a flow rate of 75 SLM), a secondary gas (H_2) pressure of 35 psi (2.5 SLM), a stand-off distance of 125 mm, a powder feed rate of 30 g/min and the robot speed was 1000 mm/s over 6 passes. These conditions were optimised prior to this study.

The YbDS spraying parameters are shown in Table 3. A parametric study was conducted varying spray power to assess how this affected YbDS phase retention and porosity in the coating. To vary the spray power, arc current and secondary gas pressure were adjusted to provide four distinct power levels, 12, 16, 20 and 24 kW (sprays 1 – 4). Following this, a similar study was conducted with fixed spray power of 12 kW as the stand-off distance was reduced from 150 mm down to 125 and 100 mm (sprays 5 – 7). Coatings containing 1.5 and 4.5 wt. % polyester powder mixed into the YbDS feedstock were also deposited using 12 kW spray power (sprays 10 and 11). Initially, 75-100 µm coatings were deposited to conduct basic characterisation, for sprays 8-11 a target thickness of 350-400 µm was desired for more in-depth characterisation. Initially (sprays 1-7) a robot scanning speed of 610 mm/s was used; however, when attempting to deposit thicker coatings this was found to induce deboning of the bond coat and EBC from the SiC substrate likely due to deposition rate residual stress effects, to eliminate this the robot speed was increased to 1000 mm/s in subsequent coating trials (sprays 8-11). Due to the highly amorphous nature of the as-sprayed coatings, a crystallization heat treatment was conducted to form crystalline phases [151]. This was done at 1200 °C (Elite Thermal Systems Ltd., UK) for two hours, with heating and cooling rates of 5 °C/min in air [59, 60]. Prior to the crystallisation heat treatment, the polyester containing coatings underwent a burn-out heat treatment at 500 °C for 3.5 h with a heating rate of 5 °C/min, to burn off any remaining organic material.

Table 3. YbDS APS parameters for all 11 spray runs with coating thickness.

Spray Number	Power (kW)	Current (A)	Ar (psi/SLM)	H_2 (psi/SLM)	Stand-off Distance (mm)	Robot Scanning Speed (mm/s)	Feedstock	Number of Passes (Thickness µm)
Effect of Spray Power								
1	**12**	400	95/85	30/2	150	610	YbDS	2 (70 ± 10)
2	**16**	300	95/85	40/3	150	610	YbDS	2 (81 ± 8)
3	**20**	400	95/85	40/3	150	610	YbDS	2 (90 ± 7)
4	**24**	500	95/85	40/3	150	610	YbDS	2 (96 ± 8)
Effect of Stand-off Distance								
5	12	400	95/85	30/2	**100**	610	YbDS	10 (322 ± 22)
6	12	400	95/85	30/2	**125**	610	YbDS	10 (313 ± 20)
7	12	400	95/85	30/2	**150**	610	YbDS	10 (247 ± 30)
Effect of PE Addition								
8	24	500	95/85	40/3	150	1000	**YbDS**	20 (350 ± 40)
9	12	400	95/85	30/2	125	1000	**YbDS**	25 (385 ± 34)
10	12	400	95/85	30/2	125	1000	**YbDS + 1.5 wt.% PE**	25 (397 ± 36)

11	12	400	95/85	30/2	125	1000	**YbDS + 4.5 wt.% PE**	35 (410 ± 25)

The temperature and velocity of both the Si and YbDS feedstock particles were measured using a Tecnar Accuraspray 4 (Tecnar, Canada) in order to better understand the condition of the particles as they impacted the substrates. The Accuraspray has a large measurement volume of 750 mm^3 (3 mm x 25 mm x 10 mm) allowing for temperature and velocity data as an average of all of the particles passing through the measurement volume to be measured [152]. As particles pass through the focal plane of the Accurapsray system, pulses are generated by two slits in the sensor; knowing the time between the pulses and the distance between the slits the particles' velocity can be calculated. Temperature is measured using a two-colour pyrometer. The accuracy of the readings is 3 % for the particle temperature measurements and 2% for the particle velocity measurements. The signal amplification factor and exposure time settings were different for the different spray parameters and stand-off distances but were comprised in the range of 20-32 times and 16-41 ms, respectively. The response time was set to 1 s. Before the data was acquired, a period of 60 s was allowed for flame stabilisation. A series of 60 measurements were acquired over a time frame of 60 s, and then averaged to give the resulting values.

4.2.3. Sample Preparation and Characterisation

Coated samples were sectioned using a Qcut 200 precision cutting machine (Metprep, UK) and abrasive diamond cut-off wheels (Metprep, UK) with a cutting speed of 0.025 mm/s. Samples in Section 3.1.1. were then hot-mounted using conducto-mount (Metprep, UK). Subsequently, the coated substrates were mounted with EpoFix resin and hardener (15:2 volumetric ratio) (Struers, Denmark) and then sectioned. The cross-sections were mounted again using EpoFix resin and hardener (Struers, Denmark). The mounted samples were then ground using a 200 grit diamond lapping disc (DK Holdings Ltd, UK). Lastly, the ground samples were polished using diamond polishing pads to a surface finish of 6 µm and 1 µm.

The morphology of the YbDS powder, the microstructure of the coating and the surface topography of the coating were characterised using a FEI XL30 scanning electron microscope (SEM) (Phillips FEI, Netherlands) operated in secondary electron (SE) and backscattered electron (BSE) modes, using an accelerating voltage of 20 kV, spot size of 5 nm and working distance of ~10 mm. The SEM was equipped with energy-dispersive x-ray spectroscopy (EDX) (Oxford Instruments, UK) which was used to perform elemental analysis. The level of porosity was measured using ImageJ image processing software (National Institute of

Health, USA). BSE images taken at 1000 times magnification, covering around 600 μm^2 of the cross-section, were converted into black and white maps upon setting a threshold, which was kept constant for all coatings. Then the area percentage of the image covered by porosity was measured, returning an overall value per image. An average of the porosity across the five images of each coating was calculated and the standard deviation was presented as the error associated with each measurement. The ImageJ measurement function was used to measure the thickness of the coatings. One measurement was taken from five BSE images taken at 250 times magnification per coating, the average and standard deviation of the five results were calculated.

Microhardness measurements were performed using a Vickers hardness indenter (Buehler, USA), an average of 5 indents was reported. A load of 100 gf was applied to the samples, testing under this load did not form cracks, and hence the only form of energy dissipation was due to the indent itself.

4.2.4. X-ray Diffraction

The phase analysis on the feedstock powder and as-sprayed coating was conducted by XRD using a D8 Advance (Bruker, UK) from 10 to 80° 2θ, using Cu Kα radiation (0.154 nm wavelength), a 0.02° step size and 0.2 s per step using Bragg-Brentano geometry. Phase identification in the coatings was completed using EVA software (Bruker, UK) supported by data from the PDF-2 database (ICDD-PDF). Phase quantification (in wt. % according to Hill and Howard [141]) was performed using Rietveld refinement in TOPAS V5 (Bruker, UK) with reference to the guidelines outlined by McCusker et al. [142]. Rather than measuring a sample without any broadening effects, the instrumental broadening was accounted for by employing a fundamental parameters approach whereby the details of the experimental set-up (radiation source, slits, detector, etc.) are used for instrumental function calculations [143]. For all the phases observed, standard structures were taken from the Crystallography Open Database and used in the refinements.

4.3. Results

4.3.1. Powder Characterisation

SEM analysis was carried out on the YbDS and PE powders used in this study in order to understand their morphology, micrographs of the powder particles can be seen in Figure 26.

The YbDS powder exhibits a spherical morphology with some internal pores visible from the surface, typical of agglomerated and sintered powders.

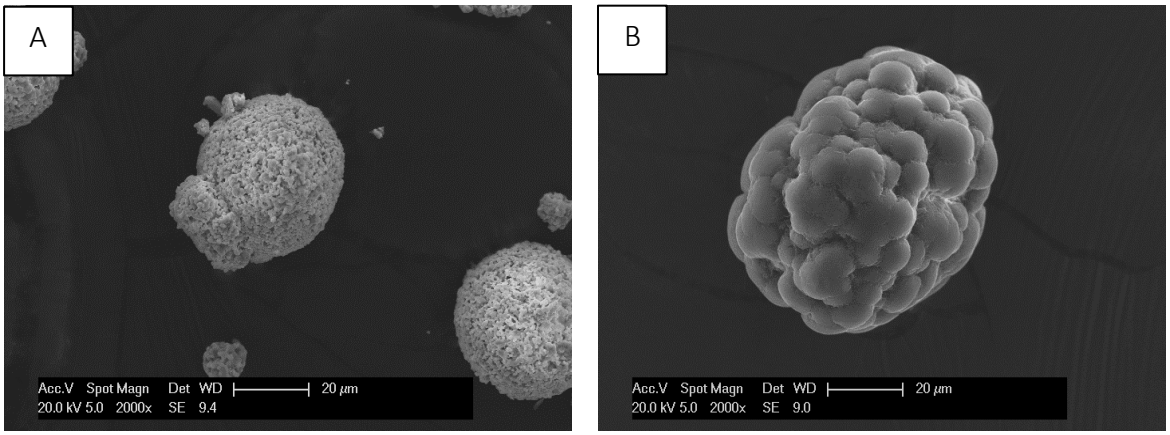

Figure 26. SE SEM image of (a) YbDS and (b) PE powder showing sintered and agglomerated structure with some porosity.

XRD of the powder is shown in Figure 27, the composition of the powder was mainly monoclinic YbDS (C2/m, 82-0734) with small amounts of monoclinic YbMS (I2/a, 40-0386). The phase composition of the powder was quantified using Rietveld refinement, the powder was found to contain 95.1 wt. % YbDS and 4.9 wt. % YbMS.

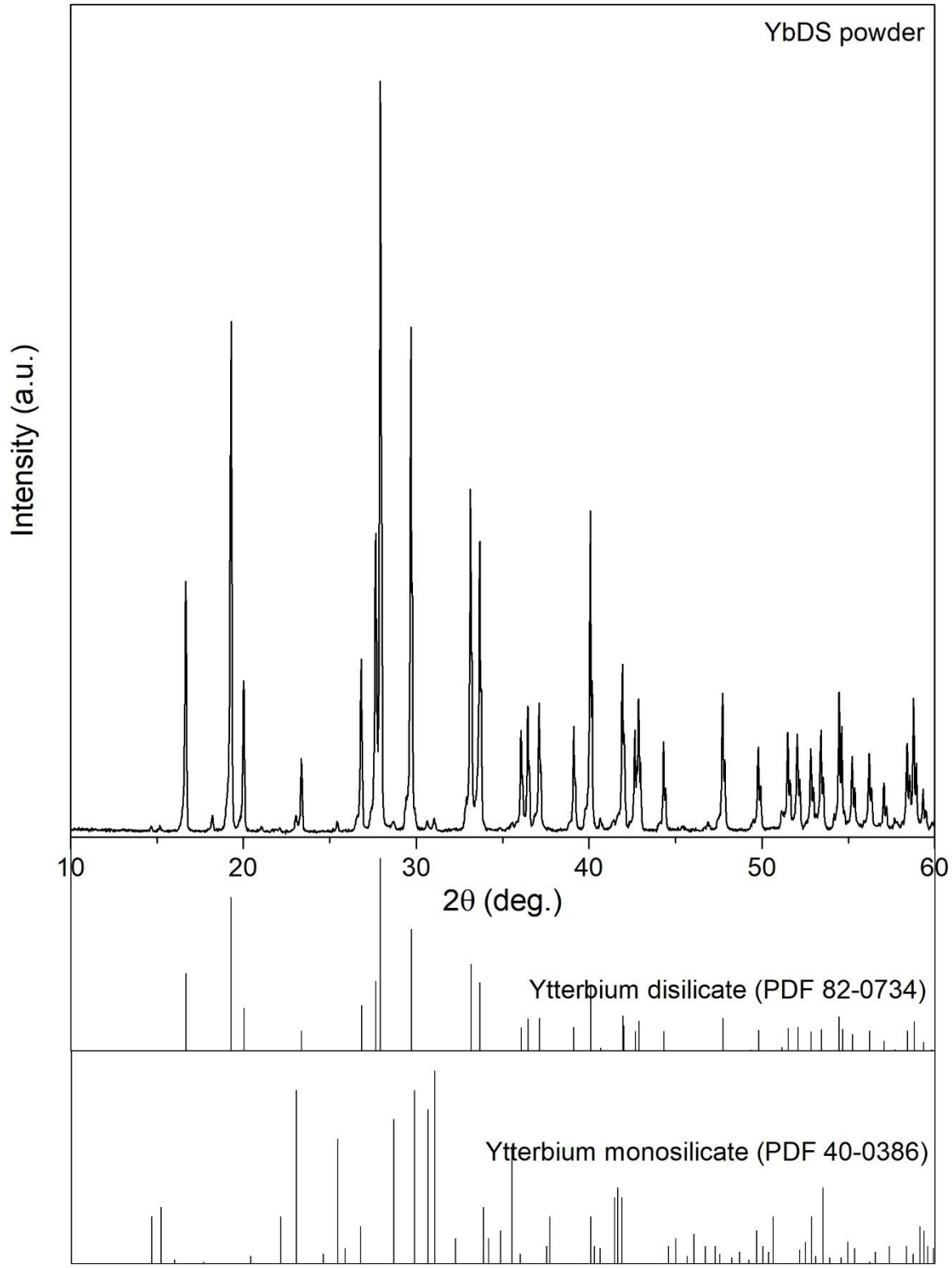

Figure 27. Diffractogram of Metco 6157 powder showing predominantly YbDS and minor YbMS peaks.

4.3.2. Effect of Spray Power

To investigate the effect spray power had on the phase composition and microstructure, 75 – 100 µm thick coatings were deposited. The spray powers used were 12, 16, 20 and 24 kW, these were selected to capture data from a broad processing window encompassing a variety of particle conditions in terms of temperature and velocity. Figure 28 shows BSE SEM images of the microstructures of the coatings deposited using the four spray powers after heat treatment. The coating deposited using 12 kW spray power was highly porous (~10 %) after heat treatment due to the presence of partially melted and un-melted particles. The microhardness of the heat-treated coatings was measured as well as the porosity, this is shown in Table 4. Generally, porosity decreased, and microhardness increased with increasing spray power in the heat-treated coatings. The deposition rate also increased with spray power, and although it was not measured directly and it can be inferred that the deposition efficiency would also increase, given the spray time/number of passes, powder feed rate and carrier gas flow were constant for all four of the sprays.

The particle velocity and temperature measured at a stand-off distance of 150 mm are shown in Figure 29, in order to understand the condition of the particles as they impacted the substrate. Both particle velocity and surface temperature increased as the spray power was increased. In this study, in order to increase the spray power, the arc current and secondary gas pressure were increased. Increasing the arc current increases the velocity and length of the plasma jet, resulting in higher particle temperatures and velocities [153]. Compared to Ar, H_2 has increased thermal conductivity and specific heat capacity leading to higher arc voltages, so the higher proportion of H_2 in the plasma gas, the more energetic the plasma [153]. Generally, higher spray powers result in a higher proportion of fully molten material (as more thermal energy is available to be transferred to the particles in the plasma), which when it impacts the substrate has the appropriate kinetic and thermal energy to form coherent, well-flattened splats, which will result in a less porous coating. The particle temperature exceeded the melting temperature of YbDS (1850 °C) [154] for all of the tested spray parameters except 12 kW, which caused a large volume of un-melted particles to be visible within the coating, causing increased porosity. While this ensures that the feedstock will be molten as it impacts the substrate, work by Richards et al. [83] has shown that at high temperatures (1000-3000 °C), the high vapour pressure of SiO_2 led to its

depletion from the molten material, resulting in the formation of YbMS and Yb_2O_3 phases in the YbDS coating.

Increasing the spray power also had a drastic effect on the phase composition of the coatings. The heat-treated microstructures of all the YbDS coatings deposited in Figure 28 exhibit a multi-phase structure, one appearing lighter in colour indicating it is rich in heavier elements, while the other has a darker contrast indicating a greater fraction of lighter elements. XRD analysis of the coatings in Figure 31 identified these two phases to be YbDS and YbMS. Previous works have shown that these bands do not represent distinct equilibrium phases but, in fact, combinations of equilibrium phases, in this case, YbDS and YbMS, with the contrast coming from the proportion of each within the band [83, 85].

Diffractograms of the as-sprayed and heat-treated coatings are shown in Figure 30 and Figure 31. The as-sprayed coatings contain mainly amorphous phases as expected in APS EBCs. Due to the high cooling rate of the particles, after they have impacted the substrate during APS, amorphous structures are formed [85, 92, 110]. In all of the diffractograms, two broad amorphous humps are visible between ~25° - 35° and ~40° - 60°; however, some crystalline peaks can be detected in the coatings produced with 12 and 24 kW spray powers. From Figure 30, the 12 kW coating contained peaks corresponding to monoclinic YbDS (C2/m, 82-0734), a further indication of a high volume of un-melted material. Meanwhile, in the 24 kW coating, one prominent peak can be identified at ~29°. This peak likely corresponds to cubic Yb_2O_3 (I213, 74-1981) (222), indicating excessive SiO_2 loss when using this spray power as no Yb_2O_3 was detected in the feedstock powder.

Heat treatment prompted crystallisation of the phases in the coatings, the diffractograms of the heat-treated coatings can be seen in Figure 31. Monoclinic YbDS (C2/m, 00-082-0734) and monoclinic YbMS (I2/a, 40-0386) phases were identified in all the coatings. This two-phase structure can be seen clearly in Figure 32 along with EDX analysis of the two phases. EDX analysis of the phases showed the darker phases to be Si and O rich compared to the lighter phase. While the limitations of measuring oxygen with EDX due to it being a light element are understood, the atomic percentages were close to the stoichiometry of the indicated phases. Figure 33 shows the composition of a suspected Yb_2O_3 particle in the coating deposited using 24 kW after heat treatment. The EDX analysis of the particle shows it to be almost Si free, containing only 1.2 at. % Si.

The phase composition of the heat-treated coatings was quantified by Rietveld refinement. The respective phase compositions of all the coatings are shown in Table 5. The phase composition of the coating is sensitive to the spraying parameters used in its deposition. In every coating except the one deposited using 12 kW, the amount of YbMS was greater than the amount of YbDS. Increasing the arc current and the amount of H_2 in the plasma gas composition increased the spray power, which led to increased particle temperatures, in turn leading to a higher rate of SiO_2 loss and a shift towards more Yb-rich compositions [154].

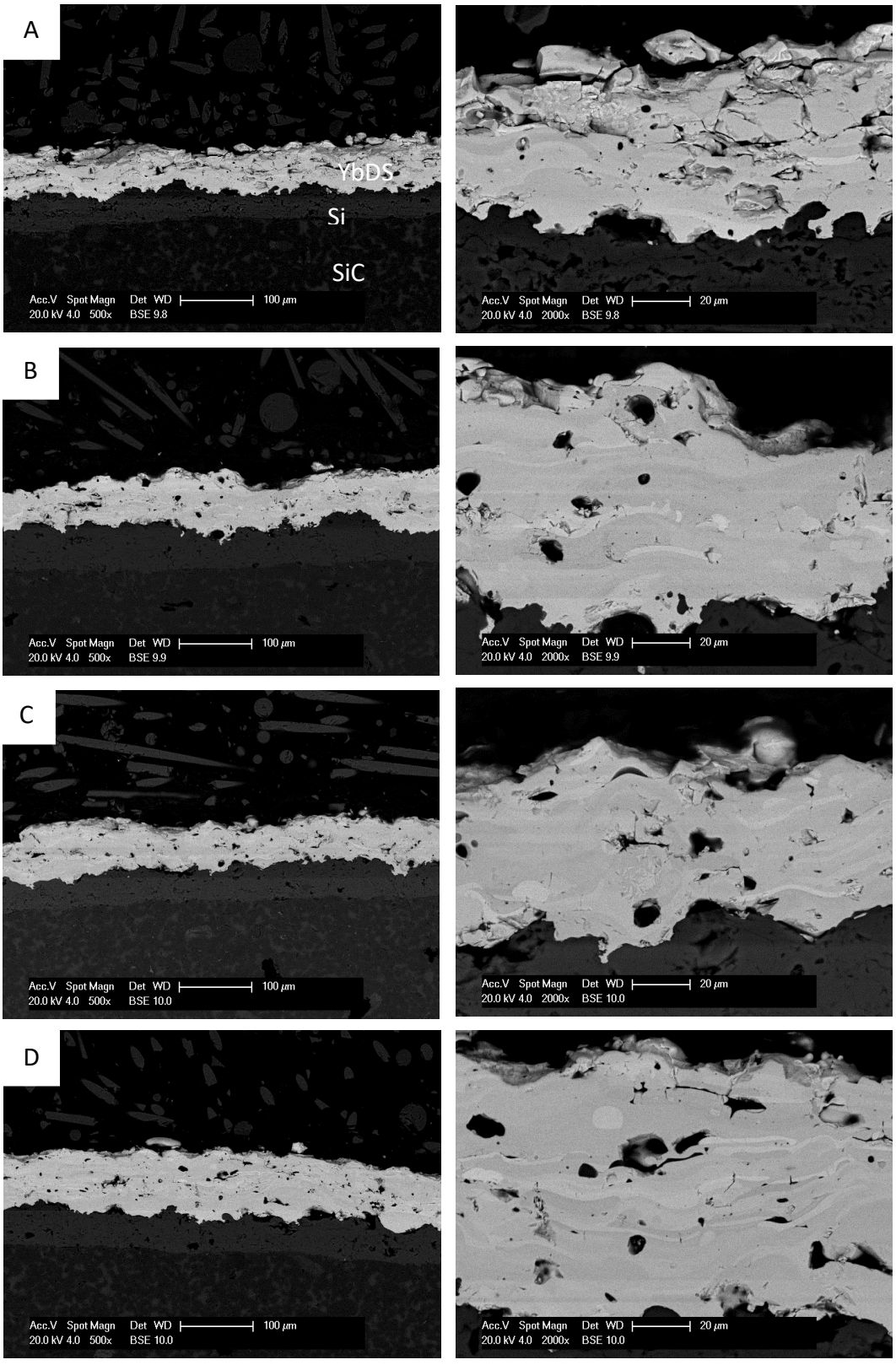

Figure 28. BSE SEM images of heat-treated YbDS coating microstructures deposited using the four sets of spraying parameters with (a) corresponding to a spray power of 12, (b) 16, (c) 20 and (d) 24 kW.

Table 4. Porosity and microhardness measurements for coatings deposited using the four spray powers.

Spray Number	Spray Power (kW)	Deposition Rate (μm/pass)	Porosity (heat-treated) (% area)	Microhardness (heat-treated) (HV0.1)	Particle Velocity (ms^{-1})	Particle Temperature (°C)
1	12	35	9.8 ± 1.1	463.4 ± 90.9	89 ± 1	1687 ± 43
2	16	41	8.3 ± 1.1	686.7 ± 77.3	100 ± 1	1889 ± 8
3	20	45	7.2 ± 0.9	718.4 ± 81.9	114 ± 1	2014 ± 11
4	24	48	5.6 ± 0.5	736.2 ± 51.5	129 ± 1	2095 ± 13

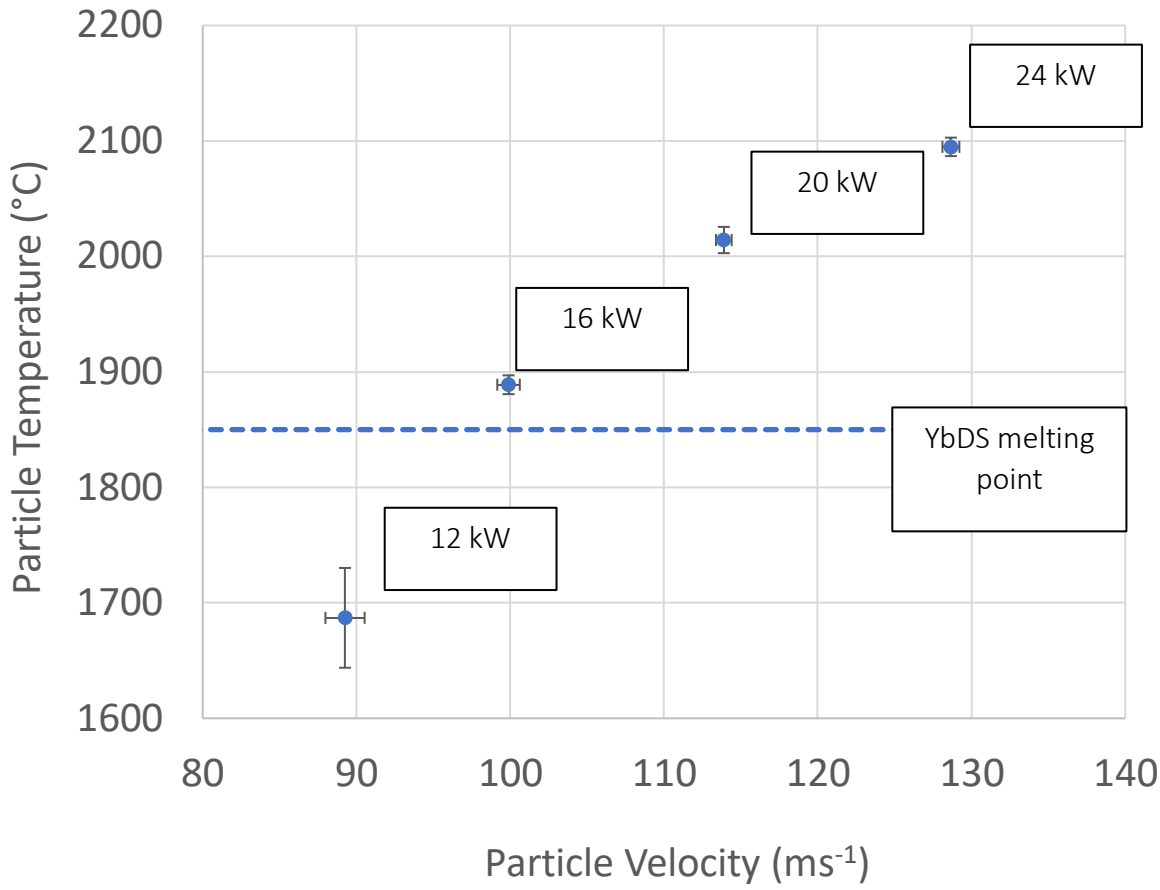

Figure 29. A graph showing particle velocity vs particle temperature, measured with a Tecnar Accuraspray 4, for the four different spray powers.

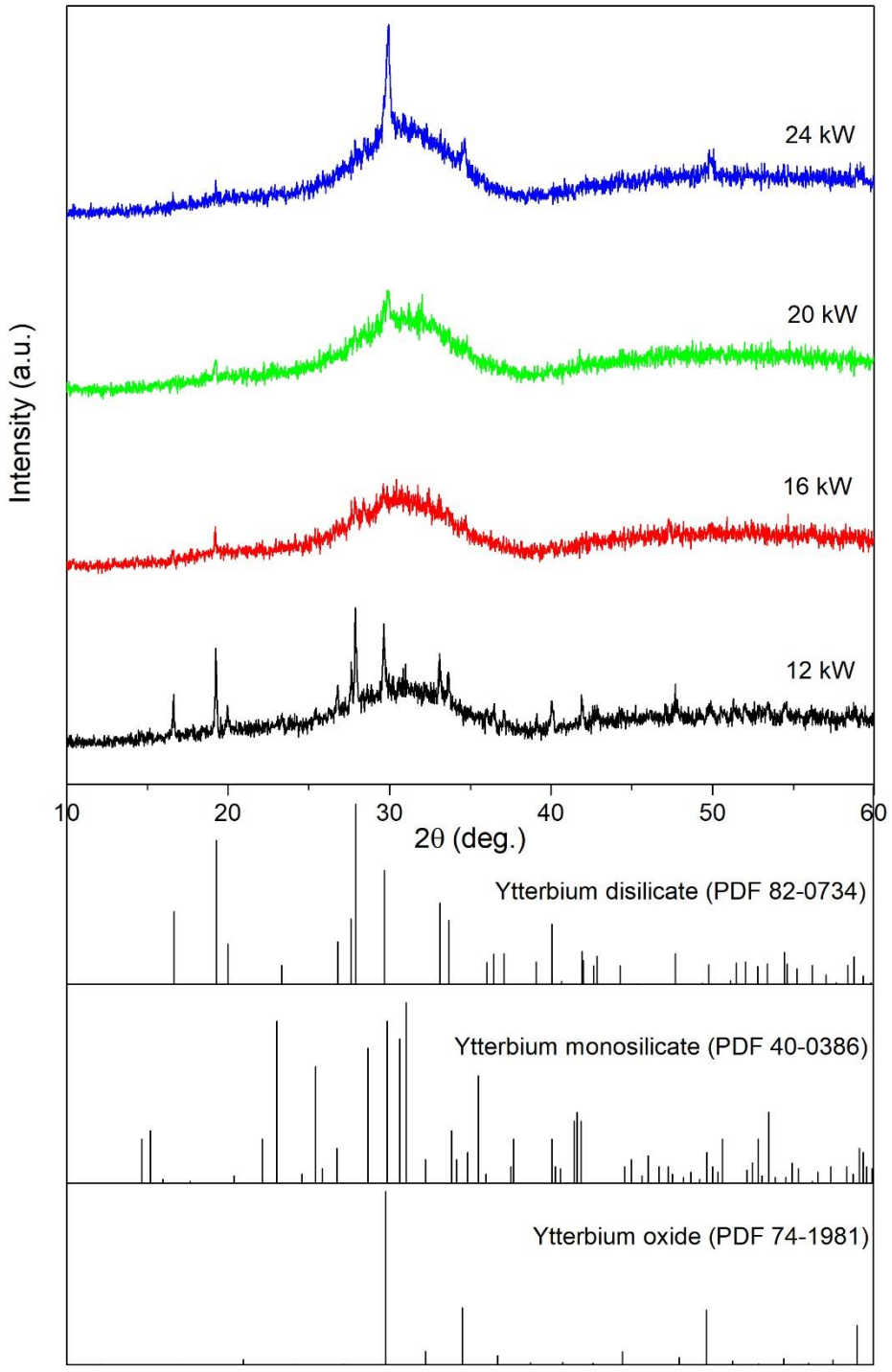

Figure 30. XRD diffractograms for the as-sprayed coatings sprayed at 12, 16, 20 and 24 kW.

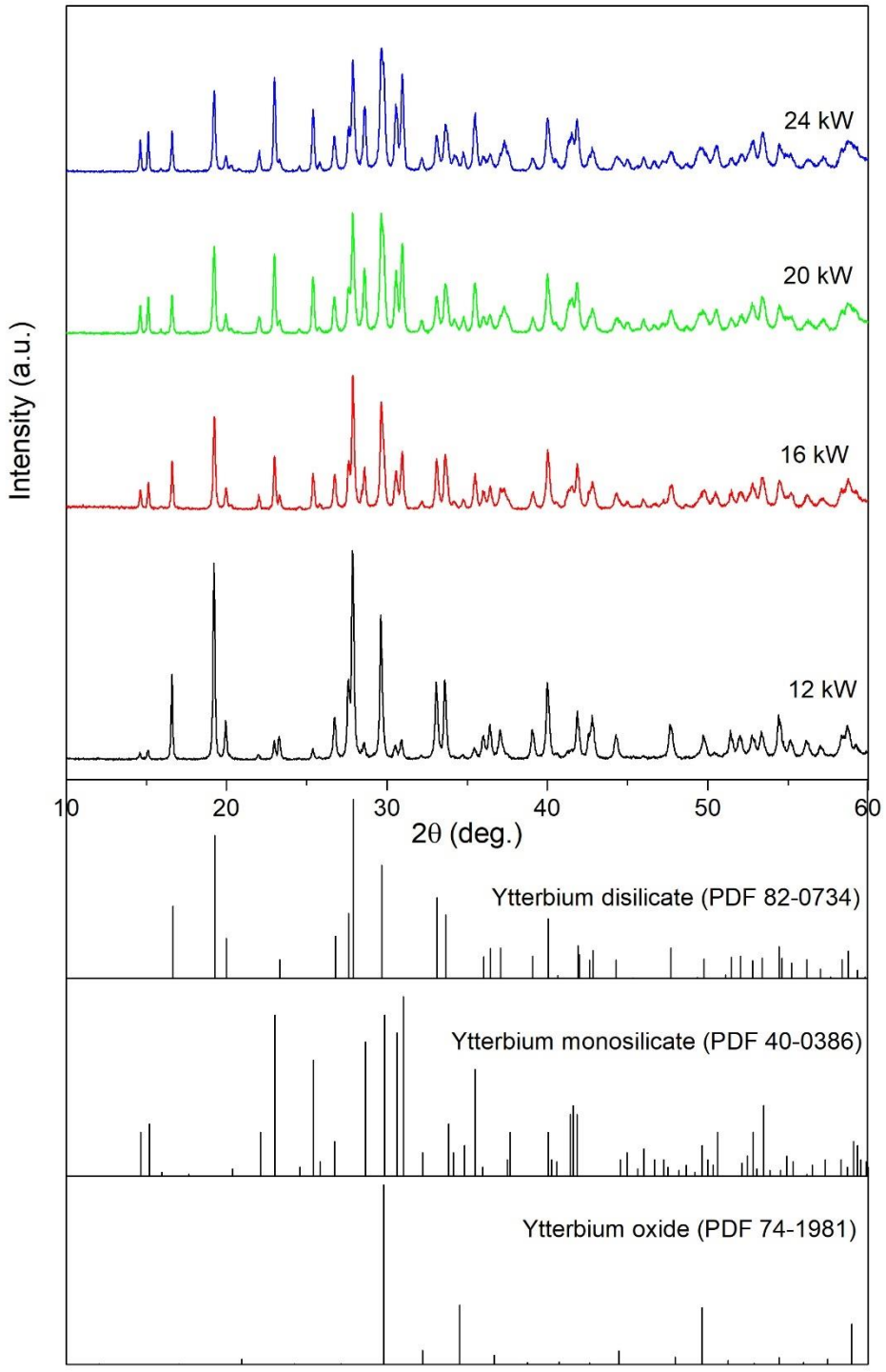

Figure 31. XRD diffractograms of the heat-treated coatings sprayed at 12, 16, 20 and 24 kW.

Table 5. YbDS, YbMS and Yb_2O_3 content for coatings deposited using the four spray powers.

Spray Number	Spray Power (kW)	YbDS Content (wt. %)	YbMS Content (wt. %)	Yb_2O_3 Content (wt. %)
1	12	87.0 ± 0.2	13.0 ± 0.2	-
2	16	60.1 ± 0.3	39.9 ± 0.3	-
3	20	48.7 ± 0.2	51.3 ± 0.2	-
4	24	43.2 ± 0.2	52.0 ± 0.2	4.8 ± 0.1

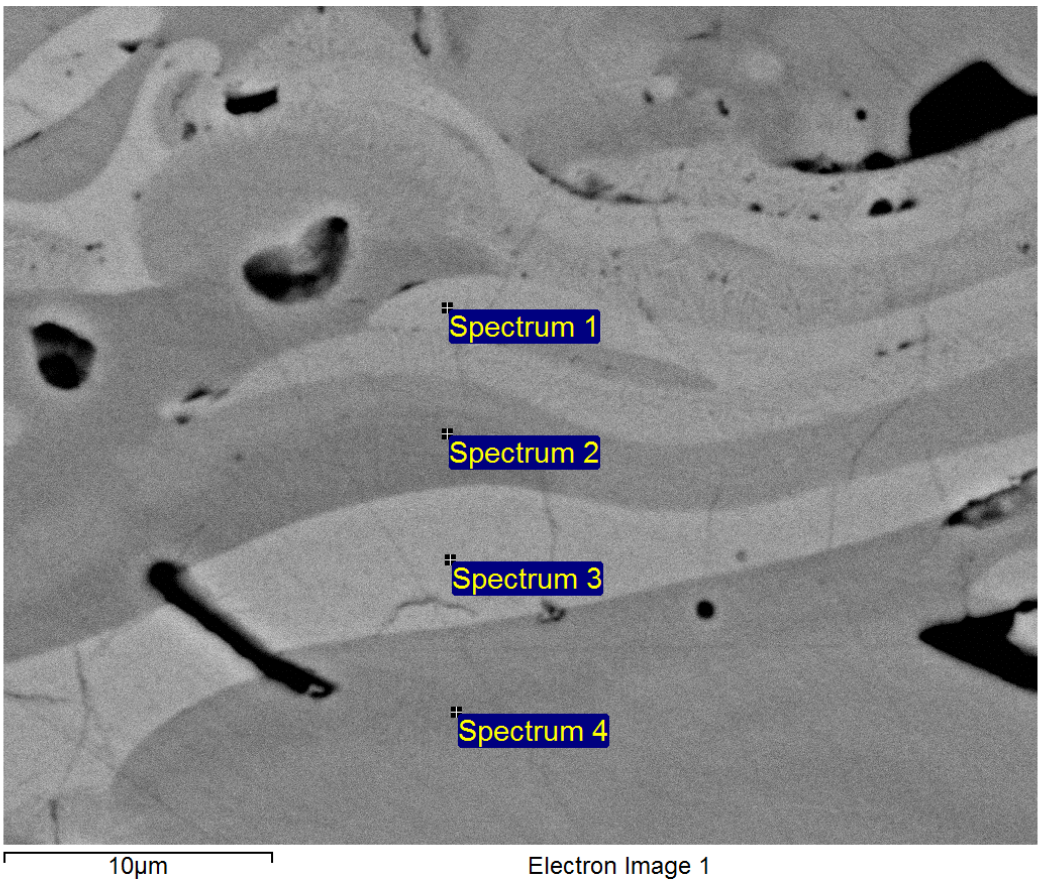

Figure 32. A high magnification SEM image of a heat-treated YbDS coating microstructure, deposited using 24 kW parameters (spray 1). The greyscale contrast shows the presence of multiple phases. For reference, the EDX spot analysis was ~1 µm in size.

Table 6. EDX results from the SEM image shown in Figure 32. Spectrums 1 and 3 show EDX analysis of a brighter appearing phase while spectrums 2 and 4 show EDX analysis of a darker phase. Compared to the lighter phase the darker phase is Yb rich and Si depleted.

Element (at. %)	Yb	Si	O
Spectrum 1	27	11	62
Spectrum 2	21	16	63
Spectrum 3	27	11	62
Spectrum 4	22	15	63

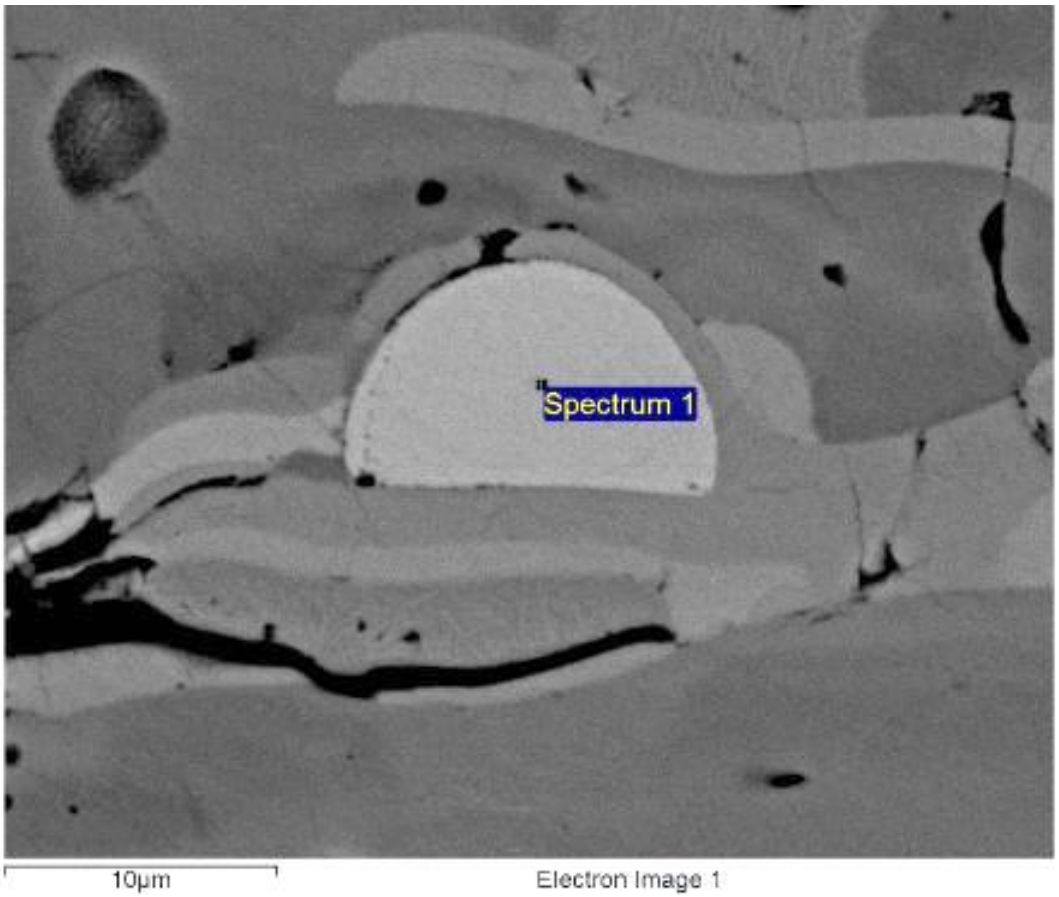

Figure 33. EDX analysis of a suspected Yb_2O_3 particle in the coating deposited using 24 kW (spray 1) after heat treatment, spectrum 1 contained 35.1 at. % Yb, 1.2 at. % Si and 63.7 at. % O.

4.3.2. Effect of Stand-off Distance

While the level of porosity achieved using 12 kW spray power was desirable for an abradable coating, the microhardness of the coating was relatively low when compared to the other coatings produced. In an effort to increase the microhardness of the coatings the effect of stand-off distance was investigated while the other spray parameters remained constant. The heat-treated microstructures of the coatings deposited at 12 kW using three different stand-off distances can be seen in Figure 34. Despite the stand-off distance being altered, the microstructures appear largely similar. All of the coatings exhibit large pores and a combination of fully, partially and un-melted particles. From Table 7, it can be seen that for all of the coatings, the level of porosity remains largely constant irrespective of the stand-off distance used in the spraying process. Despite the level of porosity remaining relatively stable the microhardness values, again shown in Table 7, increased as the stand-off distance was shortened. Increasing the stand-off distance also reduces the deposition rate and, effectively, the deposition efficiency, as explained in the previous section.

Figure 35 shows a graph of particle velocity vs particle temperature for the three stand-off distances, measured using an Accuraspray 4. As the stand-off distance is reduced the particle velocity and temperature increase, leading to the increase in microhardness observed in the coatings. The particle temperature was still lower than the YbDS melting point when the particles impact the substrate meaning similar microstructures and levels of porosity were retained due to the presence of un-melted and partially melted particles. The particles at shorter stand-off distances impacted the substrate with higher velocities, which led to an increase in deformation of the particles, and created better-bonded splats, which in turn increased the microhardness of the coatings. Previous work on the effect plasma parameters have on coating properties has shown the relationship between reducing stand-off distance and increasing hardness [155, 156]. Particularly, work by Sarikaya has shown that, when spraying alumina, by increasing stand-off distance changes in hardness can be achieved without significant changes in porosity level [155]. No difference in phase composition was detected using XRD and Rietveld refinement when the stand-off distance was changed, given all the coatings were deposited using the same spray parameters, it is likely the majority of the SiO_2 volatilisation occurred earlier in the particles' flight towards the substrate, in the highest temperature part of the plasma (< 100 mm).

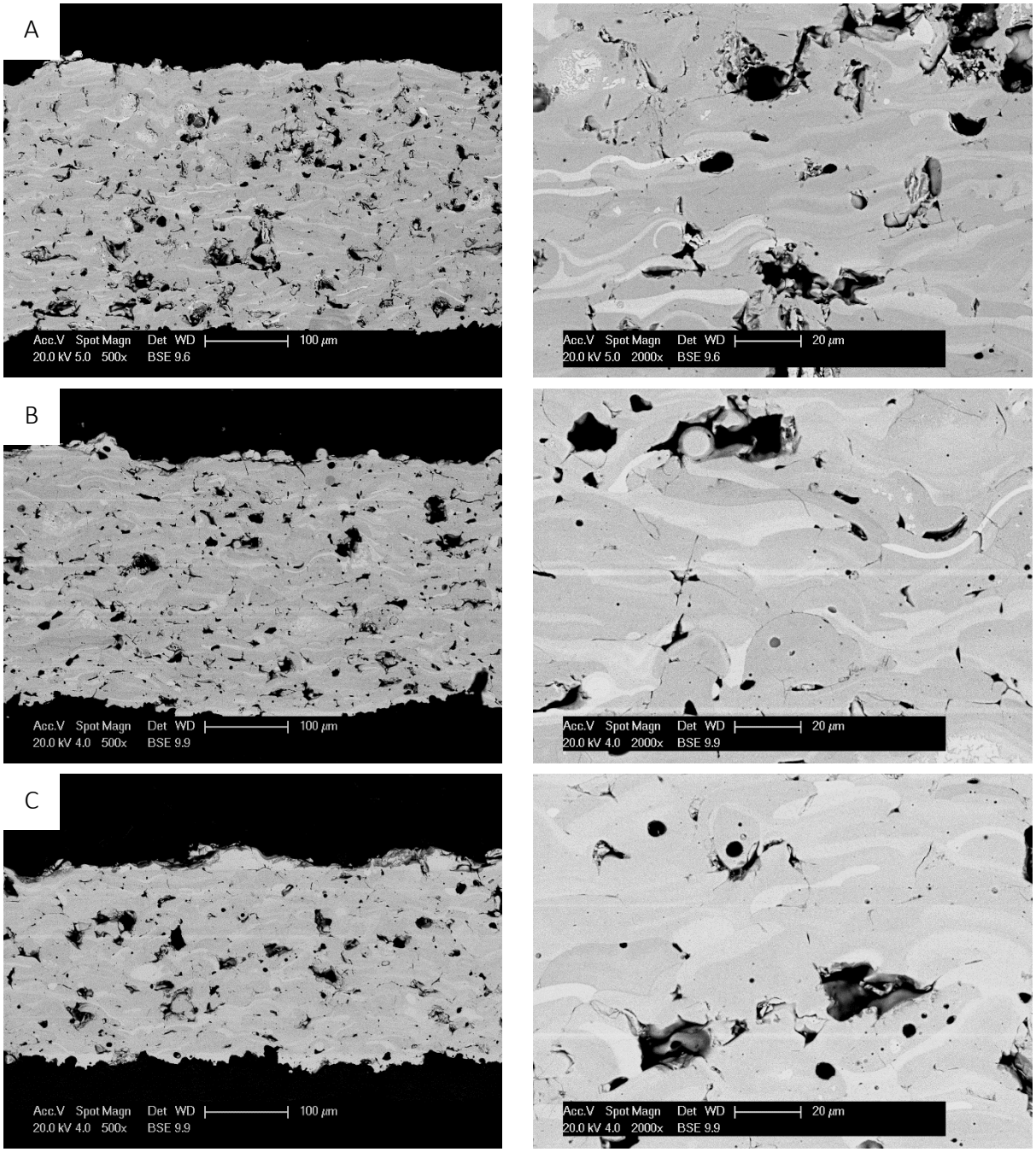

Figure 34. BSE SEM images of heat-treated YbDS coating microstructures deposited using 12 kW spray power at various stand-off distances with (a) corresponding to a stand-off distance of 100 mm, (b) 125 and (c) 150 mm.

Table 7. Porosity, taken using ImageJ, and microhardness measurements for coatings deposited using the three stand-off distances.

Spray Number	Stand-off Distance (mm)	Deposition Rate (μm/pass)	Porosity (heat-treated) (% area)	Microhardness (HV0.1)	Particle Velocity (ms^{-1})	Particle Temperature (°C)
5	100	32	12.4 ± 0.5	735 ± 79	108 ± 1	1738 ± 17
6	125	31	10.7 ± 0.4	605 ± 113	103 ± 1	1702 ± 14
7	150	25	12.4 ± 2.4	511 ± 132	89 ± 1	1687 ± 43

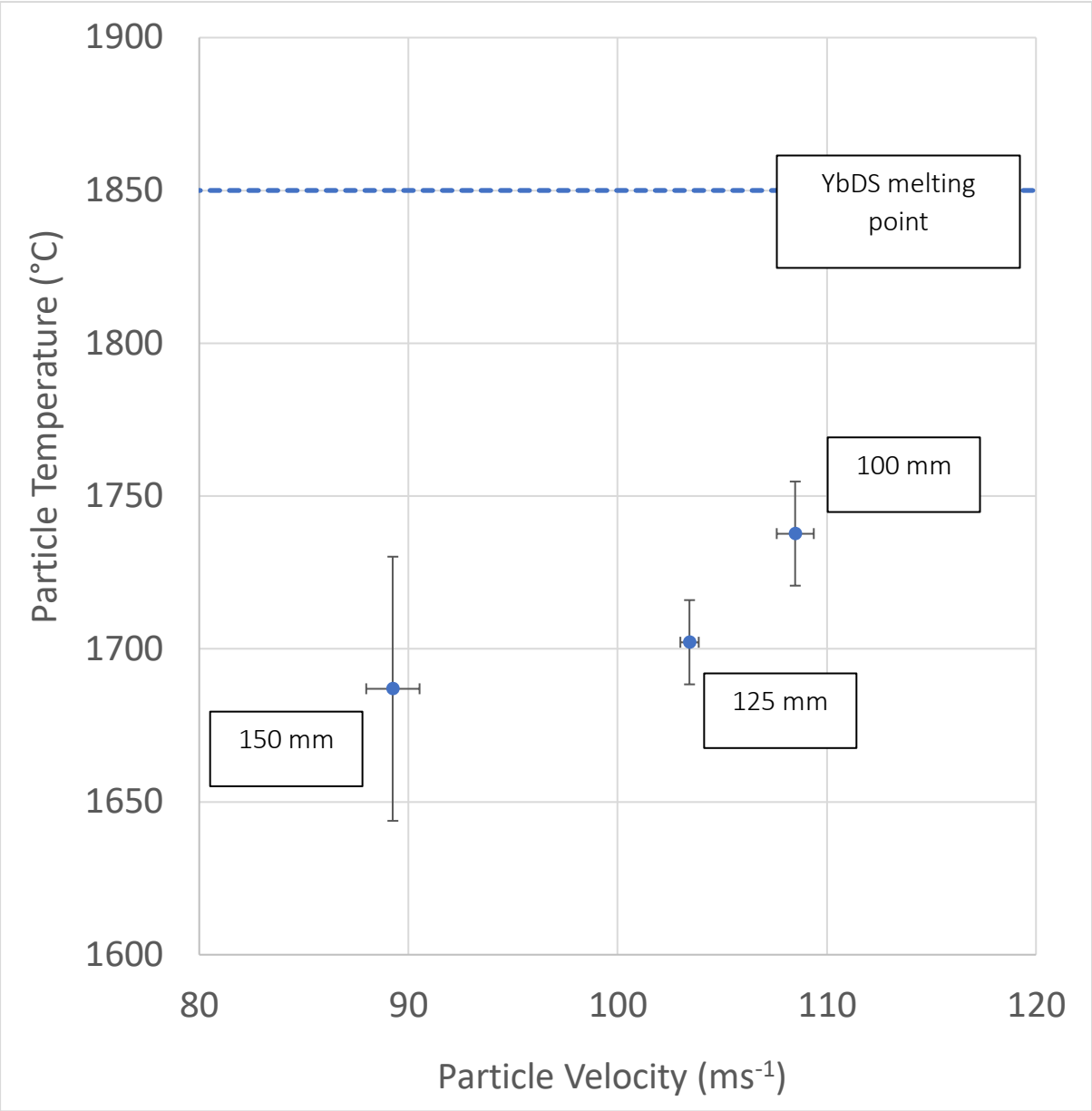

Figure 35. A graph showing particle velocity vs. particle temperature, measured with a Tecnar Accuraspray 4, for the three different stand-off distances.

4.3.3. Effect of PE Addition

Based on the work presented so far, a relatively dense YbDS EBC was deposited using 24 kW spray power at a stand-off distance of 150 mm (referred to as EBC), while a porous abradable EBC was deposited using 12 kW spray power at a stand-off distance of 125 mm (referred to as ABR). These conditions were selected to maximise the hardness of the coating and the YbDS phase. The stand-off distance of 100 mm produced highly stressed coatings with occasional delamination between the SiC substrate and the Si bond coat. To

reduce this 125 mm was selected as the optimum stand-off distance while the robot scanning speed was increased to 1000 mm/s. To increase the level of porosity further, feedstocks with 1.5 wt. % and 4.5 wt. % PE addition to YbDS were also deposited using 12 kW spray power (referred to as ABR + 1.5 wt. % PE and ABR + 4.5 wt. % PE respectively). The as-sprayed microstructures of these four coatings are shown in Figure 36, while the heat-treated microstructures are shown in Figure 37. In its as-sprayed state, the EBC microstructure has some porosity and microcracking; however, upon heat-treatment these microcracks have healed. ABR shows a highly porous structure caused by un-melted and partially melted particles previously seen in sections 3.1.1 and 3.1.2. The addition of the PE has caused further large pores in addition to the smaller pores and inter-splat pores caused by the low spray power, as can be seen in Figure 37c and d. The increased level of porosity caused by the addition of PE was quantified and is presented in Table 8. The porosity values for EBC and ABR are similar to what has been reported previously in sections 3.1.1 and 3.1.2; however, the addition of 1.5 and 4.5 wt. % greatly increases the level of measured porosity in the coating to 14.4 and 18.9 %, respectively. The addition of the PE did not cause any change in phase composition from the ABR coating, this was verified using XRD.

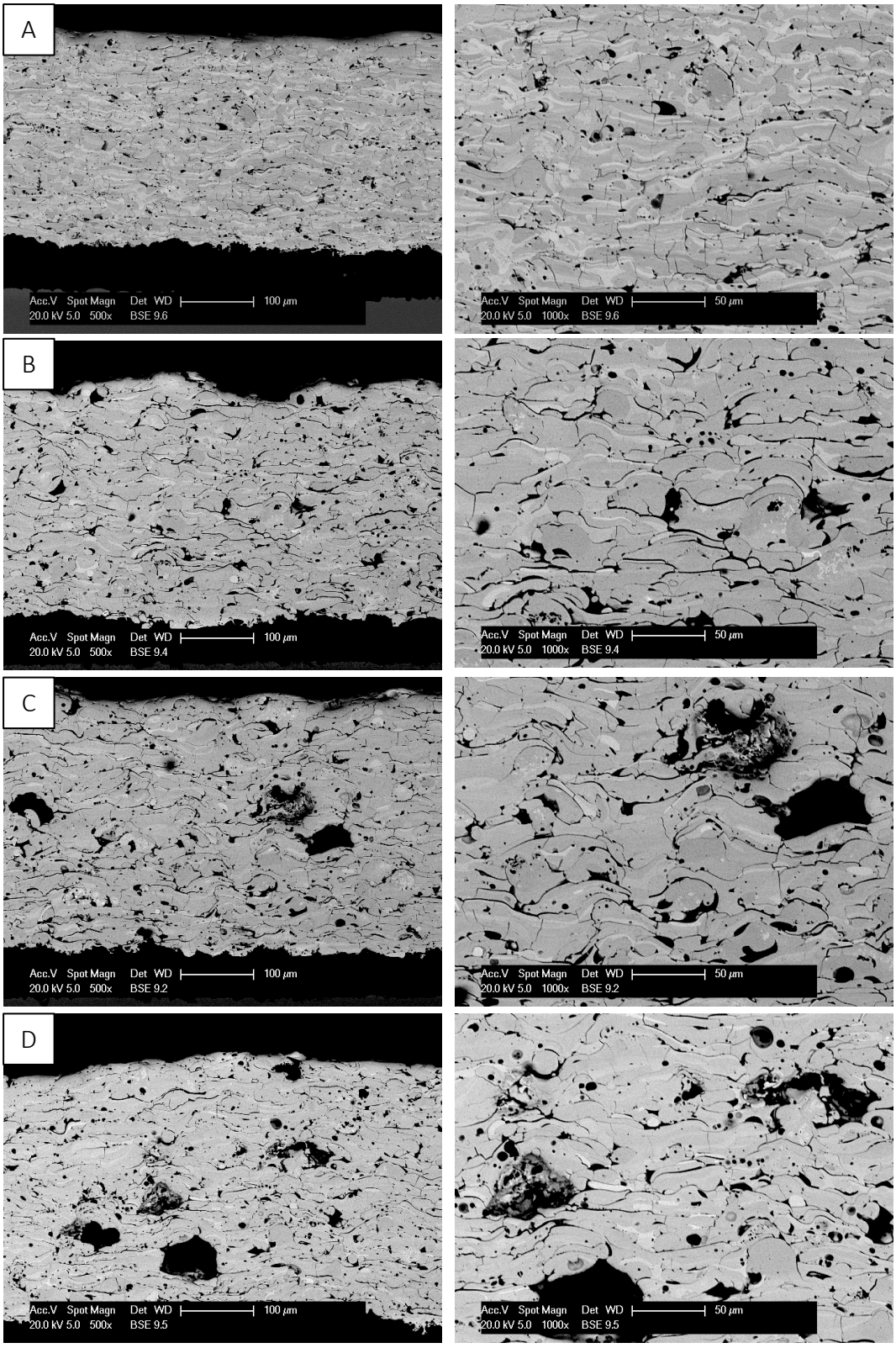

Figure 36. BSE SEM images of as-sprayed YbDS coating microstructures deposited using various feedstocks, spray powers and stand-off distances with (a) corresponding to a relatively dense YbDS EBC deposited using 24 kW spray power at a stand-off distance of 150 mm (EBC), (b) a porous abradable YbDS EBC deposited using 12 kW spray power at a stand-

off distance of 120 mm (ABR) (c) a porous abradable YbDS + 1.5 wt. % PE EBC deposited using 12 kW spray power at a stand-off distance of 120 mm (ABR+ 1.5 wt. % PE) and (d) a porous abradable YbDS + 4.5 wt. % PE EBC deposited using 12 kW spray power at a stand-off distance of 120 mm (ABR+ 4.5 wt. % PE).

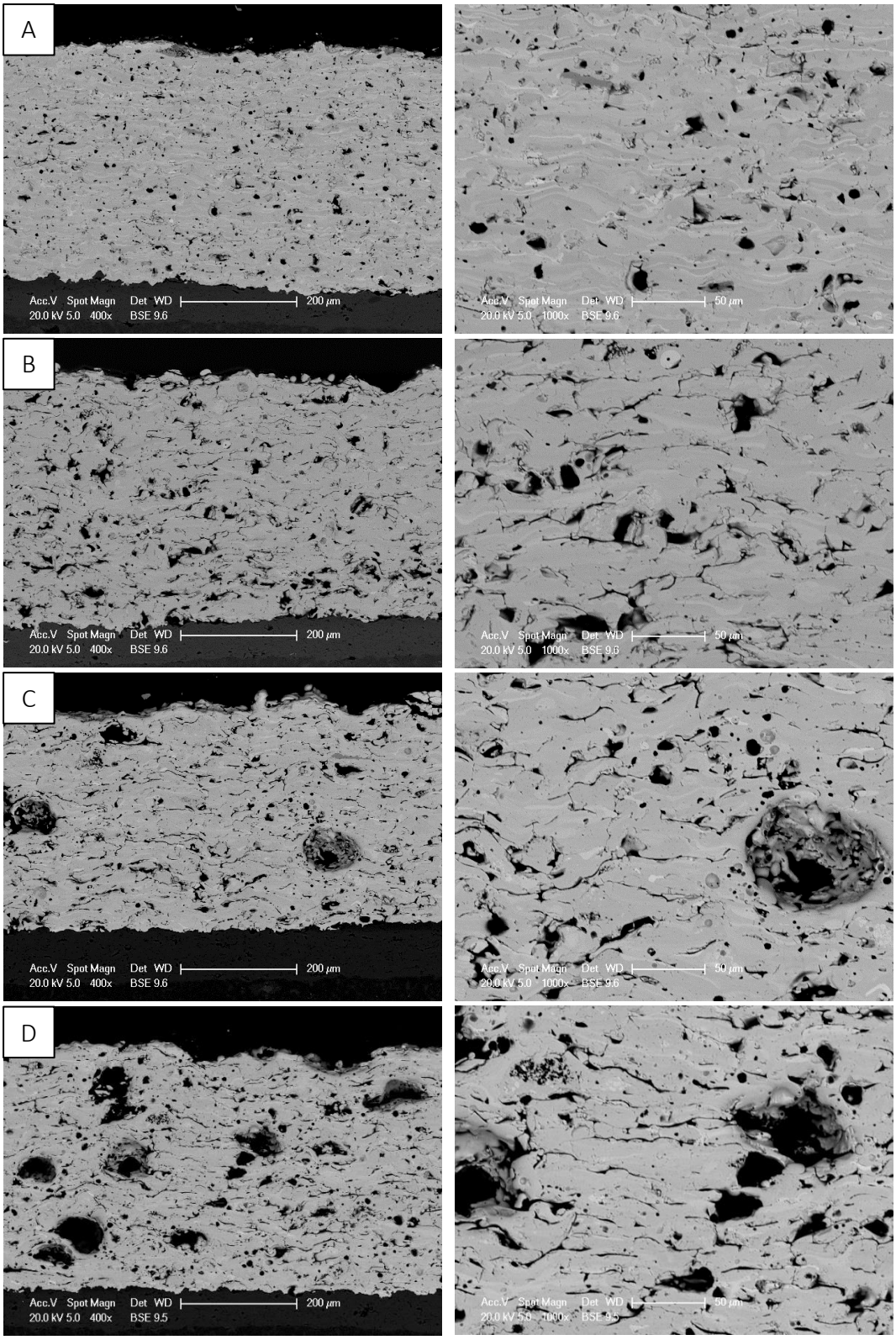

Figure 37. BSE SEM images of heat-treated YbDS coating microstructures deposited using various feedstocks, spray powers and stand-off distances with (a) corresponding to a relatively dense YbDS EBC deposited using 24 kW spray power at a stand-off distance of 150 mm (EBC), (b) a porous abradable YbDS EBC deposited using 12 kW spray power at a stand-

off distance of 120 mm (ABR) (c) a porous abradable YbDS + 1.5 wt. % PE EBC deposited using 12 kW spray power at a stand-off distance of 120 mm (ABR+ 1.5 wt. % PE) and (d) a porous abradable YbDS + 4.5 wt. % PE EBC deposited using 12 kW spray power at a stand-off distance of 120 mm (ABR+ 4.5 wt. % PE).

Table 8. Porosity and microhardness measurements for the EBC and three abradable EBC coatings.

Spray Number	Coating	Porosity (Heat-treated) (% area)	Microhardness (heat-treated) (HV0.1)
8	EBC	5.6 ± 0.4	783.1 ± 28.1
9	ABR	8.8 ± 0.8	695.6 ± 42.3
10	ABR + 1.5 wt. % PE	14.4 ± 0.9	633.5 ± 27.6
11	ABR + 4.5 wt. % PE	18.9 ± 2.1	553.9 ± 50.0

4.4. Discussion

In order to optimise the deposition process of YbDS EBCs and abradable EBCs, the effect the spray parameters and feedstock modification have on phase composition and microstructure must be understood. The coatings reported in this study present vastly different phase compositions and microstructures depending on the deposition conditions employed. During the APS process, YbDS has transformed to YbMS regardless of spray power since only a small weight percentage of YbMS was detected in the feedstock powder. Richards et al. [83] proposed this was due to the higher vapour pressure of the Si bearing species leading to its preferential volatilisation at elevated temperatures above ~1000 °C, resulting in the formation of YbMS. Between 1300 and 2500 °C the vapour pressure of the Si bearing species was ~10^6 times larger than the vapour pressure of the Yb bearing species [83]. When relating the particle temperatures measured in the plasma plume for the various spray powers in Figure 29 to the phase quantification determined using Rietveld refinement results in

Table 5; it is clear that increasing the spray power (therefore increasing the particle temperature) leads to a higher rate of SiO_2 volatilisation and a greater fraction of YbMS in the coating. Increasing the spray power from 12 to 24 kW increased the average particle temperature at the point it impacted the substrate from 1687 to 2095 °C, which led to a decrease in YbDS phase content from 87 to 43 wt. %. These findings are in agreement with previous studies by Chen et al. [88] and Garcia et al. [85], who also found that higher spray powers resulted in higher particle temperatures, which in turn led to increased fractions of YbMS in the respective coatings.

In the as-sprayed XRD results, one prominent peak can be identified at ~29° in the coating deposited at 24 kW. This peak likely corresponds to the plane (222) of cubic Yb_2O_3 (I213, 74-1981), indicating excessive SiO_2 loss when using this spray power as no Yb_2O_3 was detected in the feedstock powder. Yb_2O_3 has a much higher melting point than YbDS or YbMS (2355 °C, relative to 1850 °C and 1950 °C, respectively [154]), indicating the possibility of a solid crystalline phase during the spraying process, since this is below the particle temperatures measured when using this spray power (2095 °C). While previous research has not led to the discovery of Yb_2O_3 when spraying YbDS feedstocks, Richards et al. [107] did determine its presence when spraying a YbMS powder, indicating if the level of SiO_2 volatilisation is severe enough, Yb_2O_3 will form. Compared to previous studies where particle temperature and velocity have been analysed, it can be determined that the particle velocities obtained in this study were significantly lower, even when the particles temperatures were high, at higher spray powers [85, 88]. This means that each particle has a longer residence time in the plasma, increasing its time at temperature and leading to a greater loss of SiO_2.

In order to form the amount of porosity required for an abradable coating, it was necessary to reduce the spray power to such an extent that some portion of the feedstock was un-melted and remained as such within the coating. This can be seen from the XRD data in Figure 30, where crystalline YbDS peaks could still be detected in the as-sprayed 12 kW coating. If the feedstock was fully molten, it would appear as an amorphous phase rather than crystalline, as can be seen on the diffractograms of the coatings deposited at higher spray powers. While some un-melted and partially melted particles can be seen in the heat-treated microstructures in Figure 28a and Figure 34, a lot of the splats appear to have flattened, indicating they were at least somewhat molten as they impinged onto the

substrate and formed structures typical of an APS structure. Data obtained from Accurspray 4.0 (Figure 29 and Figure 35) suggests that, when using 12 kW spray power, the average particle temperature is well below the melting point despite the prevalence of many fully molten splats. The averaged particle data collected using the Accuraspray system is known to be slightly weighted towards larger particles [157]; these particles will require higher thermal energy input to fully melt, hence will not reach as higher temperatures as smaller particles which are fully molten, thus skewing the particle temperature data.

While the majority of data on the level of porosity typically seen in the OEM abradable YbDS EBCs is not publicly available, abradable coatings tested by Tejero-Martin et al. [59] for CMAS recession, produced using similar equipment and feedstocks, were measured to have between 19.4 and 21.3 % porosity. Previous work on other ceramic abradable coatings, specifically yttria-stabilised zirconia (YSZ) containing polyester, has typically seen porosity levels between 10 and 25% [49, 158]. This suggests the abradable coatings produced in the study, as seen in Figure 37b, c and d, are suitably porous for abradable applications provided they can provide adequate protection from steam recession and CMAS corrosion. Future work will be foccused on not only this, but also how the coatings respond to abrasives in erosion testing and scaled rig testing against dummy turbine blade tips.

4.5. Conclusions

Abradable EBCs have the potential to greatly improve the efficiency of the latest generation of gas turbines that utilise SiC CMC components. In this work, for the first time, a parametric study was undertaken to understand how spray parameters affected the phase composition and microstructure, with the aim of creating a porous abradable coating with a commercially available and widely utilised SG-100 APS torch. By carefully adjusting the spray power and stand-off distance, the level of porosity, phase composition and microhardness was controlled. An abradable coating with ~10 % porosity, ~80 wt. % YbDS phase composition and ~700 HV microhardness was deposited by reducing the spray power to such a level where the particle temperature was below the melting temperature of YbDS. Subsequently, a PE pore forming phase was added to the feedstock to increase the porosity further. The addition of 1.5 and 4.5 wt. % PE resulted in porosity increasing to ~14 and ~19 %, respectively. Relationships between spray parameters and coating properties have also

been determined. Low spray powers resulting low particle temperatures and velocities produced more porous coatings yet retained greater proportions of YbDS phase. While high spray powers producing higher particle temperatures and velocities produced harder coatings with less porosity but also less YbDS phase. The high spray powers in this study produced coatings with exceptionally high amounts of YbMS relative to previous literature. It is postulated that this is due to the high spray powers producing high particle temperatures but still relatively low particle temperatures when compared to other plasma spray systems, causing excessive time at high temperature for the particles in the plasma.

Acknowledgements

This work was supported by the Engineering and Physical Sciences Research Council (EPSRC) (grant number EP/V010093/1). The project also received funding from Rolls Royce Plc in terms of a CASE PhD studentship. The authors also acknowledge the use of facilities at the Nanoscale and Microscale Research Centre of the University of Nottingham, supported by the Engineering and Physical Sciences Research Council (grant number EP/L022494/1).

Chapter 5: An investigation into the erosion and wear mechanisms observed in abradable ytterbium disilicate environmental barrier coatings

This chapter is reproduced from the paper:

A. Lynam, A. Rincon Romero, F. Xu, A. Baillieu, M. Marshall, G.J. Brewster, G. Pattinson, T. Hussain, An investigation into the erosion and wear mechanisms observed in abradable ytterbium disilicate environmental barrier coatings, Journal of the European Ceramic Society, Volume 44, Issue 12, 2024, Pages 7310-7327, https://doi.org/10.1016/j.jeurceramsoc.2024.05.008.

Abstract

Abradable environmental barrier coatings (EBCs) are used to reduce clearances between blades and casings in the hottest parts of aero gas turbines, increasing the overall efficiency of the turbine, however, research into the mechanical performance of such coatings is limited. The aim of this work was to better understand the relationship between microstructure and erosion and wear performance in abradable EBCs, since publicly available literature regarding such coatings is scarce and the potential efficiency gains in gas turbines are significant. In this study, ytterbium disilicate abradable EBCs containing three different porosity levels (determined by fugitive polyester phase addition) were deposited using atmospheric plasma spraying with porosity levels of 8, 15 and 21.5 % by area. These coatings were then characterised in numerous ways; the porosity was quantified, the thermal conductivity was measured, the superficial hardness and erosion resistance were measured, and finally, the coatings were subjected to a rig test designed to simulate in-service cutting mechanisms against a tipped turbine blade. The results show that increasing the level of porosity via increasing the amount of pore forming phase in the feedstock, led to reduced erosion resistance and improved cutting by a turbine blade.

5.1. Introduction

Abradable coatings have been widely used within gas turbines for 40 years as essential design features for the smooth operation of the engines. These are employed on engine casing walls and allow clearances between rotating components such as fins and blades to be minimised, leading to an increase in efficiency and a reduction in fuel consumption [16]. The coatings are designed in such a way that when the rotating component strikes them, they will easily wear away rather than damaging the blade, thus creating a minimal clearance between the two. This is achieved by creating a porous coating (usually through the addition of a fugitive polymer), sometimes with the addition of dislocators and/or solid lubricants such as hexagonal boron nitride (hBN), graphite or bentonite [23, 36, 159]. Abradable coatings are almost universally deposited using atmospheric plasma spraying (APS). Much of the research into abradable coatings has focussed on metallic materials such as Aluminium-Silicon (Al-Si), Nickel (Ni)-based, and MCrAlY which has base metal (M) of Ni or Cobalt (Co) combined with chromium (Cr), aluminium (Al), and Yttrium (Y) (with the aforementioned additions) [22, 23, 42, 159]. These materials are utilised in the low temperature compressor stage of the turbine, however, more recently, there has been an increase in interest in high temperature yttria stabilised zirconia (YSZ) ceramic abradable coatings, which can be deployed in the high-pressure turbine section [47, 49, 160].

As the service temperatures continue to increase and superalloys reach the limit of their performance, ceramic based structural components are becoming adopted in the hot section of the turbine. SiC-SiC ceramic matrix composites (CMCs) are the next-generation lightweight materials with superior properties in the hot section of the turbine. Environmental barrier coatings (EBCs) are required to protect SiC based composites from recession due to the presence of water vapour produced as a result of the combustion process. Ytterbium disilicate (YbDS) has been widely researched as an EBC owing to its closely matched coefficient of thermal expansion (CTE) (4.1 $x10^{-6}$ K^{-1}, measured over a range of 303–1873 K), phase stability and the protection it offers from steam recession [9].

It follows that the drive towards higher temperatures and increased efficiency would lead to abradable EBCs being the next logical step in terms of high-pressure turbine protective coating development, however, publicly available research into such coatings is limited. Tejero-Martin et al. [59, 60], examined the microstructure, steam recession and CMAS

(calcium magnesium aluminium silicate) designed to represent the corrosive nature of molten sand/ash which may be ingested by the turbine. Despite this, the tribological investigation into abradable EBCs is limited to work by Qin et al. [61], who performed a pin-on-disc wear test of YbDS with additions of hBN. While this work showed a reduction in coefficient of friction and an increase in coating wear with increased levels of hBN, the wear mechanisms observed in the abradable coating may differ from those seen in service [30].

Instead, much of the work in published literature analysing the abradability of these coatings has been conducted on the metallic based systems and ceramic YSZ systems (albeit to a lesser extent) mentioned previously. Such research has largely been conducted on specially designed test rigs, incorporating a moving stage on to which the abradable coating is mounted (controlling the incursion rate) and a turbine blade rotating at high speeds to match the tip velocities found in service [19, 22, 30, 48, 161-163]. The wear mechanisms observed in abradable coatings (from analysis of parts that had been in service) was first described by Borel et al. [19]. Three main mechanisms were identified: cutting, adhesion and deformation. Cutting is similar to a turning process, where the blade tip acts as the cutting tool, and material is removed in a brittle manner, even in ductile material, and is the most efficient mechanism [19]. Adhesion and deformation were noted as being undesirable mechanisms. Adhesion involves the transfer of the abradable material to the blade or vice versa and is associated with overheating of the system and the creation of an undesirable hard transfer layer. Deformation can refer to either the plastic flow of the abradable material on the surface or a compaction/densification of the porosity in the radial direction. Compaction is particularly detrimental as the densification of the abradable means it is less likely to give way during future blade impacts [19, 23]. In metallic abradable coatings, the cutting mechanism is generally associated with high incursion rates, while at low incursion rates, adhesive wear is dominant [22, 23, 26, 27, 159]. Conversely, in ceramic abradable coatings, the wear mechanisms appear to be linked to the total porosity level, with a higher level of porosity leading to better cutting of the abradable and less blade wear independent of incursion rate [47]. Abradable coatings must also show a resistance to erosion resistance; while the coating must be able to be worn away by the blade, it must also have some resistance to erosion by foreign bodies which find their way into the turbine [16, 24, 48, 164]. The erosion resistance and abradability of the coating are conflicting properties, given

the coating must be resistant to damage by foreign bodies yet wear easily against the blade, not causing any damage. Given this, a range of 2-4 s/mil (s/mil being seconds taken to erode 25.4 µm of coating) is considered for abradable coatings when subjected to the industry standard GE E50TF121CL erosion test [16, 66].

Given the dearth of available literature surrounding abradable EBCs and the obvious potential benefits of their use, the aim of this study was to gain a better understanding of the erosion resistance and abradability of porous YbDS EBCs and how this is related to microstructure. This was achieved by depositing YbDS with three porosity levels, created by the addition of various amounts of polyester (PE), using APS. Subsequently, the erosion resistance of each abradable coating was measured, the eroded surfaces characterised and mechanisms investigated. In addition, a specially designed abradable rig was used to investigate the abradability of the coatings against cubic boron nitride (cBN) tipped blades. The wear mechanisms were analysed via a combination of in-situ measurement systems and post-test characterisation.

5.2. Materials and methods

5.2.1. Materials

Commercially available Si powder (Metco 4810) and YbDS (Metco 6157) (both Oerlikon Metco AG, Switzerland) were used as feedstocks for the respective layers. Finally, Metco 600NS (Oerlikon Metco AG, Switzerland), a polyester (PE) powder, was mixed with the YbDS powder at 1.5 and 4.5 wt. %. The Si powder had a nominal size range of 15-75 µm and contained < 1.5 wt. % SiO_2 and a balance of Si. The YbDS powder had a nominal size range of 11-90 µm and contained a maximum of 5 vol. % of unreacted Yb_2O_3 and YbMS. Prior to spraying, the powders were treated at 80 °C for 12 hours using a box furnace (Elite Thermal Systems, UK) to remove any moisture. The pore former was a crystalline aromatic polyester powder with a nominal size range of 45-125 µm. The mixture was homogenised using a Labram acoustic mixer (Resodyn Acoustic Mixers, USA). Prior to spraying, the powders were treated at 80 °C for 12 hours using a box furnace (Elite Thermal Systems, UK) to remove any moisture. Stainless steel test plates 50 x 50 mm and 5 mm thick, designed to be fixed into the abradable test rig, were used as the substrates.

5.2.2. Coating deposition

The coatings were deposited using atmospheric plasma spraying (APS). The coating system is comprised of a stainless steel substrate test plate, an intermediate Si bond layer and YbDS as a protective top layer. The substrates were grit blasted using a blast cleaner (Guyson, UK) with 100 mesh Al_2O_3 particles (Guyson, UK) at a pressure of 6 bar. An SG-100 plasma spray system (Praxair Surface Technology, USA) was used to deposit the coatings. The spray gun was fitted with a 02083-175 anode, 02083-120 cathode and a 03083-112 gas injector for both Si, YbDS and YbDS-Polyester coatings. The three coatings were labelled ABR (for the coating containing no polyester), 1.5 wt.% PE and 4.5 wt.% PE. Ar was used as the primary gas, and H_2 was used as the secondary gas. The Si bond coat was deposited using a spray power of 27 kW, a current of 400 A, primary gas (Ar) pressure of 95 psi (equivalent to a flow rate of 85 SLM), a secondary gas (H_2) pressure of 30 psi (2 SLM), a stand-off distance of 125 mm and the robot speed was 1000 mm/s over 6 passes. The 3 abradable EBCs were deposited using a spray power of 12 kW, a current of 600 A, primary gas (Ar) pressure of 85 psi (equivalent to a flow rate of 75 SLM), a secondary gas (H_2) pressure of 35 psi (2.5 SLM), a stand-off distance of 125 mm, and the robot speed was 1000 mm/s over 100 passes. This led to ~2 mm thick abradable coatings.

Free-standing coatings were prepared for thermal diffusivity measurements. Inconel 718 discs measuring 12.7 mm in diameter were lightly grit blasted with 100 mesh Al_2O_3 particles (Guyson, UK) at a pressure of 1 bar and subsequently coated with graphite spray (Kontakt Chemie, Germany), which led to the coatings completely detaching from the substrate, in one piece, after the spray was completed. The spray parameters were kept the same except for the number of passes which was reduced to 35, resulting in coatings that were ~400 µm thick. Further details about the powders and optimisation of the spray parameters can be found in [165].

5.2.3. Sample preparation

Coated samples were vacuum impregnated with EpoFix resin and hardener (15:2 volumetric ratio) (Struers, Denmark) and then sectioned. The cross-sections were mounted again using EpoFix resin and hardener (Struers, Denmark). The mounted samples were then ground using a 200 grit diamond lapping disc (DK Holdings Ltd, UK). Lastly, the ground samples were polished using diamond paste (Struers, Denmark) to a surface finish of 6 µm and 1 µm.

5.2.4. Sample characterisation

The surface and cross-section of the as-sprayed coatings were characterised using an SEM (FEI XL30, Thermo Fisher Scientific, USA) in secondary electron (SE) and backscattered electron modes (BSE), respectively. The level of porosity was measured using ImageJ image processing software (National Institute of Health, USA). BSE images taken at 1000 times magnification, covering around 600 μm^2 of the cross-section, were converted into black and white maps upon setting a threshold, which was kept constant for all images. Then, the area percentage of the image covered by porosity was measured, returning an overall value per image. The area of each individual pore was collated to form a pore size distribution, then a threshold of individual pore area was applied, and the pores were classified as being either small or large depending on which side of the threshold they fell.

5.2.5. Thermal conductivity

The thermal diffusivity of the coatings was measured using a Netzsch LFA 467 HT HyperFlash (Netzsch GmbH, Germany) from room temperature up to 1200 °C at 200 °C intervals, the heating rate was 5 °C/min and the analysis was conducted in a N_2 atmosphere. For the thermal diffusivity measurements, free standing coatings measuring 12.7 mm in diameter and ~400 µm thickness were prepared. Prior to thermal diffusivity measurements, a thin graphite coating (Kontakt Chemie, Germany) was applied to all surfaces of the free-standing coating to ensure absorption of the laser pulse (as per the methodologies described in [79, 166, 167]). Accurate thickness measurements were obtained from SEM imaging, with an average of 4 measurements taken from across the entire width of the coating. The specific heat capacity of the coatings was calculated from the constituent oxides using the Neumann-Kopp rule [146] with values obtained from [168] for all the tested temperatures. The density of the coatings was measured following Archimedes principle using a precision balance (Mettler Toledo Inc., Switzerland) and averaging 3 measurements. Using these measurements, the thermal conductivity of the coatings was calculated using the following equation:

$$k = \alpha \, \rho \, C_P \quad \text{(Equation 4)}$$

Where k is thermal conductivity, α is thermal diffusivity, ρ is density and C_P is specific heat capacity. The errors associated with each measurement were propagated using the appropriate formulae to give the error of the thermal conductivity value [169].

5.2.6. Microhardness measurement

The microhardness of the as-sprayed coatings was measured using a hardness tester (Wilson, UK) using the HR15N superficial Rockwell scale, commonly used for abradable coatings [16]. The as-sprayed surface was lightly ground using 800 grit SiC grinding paper (Sturers, Denmark) prior to indentation. The average of 5 measurements was taken, as well as the standard deviation.

5.2.7. Erosion testing

Erosion testing was performed using a specially designed air-jet erosion tester (SJS Engineering, UK) on samples in the as-sprayed state. Prior to testing, the abradable EBC samples were sonicated in industrial methylated spirit (IMS) using a FB-505 ultrasound probe (Fischer Scientific, UK) in pulse mode (1 s pulse every 2 s) at 60% amplitude. After drying, the mass and thickness of the samples were measured with a precision balance (Fisher Scientific, UK) and ball micrometre (Mitutoyo, UK), respectively. Two methods of erosion testing were conducted; the first, in reference to ASTM G76 used white alumina grit (220 mesh, Guyson, UK) at a pressure of 0.1 MPa [170]. The samples were held at a stand-off distance of 100 mm and an angle of 90° relative to the nozzle exit. The nozzle (Lindberg Products Co., USA) itself was 95.25 mm long with a diameter of 4.78 mm. After being subjected to erosion for 5s intervals, the samples were removed, and the mass and thickness (using the same balance and micrometre) at the deepest point of erosion were measured; this process was repeated until each sample had been subject to 25s of erosion. The second method of testing, in reference to GE E50TF121 [66], used the same alumina grit but at a pressure of 0.175 MPa. The samples were held at a stand-off distance of 101.6 mm and an angle of 20°. After 200 g of grit was fed into the system (the average duration of the tests was 31 ±1s), the eroded samples were weighed, and the thickness at the deepest point of erosion was measured. This particular method of erosion testing is widely used as a predictor for abradability [16]. The surface and cross-section of the eroded coatings were characterised using an SEM in SE and BSE modes. The erosion rate was also calculated for all samples, this is defined as the time taken for 25.4 µm of the coating to be eroded and is

described by the unit s/mil. An average erosion rate of 5 measurements was reported for each coating.

5.2.8. Abradable test rig

The coatings were also subjected to an abradable rig test which is designed to approximate the conditions and wear mechanisms found inside a turbine. This test platform has been detailed previously [27, 30], however, a brief outline of its operation and conditions is presented here. Two blades, one dummy and one cutting, are mounted on a spindle, the speed at which the spindle rotates controls the tip speed of the blade. The blades themselves were Inconel 718 tipped with cBN grits embedded in a NiCoCrAlY binder (Praxair TBT429, Praxair Surface Technology, USA). The abradable coating itself was mounted on a motorised single-axis movable stage, which moves the abradable into the cutting blade at a defined speed or incursion rate. The stage is connected to a dynamometer (Kistler Group, Switzerland), which measures the magnitude of the forces (normal and tangential to the wear direction) exerted on the abradable coating. The test is completed when a desired incursion depth is reached. Images showing the layout of the rig are presented in Figure 38. During the test, the temperature on the surface of the abradable is measured using a single wavelength pyrometer (OptoSigma, Japan) pointing at the centre of the wear scar. The pyrometer has a spectral response at 2.3 µm. An emissivity of 1 was used for the ytterbium disilicate coatings. Images of the blade, both front-on and side-on, are captured during the test to allow the change in blade profile to be monitored during the test. This is achieved using two stroboscopic imaging systems (Gardasoft, UK) whereby LEDs are used to illuminate the blade and images of the blade are captured after a certain delay every rotation, in-depth description of these systems can be found in previous works [29, 30].

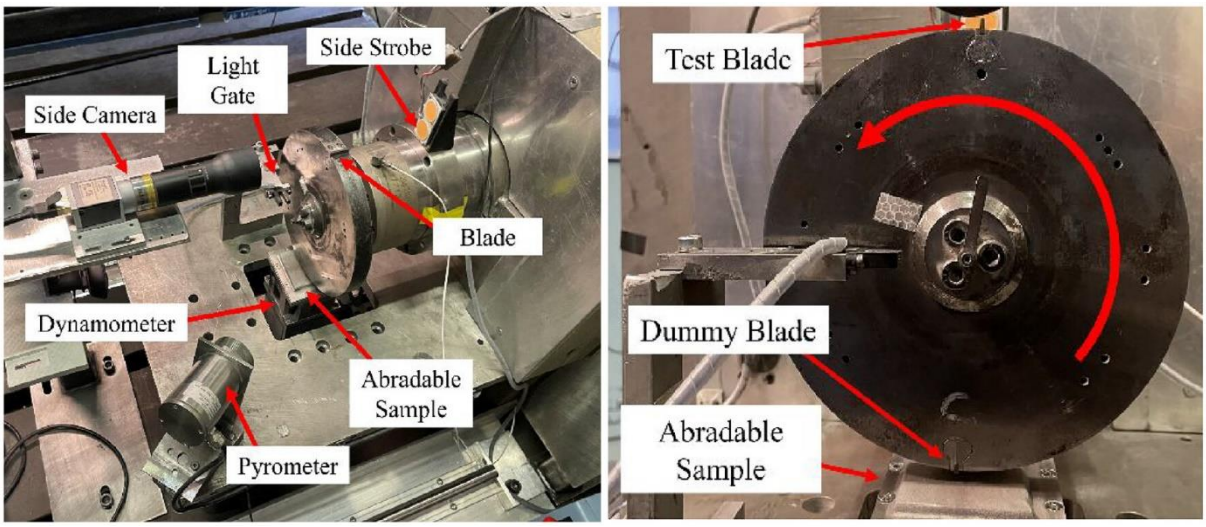

Figure 38. The test rig, with the key components labelled, taken from [25].

The coatings were tested under 2 different conditions, a high incursion rate whereby the abradable was moved towards the blade at a rate of 0.3 µm per pass and a lower incursion rate of 0.02 µm per pass. The blade tip speed was 200 m/s and the incursion depth was 1 mm, both of these were kept constant throughout the testing, details of which can be found in Table 9. After the tests, the surface worn coatings and blades were characterised using an SEM in SE mode, while the cross-sections of the coatings were characterised using an SEM in BSE mode. Prior to testing, the surfaces of the abradable coatings were also analysed using an Alicona G5 (Bruker Alicona, France). 3D images of the worn surfaces were stitched together using 100 x magnification, any form was removed using functions provided in the instruments software and surface roughness measurements (S_a) were made. The surfaces of the worn abradable coating and blades were also analysed using the same method. Contour maps of the worn blade surface were also created.

Table 9. Test matrix of the attempted abradable tests on the rig in Figure 38.

Test	Material	Incursion Rate (µm/pass)	Incursion Depth (µm)	Total Rub Length (m)
1	ABR	0.3	1000	62
2	1.5 wt.% PE	0.3	1000	62
3	4.5 wt.% PE	0.3	1000	62
4	ABR	0.02	1000	924
5	1.5 wt.% PE	0.02	1000	924
6	4.5 wt.% PE	0.02	1000	924

5.3. Results

5.3.1. Coating characterisation

The as-sprayed surfaces are shown in Figure 39, with typical APS splats visible in all the coatings. The large dark particles visible in Figure 39c and e are residual PE particles that have survived the thermal spray process. The microstructures of the as-sprayed coatings are shown in Figure 40. The coatings were designed to have 3 separate porosity levels, created by the addition of the pore forming, fugitive PE phase at 2 levels, 1.5 wt.% and 4.5 wt.%. In all the coatings, a combination of phases can be identified, the darker phase corresponding to YbDS rich splats while the lighter phase corresponds to YbMS rich splats. This is shown through a combination of XRD and EDX in [165]. The phase composition for all of the coatings was ~80 wt.% YbDS and ~20 wt.% YbMS, calculated using Rietveld refinement [165]. It is clear from Figure 40c and e that the addition of PE forms large pores in addition to the small globular pores, inter-splat pores and microcracking already present in ABR. In order to characterise the level of porosity, a porosity distribution curve is shown in Figure 41, while a breakdown of the total porosity, small and large pores (formed by PE) is presented in Table 10. The large pores are defined as being larger than 650 μm^2. While arbitrary, this limit was chosen since every pore in ABR was smaller than this, meaning only pores formed by the PE would be defined as large pores, generally these were of the order of 1000 μm^2. As expected, the total porosity increases with PE addition, while the level of small pores stays constant, indicating this porosity is inherent to the APS process. The increase in large pores drives the overall increase in porosity.

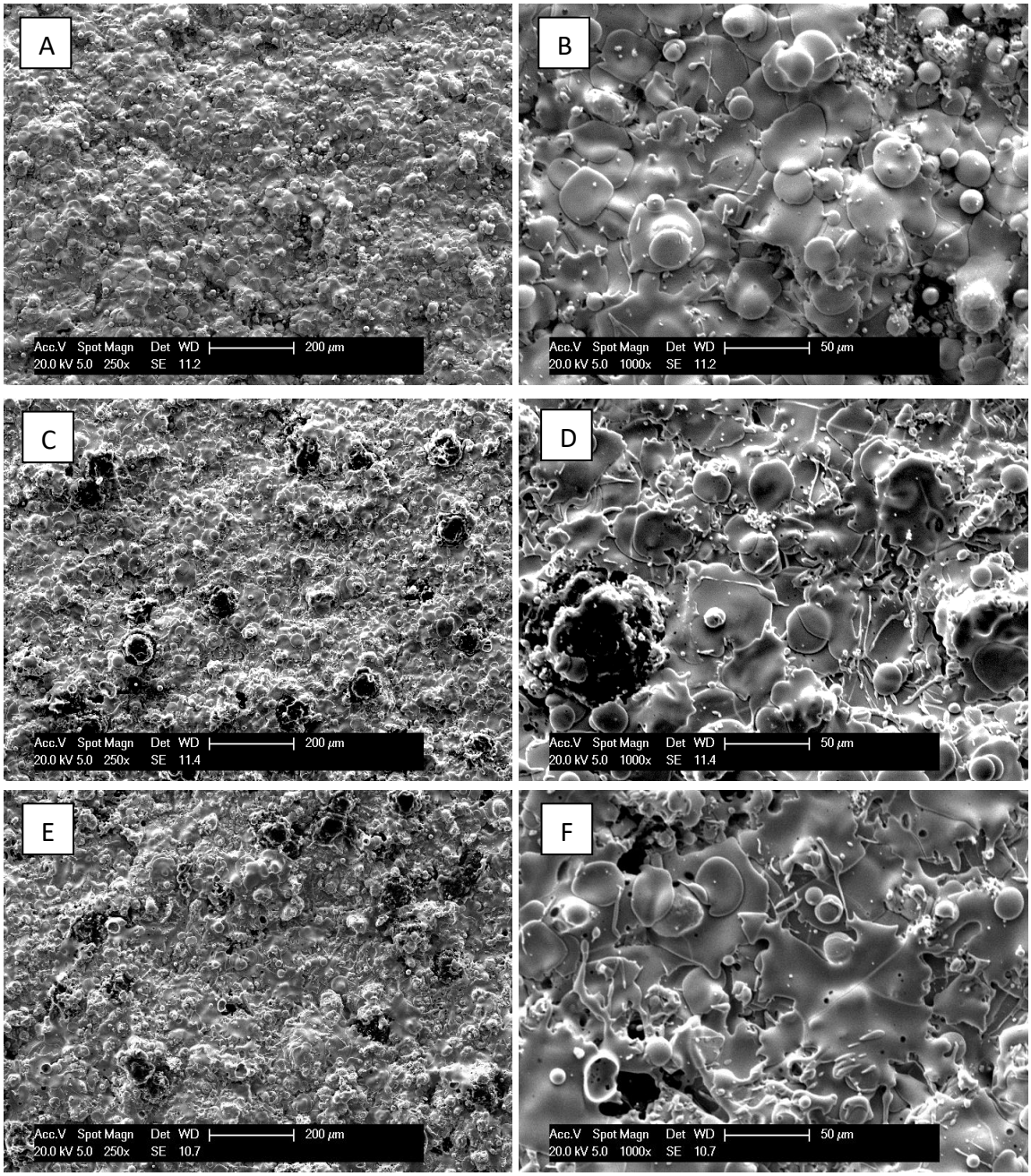

Figure 39. Low and high magnification SE SEM images of the surface topography of the as-sprayed coatings. With a) and b) showing ABR, c) and d) showing 1.5 wt.% PE and e) and f) showing 4.5 wt.% PE. The morphology of the large dark particles on the surface of 1.5 wt.% PE and 4.5 wt.% PE coatings suggests they are most likely polyester particles which have not completely burned off during the plasma spray deposition.

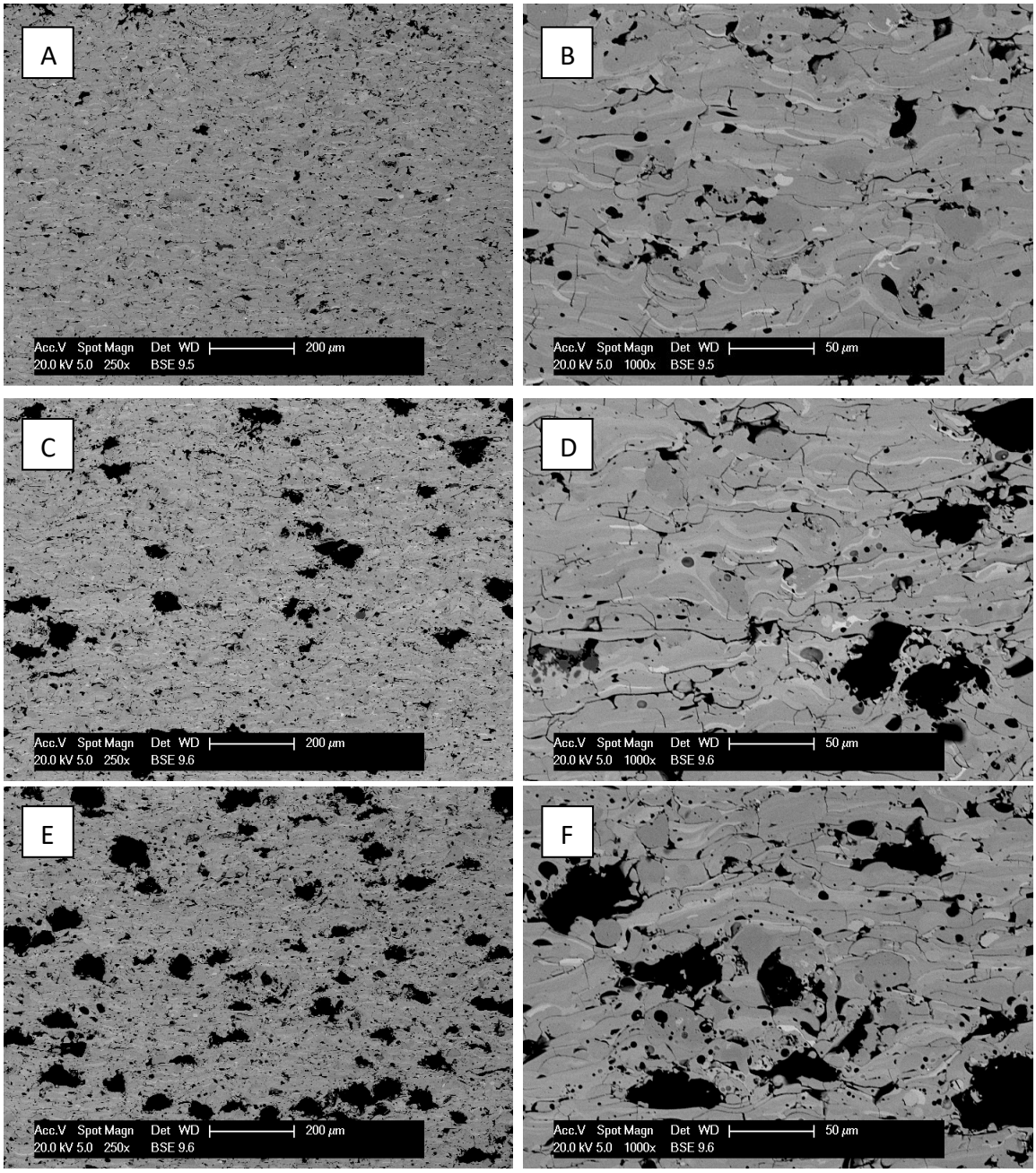

Figure 40. Low and high magnification BSE SEM images of the microstructures of the as-sprayed coatings. With a) and b) showing ABR, c) and d) showing 1.5 wt.% PE and e) and f) showing 4.5 wt.% PE.

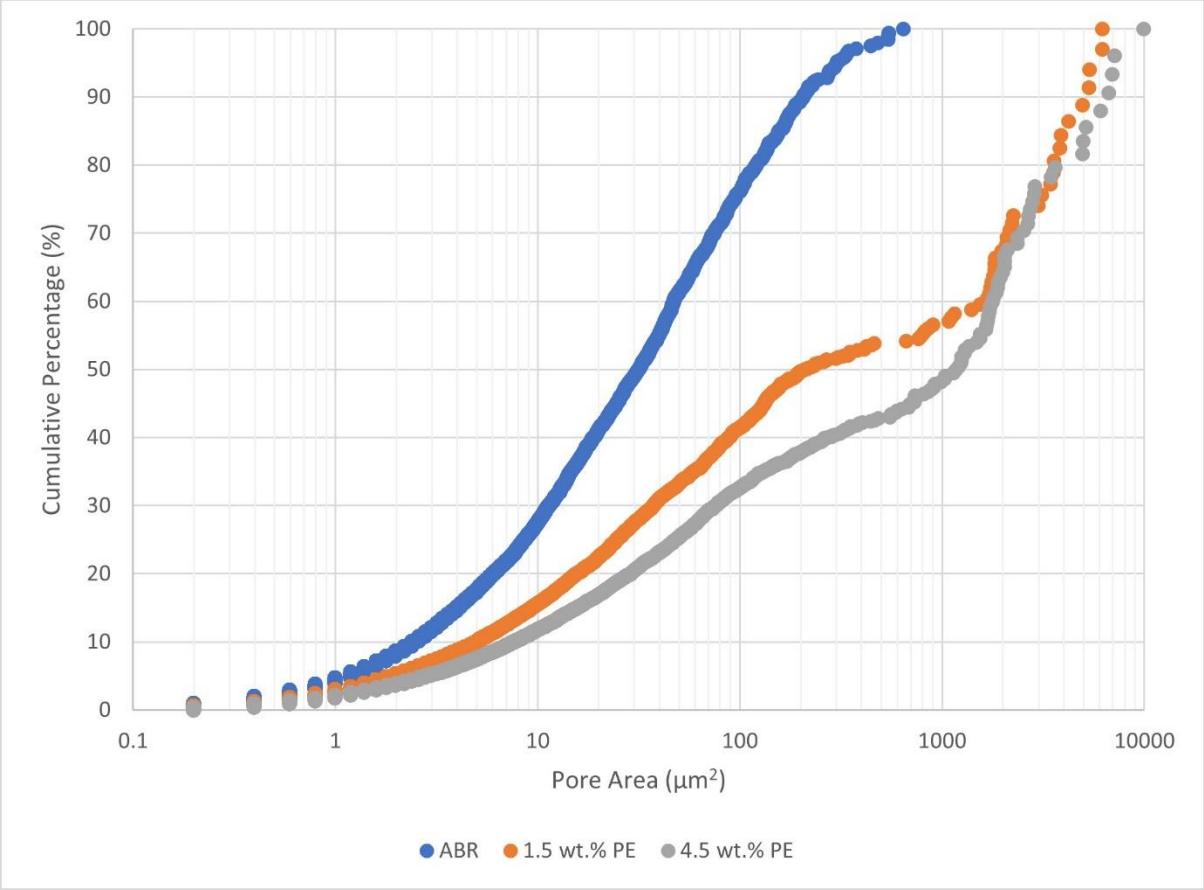

Figure 41. Distribution of pore area for ABR, 1.5 wt.% PE and 4.5 wt.% PE coatings.

Table 10. A breakdown of the porosity in the coatings. Small pores are defined as being below 650 µm² while large pores are any larger than this, likely caused by the pore forming PE phase.

Coating	Total Porosity (%)	Small Pores (%)	Large Pores (%)
ABR	8.0 ± 0.2	N/A	N/A
1.5 wt.% PE	15.1 ± 1.8	8.1 ± 0.6	7.0 ± 1.5
4.5 wt.% PE	21.5 ± 2.9	9.5 ± 0.6	12.0 ± 3.4

5.3.2. Thermal properties

At room temperature, ABR has a thermal conductivity of 3.6 W/m K, 1.5 wt.% PE 2.6 W/m K and 4.5 wt.% 2.1 W/m K. As shown in Figure 42 as the level of PE is increased, the thermal conductivity is decreased across the whole tested temperature range, likely due to the increased level of porosity in the PE containing coatings.

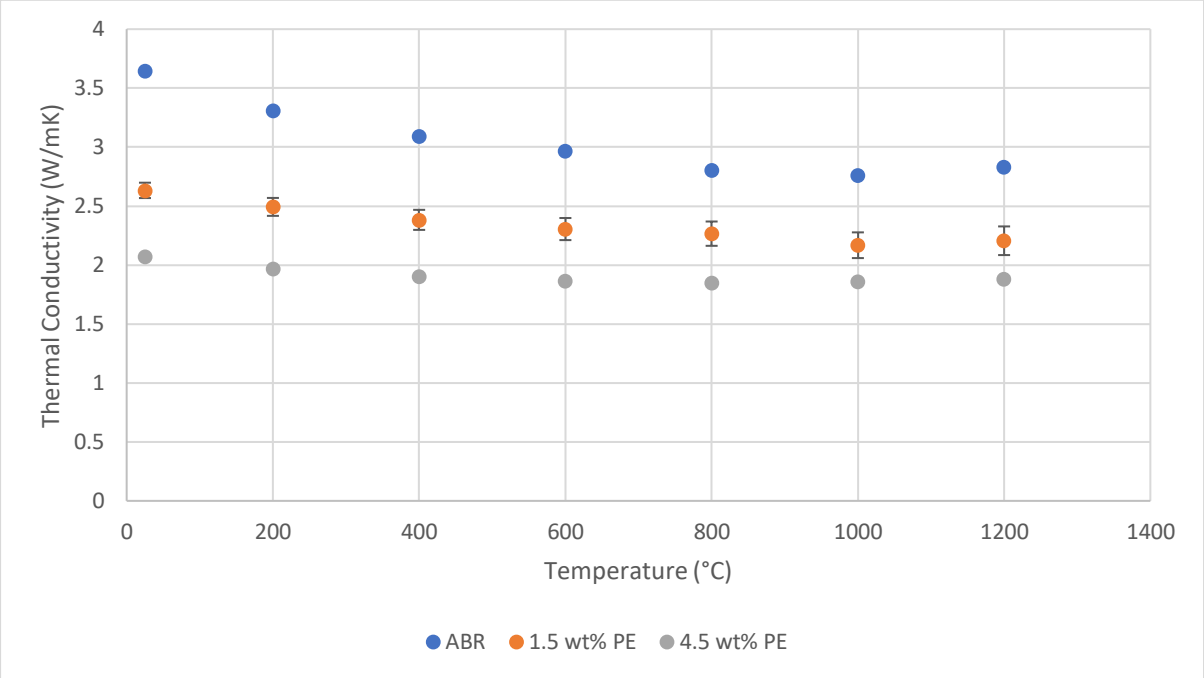

Figure 42. Thermal conductivity values for ABR, 1.5 wt.% PE and 4.5 wt.% PE coatings, from room temperature (25 °C) up to 1200 °C, as the level of porosity in the coating increases the thermal conductivity decreases. The error associated with the ABR and 4.5 wt.% PE coatings was much lower than the 1.5 wt.% PE coating (the error for both was ±0.01-0.02 W/mK across the temperature range). The reason for this increase was a larger variation in the density and thickness measurements for the 1.5 wt.% PE coating.

5.3.3. Superficial hardness

Softer materials may wear more readily however harder materials will have greater resistance to erosion. The superficial hardness values for the coatings are shown in Figure 43, as the level of PE is increased, the superficial hardness decreases.

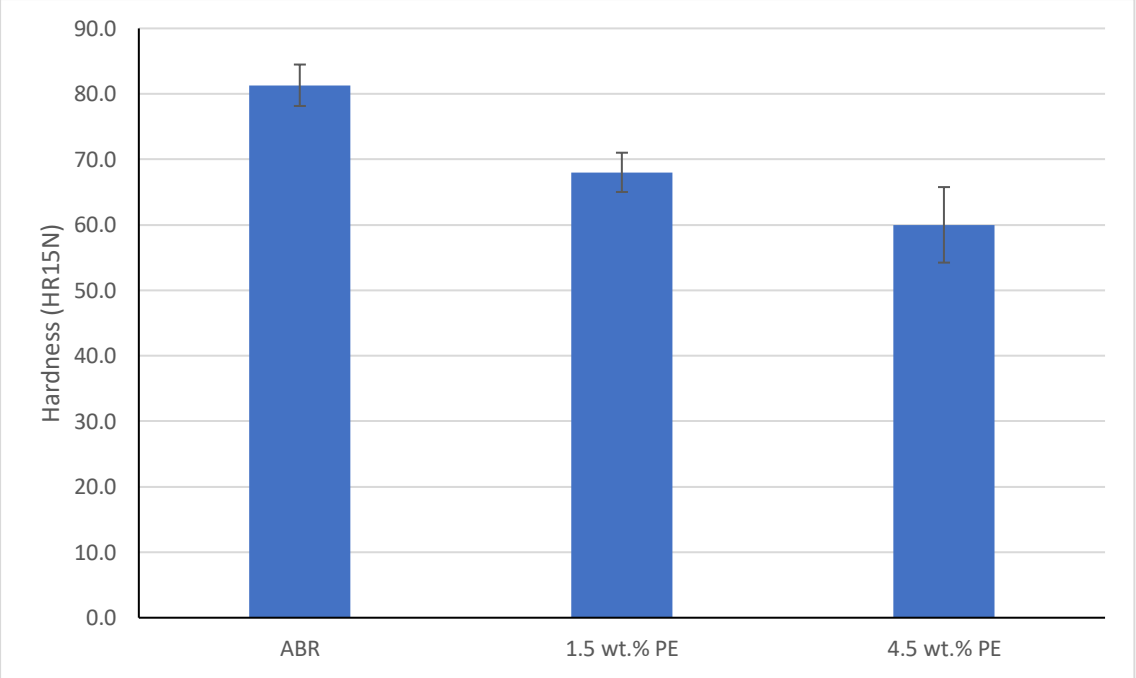

Figure 43. Superficial hardness (HR15N) values for ABR, 1.5 wt.% PE and 4.5 wt.% PE coatings.

5.3.4. Erosion resistance

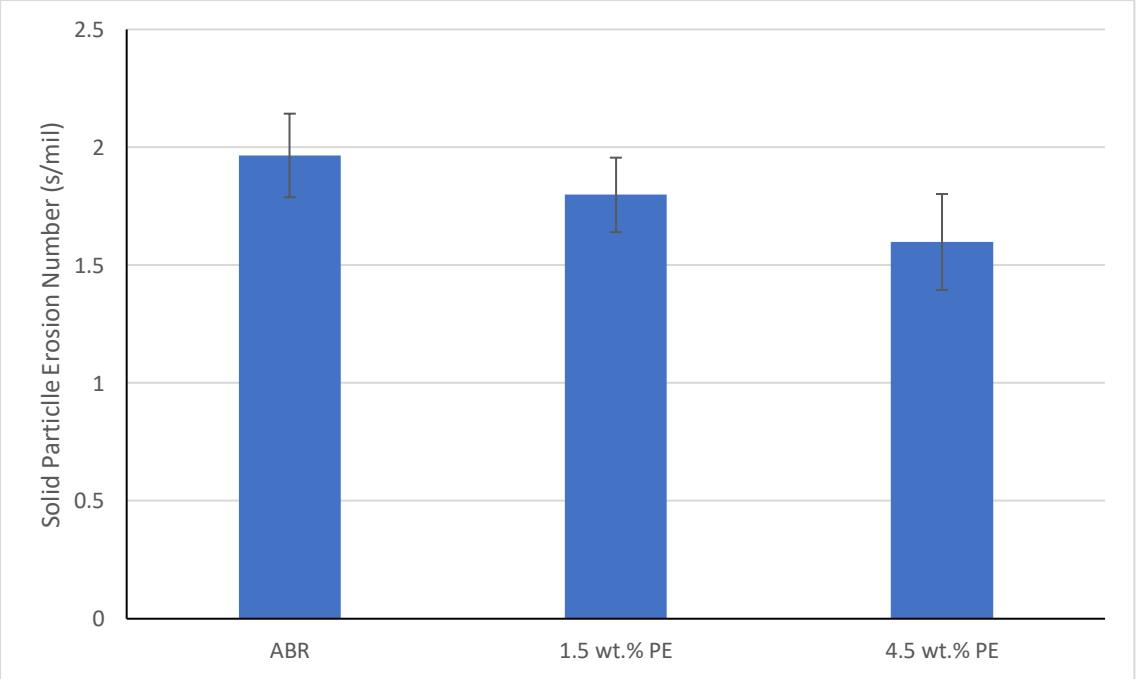

Figure 44. Solid particle erosion number for ABR, 1.5 wt.% PE and 4.5 wt.% PE coatings measured in s/mil.

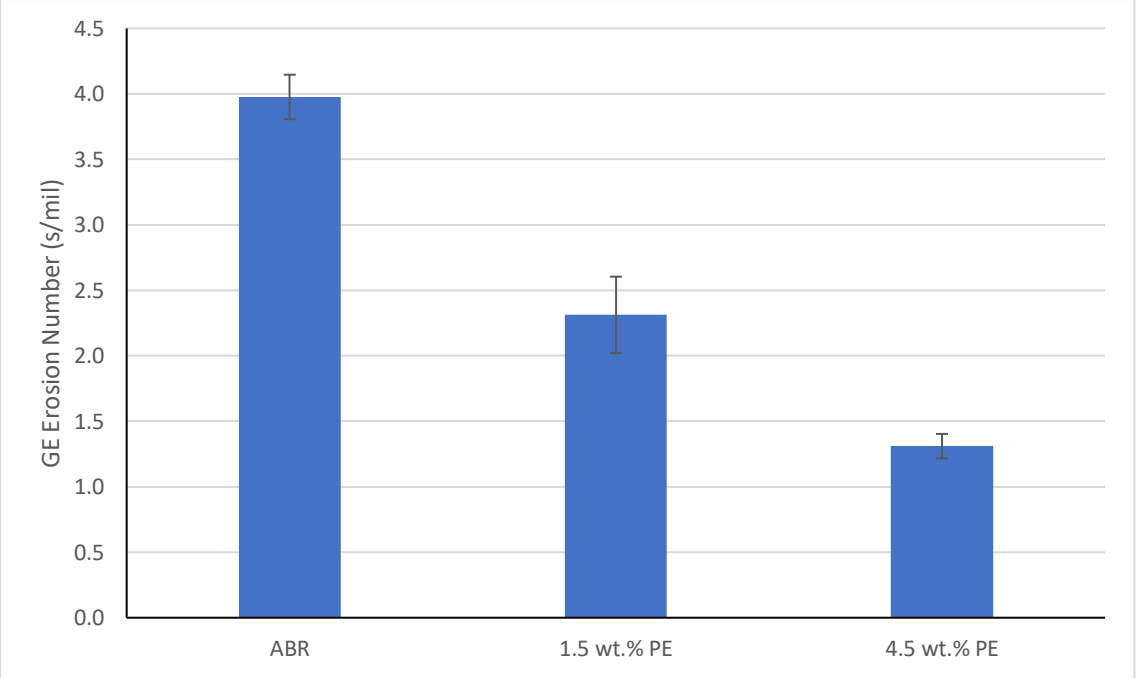

Figure 45. GE erosion number for ABR, 1.5 wt.% PE and 4.5 wt.% PE coatings measured in s/mil.

The first erosion test demonstrates the coating's resistance to solid particle erosion, using an erodent impact angle of 90°. Figure 44 shows the solid particle erosion number of the abradable coatings. The ABR, 1.5 wt. % PE and 4.5 wt. % PE coatings all have similar erosion numbers between 1.6 and 2.0 s/mil, with the addition of a larger volume of pore forming phase only results in a small decrease in solid particle erosion resistance. Figure 46a, c and e show SEM images of the eroded surface of the abradable coatings at the centre of the erosion pit after 25 s of erosion testing. All the eroded surfaces appear similar; cracks extending internally through splats are visible on the surface as well as areas of inter-splat porosity via which the cracks can propagate.

The GE erosion number of the abradable coatings is shown in Figure 45, a higher erosion number indicates a higher resistance to erosion. The presence of the pore forming phase appears to have a large impact in terms of erosion number for this test, with the coatings resistance to erosion greatly diminished by the increased PE addition. The addition of 1.5 wt.% PE reduces the erosion number from 3.9 s/mil to 2.4 s/mil, while increase the amount of PE to 4.5 wt.% decreases this further to 1.6 s/mil. A GE erosion number of below 4 s/mil is generally considered appropriate for an abradable coating [16].

SEM images of the eroded surface of the abradable coatings, taken at the centre of the erosion pit, are shown in Figure 46b, d and f. A clear difference in surface morphology is visible across the three coatings. The erodent has caused severe plastic deformation, via a ploughing mechanism, to the splat structure of the ABR coating, so much so that the splats are barely visible. In contrast to this, the splat structure of the 4.5 wt.% coating is still largely visible, with minimal ploughed troughs visible. Since this coating has a lower erosion number than the ABR coating, this indicates that the addition of PE is causing the splats to be dislocated from the coating by the erodent, rather than be plastically deformed. The 1.5 wt.% shows a combination of these two mechanisms with some ploughed troughs visible but also many splats still intact.

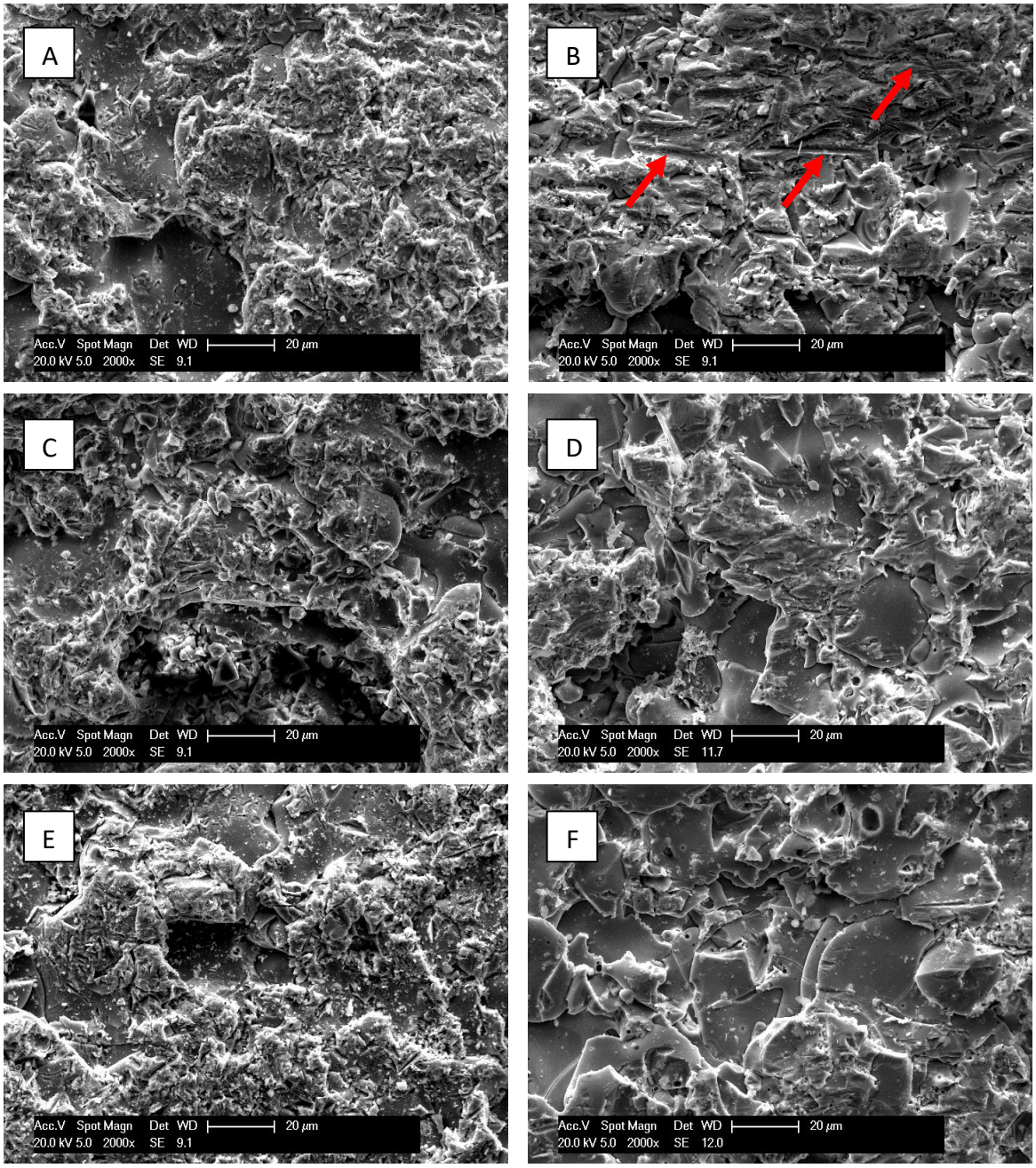

Figure 46. SE SEM images of the surface topography of a) and b) ABR, c) and d) 1.5 wt.% PE and e) and f) 4.5 wt.% PE coatings after solid particle and GE erosion testing, respectively. The different mechanisms in the GE erosion test are clearly visible b) shows a large amount of plastic deformation to the splats while (shown with the red arrows) *f) shows a number of undamaged exposed splats, indicating debonding and subsequent ejection of wear debris is more favourable. In d) a combination of the two mechanisms is visible.*

5.3.5. Abradable rig test

The maximum and mean normal force, tangential force and temperature are shown in Table 11, as well as post-test surface roughness measurements for the blade and abradable coating. The surface roughness of the pre-test surfaces was also measured, the ABR, 1.5 wt.% PE and 4.5 wt.% PE coatings had S_a values of 10.7, 11.0 and 12.8 µm respectively. Plots of the normal and tangential forces against rub length are shown in Figure 47. ABR experienced a catastrophic failure of both abradable and blade at both incursion rates. Figure 47a shows that almost immediately as the rub began in test 1 (at an incursion rate of 0.3 µm/pass), the normal force rose to unsustainable levels, ~3700 N, and after a rub length of ~10 m both coating and blade failed, reliable temperature measurements could not be ascertained due to the extreme number of sparks created during the test. A similar phenomenon was observed in test 4, where the incursion rate was significantly reduced (0.02 µm/pass). Initially the forces remained low and stable however after ~600 m rub length, the forces spiked and both coating and blade failed. This corresponded with very high surface temperature on the abradable, ~750 °C, just before the point of failure. Figure 48 shows low magnification images of the abradable coatings and the blade after each test. Good cutting and no blade damage can be observed after the majority of tests. The extensive damage caused to both the abradable coating and blade can be seen in Figure 48g, h and i. Failure between the abradable coating and the bond coat can be observed, while the blade itself has completely deformed and the majority of the tip has been removed.

At both incursion rates, the addition of PE creates an abradable coating which cuts without failure. As the level of PE is increased in the coatings, the mean and maximum forces and temperature are reduced. As a rule of thumb, if the measured forces scale with the increase in incursion rate, the wear mechanism is likely to remain the same [27, 31, 159]. In the case of both PE containing abradable coatings, the forces are lower at the higher incursion rate than would be expected given the incursion rate increase (15x). This could be a sign of more efficient cutting of material at the higher incursion rate. The normal force increases steadily throughout the test for both abradable coatings at both incursion rates. Conversely, the tangential force remains largely steady after increasing slightly initially during all tests. Also shown in Table 11 is the ratio of tangential to normal force. A low force ratio could indicate

consolidation and compaction of the abradable coating as opposed to cutting [27]. This is due to compaction (high normal force) and smearing of the surface (low tangential force). A higher force ratio indicates that chip formation is occurring. For test 3, the force ratio is low, at 0.21, while in test 2 it is slightly higher at 0.36. In tests 5 and 6 the force ratios are extremely low, 0.05 and 0.11, respectively. Whether pore compaction was contributing to the low force ratios was examined using image analysis. Cross-section images of the worn surface were segmented into 100 µm sections, extending from the worn surface to a depth of 500 µm, and the porosity of each section was measured using the same method as explained in section 2.4. The measured porosity of each section was then normalised against the average porosity for each coating in its as-sprayed state. No statistically significant reduction in porosity was identified in the near surface region in any of the tested coatings.

Table 11. The mean and maximum normal force, tangential force, force ratio, surface temperature and the post-test surface roughness of the abradable and blade from the four completed tests.

Test	Coating	Normal Force (N)		Tangential Force (N)		Force Ratio		Surface Temperature (°C)		Surface Roughness S_a (µm)	
		Max.	Mean	Max.	Mean	Max.	Mean	Max.	Mean	Abradable	Blade
1	ABR	3743	933	617	200	0.26	0.20	N/A	N/A	N/A	N/A
2	1.5 wt.% PE	456	267	166	107	0.62	0.39	300	247	18.8	26.0
3	4.5 wt.% PE	191	125	42	24	0.39	0.21	233	208	23.9	28.7
4	ABR	3329	251	482	77	1.23	0.41	751	326	N/A	N/A
5	1.5 wt.% PE	43	16	10	0.8	1.02	0.05	185	175	24.3	27.5
6	4.5 wt.% PE	28	6	7	0.4	1.38	0.11	182	175	24.4	30.1

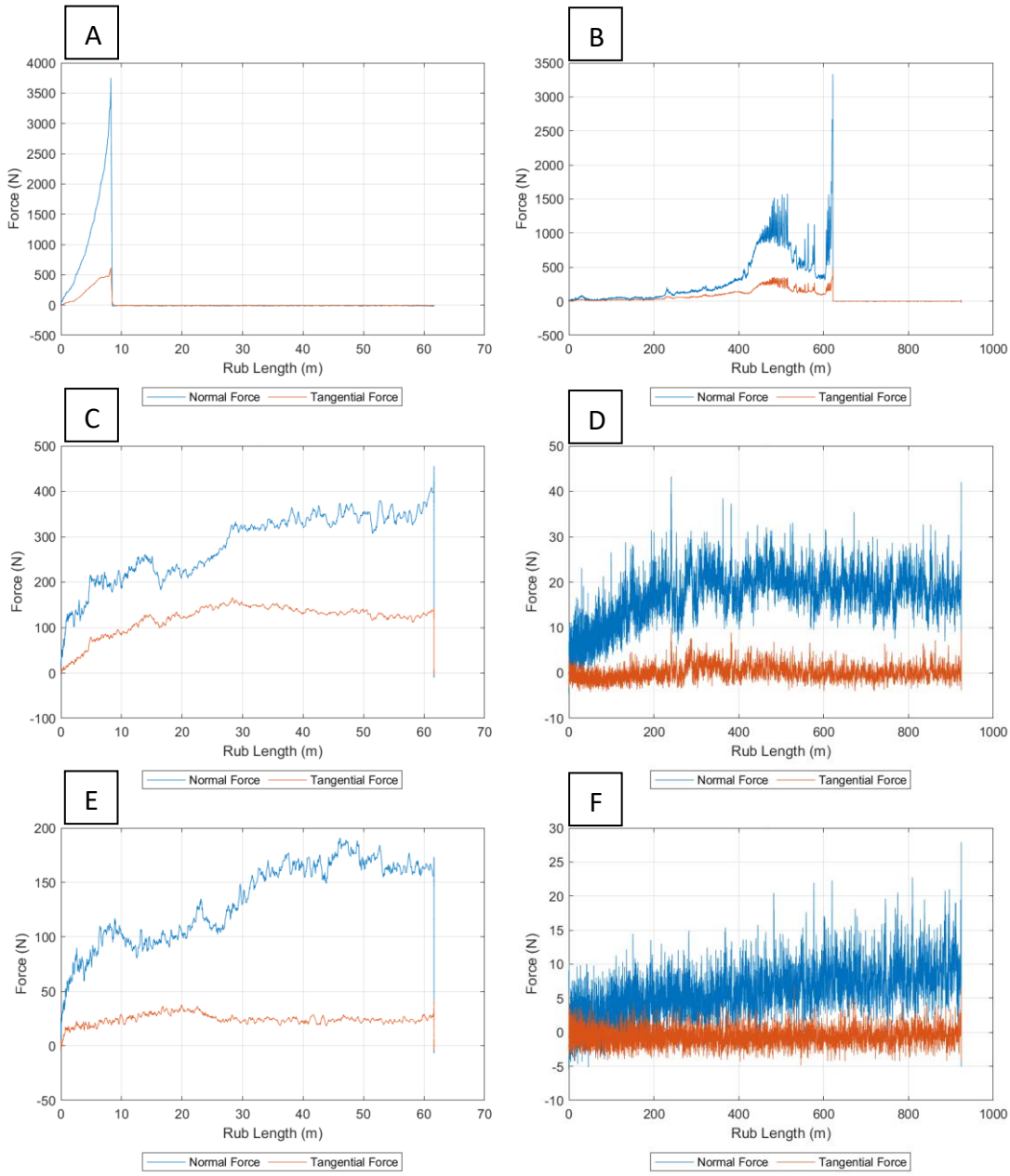

Figure 47. Graphs showing the normal and tangential forces against rub length for tests 1-6. Where a) and b) correspond to ABR at high and low incursion rates (tests 1 and 4), respectively, c) and d) 1.5 wt.% PE at high and low incursion rates and e) and f) 4.5 wt.% PE at high and low incursion rates. The normal force spikes on the ABR tests indicate when the abradable coating and blade tip failed, at ~ 10 m rub length for the high incursion rate test and ~600 m rub length for the low incursion rate test.

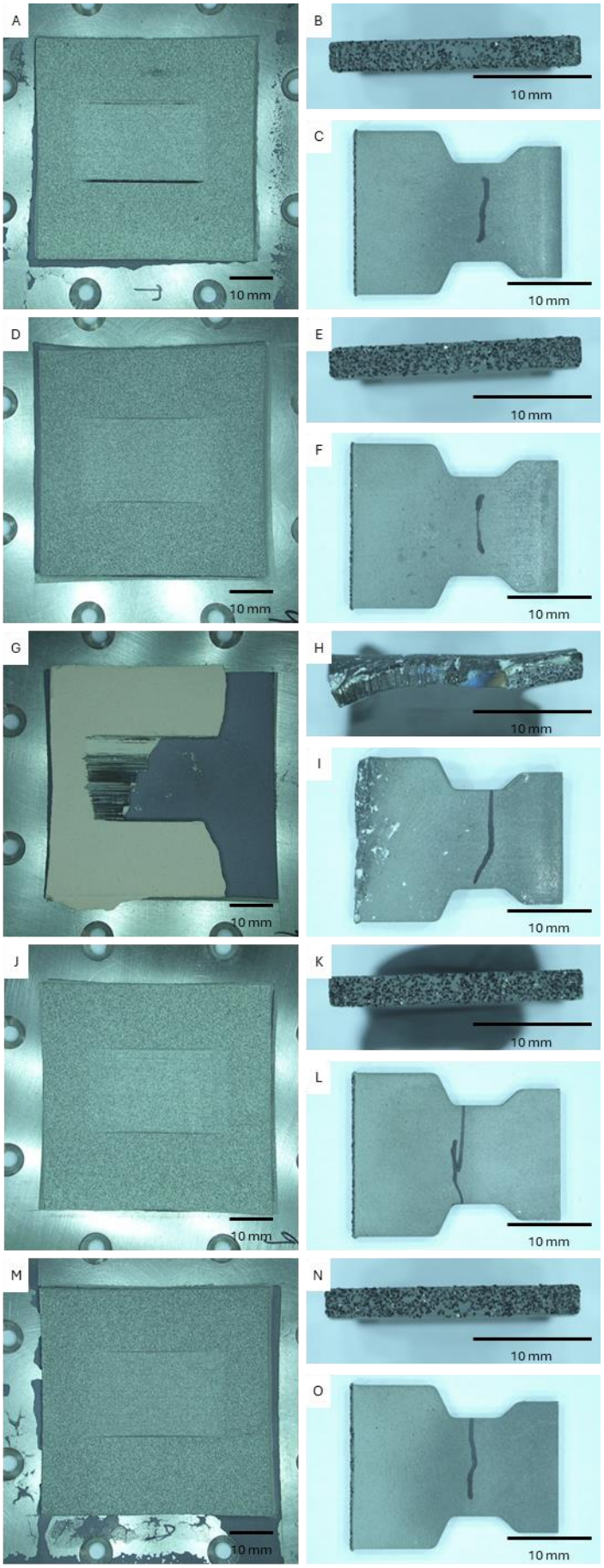
A
10 mm
B
10 mm
C
10 mm
D
10 mm
E
10 mm
F
10 mm
G
10 mm
H
10 mm
I
10 mm
J
10 mm
K
10 mm
L
10 mm
M
10 mm
N
10 mm
O
10 mm

Figure 48. Low magnification images of the abradable coating and blade (surface and profile respectively) after the test, where a), b) and c) correspond to test 2, d), e) and f) to test 3, g), h) and i) to test 4, j), k) and l) to test 5 and m), n) and o) to test 6. The coating and blade from test 1 are not shown as they were destroyed during the test.

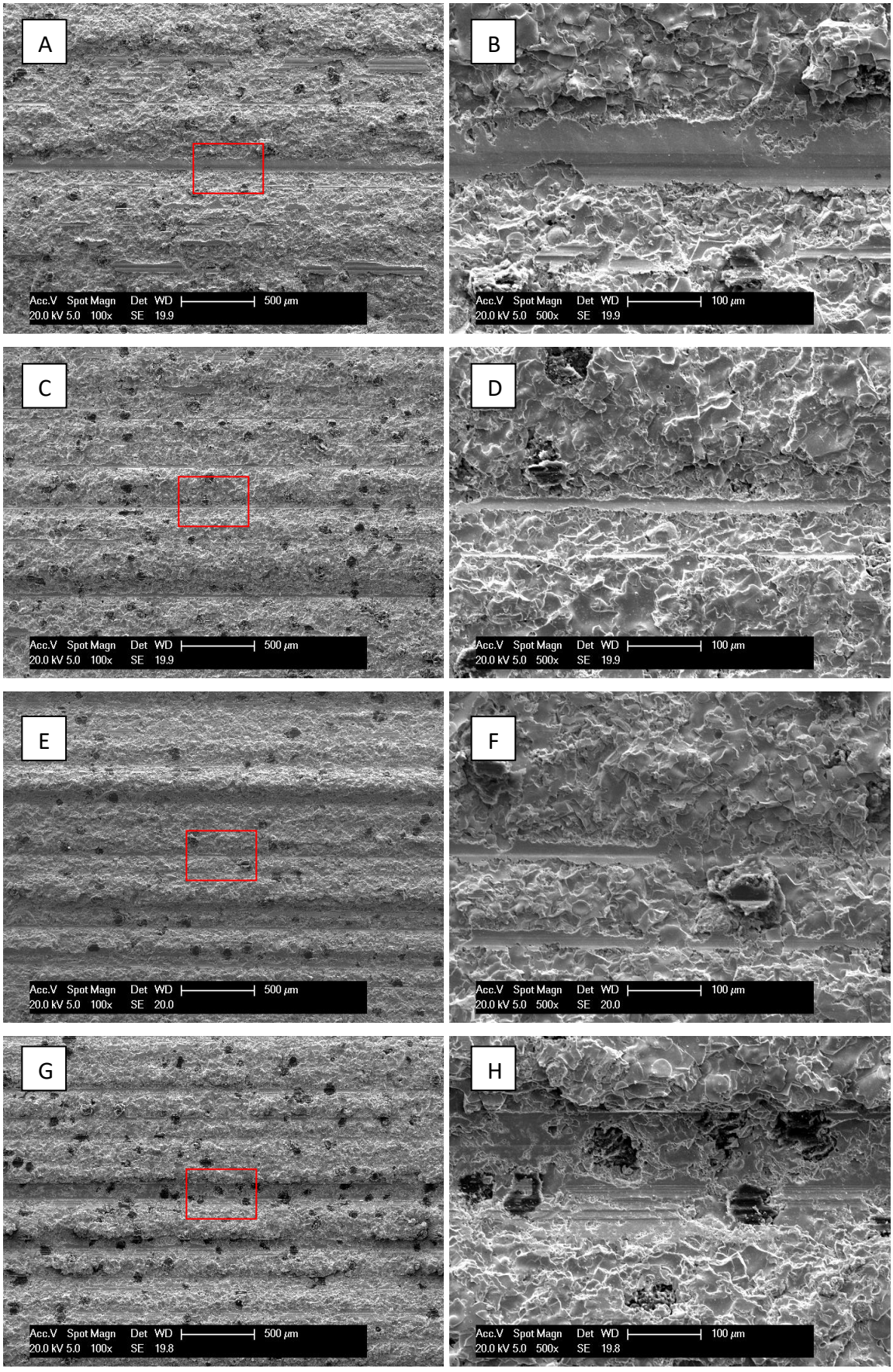
A
Acc.V Spot Magn Det WD 500 µm
20.0 kV 5.0 100x SE 19.9
B
Acc.V Spot Magn Det WD 100 µm
20.0 kV 5.0 500x SE 19.9
C
Acc.V Spot Magn Det WD 500 µm
20.0 kV 5.0 100x SE 19.9
D
Acc.V Spot Magn Det WD 100 µm
20.0 kV 5.0 500x SE 19.9
E
Acc.V Spot Magn Det WD 500 µm
20.0 kV 5.0 100x SE 20.0
F
Acc.V Spot Magn Det WD 100 µm
20.0 kV 5.0 500x SE 20.0
G
Acc.V Spot Magn Det WD 500 µm
20.0 kV 5.0 100x SE 19.8
H
Acc.V Spot Magn Det WD 100 µm
20.0 kV 5.0 500x SE 19.8

Figure 49. Low and high magnification SE SEM images of the surface topography of the completed abradable rig test samples. With a) and b) showing test 2 (1.5 wt.% PE tested at 0.3 µm/pass incursion rate), c) and d) showing test 3 (4.5 wt.% PE tested at 0.3 µm/pass incursion rate), e) and f) showing test 5 (1.5 wt.% PE tested at 0.02 µm/pass incursion rate) and g) and h) showing test 6 (1.5 wt.% PE tested at 0.2 µm/pass incursion rate). The red box in the low magnification image corresponds to the region shown in the higher magnification image.

Low and high magnification images of the worn surfaces of the low and high incursion rate tests of the PE containing abradable coatings are shown in Figure 49. Figure 49a and b show the wear track of the 1.5 wt.% PE abradable tested at 0.3 µm/pass, the surface shows a combination of heavily deformed ploughed tracks running parallel to the blade's direction of travel and exposed splats. The tracks are discontinuous across the wear scar and contain a network of cracks on their surface, indicating that at some point, they partially fractured, and the debris was ejected. A similar mechanism can be observed in Figure 49c and d, on the wear scar of the 4.5 wt.% PE abradable, also tested at the high incursion rate, although the deformed tracks appear to be smaller, which is also observed in Figure 49e and f (1.5 wt.% PE abradable tested at 0.02 µm/pass incursion rate). A slightly different surface topography can be observed in the wear track of the 4.5 wt.% PE abradable tested at the low incursion rate. While a combination of deformed tracks and exposed splats are still seen, the level of compaction and consolidation of the deformed material appears to be reduced, as some splat structure is still visible within the tracks. No evidence of adhesive transfer from the blade was observed in any of the images.

SEM images of the wear track cross-sections are shown in Figure 50, with the low magnification images showing a general overview of the cross-section, while the high magnification images focus on the surface and near-surface features. From the low magnification images, it can be observed that there is no obvious compaction of the bulk material, and the large pores have not collapsed, a common problem in Al-Si based abradable coatings which can lead to poor performance [23]. The high magnification images all show similar mechanisms of crack propagation in the abradable coatings. Some surface splats appear to have undergone cracking, leaving a highly fractured, poorly consolidated structure visible in Figure 50b, d, f and h. The damage also appears to extend into the sub-

surface region, with larger cracks extending laterally through the abradable, propagating along the inter-splat boundaries.

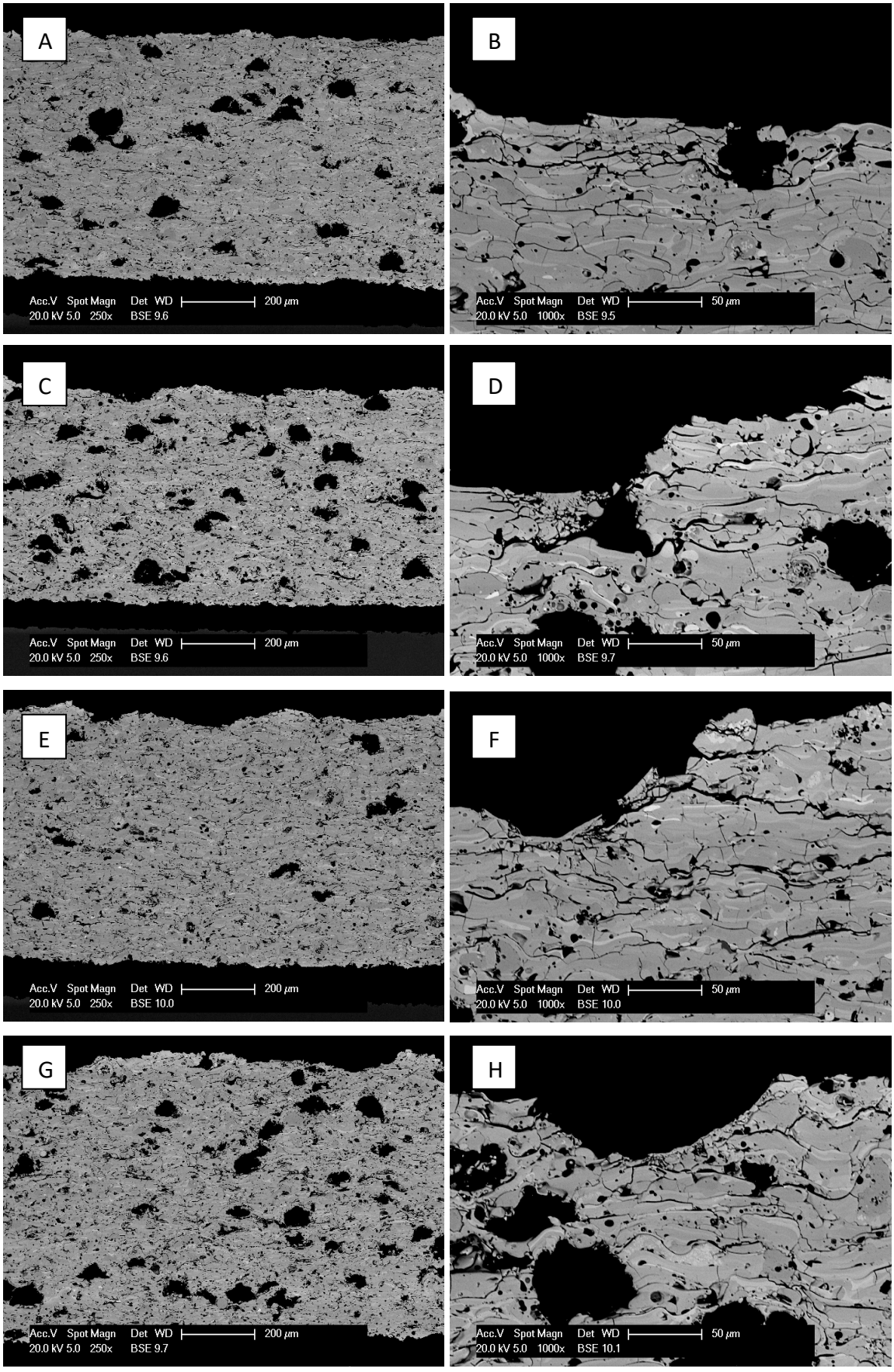
A
Acc.V Spot Magn Det WD 200 µm
20.0 kV 5.0 250x BSE 9.6
B
Acc.V Spot Magn Det WD 50 µm
20.0 kV 5.0 1000x BSE 9.5
C
Acc.V Spot Magn Det WD 200 µm
20.0 kV 5.0 250x BSE 9.6
D
Acc.V Spot Magn Det WD 50 µm
20.0 kV 5.0 1000x BSE 9.7
E
Acc.V Spot Magn Det WD 200 µm
20.0 kV 5.0 250x BSE 10.0
F
Acc.V Spot Magn Det WD 50 µm
20.0 kV 5.0 1000x BSE 10.0
G
Acc.V Spot Magn Det WD 200 µm
20.0 kV 5.0 250x BSE 9.7
H
Acc.V Spot Magn Det WD 50 µm
20.0 kV 5.0 1000x BSE 10.1

Figure 50. Low and high magnification BSE SEM images of the microstructure of the tested coatings, in the surface region of the wear scar. With a) and b) showing test 2 (1.5 wt.% PE tested at 0.3 µm/pass incursion rate), c) and d) showing test 3 (4.5 wt.% PE tested at 0.3 µm/pass incursion rate), e) and f) showing test 5 (1.5 wt.% PE tested at 0.02 µm/pass incursion rate) and g) and h) showing test 6 (1.5 wt.% PE tested at 0.2 µm/pass incursion rate). The mechanism appears similar for all of the tests with internal cracks in some surface splats and cracks extending through the inter-splat porosity, sometimes through the large voids formed by the PE, in the near-surface region.

No discernible wear of the blades could be captured from the stroboscopic camera data (not shown here) however the removal of some cBN grits could be detected. Contour maps of the surface and SEM analysis reveal the mechanism of cBN grit failure occurring during the tests. Images of the worn blade surfaces are shown in Figure 51, no material transfer from the abradable coating can be observed either on the grits or in-filling the surrounding binder. The contour maps shown in Figure 51b, d, f and h with the green areas represent the binder plane. The elevated zones are in yellow/orange and correspond to the protruding cBN grits, a few craters are noticeable as well, represented in blue. These are likely to be the result of cBN grits being pulled out in their entirety from the binder. A clear example of such a crater is shown in Figure 52a, taken from the blade used in test 2 (1.5 wt.% PE at an incursion rate of 0.3 µm/pass). A second possible mechanism of grit failure is shown in Figure 52b. The grit surface appears in-plane with the binder, and a fracture surface is visible on the grit. It is hypothesised that as well as grit pull-out, failure also occurs by fracture of the cBN grit, with the remaining cBN grit still embedded in the binder. The number of grit pull-outs and fractures that occurred during the completed tests is shown in Table 12.

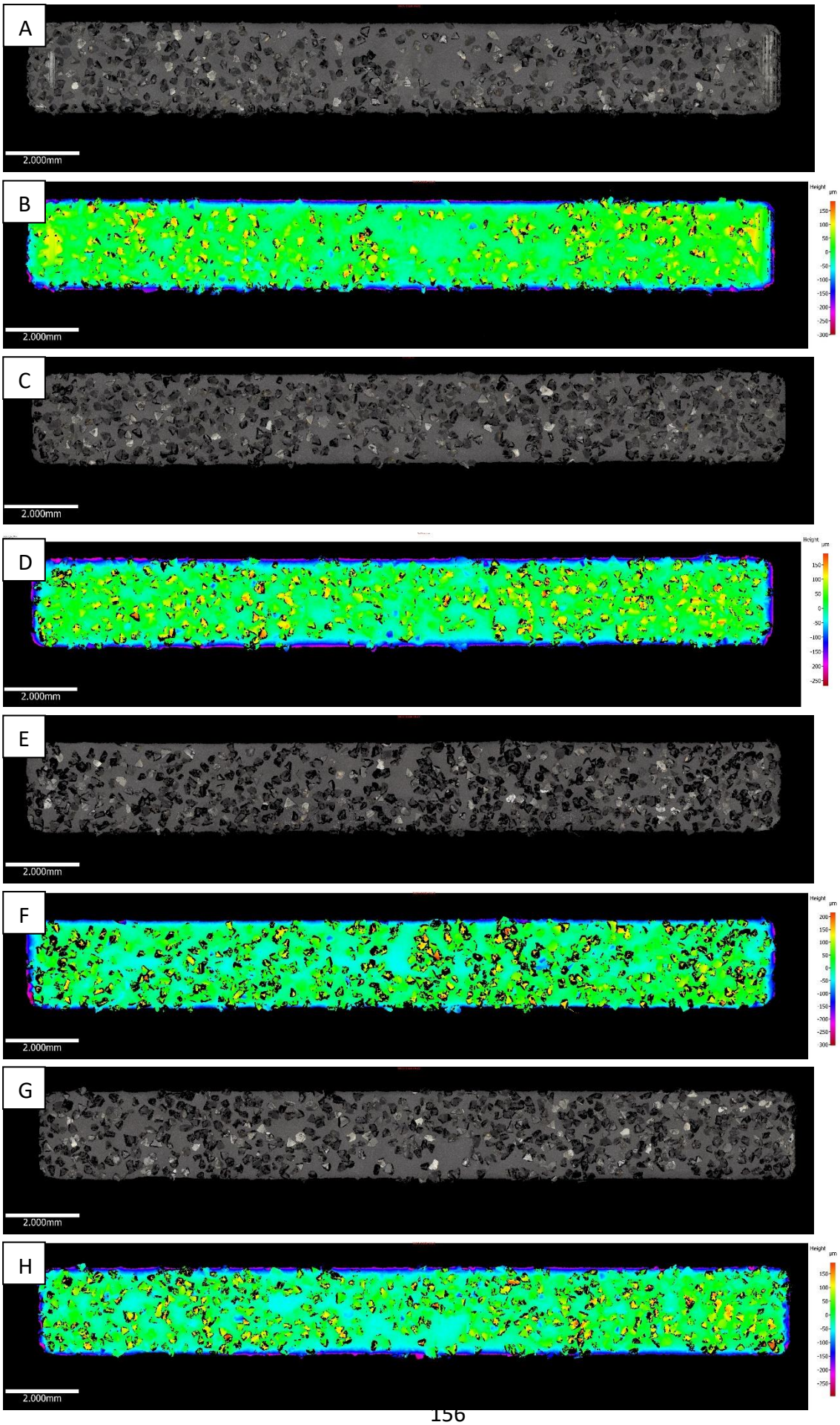
A
2.000mm
B
2.000mm
C
2.000mm
D
2.000mm
E
2.000mm
F
2.000mm
G
2.000mm
H
2.000mm

Figure 51. Images of the tipped blade surfaces from the completed tests taken using an Alicona G5 with a), c), e) and g) showing the blade surface of tests 2, 3, 5 and 6, respectively, while b), d), f) and h) show the same image with colouration to indicate contours, where red indicates peaks corresponding to the grits and blue indicates troughs where grits have been pulled out during the test.

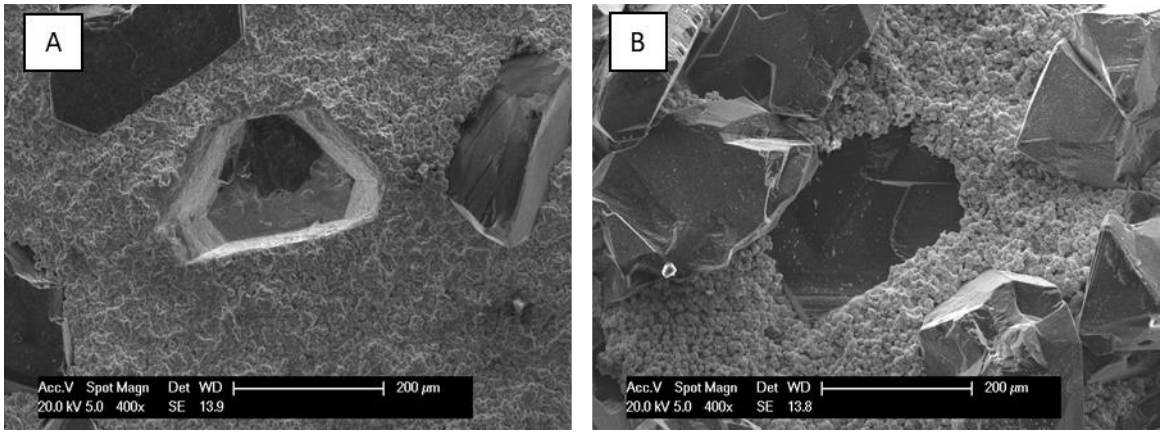

Figure 52. SE SEM images showing a) a site where a grit has been pulled out from the binder (test 2) and b) a fractured grit (test 5).

Table 12. A table summarising the number of blade grit pull-out and fracture events that occurred during the completed tests.

Test	Grit Pull-out (No.)	Grit Fracture (No.)
2	10	17
3	11	19
5	8	14
6	13	18

5.4. Discussion

5.4.1. Erosion mechanisms and performance

While erosion testing is usually performed on TBCs/less porous EBCs to make sure they can withstand the rigours of gas turbine applications, it can also be a useful test for determining the abradability of coatings [16]. The erosion number is defined as the time taken to erode 25.4 µm of the coating. It is clear from the results presented in Figure 46 that the erosion resistance of the coatings is drastically different depending on the impact angle of the erodent and the porosity level of the abradable coatings.

In order to understand why the spray parameters used to deposit a coating can affect its erosion resistance, the mechanism by which thermal spray coatings erode needs to be analysed alongside the microstructures of the coatings tested in this study. It has been proposed that the erosion rate in porous ceramic APS coatings is determined by the amount of inter-splat porosity relative to the total porosity level [171]. Typically, ceramic thermal spray coatings erode by the mechanism proposed by Nicholls et al. [172], whereby an APS yttria-stabilised zirconia (YSZ) coating fails by propagation of cracks around splat boundaries and through the inherent microcrack network found in such coatings. While public domain literature on the erosion of thermal spray YbDS EBCs is limited, Presby et al. [173] have examined the erosion of APS YbDS and found similar mechanisms to those reported in other ceramic coatings. Presby and Harder [174] have also reported on the mechanism observed in dense PS-PVD YbDS EBCs. The authors found the structure of the PS-PVD coating to be a lamellar structure similar to that of the splat structure found in an APS coating, and hence the erosion mechanism was also similar.

At 90° impact angle, the difference in erosion resistance between the coatings is minimal. From Figure 44, increasing the PE content from nothing to 1.5 wt.% and then 4.5 wt.% reduces the erosion number from 2.0 s/mil to 1.8 s/mil and then 1.6 s/mil, respectively. Sharp plastic deformations likely caused by the impact of angular alumina particles are visible on all the eroded surfaces in Figure 46. Small cracks extending out of these impact sites are also visible, in line with previous findings when eroding YbDS EBCs at 90 ° [173, 174]. These cracks caused by the eroding particles will extend through the near-surface region of the coating into sub-surface porosities, and the prevalence of inter-splat pores

facilitates the removal of material, resulting in a higher erosion rate, such pores can be seen throughout the microstructures of all the coatings and are visible on the eroded surface. It is understood from the literature that increasing the level of porosity in a coating will reduce the energy required to dislodge material from the said coating and, hence, increase its susceptibility to erosion [49, 55]. The addition of PE to form larger pores also acts in the same way, further reducing the cohesion of the splats and increasing the erosion rate, however, the effect of this is small. This indicates that the presence of a high fraction of inter-splat pores is the primary path for increasing the erosion rate at 90 °. A schematic detailing these mechanisms is shown in Figure 53.

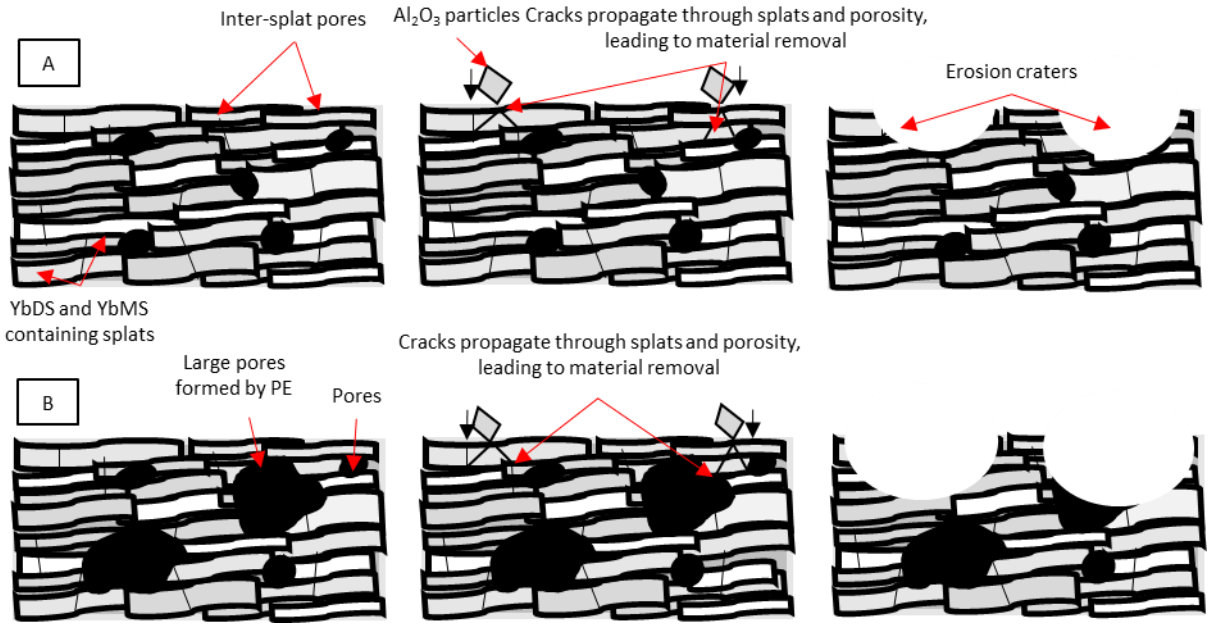

Figure 53. Schematic of the different erosion mechanisms of abradable EBCs at 90°. With (a) corresponding to ABR and (b) corresponding to ABR + 1.5 & 4.5 wt.% PE. The presence of inter-splat porosity is the main driver for erosion. The presence of large pores formed by the PE leads to a slightly higher erosion rate.

For an abradable coating, an erosion number of 2-4 s/mil is desirable when considering the GE erosion test [175]. This results in a coating that is resistant to erosion by third bodies in the gas turbine but can easily be worn away by an abrasive blade tip. Unlike the test conducted at 90 ° impact angle, reducing the angle to 20 ° has a profound effect on the erosion rate and erosion mechanism. As seen in Figure 45, increasing the PE content in the

feedstock to 1.5 wt.% results in a decrease in erosion number (and therefore decrease in erosion resistance) from 4.0 s/mil to 2.4 s/mil while increasing the PE content to 4.5 wt.% gives a further reduction to 1.3 s/mil, a similar relationship between the porosity of ceramic abradable coatings and their erosion numbers has been previously reported [47]. These findings are in agreement with work by Steinke et al. [55], whereby alumina magnesia spinel coatings with various levels of porosity were subjected to erosion. The erosion rate of three coatings labelled soft, medium and hard was found to depend on the amount of porosity present in the coating. The soft coating presented a highly porous structure, with a high fraction of inter-splat porosity and un-melted particles corresponding to the lowest erosion resistance, while the hard coating, which had small, isolated pores, was the most erosion resistant. The erosion test results from this study also correlated with subsequent blade incursion tests to analyse the coating's abradability.

The topography of the eroded surface differs greatly depending on the PE content of the coating, this can be observed clearly in Figure 46. The eroded surface of the ABR coating shows cutting and ploughing of the exposed splats, which is consistent with previous studies of abradable coatings and EBCs using a low angle impact erosion test [164, 173, 174]. What is interesting, however, is the obvious change in mechanism visible on the eroded surface of the coating containing 4.5 wt.% PE. While some ploughing/cutting is still visible, most of the visible splats remain undamaged indicating a transition from ductile to brittle failure, while the 1.5 wt.% PE containing coating presented a combination of the two mechanisms. This indicates that the addition of PE to the coatings reduces the energy required for the erodent to dislodge the splats. While for ABR coating a lot of deformation is visible on the exposed splats. As material is being preferentially removed in the PE containing coatings (unlike ABR, where the material is being deformed) the erosion rates are higher. Unlike the 90 ° impact erosion test, the addition of the PE pore forming phase does have a large impact on the erosion resistance of the abradable coatings at 20°. A schematic detailing these mechanisms is shown in Figure 54.

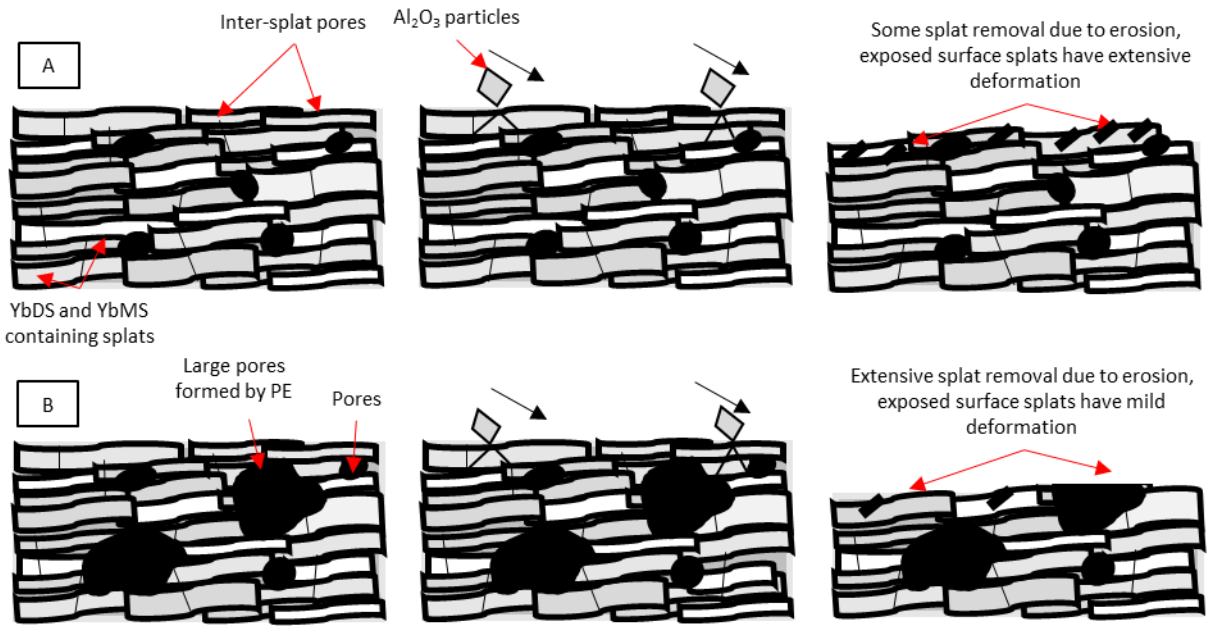

Figure 54. Schematic of the different erosion mechanisms of abradable EBCs at 20°. With (a) corresponding to ABR and (b) corresponding to ABR + 1.5 & 4.5 wt.% PE. The eroded surface of the ABR coating shows severe deformation. The eroded surfaces of the PE containing coatings present many un-damaged splats, indicating material is being removed rather than deformed and a transition from ductile to brittle failure.

5.4.2. Abradable rig test

Many researchers have examined the wear performance of abradable coatings however the work, particularly characterisation of worn surfaces, on ceramic abradable coatings and ceramic tipped blades is minimal. It has been reported that thermal properties play a role in the abradability of metallic coatings, especially at low incursion rates [23]. If the abradable has poor thermal conductivity, the temperature can build up near the surface of the abradable during the rub, leading to increased wear. When comparing the data in Figure 42 to the surface temperatures recorded during the abradability test, this is not happening with these abradable EBCs. Despite having the lowest thermal conductivity, the 4.5 wt.% PE coating has the lowest surface temperatures during the test. This is likely due to the efficiency with which material was worn and debris ejected (evident from the low forces seen in Table 11), preventing temperature build-up.

From Figure 47, increasing the PE content in the coating and lowering the incursion rate of the blade reduces the normal and tangential forces during the test. Typically, in abradable

coatings for low temperature applications (such as Al-Si) the wear mechanism is controlled by incursion rate [27]. At high incursion rates, high force ratios are observed, and the material cuts well, whereas, at lower incursion rates, low force ratios are observed and adhesive wear is the dominant mechanism [23]. In ceramic abradable coatings, however, this doesn't appear to be the case, likely due to the low fracture toughness inherent to ceramic materials [176]. Generally speaking, the 1.5 wt.% and 4.5 wt.% coatings cut well at both incursion rates, with a combination of brittle and ductile failure mechanisms observed however there were small differences caused by increasing porosity and incursion rate. In Figure 49a and b, large, smooth, ploughed tracks are visible in the wear scar of the 1.5 wt.% abradable coatings however when the porosity is increased these tracks become smaller (as visible in Figure 49c and d and the increase in surface roughness for the worn surfaces from test 2-3 in Table 11). This indicates an increase in porosity leads to preferential brittle fracture (material removed and unworn splats visible in wear scar) rather than deformation (as described by Borel et al. [19]). This is in agreement with previous work by Sporer et al. [47], whereby increasing the porosity was found to promote good cutting of abradable YSZ coatings against cBN tipped blades. The same also appears to be true when reducing incursion rate comparing Figure 49 and b, Figure 49e and f and the surface roughness values for tests 2 and 5 in Table 11. As no compaction of the porosity was identified, the low force ratios can be explained by the PE addition making the coating weaker in the tangential direction, leading to the reduction in force ratio being driven by this as opposed to an increase in normal force that would be associated with compaction. As despite the low force ratio and some smearing of material visible on the worn surfaces, the abradable still cuts well. A reduction in strength in the tangential direction can also be observed in the erosion test data. At 90° incident erodent angle the PE only causes a small reduction in erosion resistance, while at 20° the reduction in erosion resistance is much greater.

The idea of brittle failure is also analogous to the machining of brittle materials. The mechanism of brittle mode cutting has been described in a review by Antwi et al. [177]. During brittle mode cutting, the abrasive will cause brittle chip removal by material fracture and leave behind subsurface crack networks, which will propagate through the material. A similar phenomenon can be observed in the post-test cross-sections on the abradable coatings from the four completed tests, shown in Figure 50. Here, internal cracks in some

surface splats and cracks extending through the inter-splat porosity, sometimes through the large voids formed by the PE, in the near-surface region.

The wear of the tipped blades proved harder to quantify. Stroboscopic imaging was used to capture an image of the blade tip every cycle, and an edge detection algorithm was used to trace the height change of the blade as the tests progressed. However, due to the hardness of the ceramic tips, minimal wear was detected. This meant that slight movements of the blade or fixtures used to mount the camera during the test were dominant, so an alternative method was used. The surface of all of the blades presented two mechanisms of grit failure, fracture and pull-out, visible in Figure 51 and Figure 52. Work by Sporer et al. [47] suggests grit pull-out is associated with ceramic abradable coating density, with less porous ceramics promoting this. However, no clear trends between porosity, incursion rate and blade wear could be identified in this study.

5.5. Conclusions

Abradable EBCs have the potential to greatly improve the efficiency of the latest generation of gas turbines that utilise SiC CMC components. In this work, for the first time, the mechanical performance of abradable EBCs containing 3 different porosity levels has been examined. An abradable EBC with 8 % porosity was deposited using plasma spraying. Using the same spray parameters for the deposition, a fugitive PE pore forming phase was added to the feedstock at 1.5 and 4.5 wt. %. This resulted in a respective increase in porosity to 15 % and 21.5 % by area.

In order to quantify the performance of these coatings, these were subjected to a number of tests. The addition of PE was found to reduce the thermal conductivity from 3.6 to 2.6 to 2.1 W/mK for the ABR, 1.5 wt.% PE and 4.5 wt.% PE coatings, respectively. In terms of the mechanical properties, the increase in porosity caused a reduction in superficial hardness as well as erosion resistance. The 1.5 wt.% PE containing coating had a GE erosion number of 2.4 s/mil, ideally suited to be hard enough to resist erosion by foreign bodies but also easy to cut for the turbine blade. While the ABR coating failed during the rig test, the addition of the pore forming phase allowed the coating to be cut effectively by ceramic tipped blades. Increasing the PE from 1.5 wt.% to 4.5 wt.% led to a reduction in the temperature and forces measured during the rub.

Acknowledgements

This work was supported by the Engineering and Physical Sciences Research Council (EPSRC) (grant number EP/V010093/1). The project also received funding from Rolls Royce Plc in terms of a CASE PhD studentship. The authors also acknowledge the use of facilities at the Nanoscale and Microscale Research Centre of the University of Nottingham, supported by the EPSRC (grant number EP/L022494/1). The authors would also like to extend their thanks to John Kirk, who assisted with all aspects of the coating deposition process.

Chapter 6: Abradable ytterbium disilicate environmental barrier coatings: A story of CMAS and combined CMAS-erosion performance

This chapter is reproduced from the paper:

A. Lynam, A. Rincon Romero, B. Zhang, S. Lokachari, F. Xu, G. Pattinson, G.J. Brewster and T. Hussain, Abradable ytterbium disilicate environmental barrier coatings: A story of CMAS and combined CMAS-erosion performance, Surface and Coatings Technology, Volume 494, Part 3, 2024, https://doi.org/10.1016/j.surfcoat.2024.131502.

Abstract

Abradable environmental barrier coatings (EBCs) can be implemented to realise crucial gains in gas turbine efficiency however exposure to molten calcium magnesium alumino-silicates (CMAS) can lead to catastrophic coating failure due to mechanical and compositional changes within the coating. The aim of this study was to better understand how abradable coatings perform when exposed to molten CMAS, one of the key challenges facing current EBC design, and how this exposure affects the mechanical properties of the abradable coatings. In this study, three ytterbium disilicate ($Yb_2Si_2O_7$) abradable EBCs containing 8, 15 and 22 % porosity were deposited using atmospheric plasma spraying. These coatings were then exposed to CMAS at high temperatures for 0.5 hr, 4 hrs and 100 hrs. The results show that increasing the overall level of porosity had minimal impact on the degree of CMAS infiltration and interaction observed in the coatings during exposure. Reaction with the CMAS occurred by a dissolution-precipitation mechanism, with a reprecipitated ytterbium disilicate phase and Yb-apatite ($Ca_2Yb_8(SiO_4)_6O_2$) crystals noted as the only reaction products. After 100 hrs CMAS exposure, the erosion resistance of the coatings was investigated. For all the coatings, ductile failure was the main erosion mechanism. The change in phase composition and microstructure after CMAS exposure led to an increase in erosion resistance for all the coatings.

6.1. Introduction

The adoption of silicon carbide (SiC) based ceramic matrix composites (CMCs) for hot-section gas turbine engine components has led to breakthrough efficiency gains, due to its reduced weight and increased temperature capabilities, relative to equivalent nickel (Ni) superalloy components [2]. Nevertheless, the use of SiC CMCs is not without drawbacks, primarily their degradation in the presence of water vapour, an inherent product of the combustion process within the gas turbine [72]. To combat this, coating solutions have been developed to form a protective layer over the SiC CMC. Of these so-called environmental barrier coatings (EBCs), one of the most widely researched has been ytterbium disilicate ($Yb_2Si_2O_7$ or YbDS) due to its phase stability over the operating temperature window and similar thermal expansion coefficient to SiC (4.1 $x10^{-6}$ K^{-1}, measured over a range of 303–1873 K) [4]. As the use of CMCs matures, naturally further efficiency increases will be sought. One such way that has been employed in gas turbines for decades is the use of abradable coatings. These coatings are applied to casings and designed in such a way (highly porous structures typically created by the addition of pore-forming fugitive compounds) that they can easily be worn away by rotating components (such as blades and fins), creating a seal in-situ at start-up, allowing for increased efficiency and reduced fuel consumption [16]. It has been estimated that a 25 µm reduction in blade-tip clearance in a high-pressure turbine could lead to a 0.1 % reduction in specific fuel consumption [17]. While abradable coatings have been employed throughout various sections of gas turbine engines for decades, the published literature regarding such coatings is limited.

Despite apparent suitability, YbDS EBCs are still susceptible to a variety of damage mechanisms themselves, namely water vapour-induced recession, erosion by foreign objects ingested into the gas turbine and corrosion by calcium magnesium alumino-silicate (CMAS) species [9, 123, 178]. CMAS is typically an umbrella term for combinations of CaO, MgO, Al_2O_3 and SiO_2 originating from airborne sand or ash ingested by the turbine, which then, due to the operating temperatures of the turbine (>1200 °C), melts and adheres to the EBC surface [113-116]. Researchers have studied the interaction between a variety of CMAS compositions with YbDS (both sintered pellets and thermal spray coatings) under a variety of fluxes, exposure times and temperatures [117].

When observing sintered YbDS pellets, a minimal reaction between YbDS and CMAS has typically been described [115, 119, 120]. Whereby YbDS undergoes a dissolution and reprecipitation process with the CMAS melt, with penetration of the CMAS into the sintered body driven largely by grain boundary diffusion [121]. However, when considering plasma sprayed coatings, the picture becomes more complex. Thermal spray coatings are likely to contain at least some degree of porosity, through which CMAS may penetrate [59]. In addition, silica (SiO_2) volatilisation caused by the chemistry and temperature of the plasma during coating deposition, leads to a mixed phase coating of YbDS and ytterbium monosilicate (Yb_2SiO_5 or YbMS). Unlike YbDS, YbMS will tend to react with molten CMAS, given a high enough concentration of CaO in the melt, to form an ytterbium oxyapatite ($Ca_2Yb_8(SiO_4)_6O_2$ labelled Yb-apatite henceforth). The higher reactivity of YbMS can be explained by the theory of optical basicity, as described by Nieto et al. [118] and Padture, et al. [123]. The reactivity between an oxide glass and crystalline oxide will increase as the difference in optical basicity between the two increases. As YbMS has a larger optical basicity difference to CMAS than YbDS, YbMS is seen to be more reactive and hence more likely to form Yb-apatite. The formation of Yb-apatite is also dependant on the Ca:Si ratio of the CMAS itself [124]. At low Ca:Si ratios, below a certain threshold dependant on composition and temperature, Yb-apatite is unlikely to form, instead the dissolution of the Yb-silicates is driven by the solubility limit within the melt, with recession of the Yb-silicate only ceasing when this value is reached. At high Ca:Si ratios, Yb-apatite will form, consuming CaO from the melt, reducing the Ca:Si ratio until equilibrium is reached and the reaction stops.

A general mechanism for CMAS corrosion of mixed Yb-silicate coatings has been described by Poerschke, et al. [122]. Initially, Yb-silicates are dissolved into the molten CMAS, and then once the melt is saturated with Yb_2O_3, depending on the CaO concentration of the CMAS, the Yb-apatite phase will precipitate [125-128]. The final stage of the process is a reprecipitation of the Yb-silicate phases. When investigating plasma sprayed Yb-silicate coatings experimentally, researchers have largely drawn the same conclusions, despite the array of CMAS compositions, CMAS fluxes and exposure times and temperatures tested.

While EBCs typically exhibit low levels of porosity, abradable EBCs are porous by design, this makes the infiltration of CMAS a much bigger problem. Tejero-Martin, et al. [59] showed

that abradable EBCs were completely infiltrated with CMAS after 48 hrs exposure but that the high porosity of the abradable coatings may be useful for accommodating the strains associated with CMAS infiltration and reaction. Also of interest, especially when projecting conditions experienced by EBCs in service, is the combined effects of CMAS and other degradation mechanisms. Harder, et al. [129] found that in the presence of CMAS and steam, TGO growth could be supressed, while exposure to CMAS has been found to increase the erosion resistance of EBCs when tested simultaneously [130, 131]. What is not well understood, and is critical to determine the lifetime of EBCs, is the effects of long term or repeated CMAS exposure and how the changes this elicits in terms of microstructure and phase composition affect the coating's mechanical properties. Given this, the aims of this study are to track the infiltration of CMAS through highly porous abradable EBCs after exposure times of 0.5 hrs, 4 hrs and 100 hrs. After 100 hrs exposure, the abradable EBCs were subjected to an erosion test to examine how the resultant microstructures affect the abradability and resistance to foreign object damage relative to an as-sprayed coating.

6.2. Materials and methods

6.2.1. Coating deposition

Abradable EBC systems were deposited using atmospheric plasma spraying (APS). The coating system is comprised of a reaction bonded SiC substrate (JAI Engineers, UK), an intermediate Si bond layer and YbDS as a protective top layer. Commercially available Si (Metco 4810) and YbDS (Metco 6157) (both Oerlikon Metco AG, Switzerland) were used as feedstocks for the respective layers. The Si powder had a nominal size range of 15-75 µm and contained < 1.5 wt. % SiO_2 and a balance of Si. The YbDS powder had a nominal size range of 11-90 µm, contained a maximum of 5 vol. % of unreacted Yb_2O_3 and YbMS, as stated by the manufacturer. Prior to spraying, the powders were treated at 80 °C for 12 hours using a box furnace (Elite Thermal Systems, UK) to remove any moisture. Finally, Metco 600NS (Oerlikon Metco AG, Switzerland), a polyester (PE) powder, was mixed with the YbDS powder at 1.5 and 4.5 wt. %. The pore former was a crystalline aromatic polyester powder with a nominal size range of 45-125 µm. The mixture was homogenised using a Labram acoustic mixer (Resodyn Acoustic Mixers, USA) at an acceleration of 10 g for 10 mins. Thus, three coatings with distinct porosity levels were produced, the three coatings were labelled ABR (for the coating containing no polyester), 1.5 wt.% PE and 4.5 wt.% PE.

Reaction bonded SiC discs with a diameter of 25 mm and thickness of 10 mm, were used as substrates. These were grit blasted using a blast cleaner (Guyson, UK) with SiC (220 mesh) particles at a pressure of 9 bar. After grit blasting the surface roughness (R_a) of the SiC disc was found to be 3.1 ± 0.1 µm (average of three grit-blasted discs). Following surface preparation, the substrates were sonicated in industrial methylated spirit (IMS) using a FB-505 ultrasound probe (Fischer Scientific, UK) in pulse mode (1 s pulse every 2 s) at 60% amplitude. Finally, the substrates were dried using compressed air.

An SG-100 plasma spray system (Praxair Surface Technology, USA) was used to deposit the coatings. The spray gun was fitted with a 02083-175 anode, 02083-120 cathode and a 03083-112 gas injector. Ar and H_2 were used as the primary and secondary gases, respectively. The Si bond coat was deposited using a spray power of 27 kW, a current of 600 A, primary gas (Ar) pressure of 85 psi (equivalent to a flow rate of 75 SLM), a secondary gas (H_2) pressure of 35 psi (2.5 SLM), a stand-off distance of 125 mm, a powder feed rate of 30 g/min and the robot speed was 1000 mm/s over 6 passes. The 3 abradable EBCs were deposited using a spray power of 12 kW, a current of 600 A, primary gas (Ar) pressure of 85 psi (equivalent to a flow rate of 75 SLM), a secondary gas (H_2) pressure of 35 psi (2.5 SLM), a stand-off distance of 125 mm, and the robot speed was 1000 mm/s over 30 passes. Details about the optimisation of these parameters were reported elsewhere [165]. For longer duration CMAS exposure free-standing abradable coatings were prepared, to avoid any failures due to thermally grown oxide (TGO) formation at the coating/bond-coat interface. These were deposited using the same spray setup and parameters on a graphite plate (GPE Scientific Ltd., UK). The substrates were 60 mm x 20 mm x 5 mm thickness. Prior to deposition the graphite plates were grit blasted using a blast cleaner (Guyson, UK) with Al_2O_3 (100 mesh) particles (Guyson, UK) at a pressure of 1 bar. Following surface preparation, the substrates were cleaned using compressed air.

The polyester containing coatings underwent a heat treatment at 550 °C for 3.5 hours with a heating rate of 5 °C/min, to burn-off any remaining organic material, retained due to the short time at temperature experienced in-flight. The graphite substrates were also burned-off using the same heat treatment. As the phase content of the as-sprayed coatings was highly amorphous, a crystallising heat treatment was performed at 1200 °C for 2 hours, with

heating and cooling rates of 5 °C/min in air [165]. Both of these treatments were performed in a box furnace (Elite Thermal Systems Ltd., UK).

6.2.2. CMAS exposure

CMAS powder with a nominal composition of 35 CaO – 10 MgO – 7 Al_2O_3 – 48 SiO_2 mol. % (Oerlikon Metco AG, Switzerland) was used in this study, giving a Ca:Si ratio of 0.73. The CMAS powder was mixed with deionised water at a 1:9 ratio by weight and mixed using a magnetic stirrer to ensure homogeneity. The CMAS slurry was applied via an airbrush to YbDS coated SiC discs, which had been placed on a hotplate at ~100 °C to promote the evaporation of water from the CMAS slurry. The process of applying a layer of CMAS slurry and drying was repeated until a mass representing a 15 mg/cm^2 concentration had been applied to the surface of the samples. The CMAS-coated samples were heated to 1300 °C at 10 °C/min in a box furnace (Elite Thermal Systems, Uk). The samples were held at 1300 °C for 0.5 hrs, 4 hrs and 100 hrs before cooling to room temperature at 10 °C/min [59].

6.2.3. Erosion testing

Erosion testing was performed using a specially designed air-jet erosion tester (SJS Engineering, UK) on heat-treated and CMAS exposed samples. Prior to testing, the abradable EBC samples were sonicated in industrial methylated spirit (IMS) using a FB-505 ultrasound probe (Fischer Scientific, UK) in pulse mode (1 s pulse every 2 s) at 60% amplitude. After drying, the mass and thickness of the samples were measured with a precision balance (Fisher Scientific, UK) and ball micrometer (Mitutoyo, UK), respectively. Erosion testing was conducted in reference to GE E50TF121 [66]. The testing used alumina grit (220 mesh, Guyson, UK) at a pressure of 0.175 MPa. The samples were held at a stand-off distance of 101.6 mm (4 inches) and an angle of 20°. All the samples were exposed to a minimum of 150 s of erosion, however, for samples with particularly high erosion resistance, this was extended up to a maximum of 330 s. The samples were removed from the tester every 10 s for the first 30 s, and the mass loss and maximum erosion depth measured. From 30 s to 120 s the samples were measured every 15 s and after 120 s the samples were measured every 30 s. The method of erosion testing is widely used as a predictor for abradability [16]. The surface and cross-section of the eroded coatings were characterised using an SEM in SE and BSE modes, respectively.

6.2.4. Sample preparation and characterisation

Heat-treated and CMAS exposed samples were prepared using standard metallographic techniques, details of which have been outlined in previous work [165, 179]. Mounted samples were characterised using a FEI XL30 scanning electron microscope (SEM) (Phillips FEI, Netherlands) operated in secondary electron (SE) and backscattered electron (BSE) modes, using an accelerating voltage of 20 kV, spot size of 5 nm and working distance of 10 mm. The SEM was equipped with energy-dispersive x-ray spectroscopy (EDX) (Oxford Instruments, UK) to perform elemental analysis. The infiltration depth of the CMAS was calculated from SEM BSE cross-section images at 500 x magnification (leading to a ~500 µm x ~500 µm field of view). The infiltration depth was defined as the deepest point from the coating surface where a Ca containing phase (either residual CMAS or Yb-apatite) could be detected. An average of 5 measurements were taken per image, and 5 images were used per coating per CMAS exposure time. Image analysis was also used to track changes in porosity after CMAS exposure, relative to the heat-treated microstructure. Shape filters were applied to the threshold images to isolate the inter-splat pores, which were defined as having an aspect ratio greater than 2.5 and a size smaller range of 5 – 250 μm^2. For the CMAS exposed coatings, the same filters were applied this time to 50 µm bins of the coating thickness, to track the depth of CMAS interaction. SEM BSE cross-section images at 500 x magnification (~500 µm x ~500 µm) were analysed, and an average of 5 images were used per coating per CMAS exposure time.

Electron backscatter diffraction (EBSD) analysis was conducted using a JEOL 7100F field emission gun SEM (JEOL, Japan) using a spot size of 4 and a working distance of 10 mm. The SEM was equipped with energy dispersive X-ray spectroscopy (EDS, X-max 150, Oxford Instruments, UK) and electron backscatter diffraction (Oxford Instruments, UK) detectors. To understand the phase composition of the CMAS exposed coatings, EBSD was used with an accelerating voltage of 15 kV on the ~ 70° tiled specimen. EBSD data acquisition was performed at a step size of 0.03 µm. Crystallographic information files (CIF) of monoclinic YbDS (C2/m, 00-025-1345), monoclinic YbMS (I2/a, 00-40-0386) and hexagonal $Ca_2Yb_8(SiO_4)_6O_2$ oxyapatite (P63/m, 04-006-0320) were used to identify the suspected phases present in the CMAS exposed coatings. AZtec Crystal (Oxford Instruments, UK) was used to analyse the EBSD data.

Analysis of the phase content of the heat treated and CMAS exposed samples was conducted by XRD using a D8 Advance (Bruker, UK) from 10 to 80° 2θ, using Cu Kα radiation (0.154 nm wavelength), a 0.02° step size and 0.2 s per step using Bragg-Brentano geometry. Phase identification in the coatings was completed using EVA software (Bruker, UK) supported by data from the PDF-2 and PDF-4 databases (ICDD-PDF).

X-ray computed tomography (X-ray CT) measurements were also performed on as-sprayed and CMAS exposed coatings. Due to the resolution limitations of this technique only the most porous PE containing coatings were analysed, this allowed for detailed interrogation of the CMAS infiltration process. Free-standing 1.5 wt.% PE and 4.5 wt.% PE coatings were prepared, one sample of each coating was analysed in the heat treated state while another sample of each coating was exposed to CMAS at a concentration of 15 mg/cm^2 for 4 hrs at 1300 °C and were also analysed. The samples were scanned using a Zeiss 160 kVp Versa 510 (Zeiss AG, Germany) at the University of Southampton's µ-VIS X-Ray Imaging Centre. The samples were rotated through 360° in steps of 0.12°, giving a voxel size of 1.2 µm. A voltage of 140 kV, power of 10 W and exposure time of 10 s were used with a 4x objective lens and HE5 source filter. The resulting data was reconstructed and analysed using VGSTUDIO (Volume Graphics, USA) and image stacks were analysed using ImageJ image processing software (National Institute of Health, USA).

6.3. Results

6.3.1. Phase composition

SEM images of the feedstock powders, heat-treated coatings and diffractograms of the 4 heat-treated coatings can be found in a previous work [165]. The results show a combination of monoclinic YbDS (C2/m, 00-025-1345) and monoclinic YbMS (I2/a, 00-40-0386) phases present in all the coatings in a ratio of 87 wt.% YbDS to 13 wt.% YbMS.

The diffractograms after 0.5 hrs CMAS exposure are shown in Figure 55a, 4 hrs in Figure 56a and 100 hrs in Figure 57a, a detailed view of the 25° - 40° 2θ range is shown for improved phase identification in Figure 55b, Figure 56b and Figure 57b. In all cases, no YbMS peaks were detected, indicating that at least in the near surface region where the x-rays penetrate (~25 µm), the CMAS has fully infiltrated and reacted preferentially with YbMS. The reaction product was identified as hexagonal $Ca_2Yb_8(SiO_4)_6O_2$ oxyapatite (P63/m, 04-006-0320), small

peaks can be identified at ~32° 2θ in the 0.5 hrs and 4 hrs tests while higher intensities can be seen after 100 hrs exposure, particularly in the ABR sample. The detection of YbDS and Yb-apatite only indicates that Ca and Si containing oxides react with the coating while the Mg and Al oxides remain in the melt pool. This reaction has previously been widely reported in literature for both sintered Yb silicate pellets and coatings alike [119, 125, 136].

Interestingly, the coatings exposed for 0.5 hrs and 4 hrs show a preferred orientation of the YbDS phase in (110), (220) and (330) planes. These peaks correspond to 2θ values of 17°, 34° and 52° respectively. Such phenomena have been previously observed by Wiesner, et al. and Tejero-Martin, et al. and is likely due to grains of reprecipitated YbDS favouring growth in one direction over another [59, 120]. It is hypothesised that these crystals on the top surface of the coating that are growing within the residual CMAS glass that remain on the surface, as they are not present after 100 hrs exposure where the CMAS has fully infiltrated the coating.

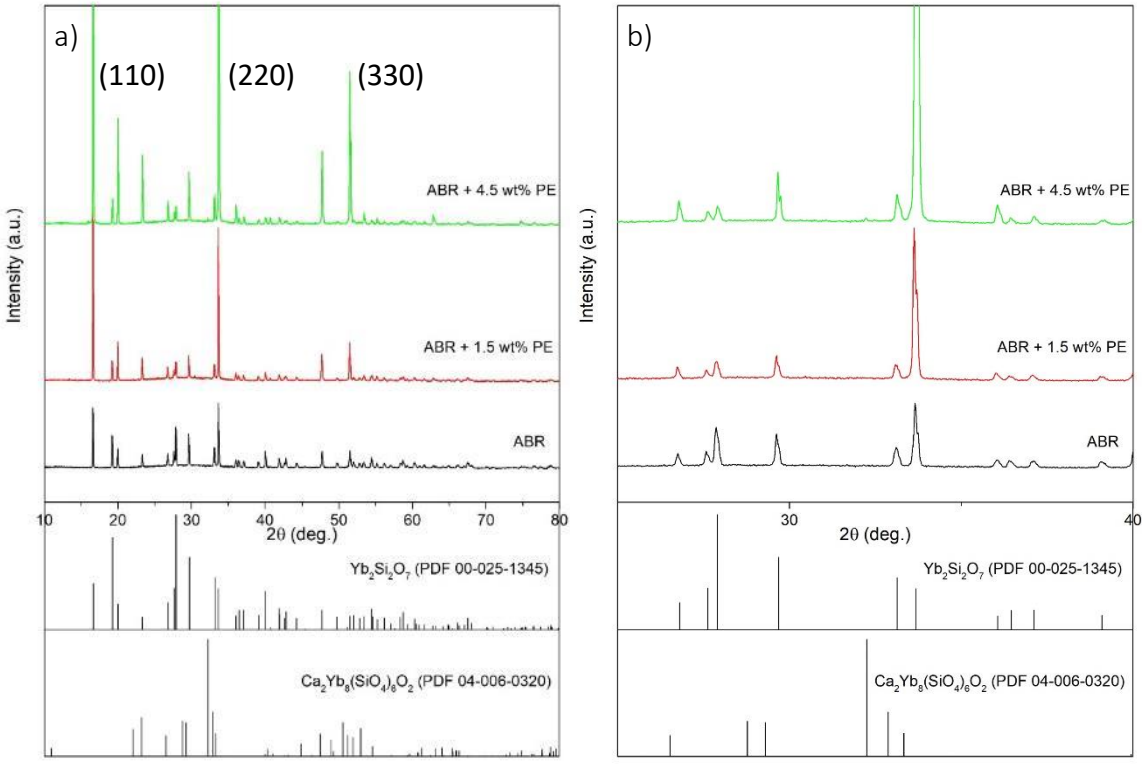

Figure 55. XRDs of coatings exposed to CMAS for 0.5 hrs at 1300 °C showing similar phase compositions for all coatings, where a) shows the 10-80° 2θ range and b) shows the 25-40° 2θ range. Only two phases were detected: YbDS and Yb-apatite. Preferred orientation of the YbDS phase in (110), (220) and (330) planes is shown.

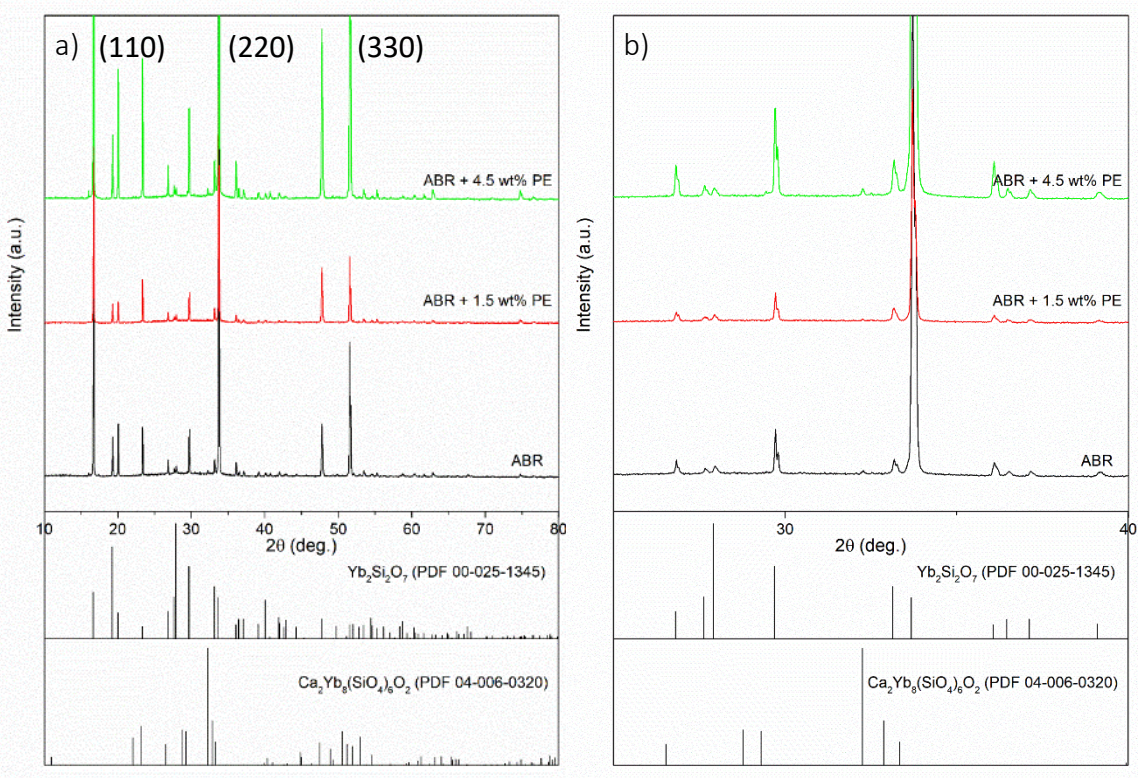

Figure 56. XRDs of coatings exposed to CMAS for 4 hrs at 1300 °C showing similar phase compositions for all coatings, where a) shows the 10-80° 2θ range and b) shows the 25-40° 2θ range. Only two phases were detected: YbDS and Yb-apatite. Preferred orientation of the YbDS phase in (110), (220) and (330) planes is shown.

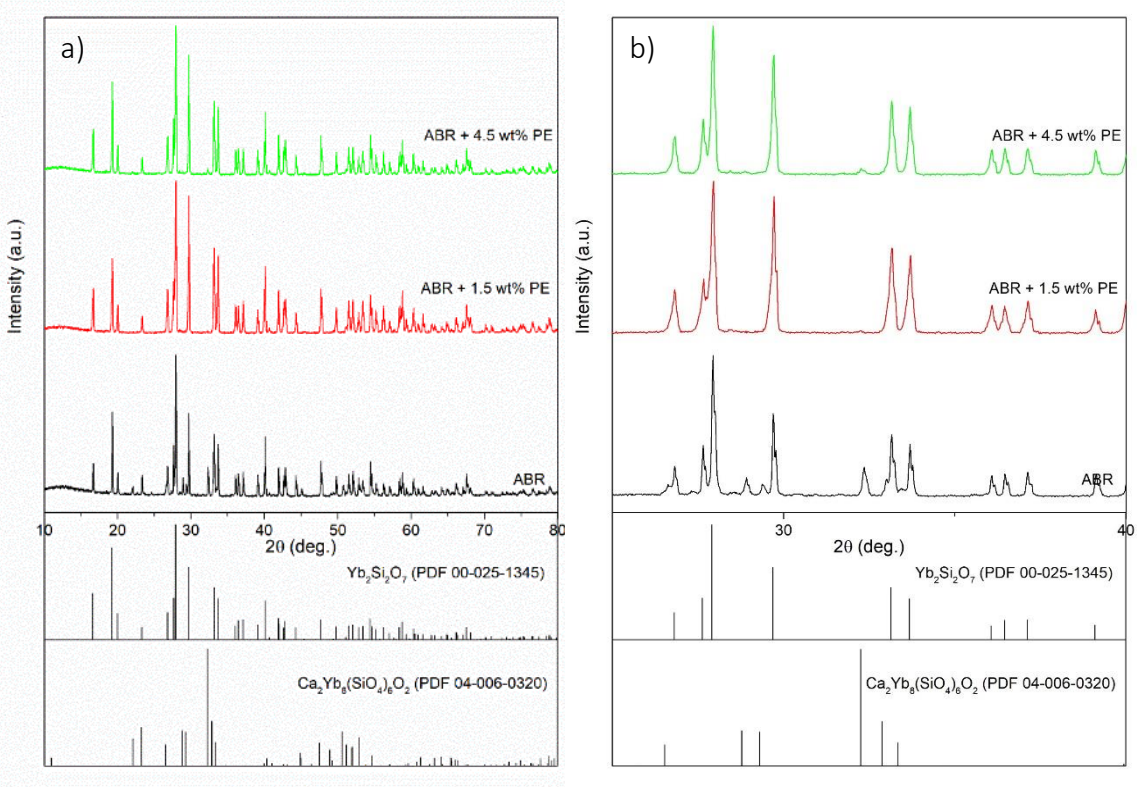

Figure 57. XRDs of coatings exposed to CMAS for 100 hrs at 1300 °C showing similar phase compositions for all coatings, where a) shows the 10-80° 2θ range and b) shows the 25-40° 2θ range. Only two phases were detected: YbDS and Yb-apatite.

6.3.2. 0.5 hrs CMAS exposure

Low magnification cross-sections of the coatings after crystallisation heat treatment but before CMAS exposure are shown in Figure 58. The addition of PE pore former manifests as the large round pores seen in Figure 58b and c.

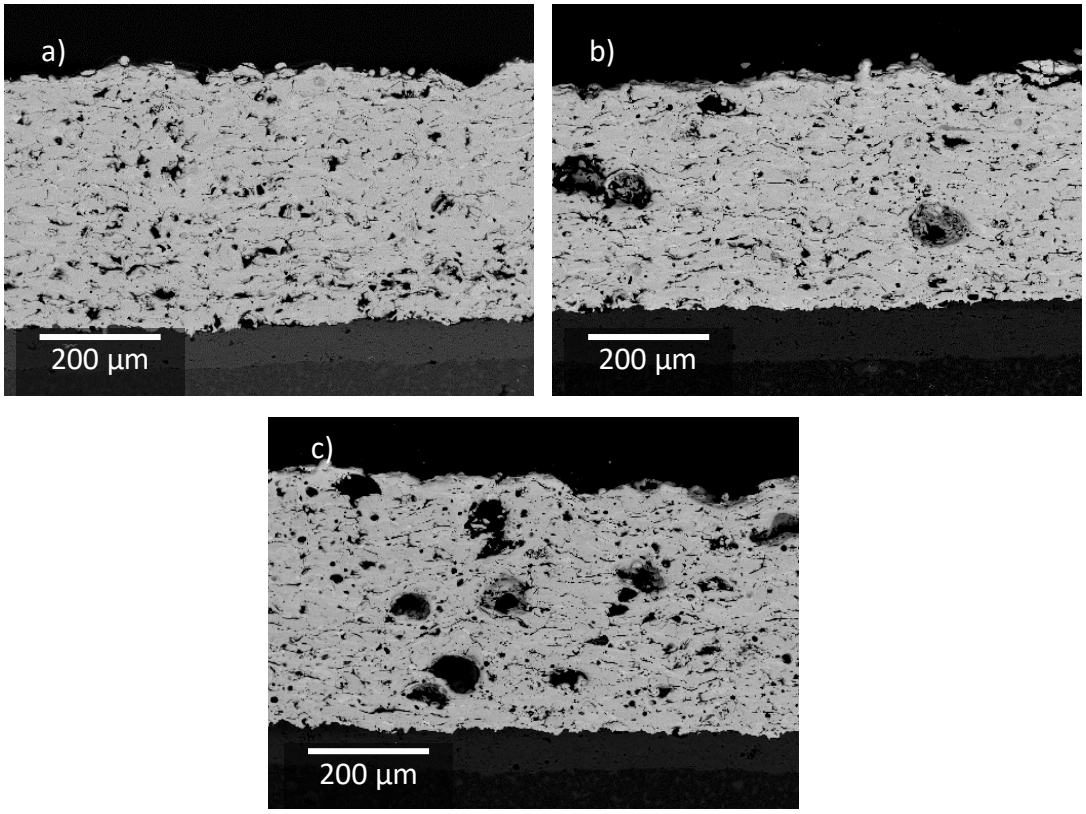

Figure 58. BSE SEM images of the coatings after crystallisation heat treatment but before CMAS exposure. Where a) shows ABR, b) shows 1.5 wt.% PE and c) shows 4.5 wt.% PE coatings.

Low magnification cross-sections of the three coatings after 0.5 hrs CMAS exposure at 1300 °C are shown in Figure 59, along with Ca (shown in blue) EDX map overlays. Previous TGA/DSC analysis of the CMAS powder used in this study determined the melting point to be 1224 °C, indicating that at 1300 °C, the CMAS should be fully molten [59]. From Figure 59 the difference in the porosity levels of the three coatings can be observed. Previous work measured these values to be 8, 15 and 22 % by area for the ABR, 1.5 wt.% PE and 4.5 wt.% PE coatings respectively, after heat treatment but prior to CMAS exposure [165]. Referring to the low magnification images in Figure 59, three distinct regions can be observed, which are similar for all 3 coatings. On the surface of the sample is a thick, residual glassy CMAS layer, indicating incomplete infiltration and reaction of the CMAS under these test conditions. Below this lies the reaction zone, where residual CMAS, reaction products (namely Yb-apatite) and reprecipitated YbDS can be identified. This zone extends roughly half through the thickness (~ 150 µm) and can be identified by the presence of Ca on the EDX map overlay in Figure 59b, d and f. Finally, below this is a region that has remained free

of any CMAS interaction, the original thermal spray splat structure remains and minimal Ca was detected. Interestingly, the large pores found in the 1.5 wt.% and 4.5 wt.% coatings remain free of CMAS or any reaction products, however this may be due to the reaction products being found around the edge of the pores and hence not detectable on the polished cross-section. Importantly, in all three coatings, no delamination between the abradable EBC layer and the Si bond coat was observed.

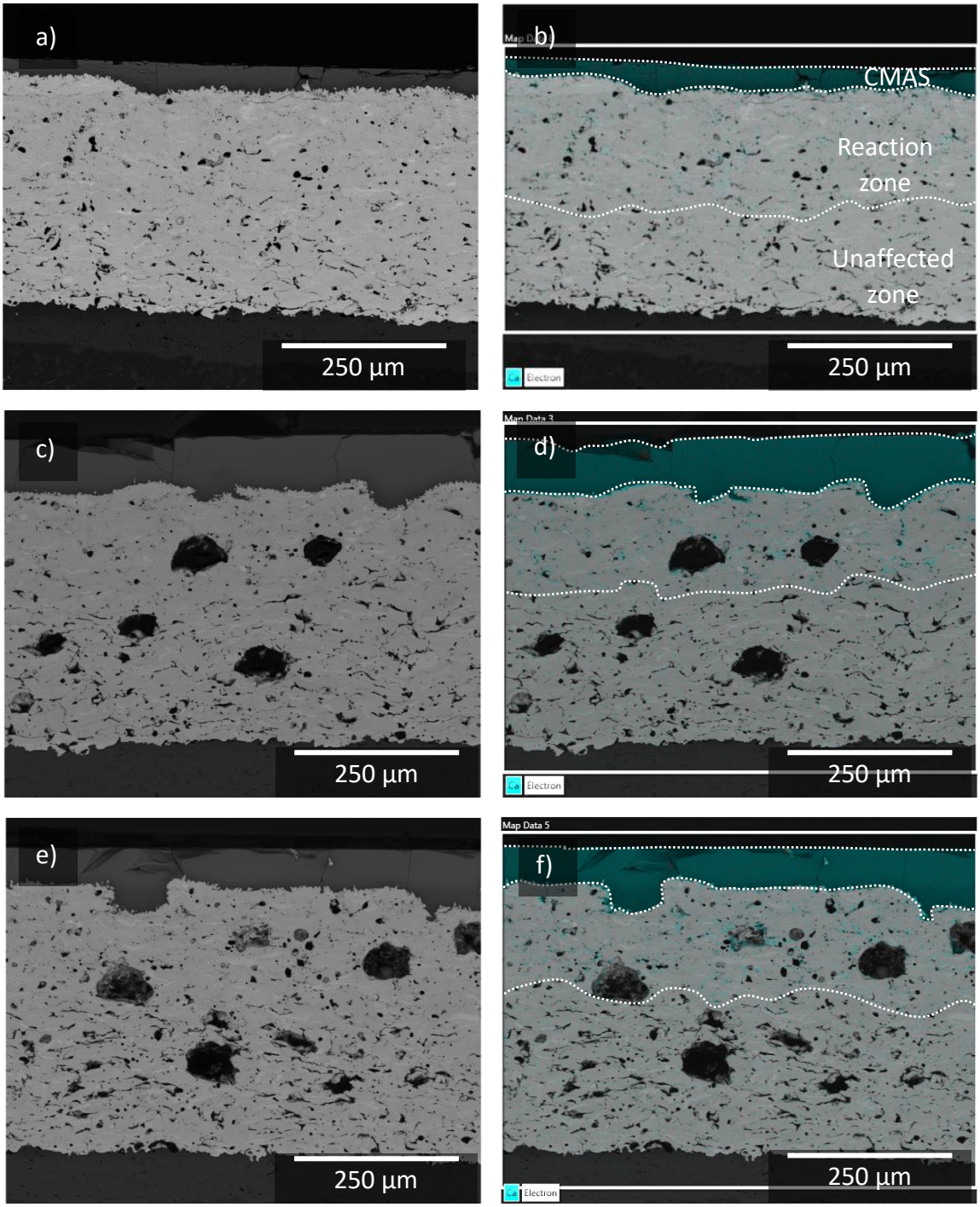

Figure 59. BSE SEM and Ca elemental map overlays of ABR (a & b), 1.5 % PE (c & d) and 4.5 % PE (e & f) coatings after 0.5 hrs CMAS exposure at 1300 °C. The dotted lines represent a rough delineation of the 3 regions of the microstructure, residual CMAS on the coating surface, reaction zone and the CMAS free zone.

To identify the microstructural and chemical changes within the coating, higher magnification images of the surface region where CMAS interaction has occurred are shown

in Figure 60. Using EDX, the chemical composition of microstructural features of interest were analysed, the EDX spots are shown in Figure 60 a, c and e, while the corresponding elemental compositions (in at.%) are shown in Table 13. Based on the composition data in Table 13 and the stoichiometry of the phases expected to be found in the coatings after CMAS exposure, possible phases corresponding to the EDX spots have been put forward. All coatings show similar features regardless of overall porosity. A residual CMAS layer was present on the surface of the coatings. In Figure 60b, d and e, a calcium rich region can be identified; this was confirmed with EDX spot analysis of Figure 60a-1, c-6 and e-10. In all the analysed spots, Ca, Mg, Al and Si were detected indicating this is residual CMAS. Other Ca rich regions can be identified within the coatings themselves; these typically present as large acicular crystals. Such crystals are shown in Figure 60a-3, c-8 and e-12 and the corresponding compositions are in Table 13. The EDX analysis shows they are rich in Yb and Si but also contain Ca, likely corresponding to the Yb-apatite phase identified in XRD analysis. Further smaller, needle-like crystals can be identified on the surface of all three coatings; however, the elemental maps in Figure 60b, d and e reveal they are not rich in Ca as per the possible Yb-apatite crystals. EDX spot analysis (Figure 60 e-11) was conducted on one such feature, and the composition was shown to be close to that of YbDS (the low-level Ca likely picked up from the surrounding residual CMAS layer). In addition, crystals with similar morphology can be identified within the coating bulk albeit less angular in shape. Such features are shown in Figure 60a-2 and c-9 and have a similar composition to e-11, indicating a possible YbDS phase.

Figure 60b, d and e show the same higher magnification image, this time with a Ca EDX map overlay. The Ca maps in Figure 60b, d and e show that these spots are surrounded by Ca rich material, potentially residual CMAS within the coating porosity. This means the possible YbDS crystals are material that has reprecipitated from the CMAS melt, on the surface of the coating and around the path through which the molten CMAS infiltrated the coating. Despite some interaction and reaction with CMAS, some typical APS splat-like structure can still be observed in all the exposed coatings, even in the near surface region. A lighter feature (typical of a splat rich in the YbMS phase, which has a higher average atomic number) was identified in Figure 60a-4, per Table 13, the chemical composition measured in this spot is similar to the stoichiometry of YbMS phase. Despite YbMS not being identified in

XRD analysis, it may still be present in small amounts. This indicates the CMAS infiltration forges a preferential path through the coating, bypassing some of these un-reacted YbMS rich splats. Darker appearing phases maintaining the original APS splat structure were also observed on the BSE SEM images. EDX spots Figure 60c-7 and e-13 indicate the stoichiometry to be similar to that of YbDS. This further demonstrates that the CMAS was not attacking the coating uniformly, leading to the dissolution and recrystallisation of YbDS and its change in morphology, but infiltrating through a path of least resistance. Interestingly, no Ca was detected in any of the large pores in the 1.5 wt.% PE or 4.5 wt.% PE coatings after CMAS exposure. This, in combination with all three coatings showing similar maximum infiltration depths would indicate that the overall porosity level is not a key driver for CMAS infiltration.

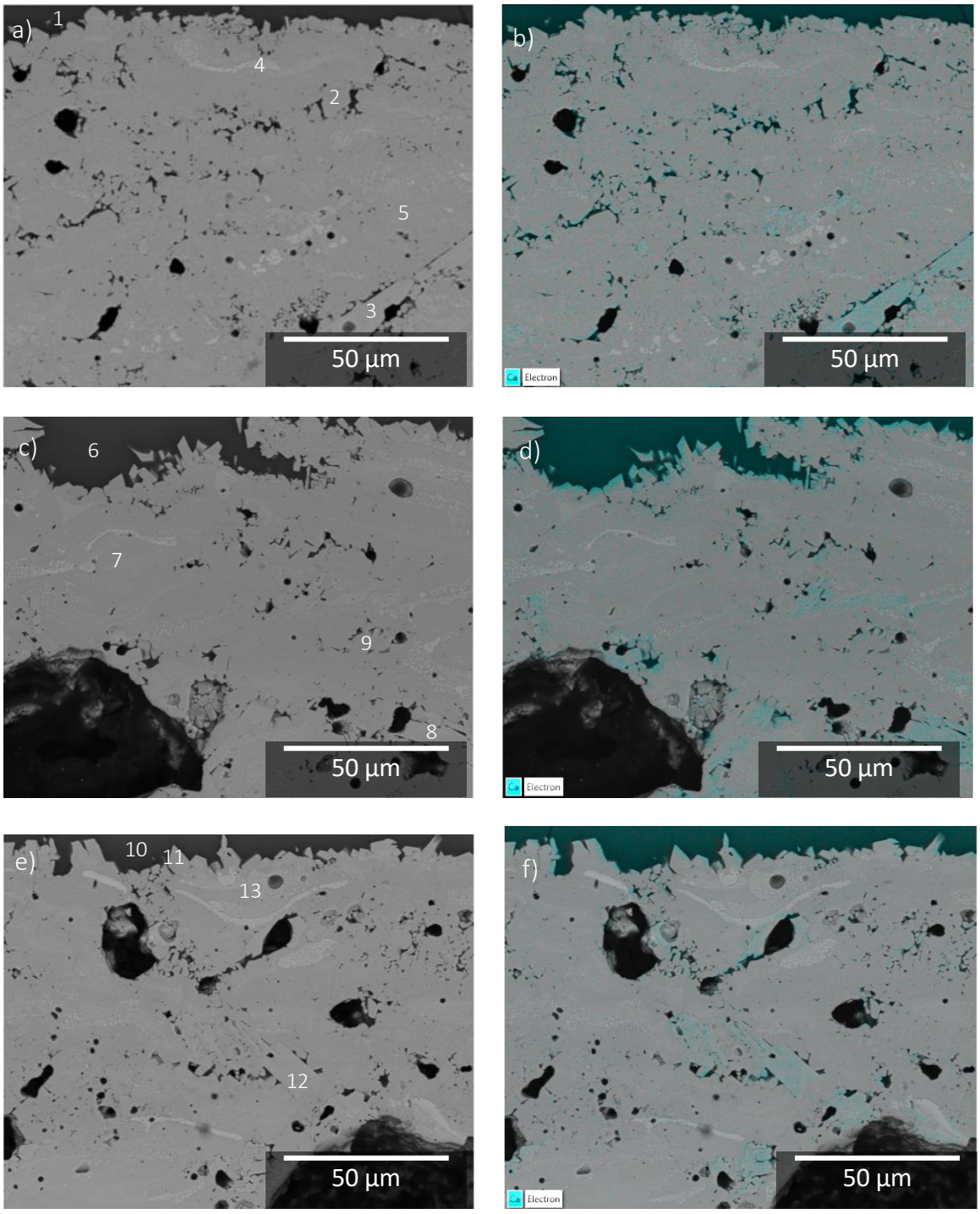

Figure 60. High magnification BSE SEM and Ca elemental map overlays of the surface region of ABR (a & b), 1.5 % PE (c & d) and 4.5 % PE (e & f) coatings after 0.5 hrs CMAS exposure at 1300 °C. The numbers refer to EDX spectra in Table 13.

Table 13. EDX Spectra (in At. %) of the surface region of the coatings after 0.5 hrs CMAS exposure at 1300 °C (corresponding to Figure 60).

Spectrum Label	Yb	Si	O	Ca	Mg	Al	Possible Phase
A-1	1.5	18.8	63.2	9.1	2.8	4.7	CMAS
A-2	17.4	20.4	62.1	0.1			YbDS
A-3	18.4	17.2	59.2	5.2			Yb-apatite
A-4	23.0	16.6	60.4				YbMS
A-5	18.5	20.3	61.2				YbDS
C-6	2.4	20.5	58.8	10.7	2.8	4.8	CMAS
C-8	21.5	17.0	56.9	4.6			Yb-apatite
C-7	21.5	19.9	58.6				YbDS
C-9	18.3	21.0	60.1	0.7			YbDS
E-10	2.0	20.4	59.3	10.6	2.8	5.0	CMAS
E-11	18.5	20.6	60.1	0.8			YbDS
E-12	20.4	16.4	57.5	5.8			Yb-apatite

E-13	21.3	20.3	58.4				YbDS

6.3.3. 4 hrs CMAS Exposure

Low magnification cross-sections of the three coatings after 4 hrs CMAS exposure at 1300 °C are shown in Figure 61, along with Ca (shown in blue) EDX map overlays. Similar to the 0.5 hrs CMAS exposure, three distinct regions can be observed in Figure 61. All three coatings show a layer of residual CMAS, a reaction zone and an unaffected zone towards the bottom of the coating. When compared to the 0.5 hrs exposure time, after 4 hrs all three coatings show slightly deeper CMAS penetration (~200 µm). Despite the longer exposure time, there is still no real difference in terms of CMAS infiltration between the three coatings. As with the previous test, no CMAS was detected in the larger pores in the PE containing coatings, and no delamination between bond coat and the abradable EBC layer was observed.

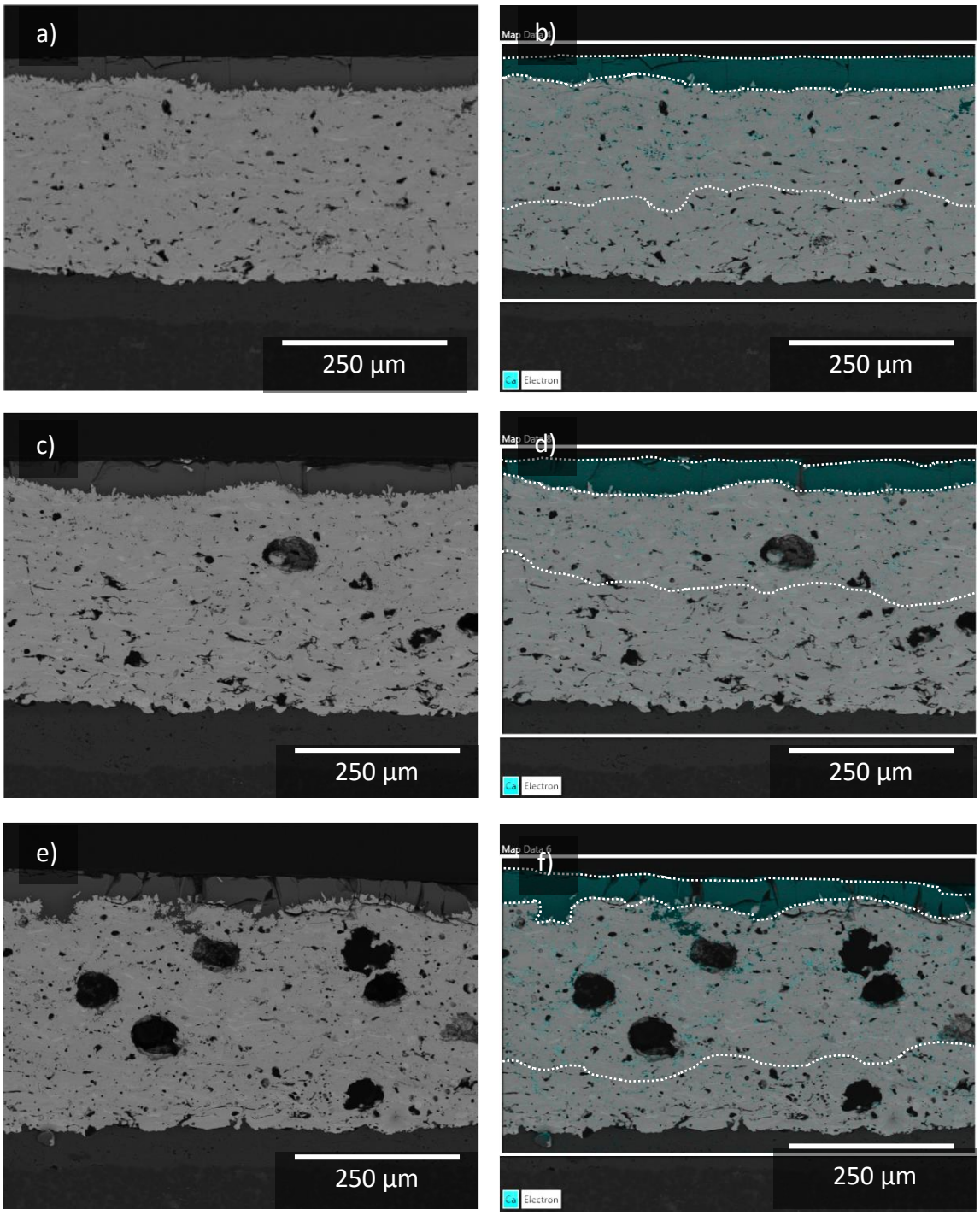

Figure 61. BSE SEM and Ca elemental map overlays of ABR (a & b), 1.5 % PE (c & d) and 4.5 % PE (e & f) coatings after 4 hrs CMAS exposure at 1300 °C. The dotted lines represent a rough delineation of the 3 regions of the microstructure, residual CMAS on the coating surface, reaction zone and the CMAS free zone.

Higher magnification images of the surface region where CMAS interaction has occurred are shown in Figure 62. EDX spots are shown in Figure 62a, c and e, while the corresponding

elemental compositions (in at.%) and their corresponding possible phases are shown in Table 14. Figure 62b, d and e show the same higher magnification image, this time with a Ca EDX map overlay. After 4 hrs CMAS exposure, similar microstructural features and phases can be identified when compared to 0.5 hrs CMAS exposure. The residual CMAS layer can be identified on the surface of the coatings. Figure 62b, d and e show this region to be rich in Ca and Figure 62a-1, c-6 and e-11 show the presence of not only Ca, but also Mg, Al and Si. From Figure 62b, d and e, further Ca containing phases can be identified within all three coatings. EDX analysis of Figure 62a-3, c-8 and e-13 shows these phases contain a similar amount of Ca but no Mg or Al, indicating these are likely the Yb-apatite crystals identified in XRD. Possible YbDS phases that do not resemble the typical APS splat structure were also identified both on the surface of the coating (Figure 62a-2) and within the coating (Figure 62c-7 and e-12). This is likely material that has dissolved into the CMAS melt and recrystallised. Both unreacted YbMS (Figure 62a-4, c-9 and e-14) and YbDS (Figure 62a-5, c-10 and e-15) that retained the original splat structure were also detected using EDX.

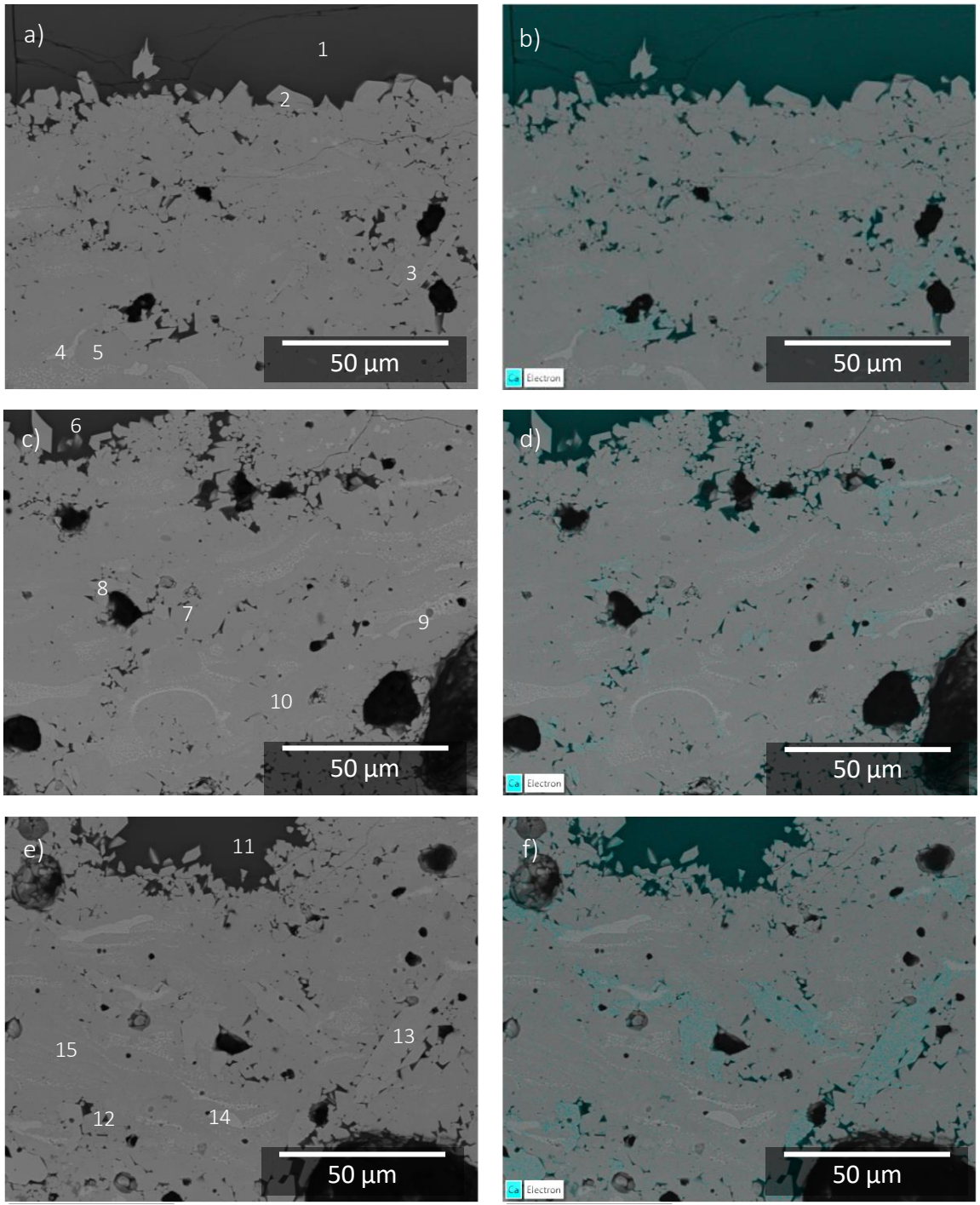

Figure 62. High magnification BSE SEM and Ca elemental map overlays of the surface region of ABR (a & b), 1.5 % PE (c & d) and 4.5 % PE (e & f) coatings after 4 hrs CMAS exposure at 1300 °C. The numbers refer to EDX spectra in Table 14.

Table 14. EDX Spectra (in At. %) of the surface region of the coatings after 4 hrs CMAS exposure at 1300 °C (corresponding to Figure 62).

Spectrum Label	Yb	Si	O	Ca	Mg	Al	Possible Phase
A-1	2.9	20.5	58.2	11.0	3.0	4.4	CMAS
A-2	19.5	21.0	59.1	0.4			YbDS
A-3	20.7	16.7	57.5	5.2			Yb-apatite
A-4	27.0	15.0	58.0				YbMS
A-5	20.8	20.9	58.3				YbDS
C-6	1.6	20.0	59.6	10.6	2.9	5.4	CMAS
C-7	20.1	20.5	59.4				YbDS
C-8	20.0	16.3	58.2	5.5			Yb-apatite
C-9	22.8	18.9	58.3				YbMS
C-10	20.1	20.6	59.4				YbDS
E-11	2.0	19.9	59.0	11.0	3.0	5.0	CMAS
E-12	20.5	20.5	59.0				YbDS
E-13	21.4	16.4	56.9	5.3			Yb-apatite
E-14	26.9	14.9	58.3				YbMS

E-15	20.6	20.3	59.2				YbDS

6.3.4. 100 hrs CMAS Exposure

Figure 63a, c and e show the cross-sections of the coatings after 100 hrs CMAS exposure at 1300 °C, while Figure 63b, d and f show the same image with a Ca EDX map overlay. When compared to the previous tests at 0.5 hrs and 4 hrs, after 100 hrs, no residual CMAS remains on the coating surface, indicating complete infiltration. From Figure 63b, d and f, the infiltration of CMAS can be seen to be much deeper than the previous tests, given the prevalence of Ca containing phases throughout all the coatings. Notably, residual CMAS can be detected at the very bottom of the ABR coating. Despite this, the two more porous coatings (1.5 wt.% PE and 4.5 wt.% PE), still show three clear regions. Towards the surface, a large reaction zone (containing reaction products and residual CMAS). Beneath this exists the CMAS infiltration front, where the transition between reaction products and unreacted materials exists, a lot of residual CMAS can be observed in this region. While the lower region of these coatings remains largely unaffected by CMAS. Even after 100 hrs exposure time, the large PE formed pores do not contain any CMAS or reaction products.

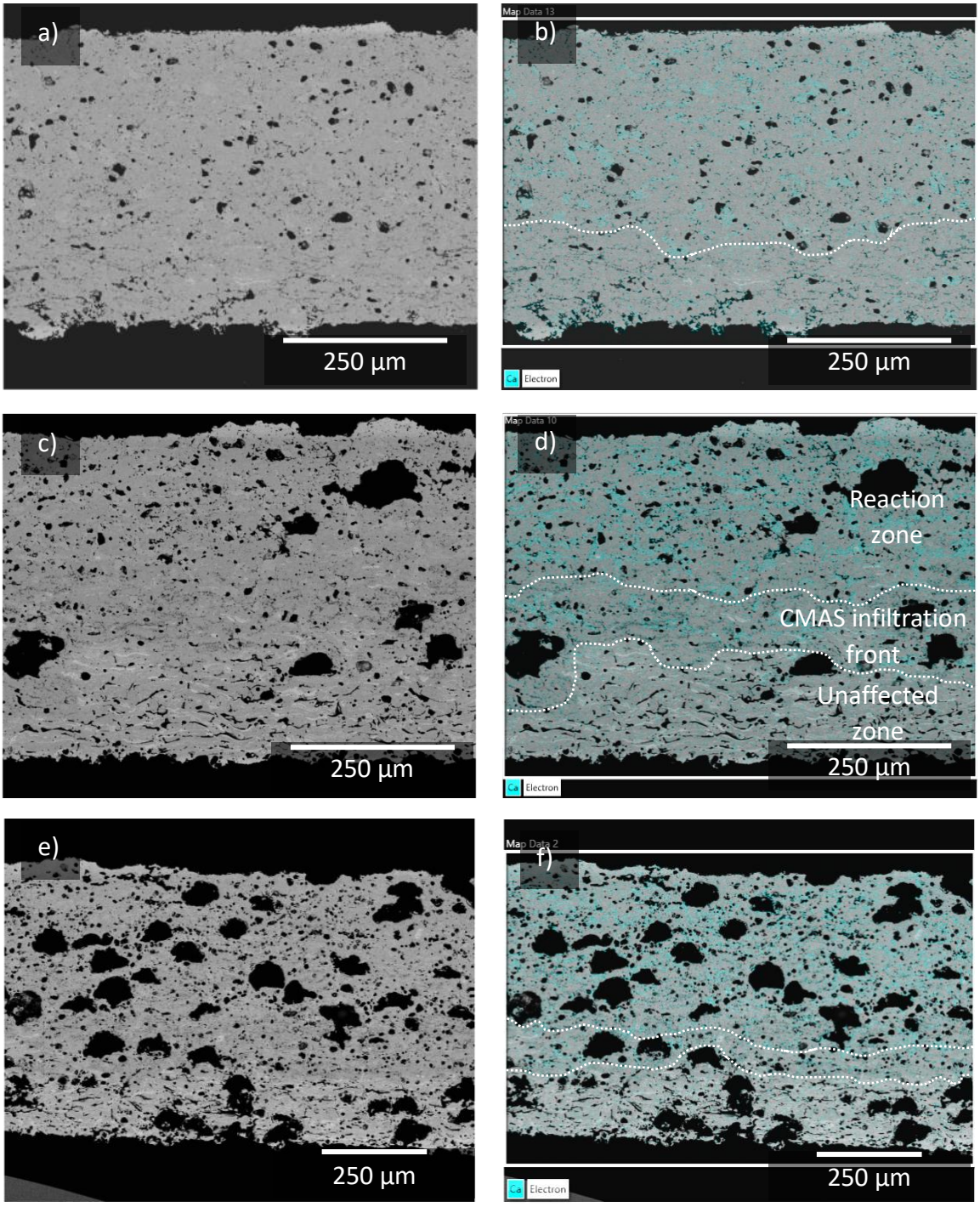

Figure 63. BSE SEM and Ca elemental map overlays of ABR (a & b), 1.5 % PE (c & d) and 4.5 % PE (e & f) coatings after 100 hrs CMAS exposure at 1300 °C. The dotted lines represent a rough delineation of the 3 regions of the microstructure, the large reaction zone containing reprecipitated YbDS and Yb-apatite nearest to the coating surface, the infiltration front of the residual CMAS and the CMAS free zone. In the ABR coating no CMAS free region was observed.

Higher magnification BSE SEM images of the near-surface region of the coatings after 100 hrs CMAS exposure are shown in Figure 64. EDX spots are shown in Figure 64a, c and e while the corresponding elemental compositions (in at.%) and the corresponding possible phases are shown in Table 15. Figure 64b, d and e show the same higher magnification image, this time with a Ca EDX map overlay. Figure 64b, d and e show a higher amount of calcium containing phase within the coating. EDX spot analysis on Figure 64a-2/3, c-5/6 and e-8/9 show that this phase contains Ca but no Al or Mg, indicating the presence of Yb-apatite, as observed from XRD. The only other phase observed was YbDS, shown in Figure 64a-1, c-4 and e-7. No YbMS or splat-like features could be identified. This indicates that after 100 hrs, at least in the near-surface region, the CMAS has completely reacted with the original coating material, leaving behind only Yb-apatite and reprecipitated YbDS.

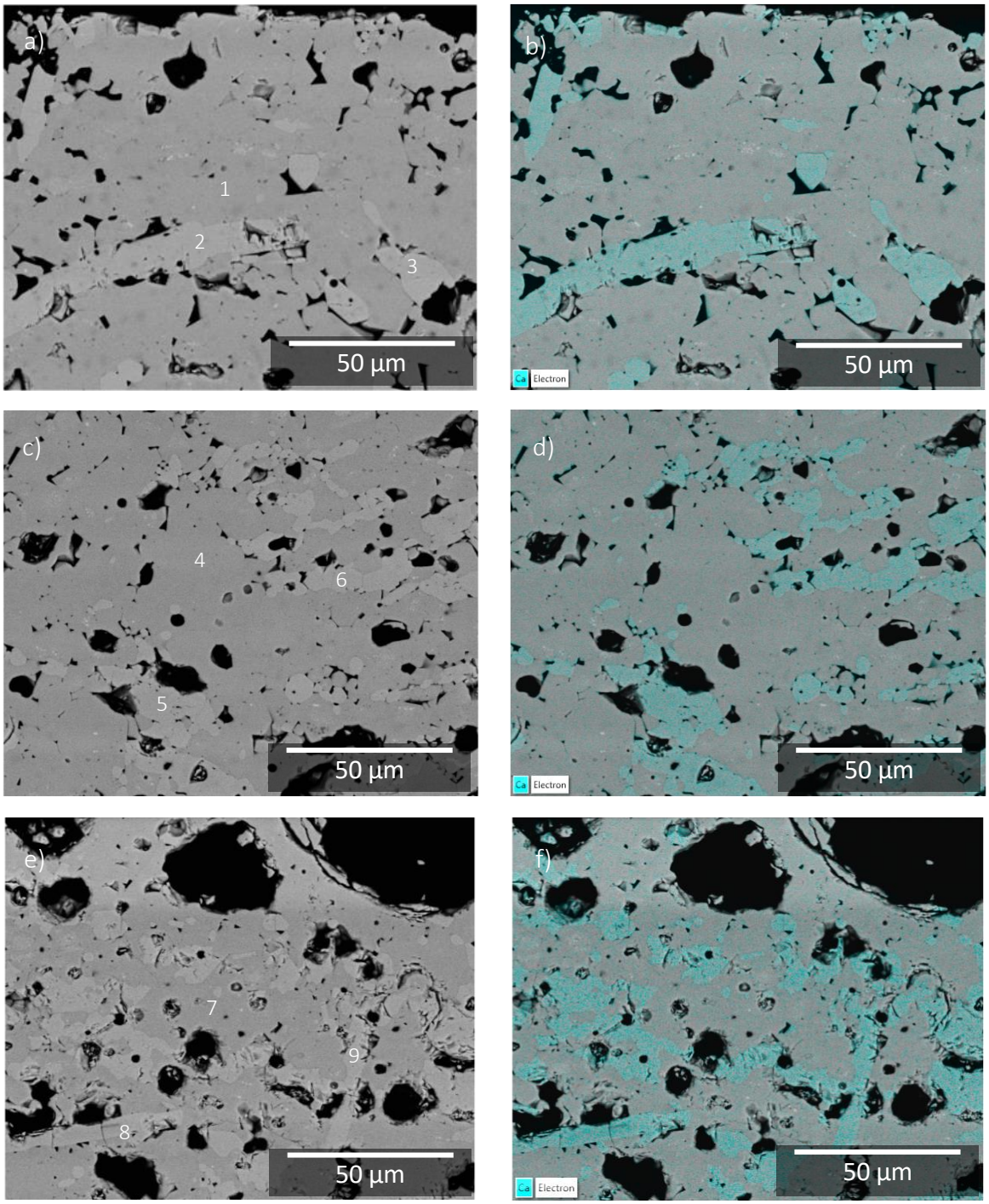

Figure 64. High magnification BSE SEM and Ca elemental map overlays of the surface region of ABR (a & b), 1.5 % PE (c & d) and 4.5 % PE (e & f) coatings after 100 hrs CMAS exposure at 1300 °C. The numbers refer to EDX spectra in Table 15.

Table 15. EDX Spectra (in At. %) of the surface region of the coatings after 100 hrs CMAS exposure at 1300 °C (corresponding to Figure 64).

Spectrum Label	Yb	Si	O	Ca	Possible Phase
A-1	20.4	19.5	60.1		YbDS
A-2	21.5	15.8	57.9	4.8	Yb-apatite
A-3	21.2	14.8	59.1	4.9	Yb-apatite
C-4	19.7	20.3	60.0		YbDS
C-5	19.7	16.0	59.1	5.3	Yb-apatite
C-6	20.5	15.7	59.0	4.8	Yb-apatite
E-7	20.2	20.2	59.6		YbDS
E-8	20.0	16.4	57.7	5.9	Yb-apatite
E-9	20.8	16.3	58.1	4.9	Yb-apatite

Higher magnification images of the transition region between the reaction zone and unaffected material are shown in Figure 65. EDX spots are shown in Figure 65a, c and e, while the corresponding elemental compositions (in at.%) and the corresponding possible phases are shown in Table 16. Figure 65b, d and e show the same higher magnification image, this time with a Ca EDX map overlay. In this region, a pair of Ca containing phases are apparent from Figure 65b, d and e. Figure 65a-2, c-6 and e-10 appear to show Yb-apatite, while Figure 65a-3, c-7 and e-11 correspond to residual CMAS per the EDX analysis in Table 16. Relative to the CMAS layer seen on the surface of the coatings in previous tests, the level of Ca detected here is somewhat reduced, indicating increased levels of interaction with the coating material. The residual CMAS appears in relatively thin bands, indicating it has filled the inter-splat pores as it has infiltrated. In this region, recrystallised YbDS grains are also visible, as shown in Figure 65a-1, c-5 and e-9. Below the CMAS front exists a combination of unreacted YbDS and YbMS that has retained the APS splat structure. A possible YbMS phase is shown in Figure 65a-4, c-8 and e-12. The remaining inter-splat porosity not yet infiltrated with CMAS is also visible in this region, especially in Figure 65e. The arrows in Figure 65b, d

and f indicate regions where Ca rich (blue regions on EDX map) have formed around a phase with a lighter contrast on the BSE SEM image (possibly YbMS rich splats as indicated by the EDX spectrum shown in Figure 65c-12. This could point to CMAS reacting preferentially with YbMS once it has infiltrated the coating to form Yb-apatite.

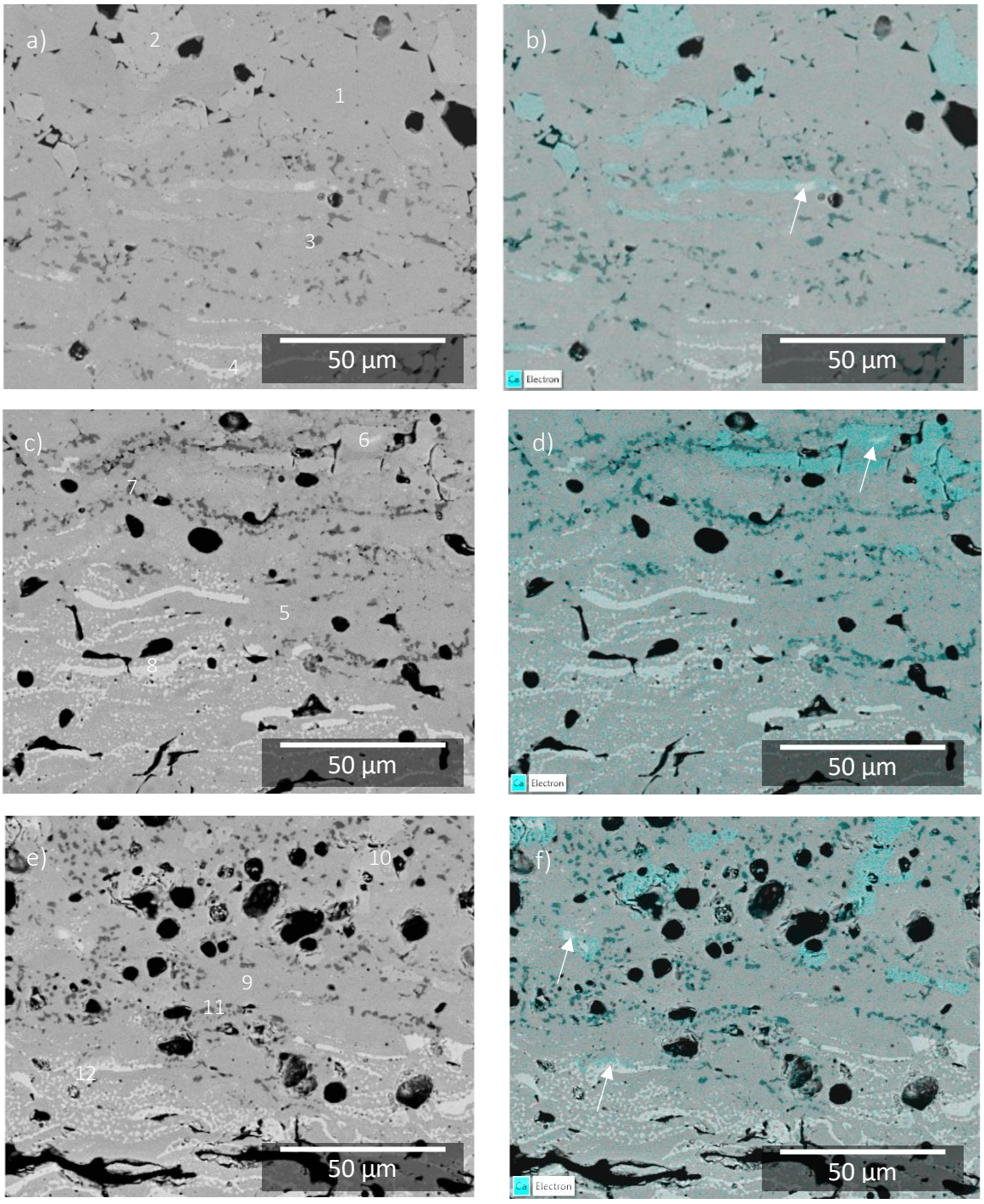

Figure 65. High magnification BSE SEM and Ca elemental map overlays of the lower region of ABR (a & b), 1.5 % PE (c & d) and 4.5 % PE (e & f) coatings after 100 hrs CMAS exposure at 1300 °C. The numbers refer to EDX spectra in Table 16. The arrows on b, d and f indicate

regions where Ca rich (blue regions on EDX map) have formed around a phase with a lighter contrast on the BSE SEM image (possibly YbMS rich splats).

Table 16. EDX Spectra (in At. %) of the lower region of the coatings after 100 hrs CMAS exposure at 1300 °C (corresponding to Figure 65).

Spectrum Label	Yb	Si	O	Ca	Mg	Al	Possible Phase
A-1	18.6	18.8	62.7				YbDS
A-2	18.9	14.9	61.5	4.8			Yb-apatite
A-3	10.4	9.3	60.1	4.4	4.8	11.0	CMAS
A-4	25.2	12.9	62.0				YbMS
B-5	19.9	20.4	59.7				YbDS
B-6	20.0	16.2	58.6	5.3			Yb-apatite
B-7	13.0	11.4	58.9	3.9	3.9	8.9	CMAS
B-8	25.9	14.2	59.9				YbMS
C-9	20.2	20.1	59.7				YbDS
C-10	20.9	15.8	58.2	5.1			Yb-apatite
C-11	14.2	11.8	59.3	3.1	3.9	7.6	CMAS
C-12	27.3	14.0	58.7				YbMS

To summarise, after all the exposure times similar phases and microstructures were observed in all of the coatings. The phases identified were primarily YbDS and Yb-apatite identified by XRD, SEM and EDX analysis, some possible YbMS was also identified using SEM and EDX analysis. Residual CMAS glass was identified on the surface and throughout the coatings exposed for 0.5 and 4 hrs, again by SEM and EDX analysis. While after 100 hrs the CMAS had fully infiltrated the coating. A dissolution-reprecipitation mechanism was

identified as the main corrosion mechanism, whereby the Yb-silicates were dissolved into the molten CMAS and YbDS and Yb-apatite were precipitated, leading to a change in microstructure. Below the maximum CMAS penetration depth, the coatings retain the typical APS splat structure.

6.3.5. EBSD

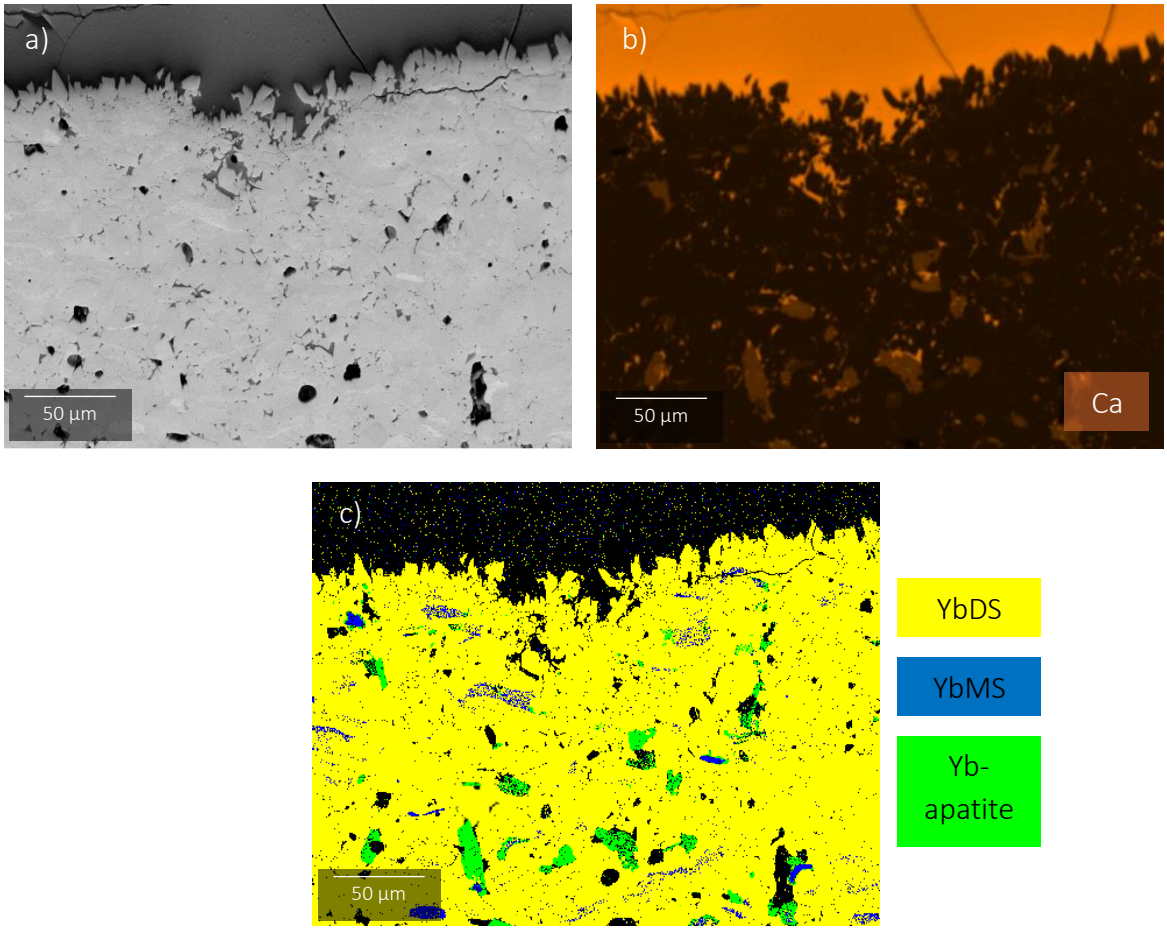

Figure 66. EDX mapping and EBSD phase analysis of ABR coating that had been exposed to CMAS for 4 hrs at 1300 °C. Where a) shows the BSE SEM image, b) shows the Ca EDX map and c) shows the phase map.

To confirm the suspected phases identified on the SEM BSE cross-sections and to align with what was detected using XRD, EBSD was used. The phase map of coating ABR, that had been exposed to CMAS for 4 hrs at 1300 °C is shown in Figure 66. From the phase map shown in Figure 66c, the angular crystals on the surface of the cross-section are indeed reprecipitated YbDS. The Ca rich residual CMAS layer on the surface of the coating can be seen in the EDX map in Figure 66, as well as some unreacted CMAS that has infiltrated the coating. When

comparing the Ca rich areas on the EDX map shown in Figure 66b to the phase map shown in Figure 66c, it can be observed that these correspond to the Yb-apatite phase. Slightly lighter phases in the SEM image in Figure 66a represent areas of unreacted YbMS.

6.3.6. CMAS infiltration depth

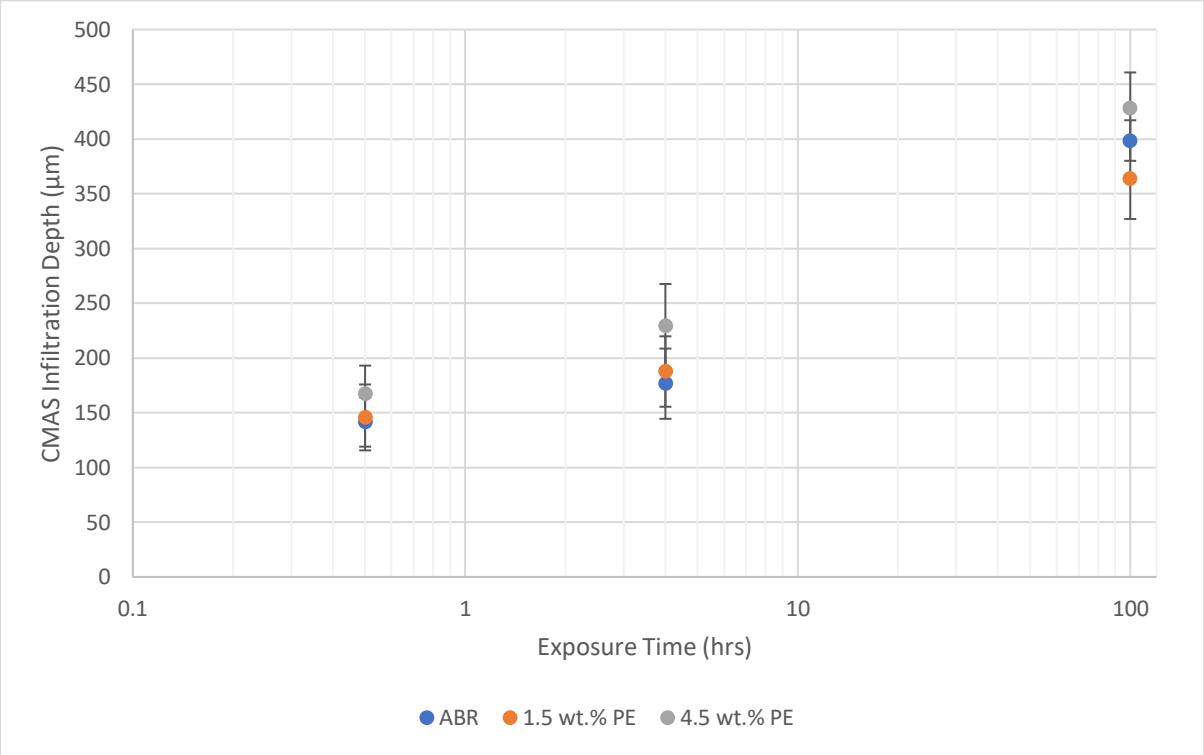

Figure 67. Maximum CMAS infiltration depths for all the coatings at the 3 exposure times. The maximum CMAS infiltration depth was measured as being the deepest detectable Ca from a random spot on the surface.

Table 17. Maximum CMAS infiltration depths for all the coatings at the 3 exposure times.

Coating	Infiltration depth (µm) after time (hrs)		
	0.5	4	100
ABR	141.4 ± 22.4	176.5 ± 32.1	398.6 ± 25.7
1.5% PE	145.7 ± 30.1	187.6 ± 32.2	364.1 ± 38.4
4.5% PE	167.3 ± 25.7	229.1 ± 37.2	428.3 ± 32.5

Figure 67 and Table 17, show the overall infiltration depth of the CMAS, in the three coatings for all the exposure times. The infiltration depth was defined as the deepest point from the coating surface where a Ca containing phase (either residual CMAS or Yb-apatite)

could be detected, an average of 5 points was recorded per image and 5 images were analysed per coating. Infiltration depth increases with exposure time for all coatings; however, despite the large difference in porosity between the coatings, there does not seem to be a correlation between porosity and CMAS infiltration.

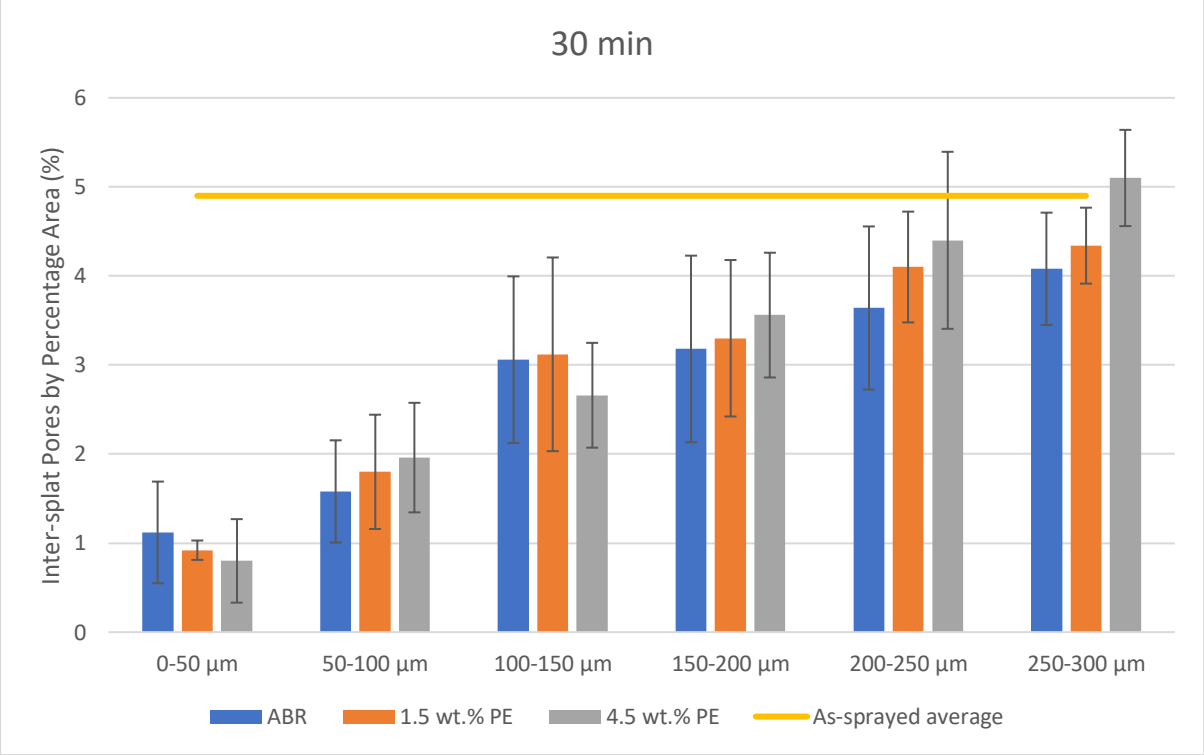

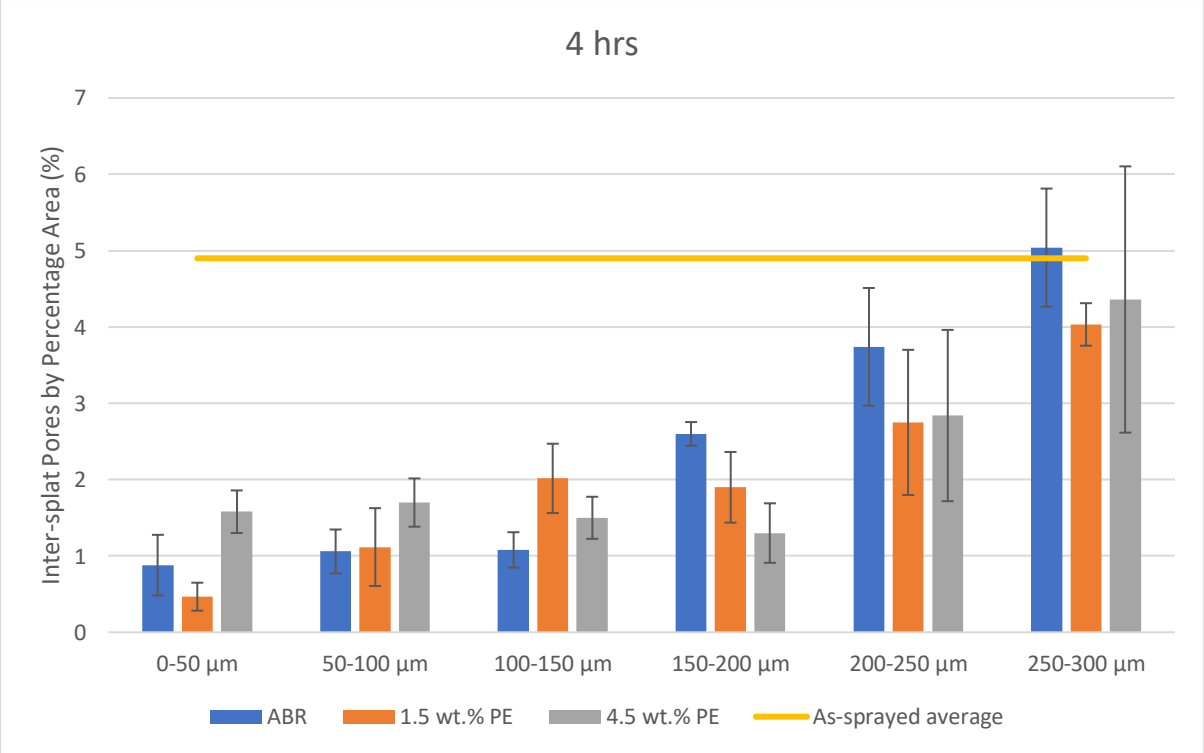

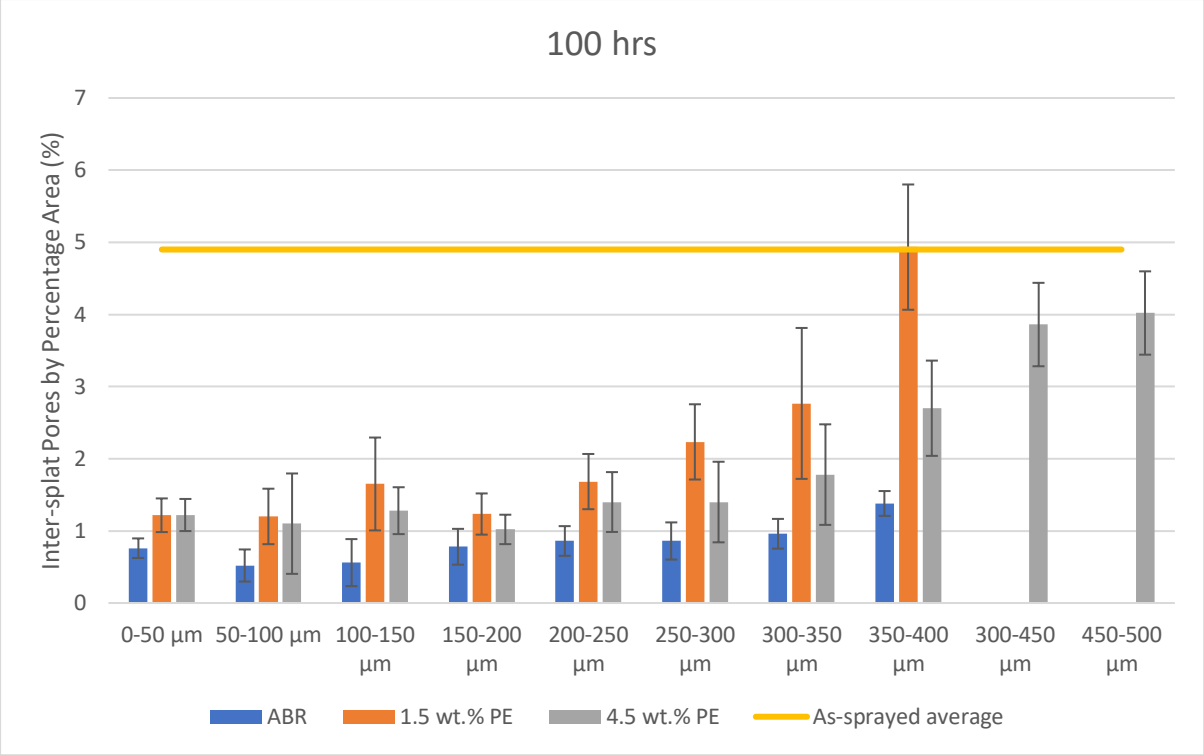

Figure 68. Graphs charting the change in porosity in all the coatings at the 3 exposure times. Inter-splat pores were defined as having an aspect ratio > 2.75 and a size of 5-250 µm^2. The percentage area porosity was separated into 50 µm bins for the depth of the coatings extending from the surface (0 µm) through the thickness of the coating, shown on the x-axis. The as-sprayed average was the amount of porosity meeting these criteria in coatings which had not been exposed to CMAS, this value was similar for all 3 coatings.

At no point after CMAS exposure were CMAS or CMAS-silicate reaction products identified in the large pores initiated by PE inclusion. Given that the overall porosity level does not appear to be a determinant for CMAS infiltration, it was postulated that CMAS was infiltrating through inter-splat porosity inherent to the APS process. In plasma spraying, the inter-splat pores are flat, thin voids filling spaces between the lamellar splats [14, 180]. With Yb-apatite and dissolved YbDS, crystallising and coarsening into these pore channels, reducing the overall level of porosity and altering its morphology in CMAS affected regions. Since all three coatings were deposited using the same YbDS powder and spray parameters, the level of this porosity was likely similar for all the coatings. To confirm this, image analysis was conducted on SEM BSE images of coatings that had been heat-treated but not yet exposed to CMAS per the same methodology described in Chapter 6.2.4. Shape filters were applied to the threshold images to isolate the inter-splat pores, which were defined has

having an aspect ratio greater than 2.5 and a size smaller range of 5 – 250 µm^2. The average level of inter-splat porosity, in terms of % area, was found to be 4.9 ± 0.9 for the heat-treated coatings (this value was similar for all 3 coatings).

For the CMAS exposed coatings, the same filters were applied this time to 50 µm sections of the coating thickness, to track the depth of CMAS interaction. The results of this are shown in Figure 68. Near the surface, the percentage of pores meeting the filter constraints is greatly reduced relative to an as-sprayed coating. As the measured depth increases towards the CMAS infiltration front, this number reduces. Towards the bottom of the CMAS exposed samples, this number returns towards the average in an as-sprayed coating. As with the CMAS infiltration depth measurements, all three coatings show a similar reduction in inter-splat pores as the respective measured depths after each exposure time. After 100 hrs, the ABR sample showed CMAS interaction across the entire through thickness of the coating. The free-standing coating produced that contained 4.5 wt.% PE was slightly thicker; hence more of the thickness could be analysed.

6.3.7. X-Ray CT

To better understand how the CMAS infiltrated the coatings, X-ray CT scans were conducted on the PE containing abradable coatings, before and after CMAS exposure at 1300 °C for 4 hrs. The PE containing coatings were selected as their increased level of large porosity meant that more features would be detectable, given the resolution (1.2 µm) of the X-ray CT scans. Figure 69 shows the porosity networks of the four coatings, whereby the coating material itself has been made transparent, and the individual pores and pore networks are represented by a colour scale determined by pore volume. In all cases, many smaller porosities can be identified, but also large networks of interconnected pores extending through the structure (which would not have been characterisable using SEM image analysis). Extracting the data of the pore networks allowed for each individual pore to be characterised in terms of volume. A pore size distribution graph is shown in Figure 70, this shows the contribution of each individual pore to the overall porosity of the coating. Smaller pores in the 4.5 wt.% coatings have a much lower contribution to the overall porosity than the larger pores when compared to the 1.5 wt.% PE coatings. The largest pores in the 4.5 wt.% PE coatings are also much larger than those in the 1.5 wt.% coatings, this indicates that the increased level of PE is creating large networks of interconnected porosity. After CMAS

exposure, the contribution of small pores (<5 x10^{-4} mm^3) to the overall porosity in the 1.5 wt.% coating is reduced, this in line with previous X-ray CT analysis of CMAS exposed EBCs [132]; however, this trend did not hold for the 4.5 wt.% coatings. CMAS exposure was found to decrease the overall porosity of each coating slightly. For the 1.5 wt.% coating, the sample that hadn't been exposed to CMAS had an overall porosity of 5.0 vol.%, while the sample that had been exposed to CMAS had an overall porosity of 3.6 vol.%. For the 4.5 wt.% PE coatings these values were 13.8 vol.% and 12.8 vol.%, respectively. The overall porosity values are reduced when compared to figures derived from image analysis due to the limitation in voxel size of the X-ray CT scan, and not being able to resolve the smallest pores that would otherwise be clear when using a high-resolution SEM image. While this methodology allowed for quantification of the overall porosity it did not include any information as to the differences between the regions where CMAS reaction had taken place and the un-affected material.

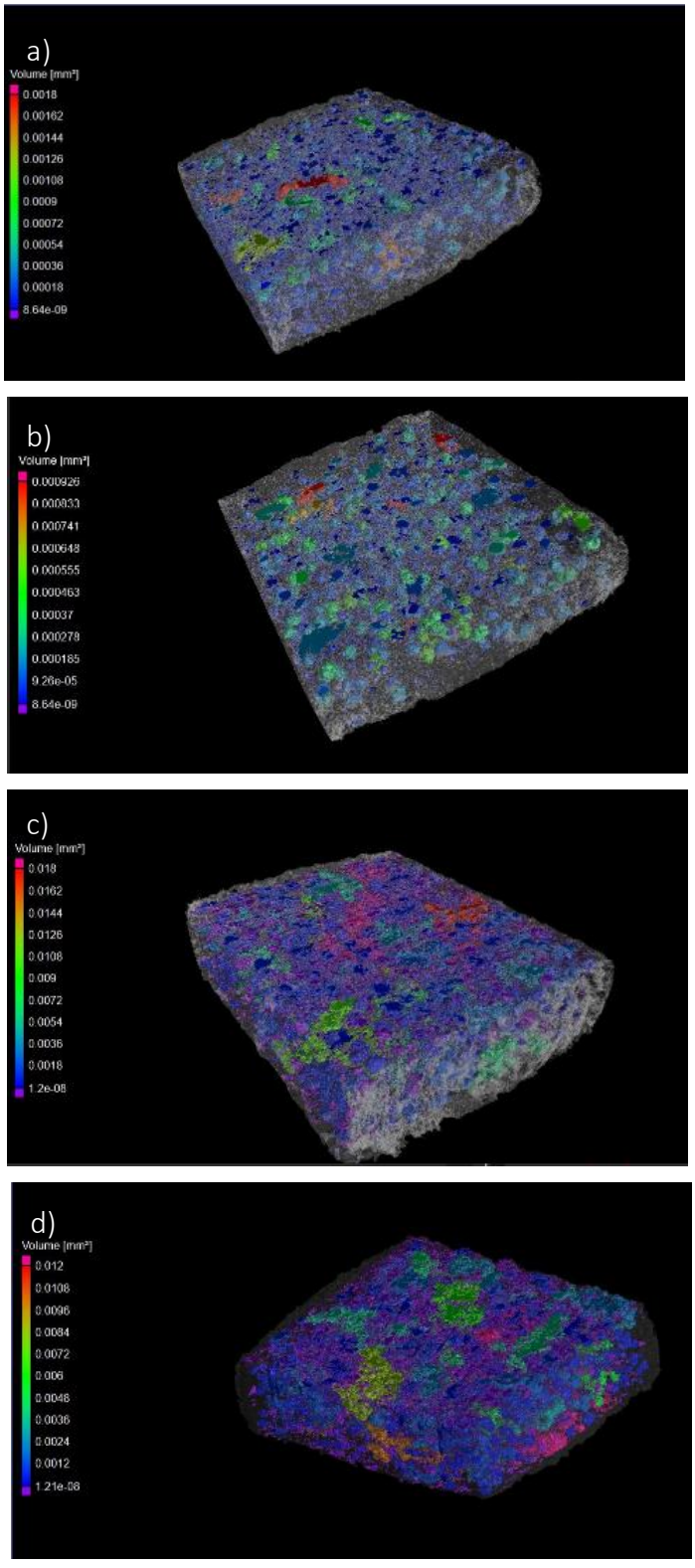

Figure 69. 3D rendered images of the X-ray CT scans, with the coating itself set to 25% transparency and the pore networks visualised with a colour scale depicting pore volume, whereby larger pores are represented by the pink side of the scale and smaller pores with

the blue. Where a) is 1.5 wt.% PE, b) is 1.5 wt.% PE after 4hrs CMAS exposure, c) is 4.5 wt.% PE and d) is 4.5 wt.% PE after 4hrs CMAS exposure.

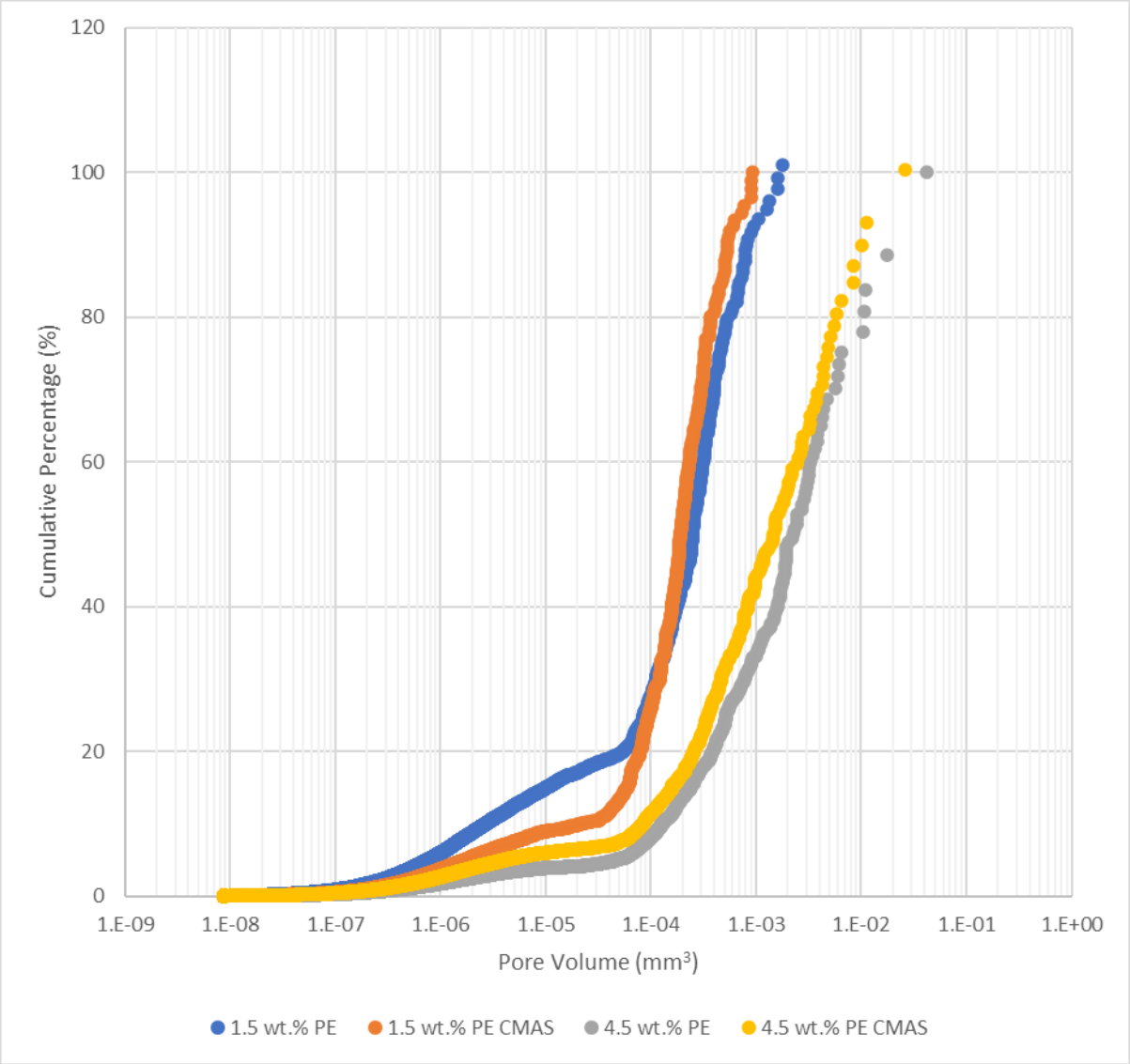

Figure 70. Distribution of pore volumes for 1.5 wt.% PE and 4.5 wt.% PE coatings (as-sprayed and after CMAS exposure).

6.3.8. Combined effects of CMAS exposure and erosion

To examine how CMAS exposure and the associated phase and microstructural changes affected the mechanical performance of the abradable coatings, an erosion test was conducted after 100 hrs CMAS exposure at 1300 °C. The 100 hrs exposure time was selected as no glassy CMAS layer existed on the surface of the coating, and the level of CMAS infiltration meant reaction products made the majority of the coatings, so any changes in performance could be fully captured. The erosion resistance of the CMAS exposed coatings

was compared to coatings which had undergone crystallisation heat-treatment only. The GE test was selected as while nominally a solid particle erosion test, it also acts as a pseudo-abradability test [16].

The results of the erosion depth of all the coatings are shown in Figure 71. Erosion resistance is greatly influenced by the overall porosity level in the coatings. For both the heat-treated and CMAS exposed coatings, increasing the level of porosity increases the erosion rate. Erosion rates, calculated from the steady state regions of the plots in Figure 71, are shown in Table 18. From Table 18, it can be observed that increasing the overall porosity in the heat-treated coatings (from 0, to 1.5 and finally 4.5 wt.% PE) increases the erosion rate from 2.9, to 4.6 and 5.8 µm/s. For the CMAS exposed coatings, the trend remains the same, with erosion rate increasing from 2.0 to 3.1 and 5.2 µm/s, for ABR, 1.5 and 4.5 wt.% PE coatings, respectively. The trend for mass loss during the erosion test is also similar. For the heat-treated coatings the rate of mass loss increases from 3.4 to 5.3 and 6.4 mg/s for the ABR, 1.5 and 4.5 wt.% PE coatings, respectively. While after CMAS exposure, the mass loss rate increases from 2.9, to 4.3 and 5.7 mg/s for the ABR, 1.5 and 4.5 wt.% PE coatings, respectively. Interestingly, after a given coating had been exposed to CMAS its erosion resistance increased. This indicates that the phase and porosity changes caused by exposure to CMAS have a great effect on the mechanical properties of the coatings.

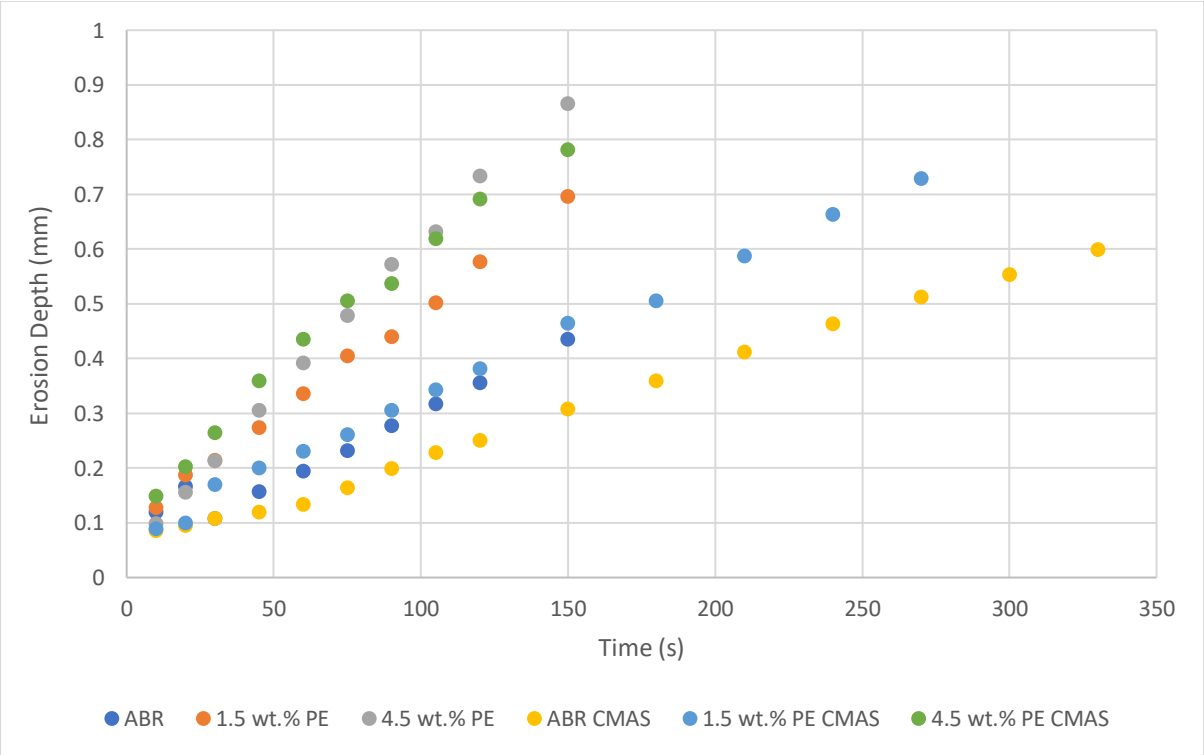

Figure 71. Chart showing the erosion depth of the various coatings over time.

Table 18. Erosion rates calculated from depth and mass loss data respectively.

Erosion Rate	µm/s	s/mil	mg/s
ABR	2.9	8.8	3.4
1.5 wt.% PE	4.6	5.5	5.3
4.5 wt.% PE	5.8	4.4	6.3
ABR CMAS	2.0	12.4	2.9
1.5 wt.% PE CMAS	3.1	8.2	4.3
4.5 wt.% PE CMAS	5.2	4.9	5.7

The surfaces of the heat-treated and 100 hrs CMAS exposed coatings before erosion testing are shown in Figure 72. Figure 72a, c and e show the heat-treated coatings, with the typical APS splat structure visible. The morphology of the coating surface after CMAS exposure is vastly different. From Figure 72b, d and f, no splat structure is visible, and the surface appears to be made up entirely of products of CMAS interaction, namely recrystallised YbDS and Yb-apatite. This aligns with the features observed in Figure 63 and Figure 64.

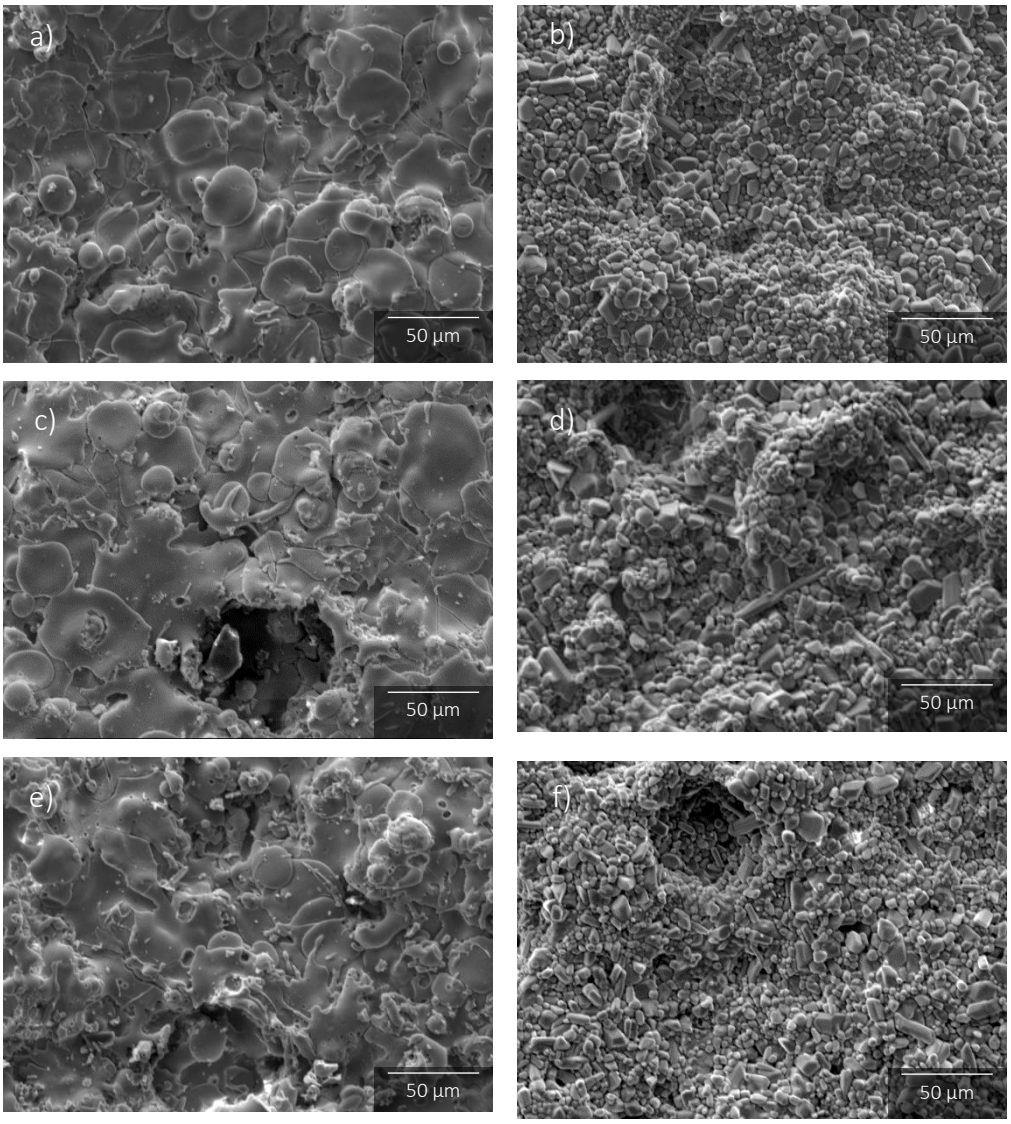

Figure 72. SE SEM images of heat-treated and 100 hrs CMAS exposed coating surfaces respectively for ABR (a & b), 1.5 % PE (c & d) and 4.5 % PE (e & f).

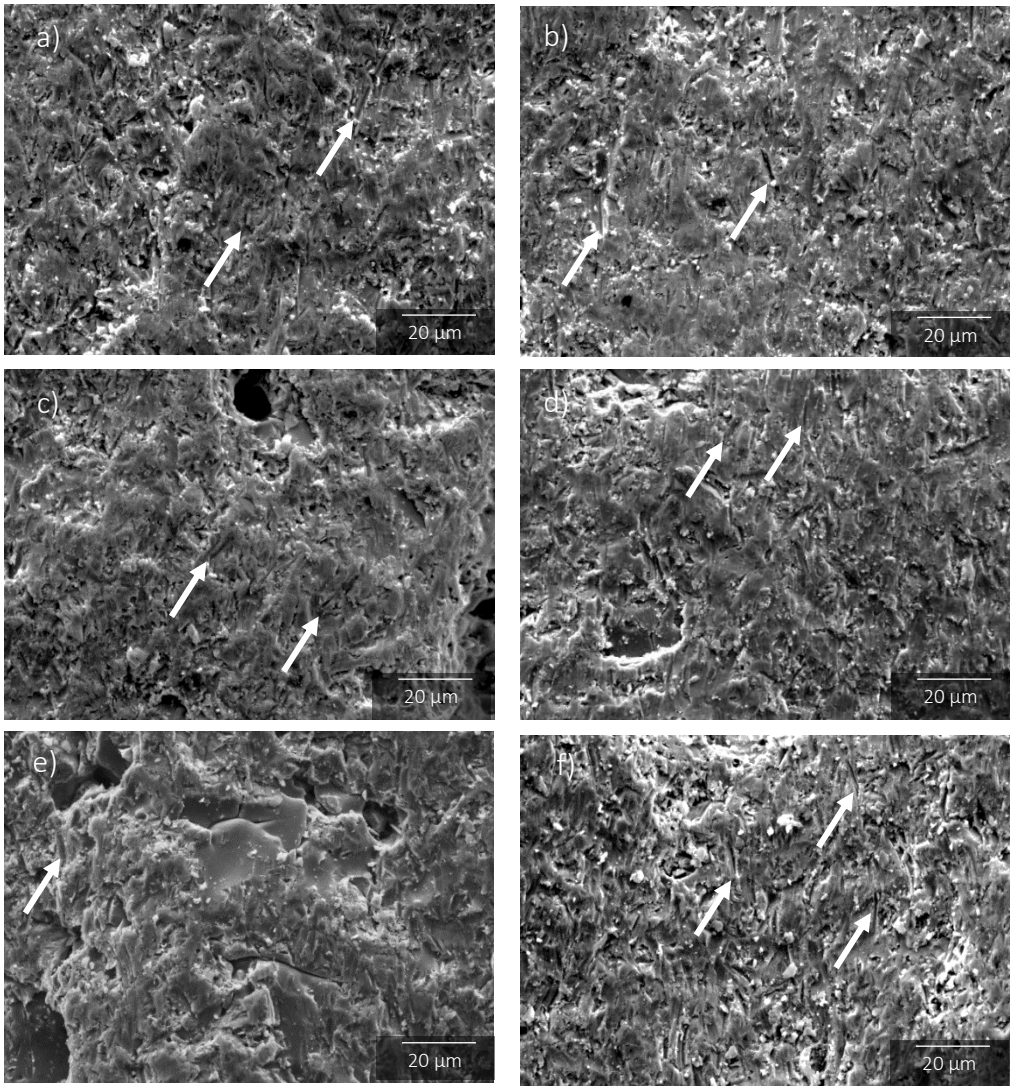

Figure 73. SE SEM images of heat-treated and 100 hrs CMAS exposed coating surfaces respectively for ABR (a & b), 1.5 % PE (c & d) and 4.5 % PE (e & f) after erosion. The white arrows indicate some of the ploughed tracks on the eroded surfaces, indicative of ductile failure.

The eroded surfaces of the heat-treated and CMAS exposed abradable coatings are shown in Figure 73. For all coatings, regardless of porosity level or CMAS exposure, the mechanism of erosion appears to be similar. Relative to Figure 72, where the splat and recrystalised structures are visible, the surfaces have been severely plastically deformed, via the erodent cutting and ploughing the original structure. This is indicative of ductile failure rather than brittle failure whereby crack propagation leads to material removal, some of these ploughed tracks are shown by the white arrows in Figure 73. Erosion testing at low angles promotes ductile failure due to the added tangential velocity component of the impacting particles.

Referring to the heat-treated 4.5 wt.% PE abradable coating, shown in Figure 73e, some splat structure is still visible. Given this coating has the lowest erosion resistance of any of those tested, the higher level of porosity is causing the splats to be dislocated from the coating by the erodent, as well as being plastically deformed. This demonstrates a combination of brittle and ductile failure mechanisms.

The cross-sections of the eroded coatings are shown in Figure 74. Minimal sub-surface damage can be seen in any of the coatings after erosion, regardless of porosity or CMAS exposure.

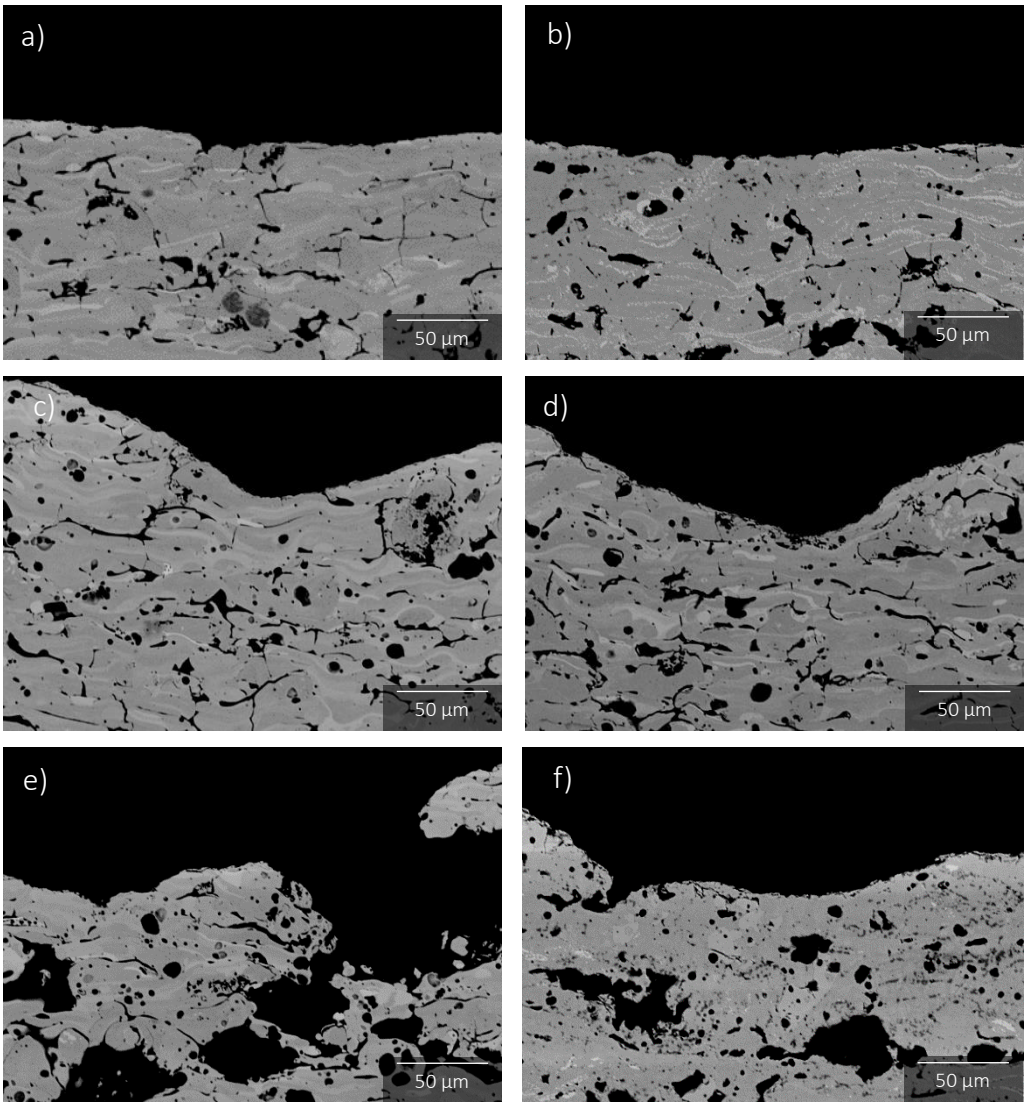

Figure 74. BSE SEM images of heat-treated and 100 hrs CMAS exposed coating cross-sections respectively for ABR (a & b), 1.5 % PE (c & d) and 4.5 % PE (e & f) after erosion.

6.4. Discussion

6.4.1. CMAS infiltration and corrosion mechanisms

Corrosion of abradable EBCs appears to be driven by the dissolution of YbDS and reprecipitation of YbDS and Yb-apatite. It has been suggested that the formation of the Yb-apatite phase, is a potentially beneficial in EBCs, acting as a barrier to further infiltration of corrosive species [134]. This occurs, in part, due to the availability of CaO in the CMAS melt to form the Yb-apatite phase [119, 135]. Here a CMAS with a Ca:Si ratio of 0.73 was used. Previous work by Stokes, et al. [119], has shown that sintered YbDS pellets readily formed Yb-apatite after exposure at 1300 °C to a CMAS with a Ca:Si ratio of 0.635, while at lower ratios no apatite was detected. In this study, while some Yb-apatite was formed, it was certainly not enough to form a protective surface layer, which could prevent further CMAS ingress, which when enough CaO is present in the melt, has been shown to be possible. Work using a similar CMAS composition to this study, found that a YbDS coating would form an Yb-apatite reaction layer at the CMAS infiltration front; however, this EBC contained a sizeable amount of YbMS phase (although, no exact phase composition was provided) and exhibited significantly less porosity than the abradable coatings examined in this study [126].

Another key driver for the corrosion of abradable EBCS by molten CMAS is the presence of YbMS in the coating. Unlike sintered bodies, in APS coatings, the presence of YbMS due to SiO_2 volatilisation during the deposition process is largely unavoidable. YbMS exhibits increased reactivity with CMAS relative to YbDS and will readily form Yb-apatite [118, 123]. It is widely accepted that this is, at least in part, due to the optical basicity difference between YbMS and the CMAS which is greater than that of YbDS and CMAS, explained by the Lewis acid-base theory. The optical basicity is calculated from the number of oxygen cations contributed to the system by the individual oxides and the optical basicity of the individual oxide [118, 123]. For YbDS, YbMS and the CMAS used in this study, the optical basicity's were 0.66, 0.73 and 0.61, respectively. The difference between the values is greater for YbMS and CMAS (0.12) than it is for YbDS and CMAS (0.05), indicating that the YbMS will react preferentially. It has been proposed that a certain degree of YbMS in an EBC composition would be beneficial for this reason, as the reaction products could potentially form a physical barrier to further CMAS infiltration [134]. While Yb-apatite was formed, it

did not prevent CMAS infiltration for any of the coatings in this work. Zhao, et al. [125] observed that in APS YbDS coatings, Yb-apatite would form precipitate preferentially at silica depleted YbMS splats. Some evidence of this mechanism was observed after 100 hrs CMAS exposure in this study. In Figure 65, Yb-apatite seems to be forming at sites of YbMS rich splats.

In this study, Figure 67 demonstrates that the overall porosity level does not impact the CMAS penetration depth as much as would be expected. This study has shown that CMAS infiltration depth was primarily driven by exposure time, rather than the level of porosity, instrumental in the study of abradable coatings. While in sintered bodies and dense EBCs, grain boundary infiltration is the dominant mechanism [121]; however, the inherent porosity in plasma sprayed coatings (especially abradable coatings) appears to change this. In porous coatings, it appears that CMAS infiltrates through porosity networks comprising primarily of inter-splat pores, similar to the mechanism proposed by Tejero-Martin, et al. [59]. For CMAS infiltration, the form the porosity takes appears to be pivotal. It is proposed that CMAS infiltrates primarily through open surface porosity and then internal inter-splat pore networks. Dissolution of the material surrounding these inter-splat channels occurs as the CMAS melt infiltrates, forming reprecipitated YbDS and Yb-apatite, and filling the inter-splat networks. As these phases precipitate and coarsen, they leave behind porosity with a different morphology. Using image analysis software and various geometric filters, it was possible to isolate these inter-splat pores and track the change in their fraction of overall porosity as the CMAS infiltration progressed. Reaction products filled the inter-splat porosity, reducing its contribution to the overall porosity level, as can be seen in Figure 68. The three coatings show similar levels of inter-splat pore reduction at each exposure time, further indicating that the overall porosity level has not contributed to the CMAS infiltration significantly. A schematic demonstrating the infiltration of molten CMAS into an abradable EBC with and without pore former addition, and the subsequent changes in microstructure with time is shown in Figure 75. Failure of the EBC system, either via through thickness cracking or between the various layers has also been observed after CMAS exposure [96, 132]. No such delamination was observed under any circumstances in this study. This could indicate that EBCs with increased levels of porosity are better equipped to accommodate

the volumetric changes associated with the formation of the various reaction products attributed to CMAS corrosion of EBCs.

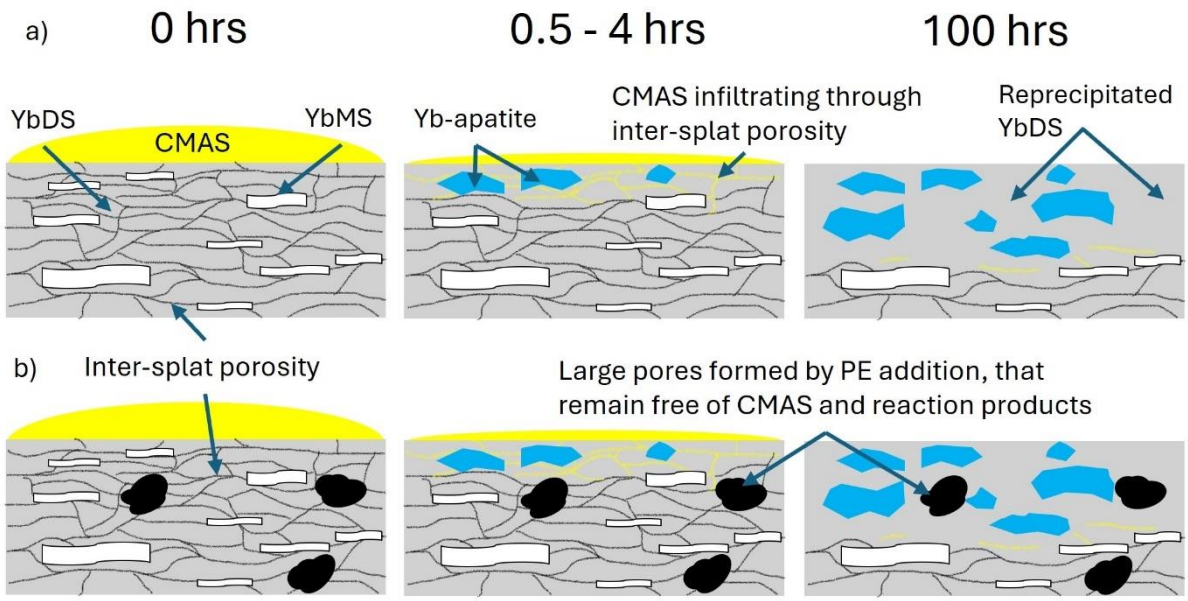

Figure 75. Schematic showing the infiltration of molten CMAS, and the phases formed due to the corrosion process in an abradable EBC a) with and b) without pore former addition.

6.4.2. Effect on mechanical properties on CMAS infiltrated coatings

While the effects of CMAS corrosion on EBCs have been studied widely, in terms of chemical and microstructural changes, how CMAS interaction affects mechanical properties is still relatively unknown. This is of particular importance for abradable coatings where the mechanical and tribological performance is key. From Figure 71, the profound effect CMAS exposure has on the erosion resistance of the abradable coatings can be observed. To establish a baseline, heat-treated coatings were subjected to the same erosion test. As the porosity level was increased, erosion resistance decreased and the erosion rate increased, in agreement with previous works on ceramic abradable coatings [47]. The literature suggests that increasing the porosity level in an abradable coating decreases the energy needed to dislodge material from it, consequently heightening its susceptibility to erosion [55]. Previous work has shown that increased porosity led to reduced hardness, reduced erosion resistance and reduced forces when subjected to cutting (hence easier material removal) by an abradable rig test designed to simulate the interaction between abradable coatings and a turbine [179].

Relative to the heat-treated coatings, after CMAS exposure, all the coatings show an increase in erosion resistance. Interestingly, the level of porosity in the 100 hr CMAS exposed samples increased versus the heat-treated samples they were compared to. The heat-treated coatings show porosity levels of 8, 15 and 22 % for the ABR, 1.5 and 4.5 wt.% PE coatings, respectively. After CMAS exposure, the porosity was measured using a similar process (image magnification, threshold level etc.) in the 200 µm closest to the surface (where complete CMAS infiltration, reaction and reprecipitation has occurred), which would be eroded initially. This region saw an increase in the overall porosity level to 9.9 ± 0.6, 18.8 ± 1.7 and 30.0 ± 1.6 % for the respective coatings. Despite this increase in porosity, the CMAS exposed coatings still demonstrated improved erosion resistance, relative to the heat-treated counterparts. This demonstrates that either the morphology changes of the YbDS phase from the APS splat structure to precipitated crystals (and the associated change in porosity morphology) or the presence of Yb-apatite is promoting the increase in erosion resistance. This is compatible with previous work on combined CMAS and erosion testing on EBCs by Stokes et al. [130, 131]. Whereby less porous EBCs were exposed to various fluxes of CMAS, for various time periods and then subjected to a hot erosion test where the alumina erodent had an incident angle of 90°. Despite the differences in experimental setup, similar conclusions were drawn, namely that exposure to CMAS improves the erosion resistance of EBCs. In the work by Stokes et al. it was demonstrated that Yb-apatite actually has a lower hardness, elastic modulus and fracture toughness that that of YbDS [131]. Three theories can then be put forward as to why the CMAS exposed samples exhibit a greater resistance to erosion, even given the reduced mechanical properties of the Yb-apatite phase. Firstly, the recrystallised YbDS an Yb-apatite may exhibit smaller grain sizes than that of the as-deposited coatings, leading to improved mechanical properties in the CMAS affected regions [181]. Secondly, as Yb-apatite is formed at high temperature, upon cooling, due to the differences in CTE between the YbDS and Yb-apatite (3.6-4.5 and 8.54 x10^{-6} °C respectively [81, 82, 182], a tensile stress field may form around the Yb-apatite crystals, slowing crack propagation, similar to strengthening mechanisms found in CMCs [183]. Finally, the residual CMAS may exhibit a strengthening effect, promoting bonding between the grains it has infiltrated.

The difference between the heat-treated and CMAS exposed surfaces before erosion can be observed clearly in Figure 72. The heat-treated coatings show a typical APS splat structure while this structure is eliminated after CMAS exposure due to the dissolution-precipitation mechanism. However, the eroded surfaces all look remarkably similar, indicating that despite differing rates of erosion, the mechanism remains the same regardless of porosity level or CMAS exposure. The heavily deformed surfaces in Figure 73 are indicative of ductile failure. Exposed splats at the centre of the erosion pit, as can be seen somewhat in Figure 73e, would show brittle failure whereby crack propagation leads to remove splats in their entirety as opposed to the ploughing/cutting that can be observed under ductile failure.

6.5. Conclusions

CMAS corrosion has proven to be a challenge in the design of EBCs, especially when considering the porous nature of abradable coatings. In this study, abradable coatings with three distinct porosity levels (8 %, 15 % and 22 % by area) were exposed to CMAS corrosion at 1300 °C for 0.5 hrs, 4 hrs and 100 hrs. Subsequently these coatings were subjected to an erosion test to test their abradability and ability to resist damage by foreign objects.

The overall porosity level did not appear to be the main driver for CMAS penetration depth, as all coatings showed similar measurements after each exposure time. Given this, it is believed that the molten CMAS infiltrates primarily through open surface porosity, into networks of inter-splat pores. These pores are then filled with reaction products. The large pores caused by PE addition play a minimal role in the CMAS infiltration and corrosion process. The main driver for CMAS penetration appears to be exposure time rather than coating porosity. Despite significant CMAS infiltration and interaction after 100 hrs, no signs of catastrophic failure were observed, and the coatings remained structurally sound.

After 100 hrs CMAS exposure, the erosion resistance of the coatings was investigated. For both the CMAS exposed and heat-treated coatings, the main erosion mechanism was ductile failure, regardless of porosity level. The erosion resistance of the coatings was found to increase with reduced porosity and after exposure to CMAS and all the phase and microstructural changes that entailed. While this is beneficial when considering foreign object damage, this could have repercussions during turbine blade incursion into the CMAS exposed abradable coatings, potentially leading to blade damage.

Acknowledgments

This work was supported by the Engineering and Physical Sciences Research Council (EPSRC) (grant number EP/V010093/1). The project also received funding from Rolls Royce Plc in terms of a CASE PhD studentship. The authors also acknowledge the use of facilities at the Nanoscale and Microscale Research Centre of the University of Nottingham, supported by the EPSRC (grant number EP/L022494/1). The use of the μ-VIS X-Ray Imaging Centre at The University of Southampton was also supported by the EPSRC (grant number EP/T02593X/1) and thanks is extended to Dr Fernando Alvarez Borges for conducting the scans. The authors would also like to extend thanks to Dr Craig Sturrock and John Kirk, both from the University of Nottingham who assisted with X-Ray CT data analysis and all aspects of the coating deposition process respectively.

Chapter 7: Abradable ytterbium disilicate environmental barrier coatings: A study of steam, CMAS and combined steam-CMAS corrosion

This chapter is reproduced from the paper:

A. Lynam, A. Rincon Romero, B. Zhang, E.B. Owusu, F. Xu, G. Pattinson, G.J. Brewster and T. Hussain, Abradable ytterbium disilicate environmental barrier coatings: A study of steam, CMAS and combined steam-CMAS corrosion. Manuscript submitted for publication.

Abstract

As efficiency gains are sought within gas turbines through ceramic matrix composites (CMCs), abradable environmental barrier coatings (EBCs) can be used to realise these. The aim of this study was to better understand how abradable coatings perform when exposed to steam, molten calcium magnesium alumino-silicates (CMAS) and combined steam and CMAS. In this study, three ytterbium disilicate ($Yb_2Si_2O_7$ or YbDS) abradable EBCs containing 8, 15 and 22 % porosity by area were deposited using atmospheric plasma spraying. These coatings were then exposed to steam, CMAS (35 CaO – 10 MgO – 7 Al_2O_3 – 48 SiO_2 mol. %) and combined steam and CMAS at 1350 °C for 100 hrs. The results show that increasing the overall level of porosity had minimal impact on the degree of steam or CMAS interaction. Exposure to steam caused the formation of a thin ytterbium monosilicate (Yb_2SiO_5 or YbMS) reaction layer. Reaction with the CMAS occurred by a dissolution-precipitation mechanism, with a reprecipitated ytterbium disilicate phase and Yb-apatite ($Ca_2Yb_8(SiO_4)_6O_2$) crystals noted as the only reaction products. After the combined exposure, the CMAS infiltration depth was higher than that observed in the standalone CMAS exposure. Also, an increased amount of Yb-apatite formation was observed within with YbMS reaction layer, and an ytterbium aluminium garnet ($Yb_3Al_5O_{12}$ or YbAG) phase was also observed.

7.1. Introduction

Silicon carbide ceramic matrix composite (SiC CMC) components are becoming widely used in in-service gas turbine engines [7]. SiC CMCs used in hot section components show significant benefits relative to nickel based superalloys which are currently widely employed within aero engines, in particular SiC CMCs exhibit better high temperature properties and reduced density [2]. The ability of hot-section components to be able to withstand higher temperatures is vital as efficiency increases are sought within the turbine. Despite the obvious benefits, the widespread use of SiC CMCs is not without challenges, the primary concern being the recession of the SiC by steam corrosion. While in the presence of air at high temperature, SiC will form a protective SiO_2 scale; however, if water vapour (a combustion product found in the gas turbine) is introduced into the environment, this will react with SiO_2, leading to recession of the ceramic, as per Equation 1 [72].

$$SiO_2 + 2H_2O\ (g) \rightarrow Si(OH)_4\ (g) \quad \text{(Equation 1)}$$

Under typical turbine operating conditions, it has been estimated that recession could be as high as 1 µm/h [73, 74], to combat this, protective environmental barrier coatings (EBCs) have been developed. In terms of EBC materials, ytterbium disilicate (YbDS) is currently state-of-the-art. YbDS exhibits phase stability at high temperatures and has a coefficient of thermal expansion (CTE) similar to that of SiC (4.1 x10^{-6} K^{-1}, measured over a range of 303–1873 K), both crucial for coating longevity given the cyclic, high temperature environment it operates in [4]. Several studies have investigated the effects of high temperature steam corrosion on YbDS, both sintered pellets [98-100] and plasma sprayed coatings [60, 96, 101-105, 184]. Typically, in the presence of high temperature water vapour, YbDS will form a gaseous silicon hydroxide, leaving behind a porous ytterbium monsilicate (YbMS) scale, as shown in Equation 2.

$$Yb_2Si_2O_7 + 2H_2O\ (g) \rightarrow Yb_2SiO_5 + Si(OH)_4\ (g) \quad \text{(Equation 2)}$$

Despite undergoing a similar corrosion process, the recession rates of YbDS are much lower than SiC, and the remaining YbMS layer offers a further level of protection. Instead of YbMS formation under high temperature water vapour exposure, some researchers have reported YbDS enrichment of the surface [60, 105]. Typically, YbDS EBCs are applied by atmospheric plasma spraying (APS); however, this leads to some silica volatilisation, leading to a mixed

Yb-silicate phase composition. It is this YbMS, formed during the deposition process, which is depleted during high temperature water vapour exposure typically forming ytterbium aluminium garnet ($Yb_3Al_5O_{12}$ or YbAG), leaving behind a YbDS rich surface layer. This mechanism has tentatively been attributed to alumina impurities present, usually occurring from the furnace tubes used for the steam exposure test [60, 105].

As well as steam corrosion, EBCs are also susceptible to corrosion by ash and sand that is ingested into the turbine. Molten combinations of CaO, MgO, Al_2O_3 and SiO_2, commonly labelled CMAS, adhere to the EBC surface, dissolving the Yb-silicates into the melt pool [122]. Depending on the YbMS content, and the CaO content of the molten CMAS, a ytterbium oxyapatite ($Ca_2Yb_8(SiO_4)_6O_2$ labelled Yb-apatite henceforth) phase will precipitate along with the reprecipitation of the Yb-silicates [118, 123, 126]. In some cases, the formation of a dense Yb-apatite layer has shown to have protective qualities, preventing further infiltration of the molten CMAS [126, 134].

While EBCs typically exhibit low levels of porosity, to form a hermetic seal protecting CMC components, highly porous abradable EBCs are also of interest when it comes to increasing efficiencies in gas turbines. Abradable coatings are applied to casings and designed in such a way that they can easily be worn away by rotating components (such as blades and fins). This creates a seal between the two components, as opposed to a typical larger clearance, increasing efficiency and reducing fuel consumption [16]. It has been estimated that a 0.1 % reduction in specific fuel consumption can be realised by just a 25 µm reduction in blade-tip clearance in a high-pressure turbine [17]. While abradable coatings have been employed throughout various sections of gas turbine engines for decades, the published literature regarding such coatings within the hot section is limited.

Since abradable EBCs are porous by design, this makes corrosion by steam and CMAS potentially a much bigger problem. Tejero Martin, et al. [59] showed that abradable EBCs were completely infiltrated with CMAS after 48 hrs exposure, while steam exposure formed a YbDS rich surface layer, although with minimal differences were detected between an EBC and an abradable EBC [59]. While much research into the corrosion of YbDS EBCs has focused on either isothermal CMAS or steam exposure, what is of more interest is how combined degradation mechanisms interact and their subsequent effects on the coating. Harder et al. [129] found that in the presence of CMAS and steam, thermally grown oxide

(TGO) growth could be suppressed, potentially indicating synergies when EBCs are exposed to simultaneous corrosion mechanisms. Given this, abradable EBCs, with three porosity levels, were subjected to steam, CMAS and combined steam and CMAS exposure at 1350 °C for 100 hrs. With the aims of understanding how steam, CMAS and combined steam and CMAS exposure affect abradable EBCs and to understand the changes these induce in terms of phase composition and microstructure.

7.2. Materials and methods

7.2.1. Coating deposition

Free standing abradable EBCs were deposited using atmospheric plasma spraying. Metco 6157 YbDS powder (Oerlikon Metco AG, Switzerland), with a nominal size distribution of 15-75 µm, containing < 5 vol. % of unreacted Yb_2O_3 and YbMS, was mixed with a polyester (PE) powder, Metco 600NS (Oerlikon Metco AG, Switzerland) which acted as a pore former. The PE was a crystalline aromatic polymer powder with a nominal size range between 45-125 µm. The YbDS and PE mixture was homogenised with a Labram acoustic mixer (Resodyn Acoustic Mixers, USA) at an acceleration of 10 g for 10 mins. Three feedstocks were created for deposition; ABR (which contained no PE powder), 1.5 wt. % PE and 4.5 wt.% PE.

Graphite substrates (GPE Scientific Ltd., UK), 60 mm x 20 mm x 5 mm thickness, were used to create the free-standing coatings. Prior to deposition, the graphite plates were grit blasted using a blast cleaner (Guyson, UK) with Al_2O_3 (100 mesh) particles (Guyson, UK) at a pressure of 1 bar. Following surface preparation, the substrates were cleaned using compressed air.

For the coating deposition process, an SG-100 plasma spray system (Praxair Surface Technology, USA) was used. The torch was fitted with a 02083-175 anode, 02083-120 cathode and a 03083-112 gas injector. Ar and H_2 were used as the primary and secondary gases, respectively. The 3 abradable EBCs were deposited using a spray power of 12 kW, a current of 600 A, primary gas (Ar) pressure of 85 psi (equivalent to a flow rate of 75 SLM), a secondary gas (H_2) pressure of 35 psi (2.5 SLM), a stand-off distance of 125 mm, and the robot speed was 1000 mm/s over 30 passes. Further details about the optimisation of these parameters can be found in previous works [165].

The as sprayed coatings were heat treated at 550 °C for 3.5 hrs with a heating rate of 5 °C/min to burn off the graphite substrates and any remaining organic material in the PE containing coatings. As the phase content of the as-sprayed coatings was highly amorphous, a crystallisation heat treatment was then performed at 1200 °C for 2 hrs, with heating and cooling rates of 5 °C/min in air. Both treatments were performed in a box furnace (Elite Thermal Systems Ltd., UK).

7.2.2. Steam exposure

To examine the effects of steam exposure on the abradable EBCs an isothermal steam test was conducted. A steam rig consisting of two interconnected tube furnaces (Elite Thermal Systems Ltd., UK), mass flow controller (Omega Engineering Inc, UK), 120S peristaltic pump (Watson-Marlow Ltd., UK) and co-axial zirconia tubes (Almath Crucibles Ltd., UK) was employed for the testing. The first furnace was used to produce the steam by boiling deionised water and was set to 400 °C. The second furnace was used to heat the abradable EBCs to 1350 °C at a rate of 2.5 °C/min. The other end of the furnace was kept open to maintain atmospheric pressure. The steam and compressed air flow created an atmosphere of 90 vol.% H_2O/10 vol.% air with a gas velocity of 1 m/s. The use of the zirconia tubes throughout the furnace prevented any alumina contamination which would promote YbAG formation within the coatings. The test ran for 96 hrs and then the furnace cooled to room temperature at a rate of 2.5 °C/min.

7.2.3. CMAS exposure

CMAS powder with a nominal composition of 35 CaO – 10 MgO – 7 Al_2O_3 – 48 SiO_2 mol. % (Oerlikon Metco AG, Switzerland) was used in this study, giving a Ca:Si ratio of 0.73. The CMAS powder was mixed with deionised water at a 1:9 ratio by weight and mixed using a magnetic stirrer to ensure homogeneity. The CMAS slurry was applied via an airbrush to YbDS free-standing coatings, which had been placed on a hotplate at ~100 °C to promote the evaporation of water from the CMAS slurry. The process of applying a layer of CMAS slurry and drying was repeated until a mass representing a 5 mg/cm^2 concentration had been applied to the surface of the samples. The CMAS-coated samples were heated to 1300 °C at 10 °C/min in a box furnace (Elite Thermal Systems, Uk) and held for 4 hrs. Subsequently the samples were heated to 1350 °C at 10 °C/min and held for 96 hrs before cooling to room

temperature at 10 °C/min. This profile was used to match that used in the combined steam and CMAS test described subsequently.

7.2.4. Combined steam and CMAS exposure

The combined effects of steam and CMAS were investigated by firstly applying CMAS slurry to the free-standing coatings, at a concentration of 5 mg/cm^2, as per the method described previously. The CMAS-coated samples were heated to 1300 °C at 10 °C/min and held for 4 hrs. This melted the CMAS powder and allowed it to infiltrate the coatings, meaning that no residual glassy layer remained on the surface of the coating, protecting it from the effects of steam exposure. The CMAS exposed samples were then subjected to the steam test as described in section 2.2., using similar zirconia tubes, an atmosphere of 90 vol.% H_2O/10 vol.% air with a gas velocity of 1 m/s, a 96 hr dwell at 1350 °C, with a heating and cooling rate of 2.5 °C/min.

7.2.5. Sample preparation and characterisation

Tested samples were vacuum impregnated with EpoFix resin and hardener (15:2 volumetric ratio) (Struers, Denmark), sectioned using a Qcut 200 precision cutting machine (Metprep, UK) using abrasive SiC cut-off wheels (Metprep, UK) with a cutting speed of 0.025 mm/s and the sections subsequently cold-mounted, again using Epofix resin and hardener (Struers, Denmark). The mounted samples were then ground using P240, P400, P800 and P1200 SiC grinding papers (Metprep, UK). Finally, the ground samples were polished using diamond paste (Struers, Denmark) to a surface finish of 6 µm and then 1 µm.

Mounted samples were characterised using a FEI XL30 scanning electron microscope (SEM) (Phillips FEI, Netherlands) operated in secondary electron (SE) and backscattered electron (BSE) modes, using an accelerating voltage of 20 kV, spot size of 5 nm and working distance of 10 mm. The SEM was equipped with energy-dispersive x-ray spectroscopy (EDX) (Oxford Instruments, UK) to perform elemental analysis. Electron backscatter diffraction (EBSD) analysis was conducted using a JEOL 7100F field emission gun SEM (JEOL, Japan) using a spot size of 4 and a working distance of 10 mm. The SEM was equipped with energy dispersive X-ray spectroscopy (EDS, X-max 150, Oxford Instruments, UK) and electron backscatter diffraction (Oxford Instruments, UK) detectors. To understand the phase composition of the CMAS exposed coatings, EBSD was used with an accelerating voltage of

15 kV on the ~ 70° tiled specimen. EBSD data acquisition was performed at a step size of 0.0285 µm. Crystallographic information files (CIF) of monoclinic YbDS (C2/m, 00-025-1345), monoclinic YbMS (I2/a, 00-40-0386), hexagonal $Ca_2Yb_8(SiO_4)_6O_2$ oxyapatite (Yb-apatite) (P63/m, 04-006-0320) and cubic ytterbium aluminium garnet (YbAG) (Ia-3d, 00-023-1476) were used to identify the suspected phases present in the CMAS exposed coatings. AZtec Crystal (Oxford Instruments, UK) was used to analyse the EBSD data.

Analysis of the phase content of the heat treated and CMAS exposed samples was conducted by XRD using a D8 Advance (Bruker, UK) from 10 to 80° 2θ, using Cu Kα radiation (0.154 nm wavelength), a 0.02° step size and 0.2 s per step using Bragg-Brentano geometry. Phase identification in the coatings was completed using EVA software (Bruker, UK) supported by data from the PDF-4 database (ICDD-PDF).

7.3. Results

7.3.1. Steam exposure

The diffractograms of the coatings after 96 hrs steam exposure are shown in Figure 76. The results show a combination of monoclinic YbDS (C2/m, 00-025-1345) and monoclinic YbMS (I2/a, 00-40-0386) phases in all the coatings; however, the ratio of these phases changed drastically after steam exposure. After the initial crystallisation heat treatment, Rietveld refinement was employed to calculate the phase composition of each coating. For all coatings, this was found to be 87 wt. % YbDS and 13 wt. % YbMS [165]. After steam exposure, the same technique was used, this time finding the ratio to be 10 wt. % YbDS and 90 wt. % YbMS. This can also be inferred from the diffractograms in Figure 76. The highest intensity peaks are YbMS peak at ~23° 2θ and the four YbMS peaks between ~28° and ~31° 2θ, while even the characteristic YbDS peak has a much lower intensity. This indicates that silica loss, per the reaction in Equation 2, is occurring in these coatings (at least in the surface region, as x-rays will penetrate the top ~25 µm of coating). While some researchers have reported at YbDS enrichment in the surface layer after steam exposure [96, 98-104], many have also reported silica depletion and an increase in YbMS [60, 105].

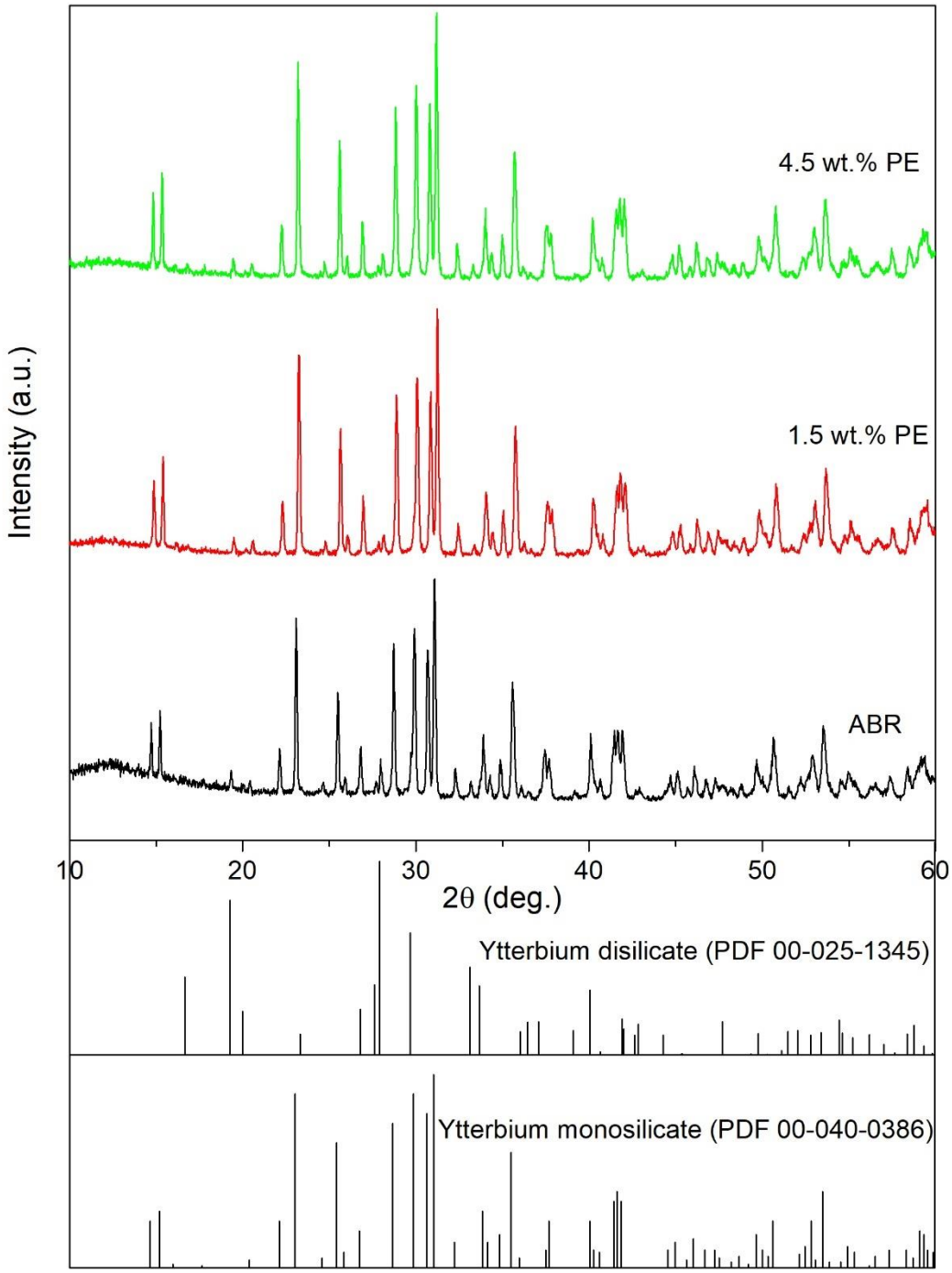

Figure 76. XRDs of coatings exposed to steam at 1350 °C for 96 hrs. All coatings show a change in phase composition from ~87 wt. % YbDS and ~13 wt. % YbMS after heat treatment to ~10 wt. % YbDS and ~90 wt. % YbMS after steam exposure (with the caveat that incident x-rays only penetrate to top ~20 µm of the coatings).

The surfaces of the coatings exposed to steam for 96 hrs can be observed in Figure 77. While the surface morphologies of all the coatings look similar and have retained a typical APS splat structure, some differences can be noted after steam exposure (the as-sprayed surfaces can be seen in previous works [179]). Firstly, small pinhole porosities can be observed, especially in the higher magnification images in Figure 77b, d and f. These are likely caused by the volatilisation of gaseous $Si(OH)_4$ due to the reaction of YbDS with the steam, per Equation 2. Another feature of note is the extensive crack networks, extending through and beyond individual splats. While some degree of microcracking is associated with as-sprayed APS coatings, this degree of cracking can plausibly be explained by the extensive phase transformation of YbDS to YbMS given in Equation 2, and its associated volume shrinkage, estimated to be 26 % [101, 102].

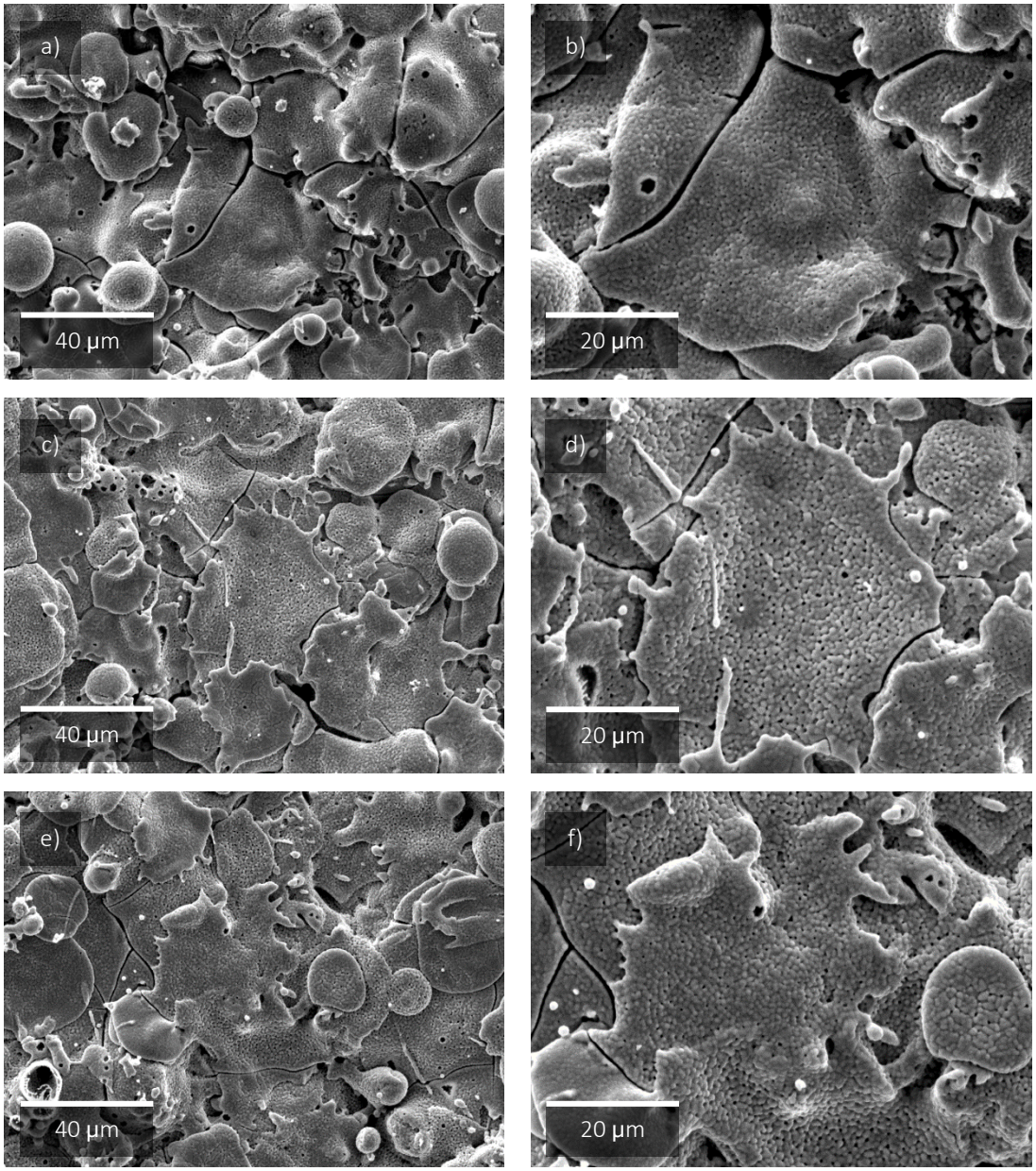

Figure 77. SE SEM images of the surfaces of the coatings after steam exposure at 1350 °C for 96 hrs. With a) and b) showing ABR (at a lower and higher magnification respectively), c) and d) showing 1.5 wt. % PE and e) and f) showing 4.5 wt. % PE. All the coating surfaces show microcracking and small pinhole-like pores within the splat structure.

Figure 78 shows the cross-sections of the coatings after 96 hrs steam exposure. Low magnification images of the entire coating cross-section are shown in Figure 78a, c and e. While higher magnification images of the near surface regions of the coatings are shown in Figure 78b, d and f. EDX spot analyses (1-9) are also shown Figure 78b, d and f, with the data (in at. %) and possible corresponding phases shown in Table 20. From the low magnification

images in Figure 78a, c and e, it can be observed that the bulk of the coating has remained unaffected by the steam exposure and retains its as-sprayed structure. Higher magnification images in Figure 78b, d and f, show a small reaction layer extending no more than 5-10 µm deep across the surface of all the coatings. This reaction layer features small pinhole pores, similar to those observed in Figure 77. The thickness of this reaction layer was measured using image analysis software, no difference in the mean layer thickness was observed as the porosity was increased, it was ~6 µm for all the coatings, this data is shown in Table 19. To confirm the phase composition of this reaction region, spot EDX analysis was conducted, these spots are shown in Figure 78b-3, d-6 and f-9 and Table 20. The relative amounts of Yb and Si detected in these spots indicate that the surface reaction region is made up of YbMS. This is backed up by Equation 2 and the XRD analysis shown Figure 76. The steam appears to be reacting with YbDS on the surface of the coatings and forming a YbMS rich reaction layer, which is only detected by XRD (given the x-ray penetration depth). Below this thin layer, the bulk of the coating remains unaffected by steam exposure. EDX analysis detected both YbDS (Figure 78b-1, d-4 and f-7) and YbMS (Figure 78b-2, d-5 and f-8).

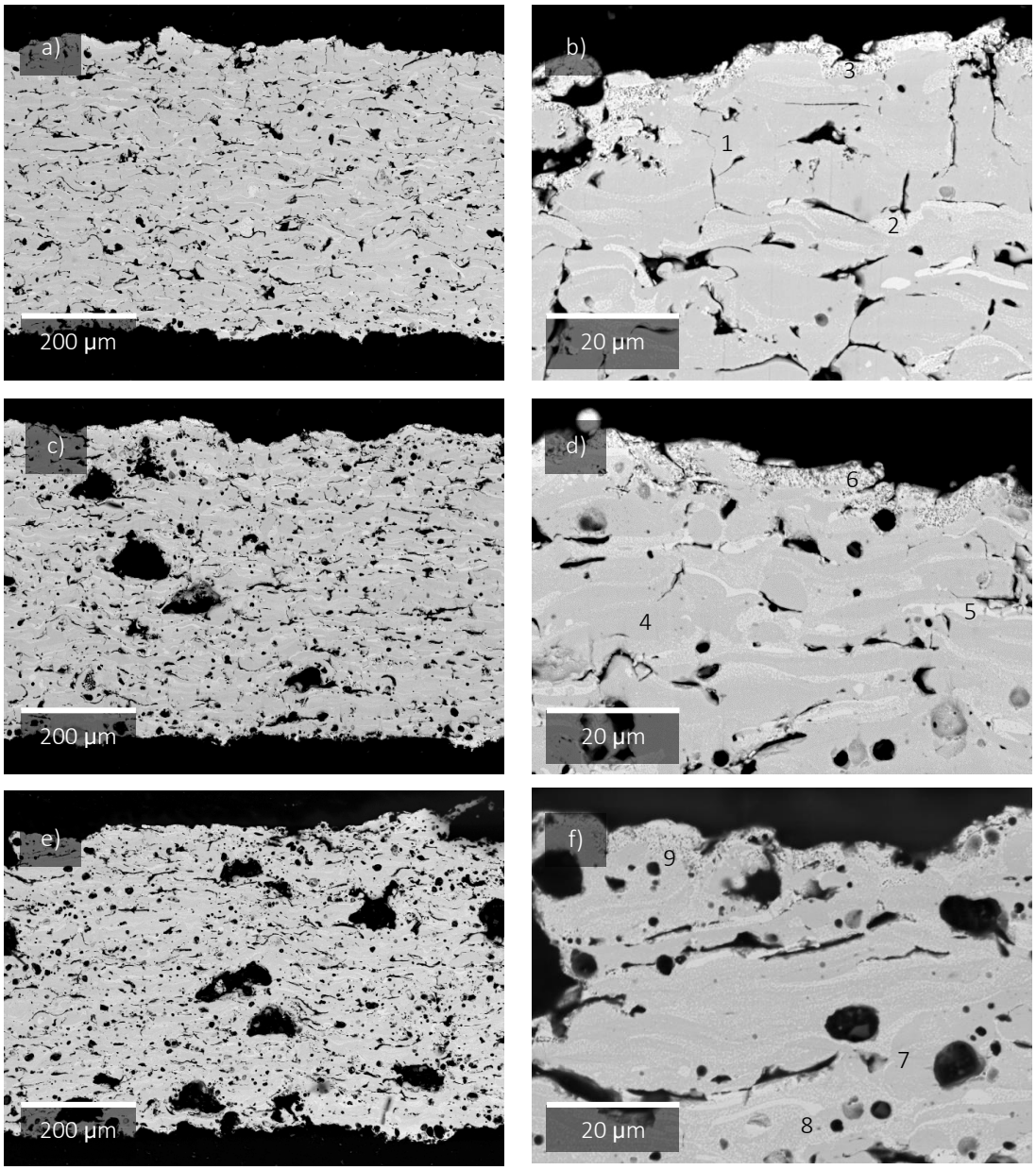

Figure 78. BSE SEM images of the cross-section of the coatings after steam exposure at 1350 °C for 96 hrs. With a) and b) showing ABR (at a lower and higher magnification of the near-surface region respectively), c) and d) showing 1.5 wt. % PE and e) and f) showing 4.5 wt. % PE. The numbers 1-9 correspond to spot EDX analysis shown in Table 20. All the coatings show a YbMS layer, a few microns thick, at the surface.

Table 19. YbMS reaction layer thicknesses measured in the coatings after steam exposure at 1350 °C for 96 hrs.

Coating	ABR	1.5 wt.% PE	4.5 wt.% PE
YbMS layer thickness (µm)	6.0 ± 4.2	6.3 ± 1.9	6.5 ± 2.4

Table 20. EDX spectra (in at. %) of the points shown in Figure 78, and the corresponding possible phase, based on the stoichiometry.

Spectrum label	Yb	Si	O	Possible phase
1	19.9	20.3	59.8	YbDS
2	23.4	15.8	60.8	YbMS
3	23.5	13.9	62.6	YbMS
4	21.2	20.2	58.6	YbDS
5	27.4	13.4	59.2	YbMS
6	22.1	13.5	64.4	YbMS
7	20.4	20.0	59.6	YbDS
8	27.0	14.3	58.7	YbMS
9	26.1	15.2	58.7	YbMS

7.3.2. CMAS exposure

7.3.2.1. 4 hrs CMAS exposure

The resultant diffractograms after the 4 hrs CMAS exposure are shown in Figure 79. For all the coatings, monoclinic YbDS (C2/m, 00-025-1345) were detected while no YbMS peaks were detected, indicating that at least in the near surface region where the x-rays penetrate, the CMAS has fully infiltrated. The reaction product was identified as hexagonal $Ca_2Yb_8(SiO_4)_6O_2$ oxyapatite (P63/m, 04-006-0320), small peaks can be identified at ~32° 2θ in all of the coatings, with intensity increasing as porosity level increases. The detection of YbDS and Yb-apatite only indicates that Ca and Si containing oxides react with the coating while the Mg and Al oxides remain in the melt pool. This reaction has previously been widely reported in literature [119, 125, 136].

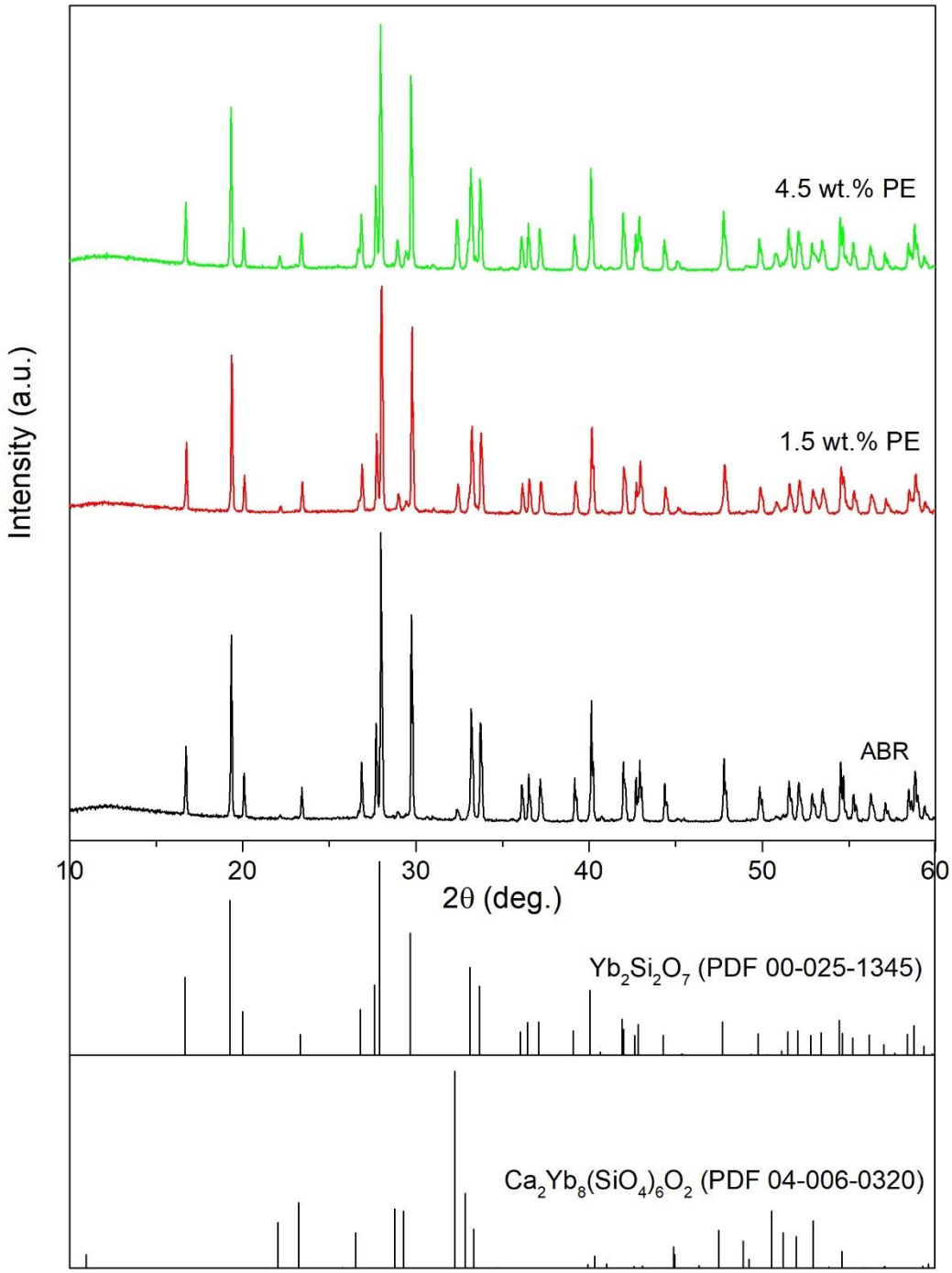

Figure 79. XRDs of coatings exposed to CMAS at 1300 °C for 4 hrs. In all the coatings, only two phases were detected: YbDS and Yb-apatite.

The surfaces of the coatings exposed to CMAS for 4 hrs can be observed in Figure 80. Unlike typical APS coatings, no splat structure is visible. This is due to the dissolution and reprecipitation of YbDS and the precipitation of Yb-apatite. All of the coatings exhibit similar surface morphologies, the long, acicular crystals are likely the Yb-apatite phase, while the

more rounded crystals are reprecipitated YbDS. Some residual glassy CMAS is visible in between the crystals, however, CMAS has for the most part infiltrated the coating.

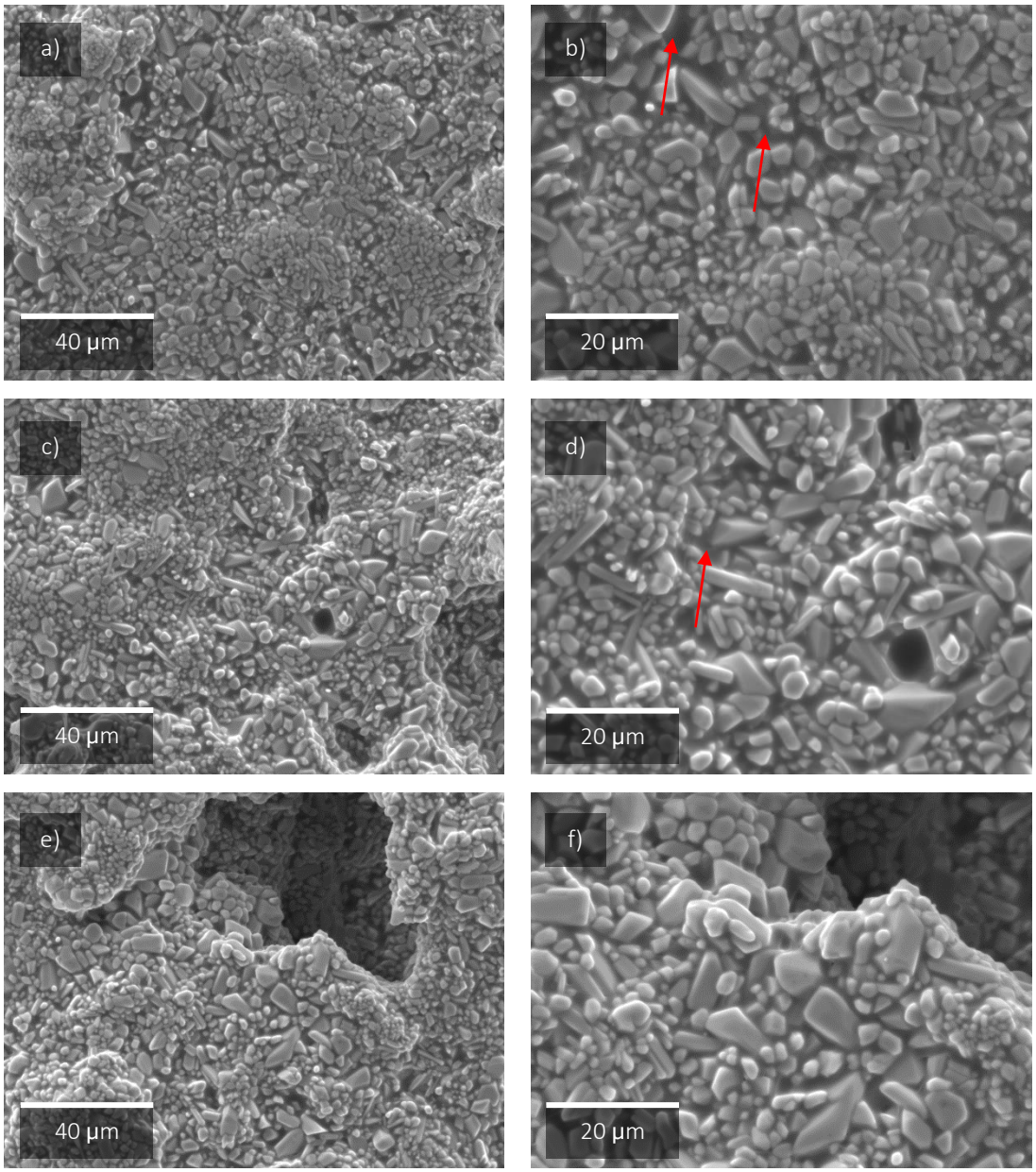

Figure 80. SE SEM images of coating surfaces exposed to CMAS at 1300 °C for 4 hrs. With a) and b) showing ABR (at a lower and higher magnification respectively), c) and d) showing 1.5 wt. % PE and e) and f) showing 4.5 wt. % PE. Some regions were residual CMAS can be observed are shown with red arrows.

Low magnification cross-sections of the three coatings after 4 hrs CMAS exposure at 1300 °C are shown in Figure 81, along with Ca (shown in blue) EDX map overlays. All three coatings show a region where CMAS has infiltrated and reacted near the surface and an unaffected

region towards the bottom of the coating. Near the surface, in the interaction region, residual CMAS, reaction products (namely Yb-apatite) and reprecipitated YbDS can be identified. The depth of CMAS infiltration was measured using image analysis software and was defined as the distance from the surface of the coating to the furthest Ca containing phase, either Yb-apatite or residual CMAS, this is shown in Table 21. From this data it can be observed that the overall porosity level in the coating has a minimal impact on the level of CMAS infiltration. Below this is a region that has remained free of any CMAS interaction, the original APS splat structure remains, and minimal Ca was detected. Interestingly, the large pores found in the 1.5 wt. % and 4.5 wt. % coatings remain free of CMAS or any reaction products.

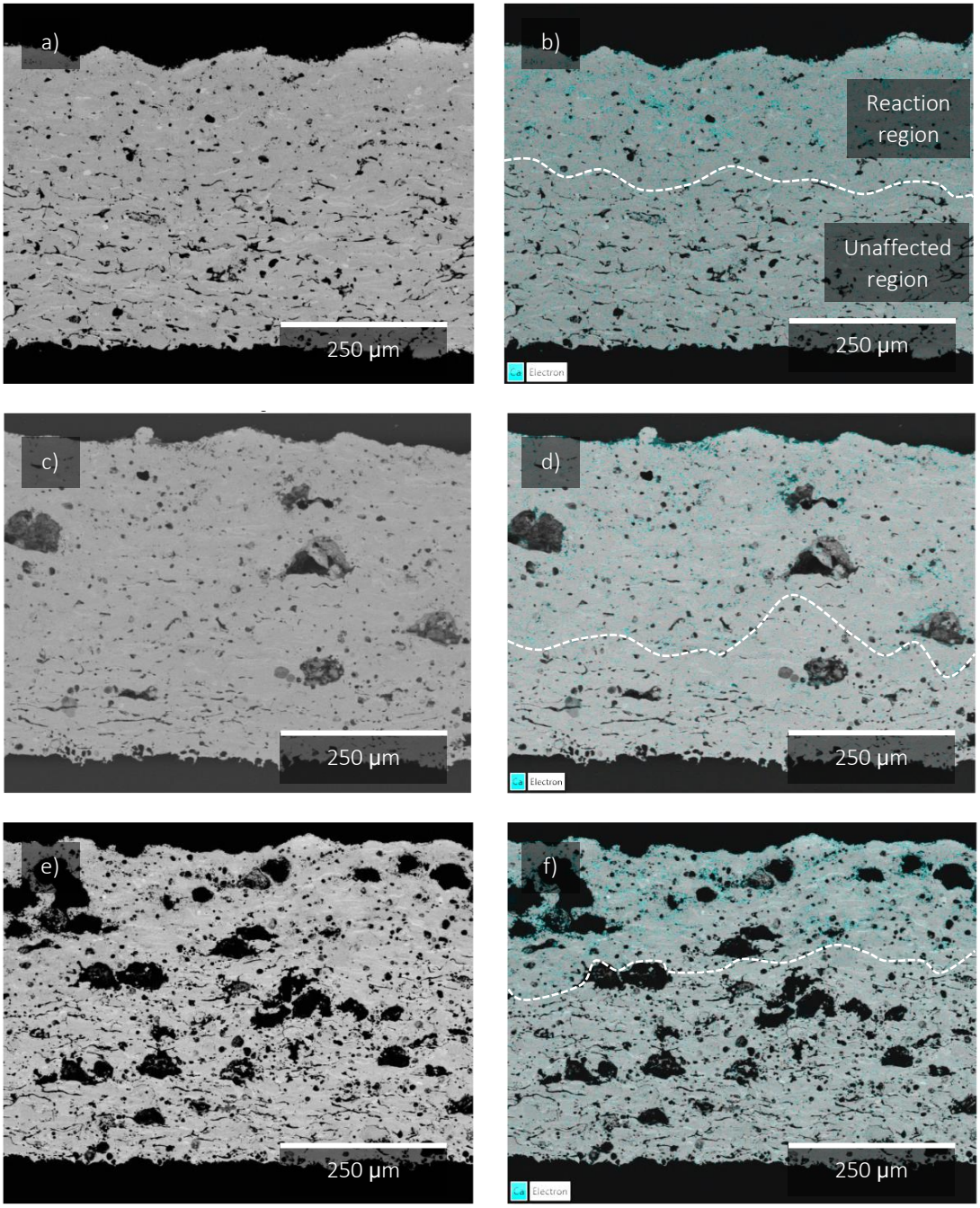

Figure 81. BSE SEM images of coating cross-sections exposed to CMAS at 1300 °C for 4 hrs. With a) and b) showing ABR (at a low magnification and with Ca elemental map overlay respectively), c) and d) showing 1.5 wt. % PE and e) and f) showing 4.5 wt. % PE. A rough delineation between the reaction and unaffected regions is shown on the images.

Table 21. CMAS infiltration depths measured in the coatings after exposure at 1300 °C for 4 hrs.

Coating	ABR	1.5 wt.% PE	4.5 wt.% PE
CMAS infiltration depth (µm)	190.2 ± 24.6	196.0 ± 89.1	176.2 ± 33.8

Higher magnification images of the near surface region of the coatings after 4 hrs CMAS exposure are shown in Figure 82. Features of interest were analysed using spot EDX analysis to obtain chemical composition information. These spots are labelled on Figure 82a, c and e and the corresponding values (in at. %) are shown in Table 22. Figure 82b, d and f show the higher magnification image but with a EDX Ca map overlay, to clearly show phases containing Ca.

All of the coatings exhibit similar features and phases, as can be seen from XRD data in Figure 79. Ca rich regions can be identified from Figure 82b, d and f, presenting as acicular crystals. Such phases are identified in Figure 82a-2, c-5 and e-9, and are rich in Yb, Si and O but also Ca (from Table 22), the stoichiometry likely corresponds to the Yb-apatite phase identified in XRD analysis. Smaller Ca containing phases, presenting as a darker grey than the bulk coating on the BSE images, can also be identified in Figure 82. From EDX spot analysis in Figure 82c-7 and e-11, these appear to be regions of residual CMAS glass due to the reduced amount of Yb relative to other phases and the presence of Al and Mg (referring to Table 22), which did not appear in any crystalline phases identified in XRD.

Further to the Ca containing phases, YbDS and YbMS were also identified based on the stoichiometry of the EDX spot analyses. Inferring from the XRD data in Figure 79, the majority of the microstructure is made up of YbDS. On the BSE images in Figure 82, this presents as the main dark grey regions. This was confirmed by EDX analysis in Figure 82a-1, c-4, and e-8 and the corresponding data in Table 22. Towards the surface of the coating, where CMAS interaction will have occurred, the YbDS morphology appears as reprecipitated crystals, as seen in Figure 80. While deeper into the coating, YbDS will retain the original APS splat structure. No YbMS was detected in the XRD data shown in Figure 79, however, small amounts are visible in the microstructures shown in Figure 82. Due to having a higher average atomic number than YbDS, YbMS presents as a light phase in the BSE images in

Figure 82. EDX spot analysis confirmed this, Figure 82a-3, c-6 and e-10 were identified as likely regions of YbMS, due to increased Yb and reduced Si at. %s relative to the possible YbDS phases, when consulting the data in Table 22.

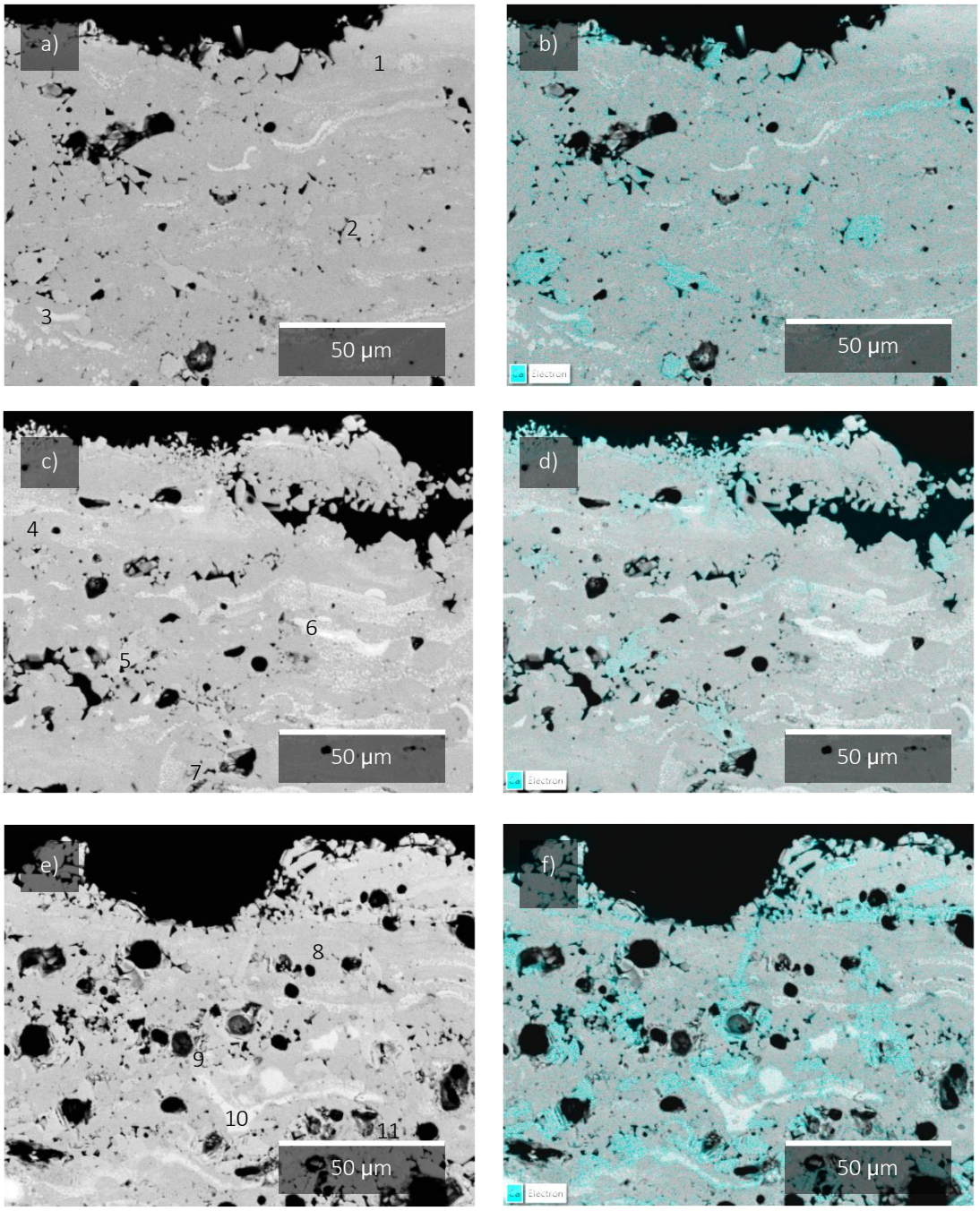

Figure 82. BSE SEM images of the near-surface region of the coating cross-sections exposed to CMAS at 1300 °C for 4 hrs. With a) and b) showing ABR (at a higher magnification and with Ca elemental map overlay respectively), c) and d) showing 1.5 wt. % PE and e) and f) showing 4.5 wt. % PE. The numbers 1-11 correspond to spot EDX analysis shown in Table 22.

Table 22. EDX spectra (in at. %) of the points shown in Figure 82, and the corresponding possible phase, based on the stoichiometry.

Spectrum label	Yb	Si	O	Ca	Mg	Al	Possible phase
1	21.0	19.8	59.2				YbDS
2	21.6	15.9	57.4	5.1			Yb-apatite
3	23.9	17.7	58.5				YbMS
4	20.0	19.8	60.1				YbDS
5	20.6	15.4	59.1	4.9			Yb-apatite
6	26.9	13.5	59.5				YbMS
7	17.8	17.0	61.8	1.5	1.8		CMAS
8	20.1	20.0	59.9				YbDS
9	20.6	15.7	59.3	4.3			Yb-apatite
10	27.8	13.5	58.7				YbMS
11	14.3	14.8	59.9	3.4	3.3	4.3	CMAS

7.3.2.2. 100 hrs CMAS exposure

To match the thermal profile of the combined steam and CMAS test, the coatings were subjected to CMAS exposure only, first for 4 hrs at 1300 °C and then for 96 hrs at 1350 °C. Diffractograms of the coatings after the 100 hrs CMAS exposure are shown in Figure 83. Similar to the 4 hrs exposure, after 100 hrs only monoclinic YbDS (C2/m, 00-025-1345) and hexagonal Yb-apatite (P63/m, 04-006-0320) were detected.

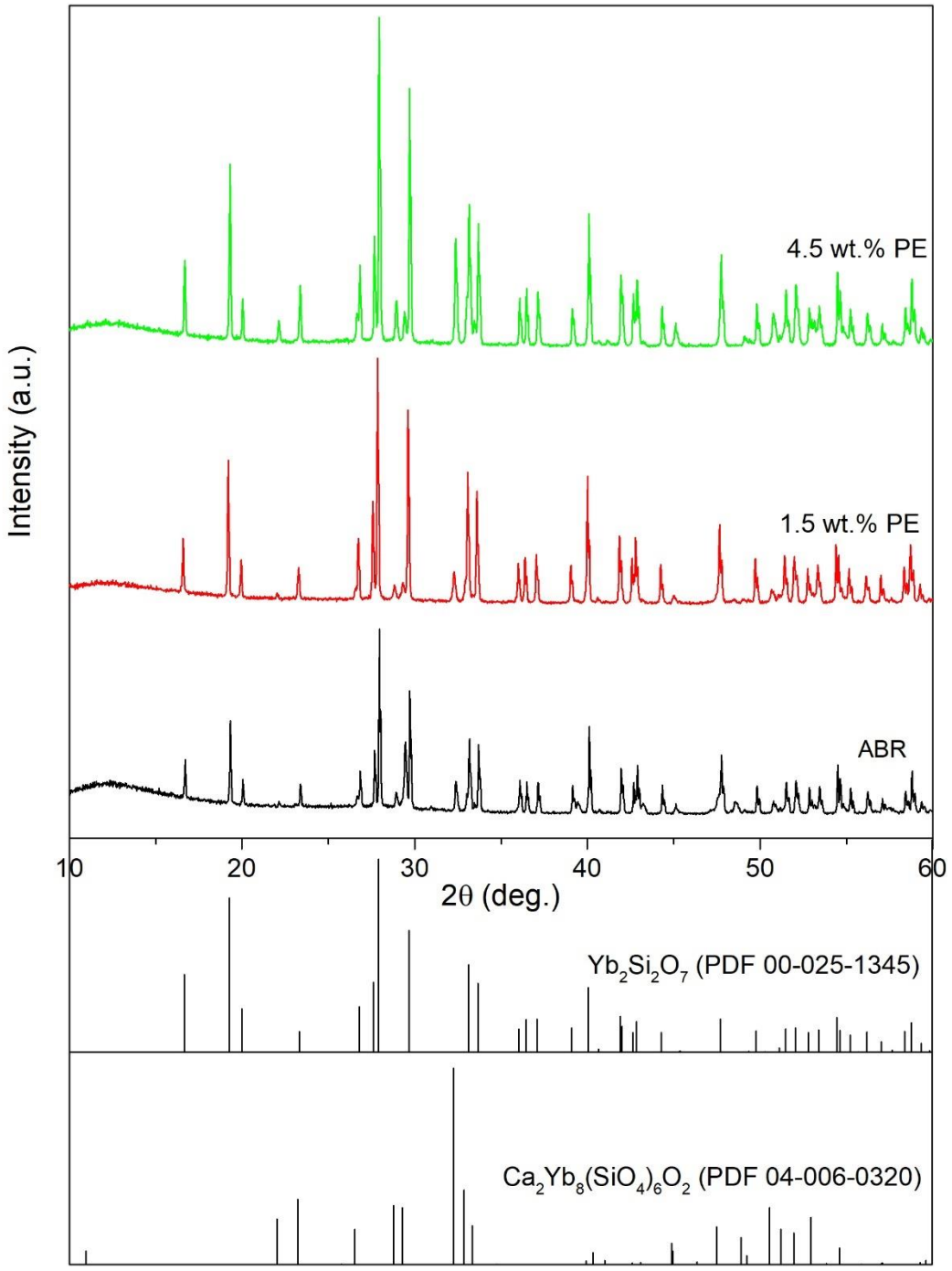

Figure 83. XRDs of coatings exposed to CMAS at 1300 °C for 4 hrs and then 1350 °C for 96 hrs. In all the coatings, only two phases were detected: YbDS and Yb-apatite.

The surfaces of the coatings after 100 hrs CMAS exposure are shown in Figure 84. All of the coatings exhibit a similar surface morphology, much the same as after 4 hrs CMAS exposure. Acicular Yb-apatite and reprecipitated YbDS crystals are visible. After 100 hrs the crystals appear coarser and no glassy CMAS is visible near the surface.

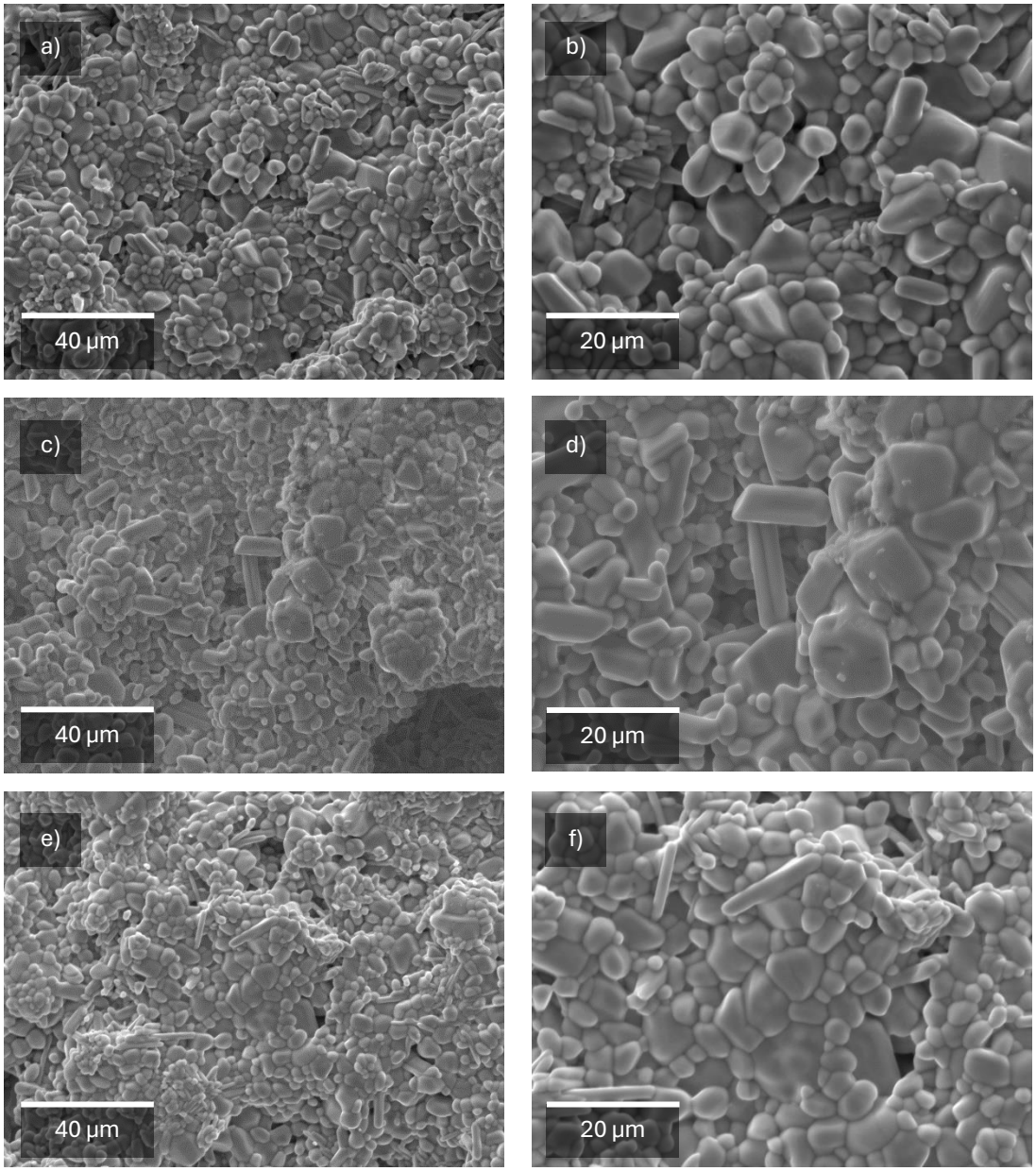

Figure 84. SE SEM images of coating surfaces exposed to CMAS at 1300 °C for 4 hrs and then 1350 °C for 96 hrs. With a) and b) showing ABR (at a lower and higher magnification respectively), c) and d) showing 1.5 wt. % PE and e) and f) showing 4.5 wt. % PE.

Low magnification BSE images of the coating cross-sections after 100 hrs CMAS exposure are shown in Figure 85a, c and e, while the same image with a Ca EDX map overlay is shown in Figure 85b, d and f. Similarly to the coatings exposed to CMAS for 4 hrs, Ca containing phases can be seen towards the surface of the coatings, however, even after 100 hrs, it appears that CMAS has not infiltrated the entire through thickness of any of the coatings (although the infiltration depth does appear to be higher than that after 4 hrs exposure).

The depth of CMAS infiltration in the coatings is shown in Table 23. The overall level of infiltration is slightly higher than after 4 hrs and again, high overall porosity did not lead to increased levels of CMAS infiltration. Notably, as with the 4 hrs exposure, no CMAS can be detected in the large pores caused by the addition of PE.

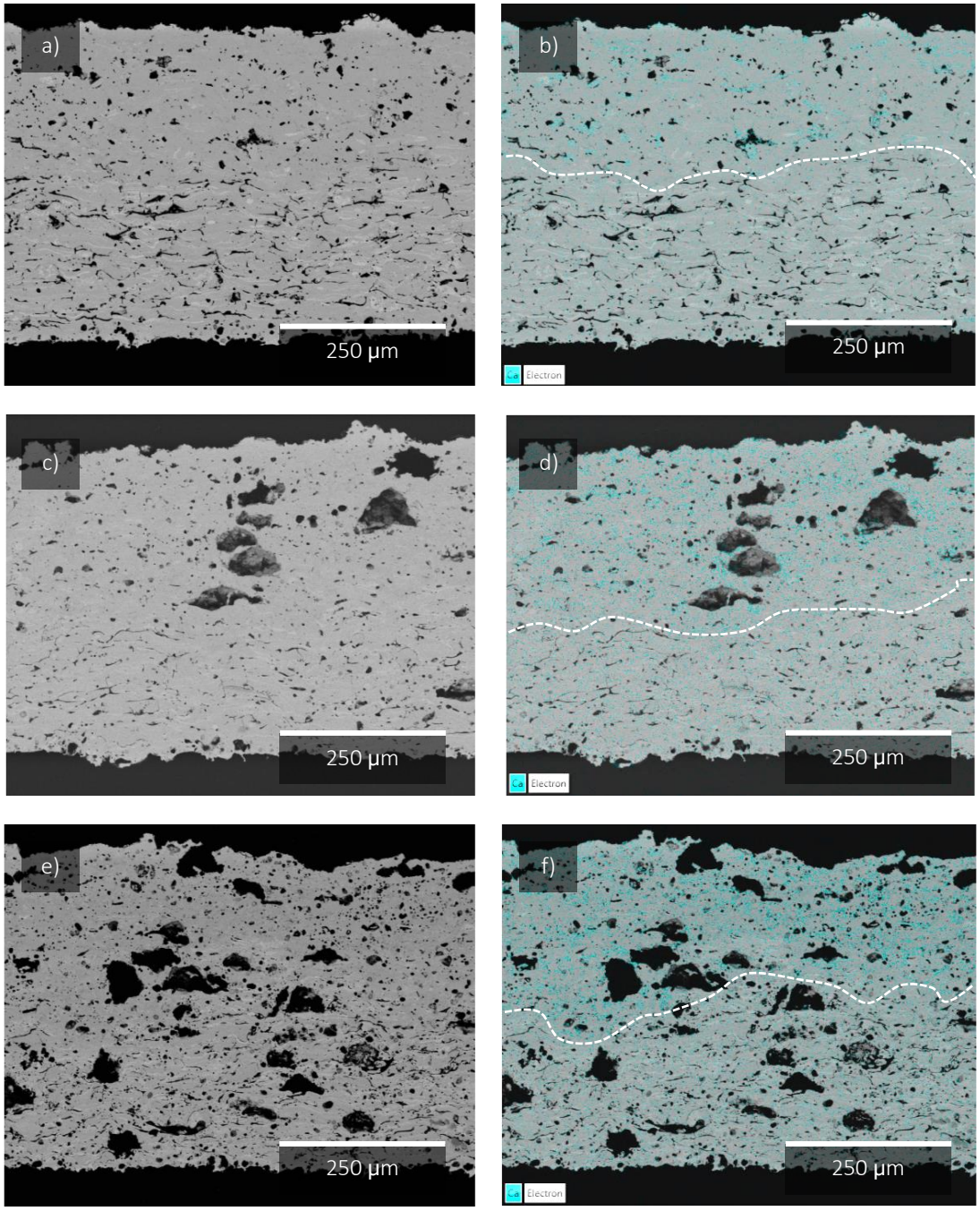

Figure 85. BSE SEM images of coating cross-sections exposed to CMAS at 1300 °C for 4 hrs and then 1350 °C for 96 hrs. With a) and b) showing ABR (at a low magnification and with Ca elemental map overlay respectively), c) and d) showing 1.5 wt. % PE and e) and f) showing 4.5 wt. % PE. A rough delineation between the reaction and unaffected regions is shown on the images.

Table 23. CMAS infiltration depths measured in the coatings after exposure at 1300 °C for 4 hrs and then 1350 °C for 96 hrs.

Coating	ABR	1.5 wt.% PE	4.5 wt.% PE
CMAS infiltration depth (µm)	200.8 ± 33.1	222.6 ± 34.9	224.6 ± 40.8

Higher magnification BSE images of the surface regions of the coatings after 100 hrs CMAS exposure are shown in Figure 86a, c and e with the numbers 1-10 corresponding to EDX spot analyses (in at. %) which are shown in Table 24, while Figure 86b, d and f shown the same BSE image with a Ca EDX map overlay. When compared to the same region of the coatings after 4 hrs exposure it is clear that the CMAS reaction shows greater progression, and minimal YbMS can be detected. Despite this, small regions of YbMS were still detected. Figure 86a-3 and d-7 show suspected YbMS regions due to their lighter contrast in the BSE images and Yb:Si ratio shown in Table 24. The bulk of the coating is composed of YbDS (as seen from Figure 86a-1, c-4 and e-8 and data in Table 24). After 100 hrs, none of the APS splat structure is visible, indicating complete dissolution and reprecipitation of YbDS in CMAS. Ca containing regions are also present in Figure 86b, d and f, corresponding to Yb-apatite (Figure 86a-2, c-5 and e-9 and Table 24) and residual CMAS (Figure 86c-6 and e-10 and Table 24).

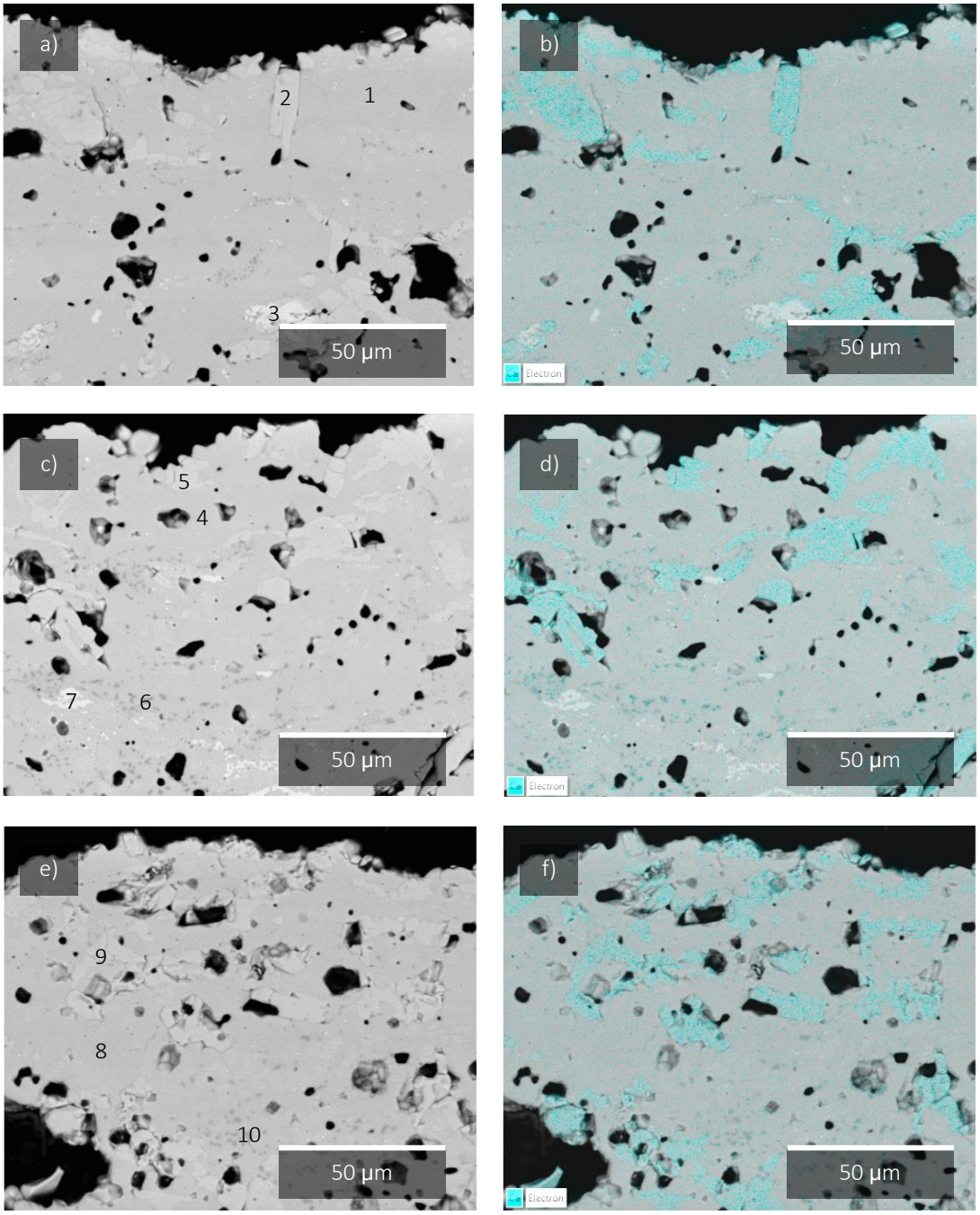

Figure 86. BSE SEM images of the near-surface region of the coating cross-sections exposed to CMAS at 1300 °C for 4 hrs and then 1350 °C for 96 hrs. With a) and b) showing ABR (at a higher magnification and with Ca elemental map overlay respectively), c) and d) showing 1.5 wt. % PE and e) and f) showing 4.5 wt. % PE. The numbers 1-10 correspond to spot EDX analysis shown in Table 24.

Table 24. EDX spectra (in at. %) of the points shown in Figure 86, and the corresponding possible phase, based on the stoichiometry.

Spectrum label	Yb	Si	O	Ca	Mg	Al	Possible phase
1	19.8	20.3	59.9				YbDS
2	20.3	16.1	58.9	4.8			Yb-apatite
3	26.8	14.0	59.3				YbMS
4	20.2	20.6	59.2				YbDS
5	19.9	16.1	59.2	4.8			Yb-apatite
6	15.5	13.0	59.3	2.2	3.2	6.8	CMAS
7	25.4	16.3	58.3				YbMS
8	19.9	20.6	59.6				YbDS
9	20.1	15.7	59.1	5.1			Yb-apatite
10	14.4	9.7	58.7	2.4	3.7	11.1	CMAS

Higher magnification BSE images of the central region of the coatings are shown in Figure 87. EDX spots are shown in Figure 87a, c and e, while the corresponding elemental compositions (in at. %) and the corresponding possible phases are shown in Table 25. This region shows the transition between the interaction region and unaffected material. Figure 87b, d and e show the same higher magnification image, this time with a Ca EDX map overlay. In this region, a pair of Ca containing phases are apparent from Figure 87b, d and e. Figure 87a-2, c-6 and e-10 appear to show Yb-apatite, while Figure 87a-3, c-7 and e-11

correspond to residual CMAS per the EDX analysis in Table 25. The residual CMAS appears in relatively thin bands, indicating it has filled the inter-splat pores as it has infiltrated. In this region, reprecipitated YbDS grains are also visible, as shown in Figure 87a-1, c-5 and e-9. Below the CMAS front exists a combination of unreacted YbDS and YbMS that has retained the APS splat structure. A possible YbMS phase is shown in Figure 87a-4, c-8 and e-12. The remaining inter-splat porosity not yet infiltrated with CMAS is also visible in this region, especially towards the bottom of Figure 87c.

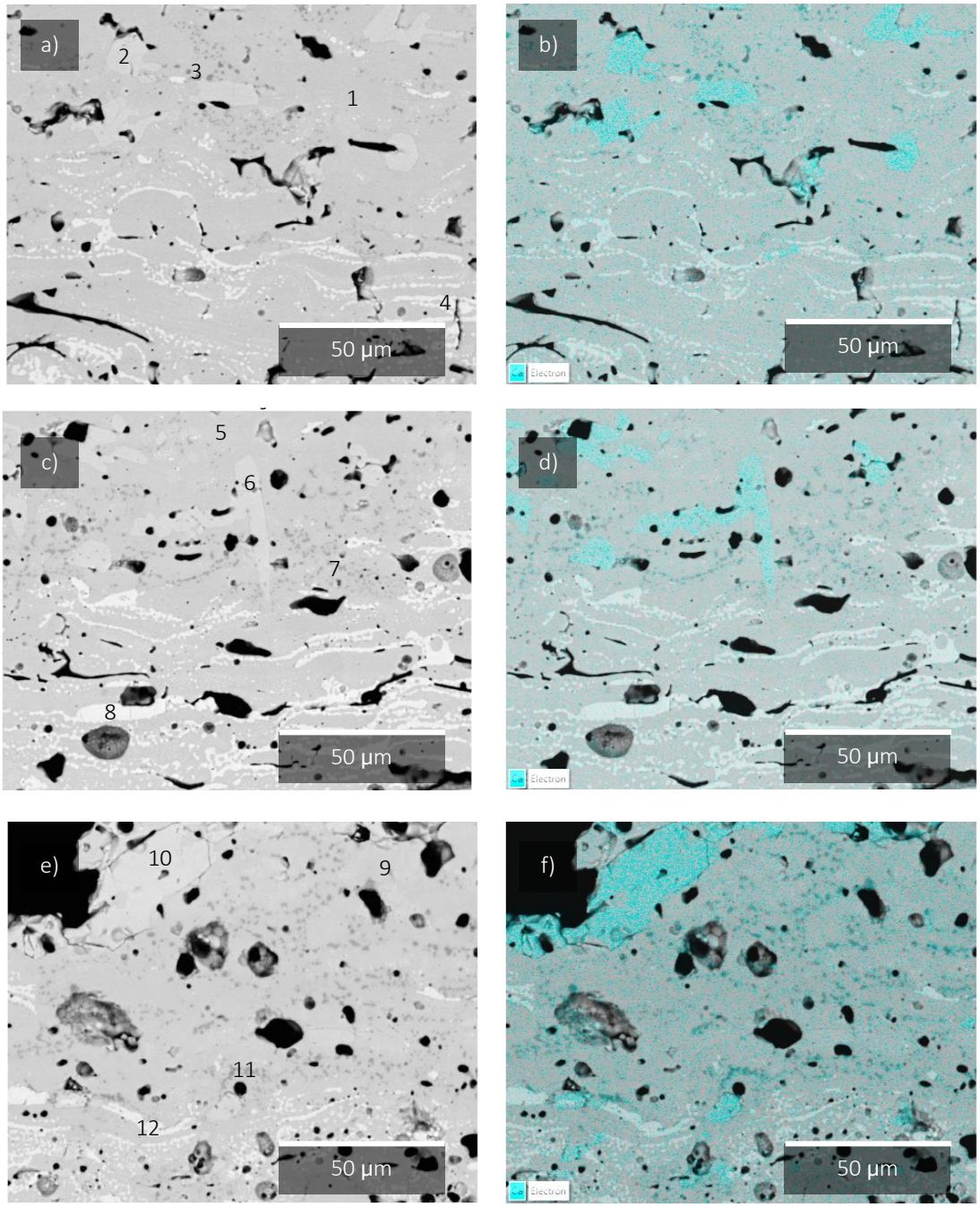

Figure 87. BSE SEM images of the central region of the coating cross-sections exposed to CMAS at 1300 °C for 4 hrs and then 1350 °C for 96 hrs. With a) and b) showing ABR (at a higher magnification and with Ca elemental map overlay respectively), c) and d) showing 1.5 wt. % PE and e) and f) showing 4.5 wt. % PE. The numbers 1-12 correspond to spot EDX analysis shown in Table 25.

Table 25. EDX spectra (in at. %) of the points shown in Figure 87, and the corresponding possible phase, based on the stoichiometry.

Spectrum label	Yb	Si	O	Ca	Mg	Al	Possible phase
1	19.7	20.0	60.1	0.2			YbDS
2	20.3	15.8	59.1	4.8			Yb-apatite
3	13.6	12.1	59.0	3.6	3.9	7.8	CMAS
4	27.1	14.8	58.2				YbMS
5	19.9	20.9	59.3				YbDS
6	21.0	16.5	57.3	5.1			Yb-apatite
7	15.7	13.4	57.4	2.2	3.2	8.0	CMAS
8	27.1	14.2	58.7				YbMS
9	19.5	20.7	59.8				YbDS
10	21.1	16.1	57.7	5.0			Yb-apatite
11	13.7	10.8	58.0	3.1	4.0	10.5	CMAS
12	25.3	14.4	60.0	0.4			YbMS

7.3.3. Combined steam and CMAS exposure

While the phase changes in abradable EBCs after steam or CMAS exposure have remained fairly simple, after combined steam and CMAS exposure the picture becomes more convoluted. The diffractograms of the coatings after combined steam and CMAS exposure

are shown in Figure 88. Again, similar phases were detected in all coatings; however, after this test a combination of four phases was identified. Monoclinic YbDS (C2/m, 00-025-1345), monoclinic YbMS (I2/a, 00-40-0386), hexagonal Yb-apatite (P63/m, 04-006-0320) and cubic ytterbium aluminium garnet (Ia-3d, 00-023-1476) were all detected. The presence of all of these phases indicates competing mechanisms are at play. Firstly, the presence of YbMS indicates to silica loss from YbDS, per Equation 2, is occurring. Simultaneously, the CMAS has fully infiltrated and reacted preferentially with YbMS to form Yb-apatite. Interestingly, the intensity of the Yb-apatite peaks after the combined exposure test is much greater than after just CMAS exposure. This would indicate that as silica depletion occurs in the near-surface YbDS phase due to steam exposure, CMAS will react with this newly formed YbMS creating a greater amount of Yb-apatite at the coatings surface. Despite the use of zirconia tubes throughout the steam furnace, an Al containing phase, YbAG, was detected after the combined steam and CMAS testing. As this phase was not detected in the isolated steam nor CMAS tests, it is postulated that this phase must also be formed from a reaction with CMAS (as that was the only source of Al) induced by the steam atmosphere. Whilst previous researchers have detected YbAG in Yb-silicate coatings after steam exposure testing, this has been explained by the presence of alumina, either within the coating itself or in the tubes used within the furnace [60, 98, 99, 105]

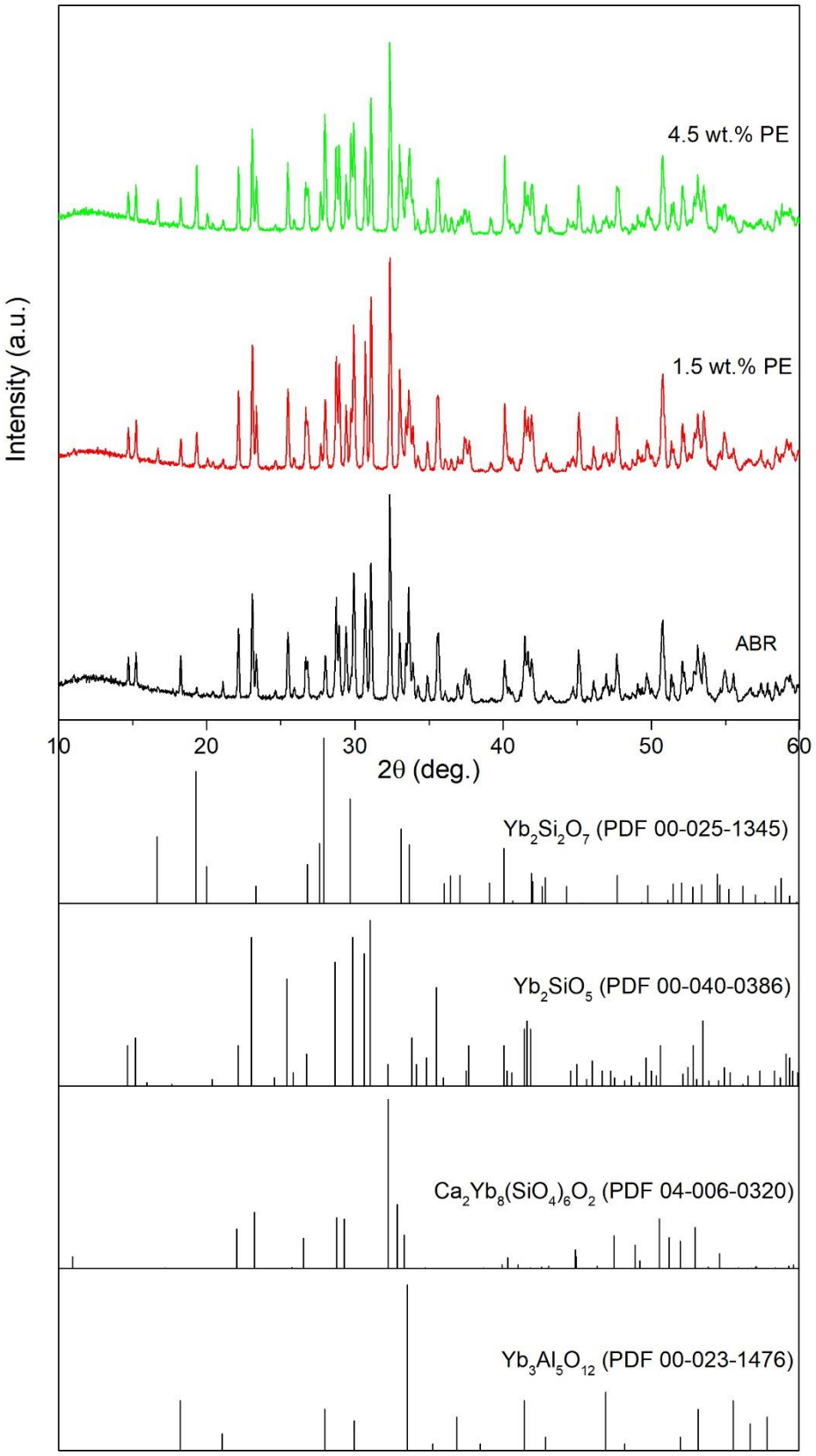
4.5 wt.% PE
1.5 wt.% PE
ABR
Intensity (a.u.)
10
20
30
40
50
60
2θ (deg.)
Yb2Si2O7 (PDF 00-025-1345)
Yb2SiO5 (PDF 00-040-0386)
Ca2Yb8(SiO4)6O2 (PDF 04-006-0320)
Yb3Al5O12 (PDF 00-023-1476)

Figure 88. XRDs of coatings after combined steam and CMAS exposure at 1350 °C for 100 hrs. In all the coatings four phases were detected: YbDS, YbMS, Yb-apatite and YbAG.

The surfaces of the coatings after 100 hrs combined steam and CMAS exposure are shown in Figure 89. The surfaces of the three coatings all appear similar and present an interesting combination of features. The presence of CMAS at high temperature has led to the dissolution-reprecipitation mechanism observed previously in Figure 80 and Figure 84 (no splats visible), indicating that the presence of water vapour does not alter the corrosion mechanism of molten CMAS. Small pinhole pores are also visible in many of the reprecipitated crystals. As with the coating surfaces in Figure 77, these are likely caused by the escape of gaseous $Si(OH)_4$ due to the reaction of reprecipitated YbDS with the steam, per Equation 2.

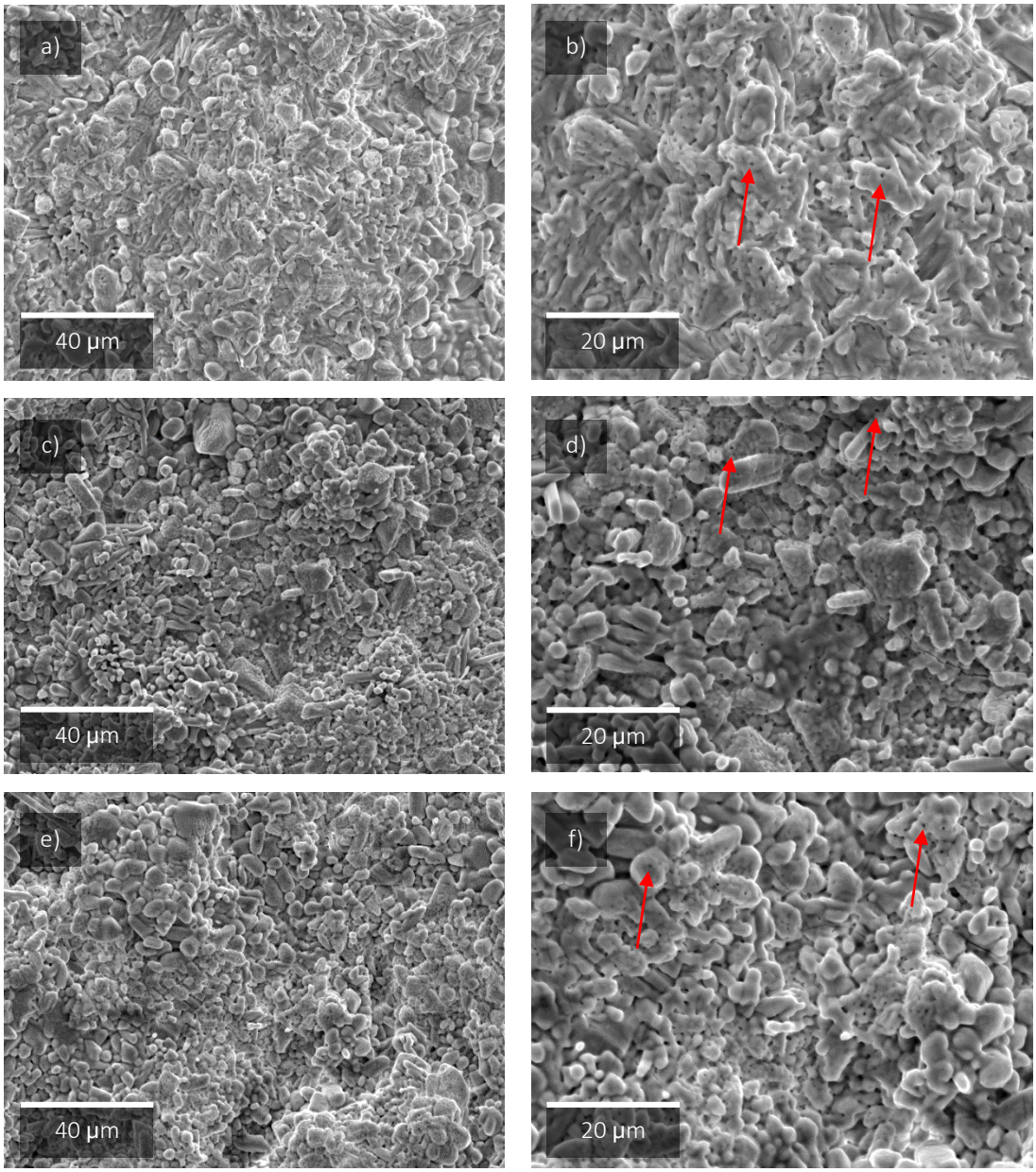

Figure 89. SE SEM images of the surfaces of the coatings after combined steam and CMAS exposure at 1350 °C for 100 hrs. With a) and b) showing ABR (at a lower and higher magnification respectively), c) and d) showing 1.5 wt. % PE and e) and f) showing 4.5 wt. % PE. Some of the pinhole pores are indicated with the red arrows.

Low magnification BSE images of the coating cross-sections after 100 hrs combined steam and CMAS exposure are shown in Figure 90a, c and e, while the same image with a Ca EDX map overlay is shown in Figure 90b, d and f. Unlike the coatings that were exposed to CMAS only for 100 hrs, Ca containing phases can be seen through the entire thickness, rather than just in the near surface regions. The measured CMAS infiltration depths are shown in Table

26, for all the coatings the depths are much larger than the standalone 100 hrs CMAS test. It has been proposed previously that the presence of water vapour can alter the viscosity of the molten CMAS, enabling deeper infiltration for a given exposure time and temperature [129]. As with the previous CMAS exposures, the large PE pores remained free of CMAS and CMAS reaction products.

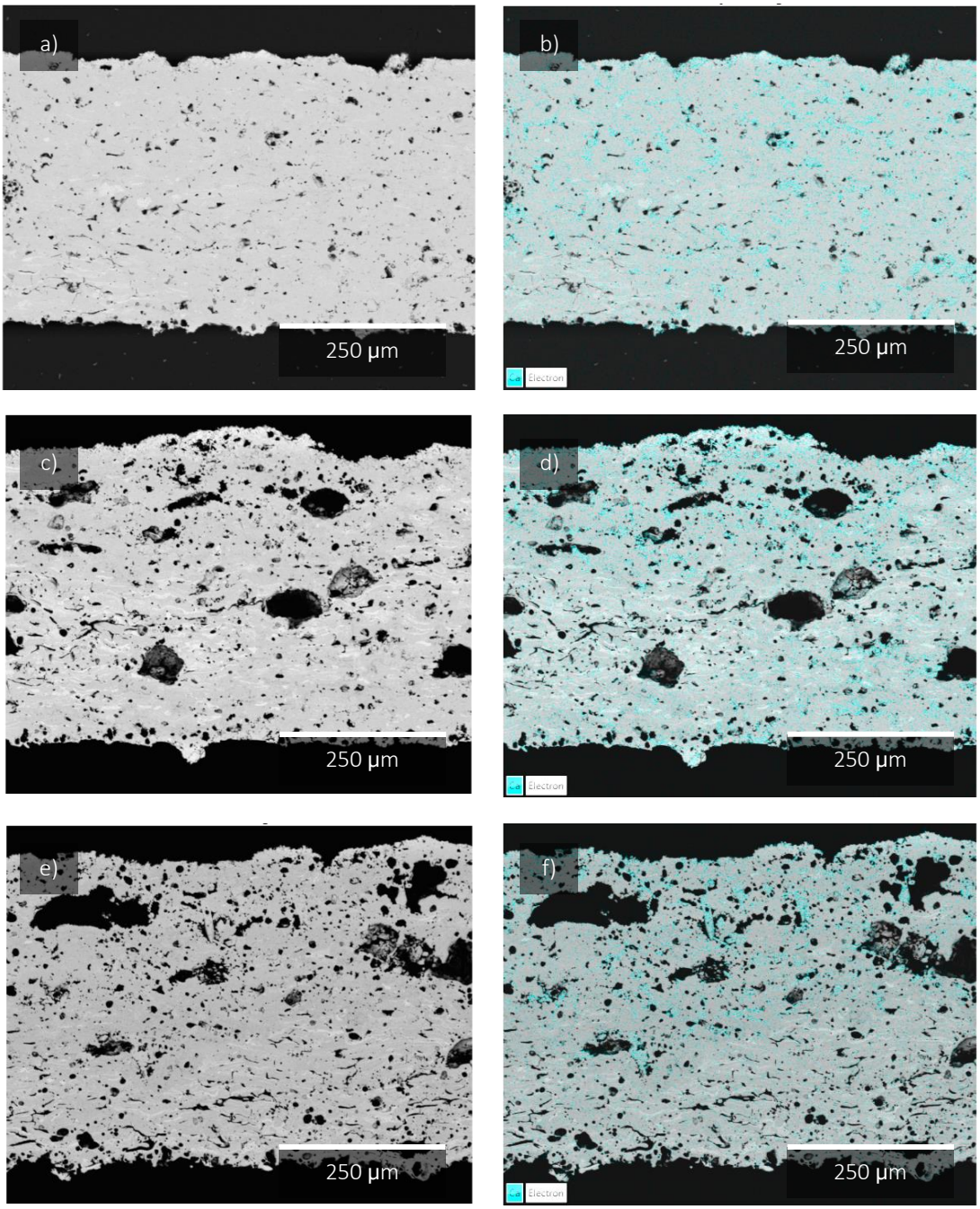

Figure 90. BSE SEM images of coating cross-sections after combined steam and CMAS exposure at 1350 °C for 100 hrs. With a) and b) showing ABR (at a low magnification and

with Ca elemental map overlay respectively), c) and d) showing 1.5 wt. % PE and e) and f) showing 4.5 wt. % PE.

Table 26. CMAS infiltration depths and YbMS reaction layer thicknesses measured in the coatings after combined steam and CMAS exposure at 1350 °C for 100 hrs.

Coating	ABR	1.5 wt.% PE	4.5 wt.% PE
CMAS infiltration depth (µm)	349.8 ± 46.9	337.5 ± 107.6	317.0 ± 53.0
YbMS layer thickness (µm)	10.7 ± 1.8	12.1 ± 6.0	10.4 ± 3.8

Higher magnification BSE images of the surface regions of the coatings after 100 hrs combined steam and CMAS exposure are shown in Figure 91a, c and e with the numbers 1-12 corresponding to EDX spot analyses (in at. %) which are shown in Table 27, while Figure 91b, d and f shown the same BSE image with a Ca EDX map overlay. The silica depleted surface reaction layer, caused by steam exposure is visible. Figure 91a-1, c-5 and e-8 show these regions are likely YbMS. The thicknesses of the YbMS reaction layers are shown in Table 26, relative to the standalone steam exposure test they are slightly larger. Aswell as YbMS, a high fraction of Ca containing phase can be seen on the surface of all the coatings. This indicates that CMAS is reacting with the YbMS produced as a result of Equation 2 and forming a surface Yb-apatite layer. Despite the formation of these surface layers, further infiltration of CMAS was not prevented. Yb-apatite can also be observed throughout the near surface region of the coatings. Figure 91a-3, c-7 and e-10 show the possible Yb-apatite phases. Reprecipitated YbDS (Figure 91a-2, c-6 and e-9), unreacted YbMS (Figure 91a-4, c-8 and e-11) and residual CMAS (Figure 91e-12) were also identified in the near surface region of the coatings.

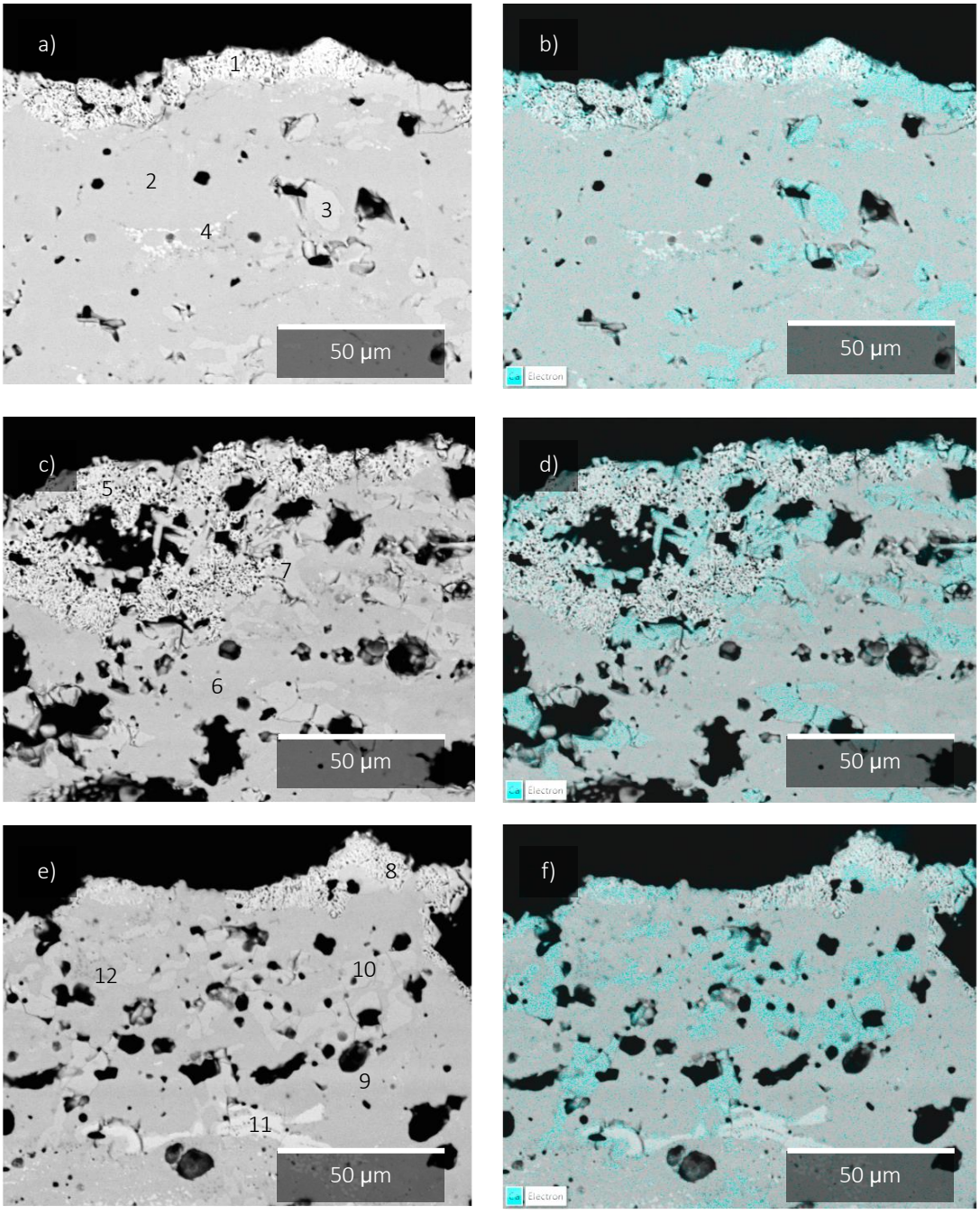

Figure 91. BSE SEM images of the near-surface region of the coating cross-sections after combined steam and CMAS exposure at 1350 °C for 100 hrs. With a) and b) showing ABR (at a higher magnification and with Ca elemental map overlay respectively), c) and d) showing 1.5 wt. % PE and e) and f) showing 4.5 wt. % PE. The numbers 1-12 correspond to spot EDX analysis shown in Table 27.

Table 27. EDX spectra (in at. %) of the points shown in Figure 91, and the corresponding possible phase, based on the stoichiometry.

Spectrum label	Yb	Si	O	Ca	Mg	Al	Possible phase
1	25.5	13.4	60.9	0.2			YbMS
2	20.1	20.5	59.4				YbDS
3	21.1	16.1	57.6	5.1			Yb-apatite
4	24.3	16.0	59.6	0.1			YbMS
5	25.6	14.0	60.2	0.2			YbMS
6	19.6	19.8	60.6				YbDS
7	20.5	15.8	58.9	4.9			Yb-apatite
8	23.3	14.5	62.0	0.2			YbMS
9	20.6	20.5	58.9				YbDS
10	21.4	16.2	56.4	6.0			Yb-apatite
11	28.5	13.9	57.6				YbMS
12	17.1	12.4	57.3	2.7	3.2	7.4	CMAS

While the effects of steam exposure are limited to the surface of the coatings, CMAS has still infiltrated the whole coating thickness. Higher magnification BSE images of the central region of the coatings are shown in Figure 92. EDX spots (1-12) are shown in Figure 92a, c and e, while the corresponding elemental compositions (in at. %) and the corresponding possible phases are shown in Table 28. This region shows the transition between the CMAS effected interaction region and unaffected material. Figure 92b, d and e show the same higher magnification image, this time with a Ca EDX map overlay. In this region, two Ca containing phases can be identified from Figure 92b, d and e. Figure 92a-2, c-6 and e-10 appear to show Yb-apatite, while Figure 92a-3, c-7 and e-11 correspond to residual CMAS per the EDX analysis in Table 25. Similarly to the coatings after 100 hrs CMAS exposure only, shown in Figure 87, the residual CMAS appears in relatively thin bands, indicating it has filled the inter-splat pores as it has infiltrated. In this region, reprecipitated YbDS grains are

also visible, as shown in Figure 92a-1, c-5 and e-9. Below the CMAS front exists a combination of unreacted YbDS and YbMS that has retained the APS splat structure, with the YbMS shown in Figure 92a-4, c-8 and e-12.

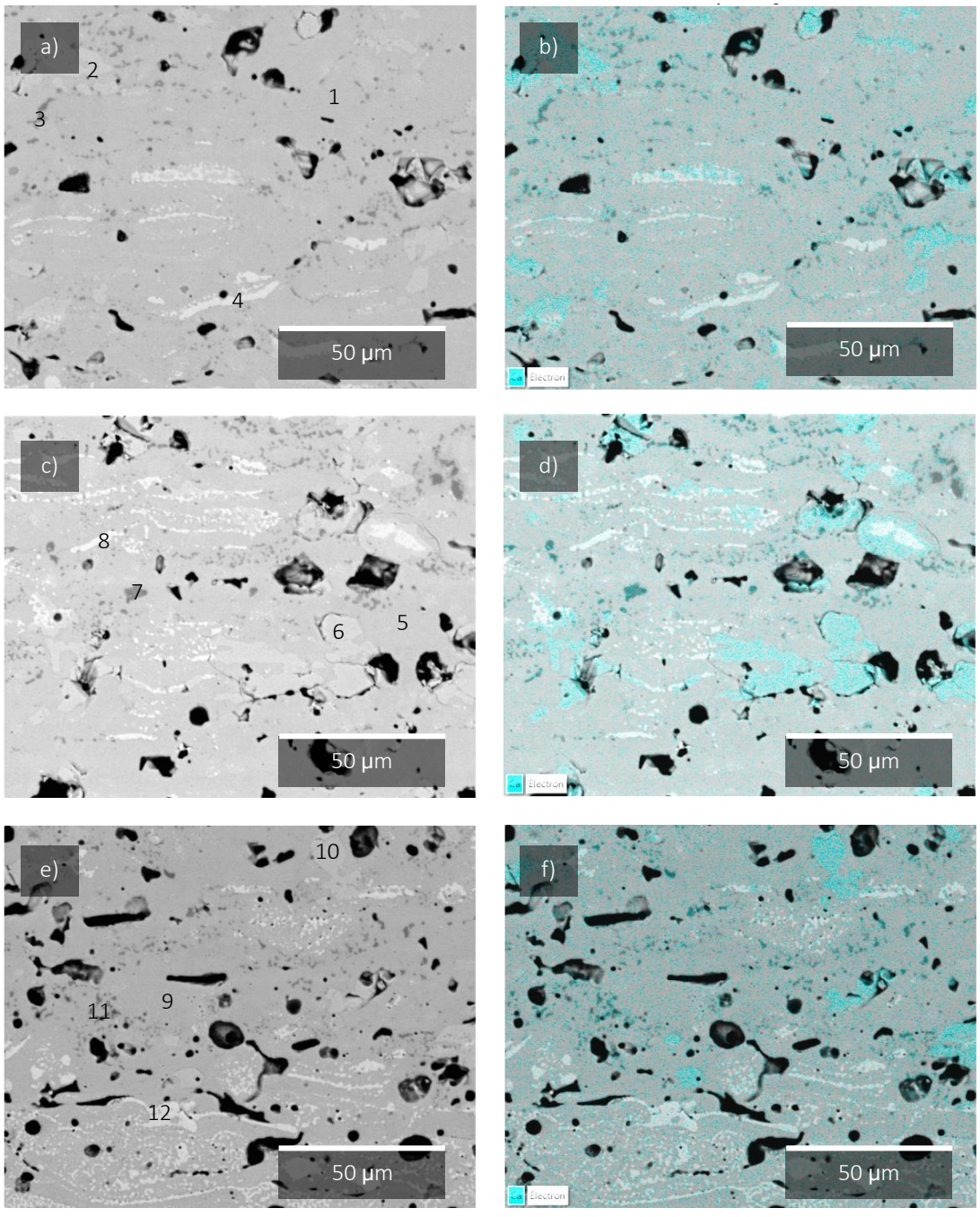

Figure 92. BSE SEM images of the central region of the coating cross-sections after combined steam and CMAS exposure at 1350 °C for 100 hrs. With a) and b) showing ABR (at a higher magnification and with Ca elemental map overlay respectively), c) and d) showing 1.5 wt. % PE and e) and f) showing 4.5 wt. % PE. The numbers 1-12 correspond to spot EDX analysis shown in Table 28.

Table 28. EDX spectra (in at. %) of the points shown in Figure 92, and the corresponding possible phase, based on the stoichiometry.

Spectrum label	Yb	Si	O	Ca	Mg	Al	Possible phase
1	20.1	20.7	59.2				YbDS
2	21.0	16.2	57.7	5.1			Yb-apatite
3	18.5	18.6	60.5	0.9	1.5		CMAS
4	25.0	16.5	58.4				YbMS
5	18.8	20.2	60.8	0.3			YbDS
6	19.8	15.8	59.3	5.1			Yb-apatite
7	11.5	9.4	58.3	3.7	5.3	11.9	CMAS
8	24.5	14.4	60.8	0.3			YbMS
9	20.6	20.3	59.1				YbDS
10	21.0	16.3	57.8	4.9			Yb-apatite
11	16.8	14.0	59.6	2.0	2.7	5.0	CMAS
12	28.1	14.2	57.7				YbMS

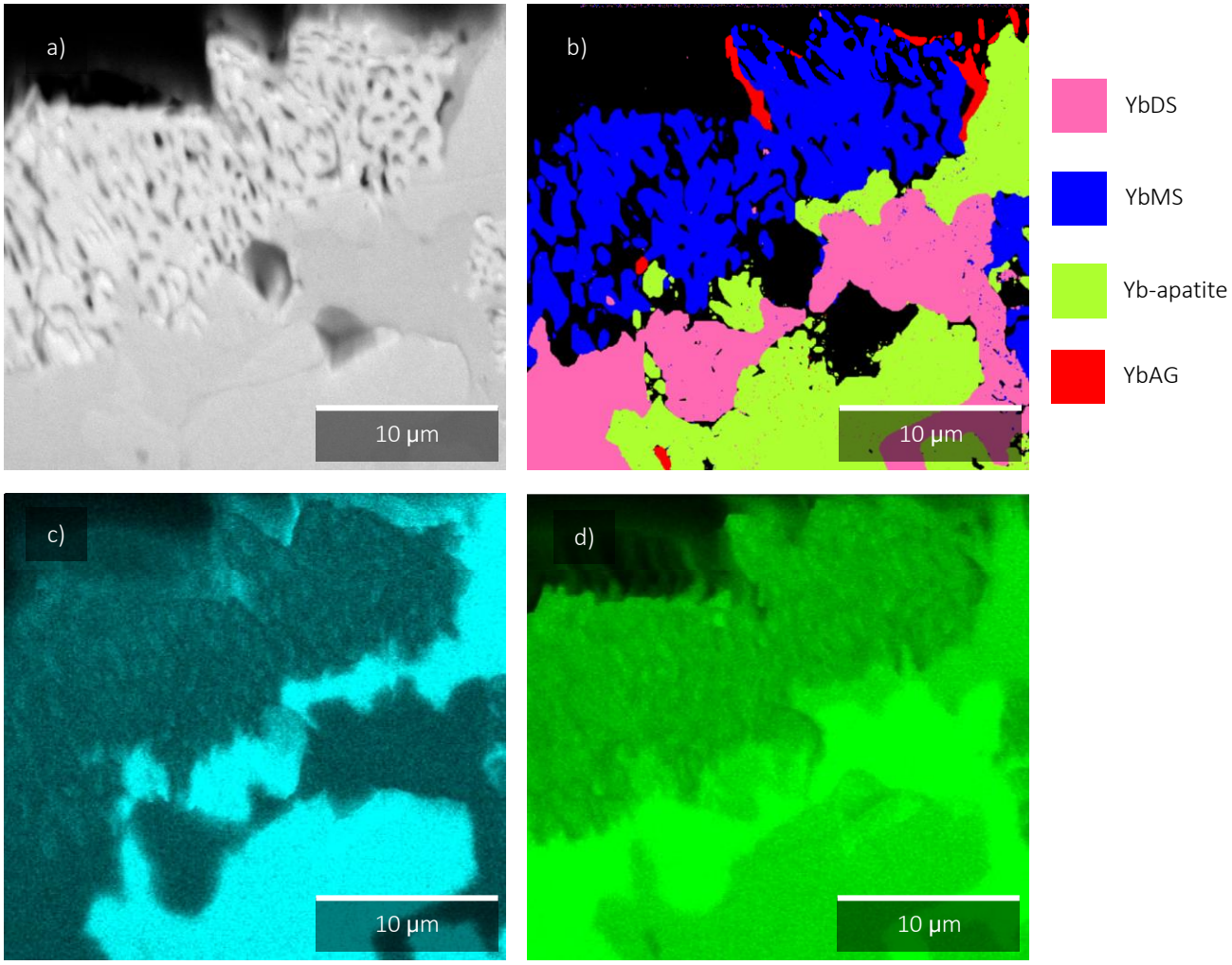

Figure 93. SEM, EBSD and EDX mapping imagery of the ABR coating after combined steam and CMAS exposure, with a) showing the SEM image, b) showing the EBSD phase map, c) showing the Ca EDX map and d) showing the Si EDX map.

To better characterise the combination of phases present at the surface of the steam and CMAS exposed coatings, EBSD and EDX analysis was conducted on the ABR coating, these images are shown in Figure 93. The YbMS rich reaction layer can clearly be observed in Figure 93a, this is corroborated by the phase map in Figure 93b and the reduced level of Si detected during EDX mapping, shown in Figure 93c. Yb-apatite is visible at the surface of the coating and also in the bulk, again shown in the phase map in Figure 93b and the Ca rich regions shown in the EDX map in Figure 93d. Below the surface, some remaining YbDS was detected (also visible in Figure 93b). Interestingly, small amounts of YbAG were also detected in Figure 93b. Small grains of this phase are visible in the reaction layer,

surrounding the YbMS and Yb-apatite, but also below the surface within larger Yb-apatite crystals. This confirms the phase identification performed using XRD, shown in Figure 88.

7.4. Discussion

7.4.1. Steam exposure

While much research into steam corrosion has focussed on EBCs, abradable EBCs present a unique challenge given their increased levels of porosity preventing a hermetic seal above the substrate. Despite this, the abradable coatings subjected to steam corrosion in the present study have shown that the corrosion mechanism appears to be a phenomenon limited to the coating surface only. After steam corrosion at 1350 °C for 96 hrs, all the coatings exhibited a YbMS rich reaction layer (visible in Figure 78), due to the reaction given in Equation 2. This layer was 6, 6 and 7 µm thick for the ABR, 1.5 wt.% PE and 4.5 wt.% PE coatings, respectively. Similar behaviour has been observed in both sintered YbDS pellets [98-100] and plasma sprayed coatings [96, 101-104]. This is much lower than the ~45 µm reaction layer thicknesses observed in similar abradable EBCs under similar conditions by Tejero-Martin, et al. [60]. This difference is likely explained by two differing corrosion mechanisms occurring. In the study by Tejero-Martin, et al. no YbMS rich reaction layer was observed, but instead a larger YbMS depleted region formed after steam corrosion. This variation is due to the presence of gaseous Al containing species, likely contamination from the use of alumina tubes with the furnace, with which YbMS would react preferentially, forming protective YbAG layers on the surface of the coating and thus preventing the YbMS rich reaction layer from forming [60, 105]. YbAG in particular has been shown to be very effective at preventing steam corrosion in YbDS based EBCs [98]. Comparatively, in the present study, only YbDS and YbMS phases were detected after steam exposure, with no Al containing phases detected (due to the use of zirconia tubes within the furnace itself).

The phase change observed in the surface reaction layer formed due to also led to some microstructural changes within all the coatings. While the typical APS splat structure remains, YbDS undergoes a phase change, per Equation 2, to YbMS. Small pores are formed within the YbMS reaction layer, shown in Figure 77 and Figure 78 [101, 104]. Previous studies have estimated the porosity of the YbMS layer to be ~20 % [100, 102]. Large cracks were also observed on the corroded surface of all the coatings, extending through the

splats, visible in Figure 77. These cracks were not present in the as-sprayed surfaces which can be seen in the authors previous work [179]. These cracks can be attributed to the 26 % reduction in volume associated with the phase change from YbDS to YbMS and the escaping $Si(OH)_4$ gaseous phase [101, 102]. As well as the CTE mismatch between the YbDS (4.1 $x10^{-6}$ K^{-1}) rich coating bulk and YbMS (7.5 $x10^{-6}$ K^{-1}) surface layer, leading to residual stresses upon cooling [4, 82, 101, 149]. While the cracks are visible on the coating surface, they do not extend through the thickness of the coating, into the bulk, as observed in the study by Richards, et al. [101] albeit after a much longer exposure time.

7.4.2. CMAS exposure

After 4 hrs, the maximum CMAS penetration depth was measured to be 190, 196 and 176 µm for the ABR, 1.5 wt.% PE and 4.5 wt.% PE coatings, respectively. While after 100 hrs it was 201, 223 and 225 µm for the ABR, 1.5 wt.% PE and 4.5 wt.% PE coatings respectively. All the coatings show a similar level of CMAS penetration despite differing levels of overall porosity. Considering capillary action infiltration will, at part, be dependent on the degree of open, interconnected porosity within the coating, this shows that irrespective of the amount of large PE pores, the interconnectedness of the pore network remains similar [185]. Even after 100 hrs the level of CMAS infiltration observed in this study was not that severe, there remains unaffected material towards the bottom of the coating visible in Figure 85. When compared to a previous study on CMAS corrosion of abradable EBCs by Tejero Martin, et al. [59], the abradable coatings were completely infiltrated with CMAS after 48 hrs. That study used a CMAS concentration of 15 mg/cm^2 whereas 5 mg/cm^2 was used here, although it has been suggested that low CMAS dosing can lead to rapid infiltration of the coating as there is no melt pool to act as a glass sink for coating dissolution or reduced formation of a continuous Yb-apatite layer [129]. After 4 hrs, nearly all of the CMAS had penetrated the coating and there was minimal residual glass remaining on the surface of the coating, the lack of remaining glass could explain the limited increase in penetration depth seen after 100 hrs. Relatively high levels of Yb were detected within the residual CMAS even after 4 hrs exposure, indicating dissolution of the Yb-silicates. Excessive CMAS penetration (especially in porous coatings) and the associated phase and microstructural changes has been shown to lead to premature failure of the EBC due to the change in stress state this induces [5].

The reprecipitated YbDS and Yb-apatite can clearly be seen on the coating surfaces in Figure 80 and Figure 84 after 4 hrs and 100 hrs exposure, respectively. While it has been suggested that a dense Yb-apatite layer can help protect the coating from further CMAS infiltration and has been observed in some studies [126, 134], the Yb-apatite observed on the surface in this study was discontinuous, interspersed amongst reprecipitated YbDS, as can be seen in Figure 82 and Figure 86 after 4 hrs and 100 hrs exposure, respectively. Generally speaking, the mechanism by which CMAS infiltrates and reacts with YbDS EBCs is now well understood. A description of the CMAS corrosion mechanism of mixed Yb-silicate coatings has been described by Poerschke, et al. [122]. Initially, molten CMAS infiltrates the coating via grain and splat boundaries, Yb-silicates are dissolved into the melt, and then once the melt is saturated with Yb_2O_3, depending on the CaO concentration of the CMAS, the Yb-apatite phase will precipitate. With YbMS reacting with the CMAS preferentially to form Yb-apatite. This is due to the reactivity between a silicate glass and crystalline oxide increasing as the difference in optical basicity between the two rises. As YbMS has a larger optical basicity difference to CMAS than YbDS, YbMS is seen to be more reactive and hence more likely to form Yb-apatite. [118, 123]. The final stage of the process is a reprecipitation of the Yb-silicate phases. This suggests that the relatively low amount of YbMS in the as-sprayed coating (~13 wt.%) prevents the precipitation of enough Yb-apatite to form a protective layer.

7.4.3. Combined steam and CMAS exposure

When compared to the standalone CMAS exposure test, the combined steam and CMAS test induces a much greater level of CMAS penetration for all coatings, regardless of porosity, for the same test parameters, namely CMAS loading, temperature and time. After 100 hrs exposure the CMAS infiltration depth increases to 350, 338 and 317 µm for the ABR, 1.5 wt.% PE and 4.5 wt.% PE coatings respectively. This affect can be seen clearly by comparing the Ca EDX maps shown in Figure 85 and Figure 90. After the combined exposure test, the CMAS has penetrated the entire thickness of the ABR and 1.5 wt.% PE coatings. Despite increased levels of Yb-apatite on the surface (which as explained previously, could be protective against further CMAS infiltration) the maximum CMAS penetration depth increased. While it has been suggested that lower CMAS loadings could be more prone to rapid infiltration when compared to larger doses (>8 mg/cm^2) [129], this seems unlikely to

be the root cause in this study, given the observations in the standalone CMAS test. A decrease in the viscosity of the molten CMAS could also explain the increased level of infiltration [186, 187]. The presence of water in molten silicate glasses has been shown to decrease the glass viscosity [188]. Also, dynamic changes in the composition of the CMAS melt could lead to viscosity changes. Given the increased amount of Yb-apatite formed after the combined steam and CMAS exposure (and the formation of YbAG), the remaining CMAS would likely be depleted of Ca and Al, relative to the CMAS in the standalone test. Although Si rich CMAS compositions will have an increased viscosity [186].

After combined steam and CMAS exposure, the three coatings exhibited a convoluted phase composition. In terms of crystalline phases, YbDS, YbMS, Yb-apatite and YbAG were all detected, as well as some residual amorphous CMAS detected using EDX. The corrosion mechanism for all the coatings appears similar, irrespective of porosity level. Molten CMAS infiltrates the coating at high temperature, leading to the formation of reprecipitated YbDS grains and Yb-apatite crystals while any YbMS is consumed by the reaction with CMAS. Concurrently, the surface of the coatings undergoes a reaction with the water vapour (as per Equation 2) whereby a YbMS rich reaction layer is formed, thus creating a compositional inhomogeneity at the surface. Unlike the steam exposure test, whereby this layer remains constant across the entire coating surface, after the combined test, the reaction layer is interspersed with large Yb-apatite crystals. The assumption being that the increase in YbMS in the reaction layer drives preferential reaction with molten CMAS (due to the observed increase in reactivity of YbMS with CMAS relative to YbDS [118, 123]), thus creating a larger fraction of Yb-apatite on the surface of the coating observed in XRD analysis shown in Figure 88. The discontinuous nature of this Yb-apatite layer is unlikely to provide protection from further CMAS infiltration. Although given much longer exposure times and enough available Ca within the CMAS melt, eventually a dense surface Yb-apatite layer may form in the presence of steam and CMAS, such a layer would likely offer protection from further corrosion due to both steam and CMAS.

While YbAG has previously been observed in YbDS EBCs subject to high temperature steam exposure, this has been attributed to alumina being used within the furnace rig itself [60, 105, 110] or from small alumina additions to the YbDS feedstock [98, 99]. In the present study however, no alumina was present in the furnace or coating (and no YbAG was

detected in the standalone steam corrosion test), the only source of alumina was from the CMAS. Given that no YbAG was detected after the standalone CMAS test conducted in air, two possible explanations exist for its formation. Either the presence of steam has facilitated a reaction between the dissolved Yb and Al within the molten CMAS, or due to the reduction in Ca available in the CMAS melt (due to increased Yb-apatite precipitation), the precipitation of YbAG, consuming Al remaining in the CMAS melt, becomes favourable. Previous literature examining combined steam and CMAS corrosion of YbDS EBCs, did not show any YbAG formation [129], perhaps due to a lower CMAS flux of 2 mg/cm^2 despite the starting CMAS composition being richer in alumina. It has previously been reported that YbAG is particularly effective as a protective layer against steam corrosion [98, 189], although this is reliant on a continuous YbAG surface layer sealing the EBC below. This is thought to because of the stronger bonding of the aluminium compound and lower oxygen vacancy concentration of YbAG, when compared to the weaker bonding of the silicon compound and higher oxygen vacancy concentration of YbDS [189]. From the EBSD phase map shown in Figure 93b, it can be observed that in this test, only small isolated YbAG grains have precipitated, either in the YbMS/Yb-apatite surface reaction layer, or within Yb-apatite crystals in the coating bulk. The discontinuous nature of the YbAG is unlikely to offer significant protective capabilities from steam corrosion. What is clear is the need for further work into the effects of combined corrosion mechanisms, as these are the most representative of in-service conditions.

7.5. Conclusions

CMAS and steam exposure are two of the most serious challenges when considering EBC design and implementation, especially with the extreme porosity levels of abradable coatings. In this study, abradable coatings with three distinct porosity levels (8 %, 15 % and 22 % by area) were exposed to steam corrosion at 1350 °C for 96 hrs, CMAS corrosion at 1350 °C for 100 hrs and combined CMAS and steam corrosion at 1350 °C for 100 hrs.

In the as-sprayed state the coatings all had the same phase composition, containing ~87 wt.% YbDS and 13 wt.% YbMS however after the various exposures this changed significantly. After steam exposure, a thin reaction layer significantly enriched in YbMS was formed on the coating surface, while the bulk microstructure remained unaffected. Microstructural changes were detected in this reaction layer, small pinhole pores within the

splats and large cracks extended through the surface of the coating were observed These were caused by the volume change associated with the YbDS to YbMS phase change and the escaping $Si(OH)_4$ gaseous phase. Meanwhile after CMAS exposure YbDS was dissolved into the melt, reprecipitated as small crystals, eliminating the typical APS splat structure, and a Yb-apatite phase was formed after reaction with the dissolved Yb-silicates and CaO from the molten CMAS.

In the combined exposure testing, the CMAS infiltration depth was higher than that observed in the standalone CMAS exposure, likely due to the water vapour in the atmosphere causing a reduction in viscosity of the molten CMAS. The YbMS rich surface layer caused by the steam exposure would react with the CMAS, forming an increased amount of Yb-apatite on the surface of the coating. While it is been proposed that a dense Yb-apatite layer on the surface of the EBC could help prevent further CMAS infiltration, this was not observed with the abradable coatings under these test conditions. A YbAG phase was also detected after the combined testing, likely caused by the presence of Al in the CMAS. In all of the tests no clear correlation between porosity level and performance was observed, indicating that the large pores in the abradable coatings formed by fugitive PE do not play a major role in the corrosion process. Overall, this testing has shown the value in more realistic testing regimes for EBCs, as combined effects that otherwise would not be detected have been studied.

Acknowledgements

This work was supported by the Engineering and Physical Sciences Research Council (EPSRC) (grant number EP/V010093/1). The project also received funding from Rolls Royce Plc in terms of a CASE PhD studentship. The authors also acknowledge the use of facilities at the Nanoscale and Microscale Research Centre of the University of Nottingham, supported by the EPSRC (grant number EP/L022494/1). The authors would also like to extend their thanks to John Kirk, who assisted with all aspects of the coating deposition process.

Chapter 8: Conclusions and future work

8.1. Conclusions

In this thesis, the relationship between feedstock, processing parameters, microstructure and performance of abradable YbDS EBCs has been established. A summary of the conclusions obtained from the various experimental chapters is presented here.

Control of the process parameters during plasma spraying is key when considering desirable microstructures and properties, as shown in Chapter 4. By controlling the spray power and stand-off distance, the phase composition, porosity and mechanical properties of YbDS EBCs can be tailored. Reducing the spray power from 24 kW to 12 kW resulted in a reduction in particle temperature (2095 °C to 1687 °C) and particle velocity (129 m/s to 89 m/s) and produced softer (736.2 HV to 463.4 HV), more porous (5.6 % to 9.8 % porosity) coatings yet retained greater proportions of YbDS phase. In fact, it was possible to deposit porous EBCs with reduced hardness by reducing the spray power to such a level where the particle temperature was below the melting temperature of YbDS. While high spray powers producing higher particle temperatures and velocities produced harder coatings with less porosity but also less YbDS phase. Subsequently, a PE pore forming phase was added to the feedstock to increase the porosity and reduce the hardness further. While much past research has been focussed on producing gas-tight EBCs, this shows that through careful selection of feedstock and processing parameters, the microstructure and basic properties of porous abradable EBCs can be optimised.

Subsequently, a more in-depth examination of the abradable EBCs microstructure and mechanical properties was presented in Chapter 5. Abradable EBCs with three distinct porosity levels, which had been optimised in Chapter 4, were subject to hardness, erosion and abradability testing using an abradable test rig at the University of Sheffield. As the porosity level increased, the hardness and erosion resistance of the coatings decreased. A change in erosion mechanism was also observed, from ductile to brittle failure, as porosity increased. This is an important observation as abradable coatings cut most efficiently when their failure is brittle. When tested on the abradable rig, a distinct difference between the least porous coating and the coatings containing PE pore former was observed. The ABR coatings showed high forces and temperatures, irrespective of the test conditions and

eventually led to failure of the coating at the top coat-bond coat interface and the ceramic tipped blade. This can help with the future design of ceramic abradable coatings as it shows that despite the intrinsic brittleness of the YbDS ceramic, and the optimisation of spray parameters to produce a porous coating with reduced hardness, some degree of feedstock modification is required to increase the porosity further and achieve good cutting of the abradable coating. Nevertheless, the abradable coatings with PE added to the feedstock, and increased levels of porosity both cut well under all the tested conditions. No failure of the abradable coating or the ceramic tipped blade was observed. Reduced forces and temperatures were observed in the most porous coating, indicating it was cutting more efficiently, however subsequent characterisation showed the mechanisms to be similar for both the PE containing abradable coatings. This means that while the more porous 4.5 wt.% PE coating cuts slightly better, the less porous 1.5 wt.% PE coating way cut well enough to be utilised, while showing more resistance to erosion and damage by foreign objects, making it more suitable for the application.

As well as showing good cutting against the turbine blades, abradable EBCs must also be able to withstand the extreme environment and various corrosive species found in the hot section of the gas turbine. In the case of EBCs, CMAS and steam corrosion are the two main degradation mechanisms regarding the implementation of said coatings into commercial gas turbines. This poses a particular challenge, as typically EBCs are designed to provide a gas tight seal above the SiC CMC substrate, while abradable EBCs are highly porous. When exposed to CMAS, Chapter 6 of this work showed that the overall porosity level of the coating did not affect the penetration of molten CMAS, which was driven by infiltration through inter-splat boundaries and pores. Crucially, even after long term high temperature exposure for 100 hrs, no coating failure was identified despite extensive infiltration and reaction. CMAS loading and exposure times were found to have a much larger impact than the coating porosity, in terms of penetration depth. CMAS exposure and the associated phase and microstructural changes increased the erosion resistance of the abradable coatings.

Similarly, when the coatings were exposed to high temperature water vapour, minimal difference was detected in the degree and mechanism of corrosion, as demonstrated in Chapter 7. A YbMS reaction layer formed on the surface and was a similar thickness for all

the abradable coatings. Finally, the coatings were exposed to simultaneous steam and CMAS corrosion, also in Chapter 7. As with the previous tests, no effect of porosity was identified in terms of penetration depth or corrosion mechanisms. Accelerated CMAS penetration was identified in the steam containing atmosphere, which could have implications when considering the environments found in-service. The presence of the steam also led to a change in the interaction between the molten CMAS and the coatings. The YbMS surface layer caused by steam exposure, reacted with calcium contained within the CMAS forming a greater quantity of a Yb-apatite phase at the surface of the coating.

In conclusion, this thesis has shown that optimisation of the plasma spray process can be used to produce porous abradable EBCs with distinct levels of porosity. With the addition of PE to form additional pores, the coatings were found to cut well against ceramic tipped turbine blades. Finally, this work demonstrates that higher porosity levels seen in abradable EBCs, show similar corrosion behaviour, with no evidence of failure when exposed to high temperature CMAS and steam corrosion. These results are crucial moving forward as the drive for increased efficiency in gas turbines drives the development of abradable EBC development.

8.2. Future work

While the work presented in this thesis has laid the foundation for research into the processing and performance of abradable EBCs, there are still some areas where more work should be undertaken. Firstly, the majority of this work into the high temperature corrosion of abradable EBCs was done on free-standing coatings. While this allowed the focus to be on the performance of the coating itself, which was the scope of this thesis, this did not allow for investigation of the TGO between the bond coat and top coat which occurs during long term high temperature exposure. TGO growth is one of the main limiting factors when it comes to EBC life and is often cited as a failure mechanism. This means the effect that the added porosity has on the diffusion of oxidisers through the abradable EBC and then the subsequent growth of the TGO has not yet been investigated, crucial for understanding how an abradable EBC will perform in service. Moving forward testing should be undertaken using SiC CMC substrates, a Si bond coat and abradable EBC top coat, to more accurately match the architecture used on gas turbine components.

Finally, efforts were made in this thesis to improve the testing and make it more representative of in-service conditions, utilisation of the abradable test rig and combined high temperature corrosion and corrosion-erosion was instrumental to this. However, this does not go far enough to capture the cyclic nature of the extreme temperatures found in gas turbine hot sections, where repeated heating and cooling will be experience throughout the coating's lifespan. Rather than isothermal testing, in the future testing should incorporate thermal cyclic for a high number of cycles to better understand the thermal stresses an abradable EBC will be expected to withstand. On top of this, efforts should be made to introduce a temperature gradient across the coated sample, this can be achieved by using oxy-acetylene torches rather than box furnaces. Again, this would be more representative of the thermal conditions found within a gas turbine hot section.

References

1. Lee, K.N., *Protective coatings for gas turbines.* The gas turbine handbook, 2006. **4**(2).
2. Padture, N.P., *Advanced structural ceramics in aerospace propulsion.* Nature Materials, 2016. **15**(8): p. 804-809.
3. Darolia, R., *Thermal barrier coatings technology: critical review, progress update, remaining challenges and prospects.* International Materials Reviews, 2013. **58**(6): p. 315-348.
4. Lee, K.N., D.S. Fox, and N.P. Bansal, *Rare earth silicate environmental barrier coatings for SiC/SiC composites and Si3N4 ceramics.* Journal of the European Ceramic Society, 2005. **25**(10): p. 1705-1715.
5. Lee, K.N., D. Zhu, and R.S. Lima, *Perspectives on Environmental Barrier Coatings (EBCs) Manufactured via Air Plasma Spray (APS) on Ceramic Matrix Composites (CMCs): A Tutorial Paper.* Journal of Thermal Spray Technology, 2021. **30**(1-2): p. 40-58.
6. Norris, G., *Hot Blades*, in *Aviation Week & Space Technology*. 2015, Penton Media.
7. Steibel, J., *Ceramic matrix composites taking flight at GE Aviation.* Am. Ceram. Soc. Bull, 2019. **98**(3): p. 30-33.
8. Clough, R. and J. Johnson. *GE Readies Engine Durability Fix for New Boeing, Airbus Planes*. 2018 [cited 2024 15 August]; Available from: https://www.bloomberg.com/news/articles/2018-03-05/ge-sees-durability-fix-for-new-jet-engine-in-second-quarter.
9. Tejero-Martin, D., C. Bennett, and T. Hussain, *A review on environmental barrier coatings: History, current state of the art and future developments.* Journal of the European Ceramic Society, 2021. **41**(3): p. 1747-1768.
10. Dearnley, P.A., *Introduction to Surface Engineering*. 2017, Cambridge: Cambridge University Press.
11. Fauchais, P., *Thermal spray fundamentals : from powder to part*, ed. J.V. Heberlein and M.I. Boulos. 2014, London: Springer.
12. Kuroda, S., et al., *Warm spraying—a novel coating process based on high-velocity impact of solid particles.* Science and Technology of Advanced Materials, 2008. **9**(3): p. 033002.
13. Davis, J.R., *Handbook of thermal spray technology*. 1st ed. ed. 2004, Materials Park: Materials Park: ASM International.
14. Odhiambo, J.G., et al., *Porosity and Its Significance in Plasma-Sprayed Coatings.* Coatings, 2019. **9**(7): p. 460.
15. Hardwicke, C.U. and Y.-C. Lau, *Advances in Thermal Spray Coatings for Gas Turbines and Energy Generation: A Review.* Journal of Thermal Spray Technology, 2013. **22**(5): p. 564-576.
16. Rajendran, R., *Gas turbine coatings – An overview.* Engineering Failure Analysis, 2012. **26**: p. 355-369.
17. Lattime, S. and B. Steinetz. *Turbine engine clearance control systems: current practices and future directions*. in *38th AIAA/ASME/SAE/ASEE Joint Propulsion Conference & Exhibit*. 2002.
18. Giovannetti, I., et al. *Clearance Reduction and Performance Gain Using Abradable Material in Gas Turbines*. in *ASME Turbo Expo 2008: Power for Land, Sea, and Air*. 2008.
19. Borel, M.O., et al., *The wear mechanisms occurring in abradable seals of gas turbines.* Surface and Coatings Technology, 1989. **39-40**: p. 117-126.
20. Baïz, S., et al., *Experimental investigation of the blade/seal interaction.* Proceedings of the Institution of Mechanical Engineers, Part J: Journal of Engineering Tribology, 2013. **227**(9): p. 980-995.
21. Bolot, R., et al., *Predicting the Thermal Conductivity of AlSi/Polyester Abradable Coatings: Effects of the Numerical Method.* Journal of Thermal Spray Technology, 2011. **20**(1-2): p. 39-47.

22. Bounazef, M., S. Guessasma, and B. Ait Saadi, *The wear, deterioration and transformation phenomena of abradable coating BN–SiAl–bounding organic element, caused by the friction between the blades and the turbine casing.* Materials Letters, 2004. **58**(27): p. 3375-3380.
23. Fois, N., M. Watson, and M. Marshall, *The influence of material properties on the wear of abradable materials.* Proceedings of the Institution of Mechanical Engineers, Part J: Journal of Engineering Tribology, 2017. **231**(2): p. 240-253.
24. Ma, X. and A. Matthews, *Evaluation of abradable seal coating mechanical properties.* Wear, 2009. **267**(9): p. 1501-1510.
25. Baillieu, A., et al., *In situ measurements of thermal-mechanical wear in blade-abradable liner contacts.* Proceedings of the Institution of Mechanical Engineers, Part C: Journal of Mechanical Engineering Science. **0**(0): p. 09544062231187204.
26. Fois, N., J. Stringer, and M.B. Marshall, *Adhesive transfer in aero-engine abradable linings contact.* Wear, 2013. **304**(1): p. 202-210.
27. Fois, N., et al., *An investigation of the relationship between wear and contact force for abradable materials.* Proceedings of the Institution of Mechanical Engineers, Part J: Journal of Engineering Tribology, 2015. **229**(2): p. 136-150.
28. Mandard, R., et al., *Mechanisms of incursion accommodation during interaction between a vibrating blade and an abradable coating.* Wear, 2015. **330-331**: p. 406-418.
29. Rahimov, E., et al., *Investigation of wear mechanisms in AlSi-polyester abradable - Ti(6Al4V) blade contacts using stroboscopic imaging.* Wear, 2022. **494-495**: p. 204207.
30. Stringer, J. and M.B. Marshall, *High speed wear testing of an abradable coating.* Wear, 2012. **294-295**: p. 257-263.
31. Zhang, B. and M. Marshall, *Investigating material removal mechanism of Al-Si base abradable coating in labyrinth seal system.* Wear, 2019. **426-427**: p. 239-249.
32. Tang, N., et al., *Identification of blade operational mode shapes during wear of abradable coating.* Journal of Sound and Vibration, 2020. **472**: p. 115204.
33. Yi, M., et al., *Friction and wear behaviour and abradability of abradable seal coating.* Wear, 1999. **231**(1): p. 47-53.
34. Tang, J., et al., *The influence of size and distribution of graphite on the friction and wear behavior of Ni–graphite coatings.* Surface and Coatings Technology, 2014. **252**: p. 48-55.
35. Soltani, R., et al., *Effect of APS process parameters on high-temperature wear behavior of nickel–graphite abradable seal coatings.* Surface and Coatings Technology, 2017. **321**: p. 403-408.
36. Ziegelheim, J., et al., *Abradable Coatings for Small Turboprop Engines: A Case Study of Nickel-Graphite Coating.* Journal of Thermal Spray Technology, 2019. **28**(4): p. 794-802.
37. Clegg, M. and M. Mehta, *NiCrAl/bentonite thermal spray powder for high temperature abradable seals.* Surface and Coatings Technology, 1988. **34**(1): p. 69-77.
38. Faraoun, H.I., et al., *Improvement of thermally sprayed abradable coating by microstructure control.* Surface and Coatings Technology, 2006. **201**(6): p. 2303-2312.
39. Jońca, J., et al., *Oxidation behaviour of a CoNiCrAlY/h-BN based abradable coating.* Corrosion Science, 2019. **153**: p. 170-177.
40. Motyka, E., R. Schricker, and K. Ceiler. *FELTMETAL™ Abradable Turbine Seal Materials: Structure and Property Responses to Blade Rub and Oxidation*. in *Turbo Expo: Power for Land, Sea, and Air*. 2022. American Society of Mechanical Engineers.
41. Cheng, X., et al., *Preparation and Performance of an Abradable NiCrFeAlBN-YSZ-NiCrAl Layered Seal Coating for Aircraft Engines.* Journal of Thermal Spray Technology, 2020. **29**(7): p. 1804-1814.
42. Irissou, E., A. Dadouche, and R. Lima, *Tribological characterization of plasma-sprayed CoNiCrAlY-BN abradable coatings.* Journal of thermal spray technology, 2014. **23**(1-2): p. 252-261.

43. Novinski, E., J. Harrington, and J. Klein, *Modified zirconia abradable seal coating for high temperature gas turbine applications.* Thin Solid Films, 1982. **95**(3): p. 255-263.
44. Sporer, D.R., et al. *Novel Ceramic Abradable Coatings With Enhanced Performance*. in *ASME Turbo Expo 2006: Power for Land, Sea, and Air*. 2006.
45. Sporer, D., et al. *On The Potential Of Metal And Ceramic Based Abradables In Turbine Seal Applications*. in *Proceedings of the 36th Turbomachinery Symposium*. 2007. Texas A&M University. Turbomachinery Laboratories.
46. Sporer, D., *Processing and properties of advanced ceramic abradable coatings.* Therm. Spray, 2007: p. 495-500.
47. Sporer, D., S. Wilson, and M. Dorfman, *Ceramics for Abradable Shroud Seal Applications*. 2010. p. 39-54.
48. Scrinzi, E., et al., *Development of New Abradable/Abrasive Sealing Systems for Clearance Control in Gas Turbines*. 2013.
49. Aussavy, D., et al., *YSZ-Polyester Abradable Coatings Manufactured by APS.* Journal of Thermal Spray Technology, 2016. **25**(1-2): p. 252-263.
50. Foroushani, M.H., et al., *Porosity analysis and oxidation behavior of plasma sprayed YSZ and YSZ/LaPO4 abradable thermal barrier coatings.* Ceramics International, 2016. **42**(14): p. 15868-15875.
51. Huang, J., et al., *High temperature abradable sealing coating for SiCf/SiC ceramic matrix composites.* Ceramics International, 2023. **49**(2): p. 1779-1790.
52. Wang, Z. and L. Du, *Stabilization of a novel mixed solution precursor used for preparing YSZ abradable sealing coatings.* Colloids and Surfaces A: Physicochemical and Engineering Aspects, 2019. **562**: p. 354-360.
53. Zhang, X., et al., *Fabrication and characterization of 8YSZ ceramic based abradable seal coatings by atmospheric plasma spraying.* Ceramics International, 2020. **46**(17): p. 26530-26538.
54. Zhao, M., L. Zhang, and W. Pan, *Properties of Yttria-Stabilized-Zirconia Based Ceramic Composite Abradable Coatings.* Key Engineering Materials, 2012. **512-515**: p. 1551-1554.
55. Steinke, T., et al., *Process design and monitoring for plasma sprayed abradable coatings.* Journal of thermal spray technology, 2010. **19**(4): p. 756-764.
56. Gebhard, S., et al. *Advanced coating systems for future shroudless turbines*. in *ASME Turbine Blade Tip Symposium*. 2013. American Society of Mechanical Engineers.
57. Ebert, S., et al., *Failure mechanisms of magnesia alumina spinel abradable coatings under thermal cyclic loading.* Journal of the European Ceramic Society, 2013. **33**(15): p. 3335-3343.
58. Guo, M., et al., *Design and characterization of BSAS-polyester abradable environmental barrier coatings (A/EBCs) on SiC/SiC composites.* Surface and Coatings Technology, 2023. **465**: p. 129617.
59. Tejero-Martin, D., et al., *Interaction of CMAS on thermal sprayed ytterbium disilicate environmental barrier coatings: A story of porosity.* Ceramics International, 2021.
60. Tejero-Martin, D., et al., *Steam Degradation of Ytterbium Disilicate Environmental Barrier Coatings: Effect of Composition, Microstructure and Temperature.* Journal of Thermal Spray Technology, 2022.
61. Qin, D., et al., *Fabrication and characterization of Yb2Si2O7-based composites as novel abradable sealing coatings.* Ceramics International, 2021.
62. Xu, M., et al., *Porous Yb2Si2O7 coating: A new-type high-temperature-resistant abradable seal coating.* International Journal of Applied Ceramic Technology, 2024. **n/a**(n/a).
63. Shi, J., L. Li, and T. Freeman, *Abradable Coatings for High-Performance Systems*. 2019, Rolls-Royce North American Technologies: USA.
64. Jackson, R., *Environmental Barrier Multi-Phase Abradable Coating*. 2020, United Technologies Corporation: USA.

65. Huang, J., et al., *A comprehensive review of thermally sprayed abradable sealing coatings: Focusing on abradability.* Chinese Journal of Aeronautics, 2024.
66. *E50TF121: Room temperature erosion test method for coatings*. 1995, GE Aviation.
67. Metco, O., *Rapid validation of turbomachinery abradable systems using Oerlikon Metco's rub-test facility.* SF-0029.0–Abradable Testing, 2020.
68. Wilson, S. *Thermally sprayed abradable coating technology for sealing in gas turbines*. in *6th International Conference on the Future of Gas Turbine Technology*. 2012. Brussels Belgium.
69. Ghasripoor, F., M. Dorfman, and R. Schmid, *Abradables improve gas turbine efficiency.* Materials world, 1997. **5**(6): p. 328-330.
70. Ali, R., et al., *Tribological performance and phase transition of MAX-phase/YSZ abradable seal coating produced by air plasma spraying.* Ceramics International, 2021.
71. Nasiri, N.A., et al., *Oxidation behaviour of SiC/SiC ceramic matrix composites in air.* Journal of the European Ceramic Society, 2016. **36**(14): p. 3293-3302.
72. Opila, E.J., *Oxidation and Volatilization of Silica Formers in Water Vapor.* Journal of the American Ceramic Society, 2003. **86**(8): p. 1238-1248.
73. dos Santos e Lucato, S.L., O.H. Sudre, and D.B. Marshall, *A method for assessing reactions of water vapor with materials in high-speed, high-temperature flow.* Journal of the American Ceramic Society, 2011. **94**: p. s186-s195.
74. Opila, E.J., et al., *SiC recession caused by SiO2 scale volatility under combustion conditions: II, thermodynamics and gaseous-diffusion model.* Journal of the American Ceramic Society, 1999. **82**(7): p. 1826-1834.
75. Federer, J.I., *Alumina base coatings for protection of SiC ceramics.* Journal of Materials Engineering, 1990. **12**(2): p. 141-149.
76. Lee, K.N., R.A. Miller, and N.S. Jacobson, *New generation of plasma-sprayed mullite coatings on silicon carbide*. 1995.
77. Lee, K., et al. *Environmental Durability of Mullite Coating/SiC and Mullite-YSZ Coating/SiC Systems*. in *Proceedings of the 19th Annual Conference on Composites, Advanced Ceramics, Materials, and Structures—B: Ceramic Engineering and Science Proceedings*. 1995. Wiley Online Library.
78. Lee, K.N., et al., *Upper temperature limit of environmental barrier coatings based on mullite and BSAS.* Journal of the American Ceramic Society, 2003. **86**(8): p. 1299-1306.
79. Al Nasiri, N., et al., *Thermal Properties of Rare-Earth Monosilicates for EBC on Si-Based Ceramic Composites.* Journal of the American Ceramic Society, 2016. **99**(2): p. 589-596.
80. Richards, B.T., et al., *Fracture mechanisms of ytterbium monosilicate environmental barrier coatings during cyclic thermal exposure.* Acta Materialia, 2016. **103**: p. 448-460.
81. Turcer, L.R. and N.P. Padture, *Towards multifunctional thermal environmental barrier coatings (TEBCs) based on rare-earth pyrosilicate solid-solution ceramics.* Scripta materialia, 2018. **154**: p. 111-117.
82. Fernández-Carrión, A.J., M. Allix, and A.I. Becerro, *Thermal Expansion of Rare-Earth Pyrosilicates.* Journal of the American Ceramic Society, 2013. **96**(7): p. 2298-2305.
83. Richards, B.T., H. Zhao, and H.N.G. Wadley, *Structure, composition, and defect control during plasma spray deposition of ytterbium silicate coatings.* Journal of Materials Science, 2015. **50**(24): p. 7939-7957.
84. Huang, J., et al., *Effect of deposition temperature on phase composition, morphology and mechanical properties of plasma-sprayed Yb2Si2O7 coating.* Journal of the European Ceramic Society, 2021. **41**(15): p. 7902-7909.
85. Garcia, E., H. Lee, and S. Sampath, *Phase and microstructure evolution in plasma sprayed Yb2Si2O7 coatings.* Journal of the European Ceramic Society, 2019. **39**(4): p. 1477-1486.
86. Di Iorio, G., et al., *Ytterbium Disilicate/Monosilicate multilayer environmental barrier coatings: Influence of atmospheric plasma spray parameters on composition and microstructure.* Coatings, 2023. **13**(9): p. 1602.

87. Jian, Y., et al., *Oxidation performance of ytterbium disilicate/silicon environmental barrier coating via optimized air plasma spraying.* Journal of Materials Science and Chemical Engineering, 2021. **9**(4): p. 19-26.
88. Chen, D., et al., *In-flight particle states and coating properties of air plasma sprayed ytterbium disilicates.* Surface and Coatings Technology, 2021. **417**: p. 127186.
89. Li, B., et al., *Influence of spraying power on microstructure, phase composition and nanomechanical properties of plasma-sprayed nanostructured Yb-silicate environmental barrier coatings.* Surface and Coatings Technology, 2024. **478**: p. 130450.
90. Vaßen, R., et al., *Correlation of Process Conditions, Porosity Levels and Crystallinity in Atmospherically Plasma Sprayed Yb2Si2O7 Environmental Barrier Coatings.* Journal of Composites Science, 2021. **5**(8): p. 198.
91. Bakan, E., et al., *Yb2Si2O7 Environmental Barrier Coatings Deposited by Various Thermal Spray Techniques: A Preliminary Comparative Study.* Journal of Thermal Spray Technology, 2017. **26**(6): p. 1011-1024.
92. Vaßen, R., et al., *Environmental Barrier Coatings Made by Different Thermal Spray Technologies.* Coatings, 2019. **9**(12): p. 784.
93. Garcia, E., et al., *Characterization of Yb2Si2O7–Yb2SiO5 composite environmental barrier coatings resultant from in situ plasma spray processing.* Ceramics International, 2020. **46**(13): p. 21328-21335.
94. Zhu, T., et al., *Influence of phase composition on microstructure and thermal properties of ytterbium silicate coatings deposited by atmospheric plasma spray.* Journal of the European Ceramic Society, 2018. **38**(11): p. 3974-3985.
95. Ryu, H.-l., et al., *Preparation of crystalline ytterbium disilicate environmental barrier coatings using suspension plasma spray.* Ceramics International, 2019. **45**(5): p. 5801-5807.
96. Owusu, E.B., et al., *Suspension plasma sprayed ytterbium disilicate coatings: Phase stability and microstructural evolution in extreme environments.* Journal of the European Ceramic Society, 2024: p. 116779.
97. Jiang, C., et al., *Ytterbium silicate environmental barrier coatings deposited using the solution-based precursor plasma spray.* Journal of Thermal Spray Technology, 2020. **29**(5): p. 979-994.
98. Paksoy, A.H., et al., *Influence of alumina addition on steam corrosion behaviour of ytterbium disilicates for environmental barrier coating applications.* Corrosion Science, 2022. **207**: p. 110555.
99. McCormack, S., et al., *The effect of porosity, mixed molecular/Knudsen diffusion, and a surface barrier layer on steam corrosion of Yb2Si2O7.* Corrosion Science, 2023. **219**: p. 111238.
100. Ridley, M. and E. Opila, *Thermochemical stability and microstructural evolution of Yb2Si2O7 in high-velocity high-temperature water vapor.* Journal of the European Ceramic Society, 2021. **41**(5): p. 3141-3149.
101. Richards, B.T., et al., *Response of ytterbium disilicate–silicon environmental barrier coatings to thermal cycling in water vapor.* Acta Materialia, 2016. **106**: p. 1-14.
102. Huang, Y., et al., *Comprehensive understanding of coupled stress characteristics in ytterbium disilicate environmental barrier coatings undergoing corrosion transformation and thermal cycling.* Ceramics International, 2022. **48**(17): p. 25528-25537.
103. Zhong, X., et al., *Corrosion behavior and mechanism of ytterbium silicates environmental barrier coatings subjected to thermal cycling in water vapor.* Journal of the American Ceramic Society, 2024. **107**(1): p. 387-403.
104. Olson, D.H., et al., *Evolution of microstructure and thermal conductivity of multifunctional environmental barrier coating systems.* Materials Today Physics, 2021. **17**: p. 100304.

105. Kane, K.A., et al., *Steam oxidation of ytterbium disilicate environmental barrier coatings with and without a silicon bond coat.* Journal of the American Ceramic Society, 2021. **104**(5): p. 2285-2300.
106. Kane, K., et al., *Evaluating steam oxidation kinetics of environmental barrier coatings.* Journal of the American Ceramic Society, 2021.
107. Richards, B.T., M.R. Begley, and H.N.G. Wadley, *Mechanisms of Ytterbium Monosilicate/Mullite/Silicon Coating Failure During Thermal Cycling in Water Vapor.* Journal of the American Ceramic Society, 2015. **98**(12): p. 4066-4075.
108. Ueno, S., D.D. Jayaseelan, and T. Ohji, *Development of Oxide-Based EBC for Silicon Nitride.* International Journal of Applied Ceramic Technology, 2004. **1**(4): p. 362-373.
109. Maier, N., K.G. Nickel, and G. Rixecker, *High temperature water vapour corrosion of rare earth disilicates (Y,Yb,Lu)2Si2O7 in the presence of Al(OH)3 impurities.* Journal of the European Ceramic Society, 2007. **27**(7): p. 2705-2713.
110. Rohbeck, N., P. Morrell, and P. Xiao, *Degradation of ytterbium disilicate environmental barrier coatings in high temperature steam atmosphere.* Journal of the European Ceramic Society, 2019. **39**(10): p. 3153-3163.
111. Bakan, E., et al., *Effect of processing on high-velocity water vapor recession behavior of Yb-silicate environmental barrier coatings.* Journal of the European Ceramic Society, 2019. **39**(4): p. 1507-1513.
112. Bakan, E., et al., *High-velocity water vapor corrosion of Yb-silicate: Sprayed vs. sintered body.* Scripta Materialia, 2020. **178**: p. 468-471.
113. Ahlborg, N.L. and D. Zhu, *Calcium–magnesium aluminosilicate (CMAS) reactions and degradation mechanisms of advanced environmental barrier coatings.* Surface and Coatings Technology, 2013. **237**: p. 79-87.
114. Liu, J., et al., *Calcium–magnesium–aluminosilicate corrosion behaviors of rare-earth disilicates at 1400°C.* Journal of the European Ceramic Society, 2013. **33**(15): p. 3419-3428.
115. Stolzenburg, F., et al., *The interaction of calcium–magnesium–aluminosilicate with ytterbium silicate environmental barrier materials.* Surface and Coatings Technology, 2015. **284**: p. 44-50.
116. Song, W., et al., *Volcanic ash melting under conditions relevant to ash turbine interactions.* Nature Communications, 2016. **7**(1): p. 10795.
117. Cao, G., et al., *CMAS hot corrosion behavior of rare-earth silicates for environmental barrier coatings applications: a comprehensive review.* Heat Treatment and Surface Engineering, 2021. **3**(1): p. 9-28.
118. Nieto, A., et al., *Calcia–magnesia–alumina–silicate (CMAS) attack mechanisms and roadmap towards Sandphobic thermal and environmental barrier coatings.* International Materials Reviews, 2021. **66**(7): p. 451-492.
119. Stokes, J.L., et al., *High-Temperature thermochemical interactions of molten silicates with Yb2Si2O7 and Y2Si2O7 environmental barrier coating materials.* Journal of the European Ceramic Society, 2019. **39**(15): p. 5059-5067.
120. Wiesner, V.L., et al., *Calcium–magnesium aluminosilicate (CMAS) interactions with ytterbium silicate environmental barrier coating material at elevated temperatures.* Ceramics International, 2020. **46**(10, Part B): p. 16733-16742.
121. Turcer, L.R., et al., *Environmental-barrier coating ceramics for resistance against attack by molten calcia-magnesia-aluminosilicate (CMAS) glass: Part II, β-Yb2Si2O7 and β-Sc2Si2O7.* Journal of the European Ceramic Society, 2018. **38**(11): p. 3914-3924.
122. Poerschke, D.L., R.W. Jackson, and C.G. Levi, *Silicate Deposit Degradation of Engineered Coatings in Gas Turbines: Progress Toward Models and Materials Solutions.* Annual Review of Materials Research, 2017. **47**(1): p. 297-330.
123. Padture, N.P., *Environmental degradation of high-temperature protective coatings for ceramic-matrix composites in gas-turbine engines.* npj Materials Degradation, 2019. **3**(1).

124. Summers, W.D., et al., *Roles of composition and temperature in silicate deposit-induced recession of yttrium disilicate.* Acta Materialia, 2018. **160**: p. 34-46.
125. Zhao, H., et al., *Molten silicate reactions with plasma sprayed ytterbium silicate coatings.* Surface and Coatings Technology, 2016. **288**: p. 151-162.
126. Zhou, B., et al., *Resistance of ytterbium silicate environmental barrier coatings against molten calcium-magnesium-aluminosilicate (CMAS): A comprehensive study.* Surface and Coatings Technology, 2024. **479**: p. 130540.
127. Zhong, X., et al., *Corrosion behaviors and mechanisms of ytterbium silicate environmental barrier coatings by molten calcium-magnesium-alumino-silicate melts.* Corrosion Science, 2021. **191**: p. 109718.
128. Liu, P., et al., *Reaction behaviors and mechanisms of tri-layer Yb2SiO5/Yb2Si2O7/Si environmental barrier coatings with molten calcium-magnesium-alumino-silicate.* Corrosion Science, 2022. **197**: p. 110069.
129. Harder, B.J., et al., *Steam oxidation performance of Yb2Si2O7 environmental barrier coatings exposed to CMAS.* Journal of the European Ceramic Society, 2023.
130. Stokes, J.L., et al. *Thermochemical/Thermomechanical Synergies in High-Temperature Solid Particle Erosion of CMAS-Exposed EBCs*. in *Turbo Expo: Power for Land, Sea, and Air*. 2023. American Society of Mechanical Engineers.
131. Stokes, J.L., et al., *Effects of molten silicate reactivity on high temperature erosion behavior of plasma sprayed Yb2Si2O7-based EBCs.* Surface and Coatings Technology, 2024. **494**: p. 131078.
132. Stolzenburg, F., et al., *The influence of calcium–magnesium–aluminosilicate deposits on internal stresses in Yb2Si2O7 multilayer environmental barrier coatings.* Acta Materialia, 2016. **105**: p. 189-198.
133. Tian, Z., et al., *Corrosion of RE2Si2O7 (RE=Y, Yb, and Lu) environmental barrier coating materials by molten calcium-magnesium-alumino-silicate glass at high temperatures.* Journal of the European Ceramic Society, 2019. **39**(14): p. 4245-4254.
134. Webster, R.I. and E.J. Opila, *Mixed phase ytterbium silicate environmental-barrier coating materials for improved calcium–magnesium–alumino-silicate resistance.* Journal of Materials Research, 2020. **35**(17): p. 2358-2372.
135. Wiesner, V.L., et al., *Molten calcium–magnesium–aluminosilicate interactions with ytterbium disilicate environmental barrier coating.* Journal of Materials Research, 2020. **35**(17): p. 2346-2357.
136. Wolf, M., et al., *Resistance of pure and mixed rare earth silicates against calcium-magnesium-aluminosilicate (CMAS): A comparative study.* Journal of the American Ceramic Society, 2020. **103**(12): p. 7056-7071.
137. Sternlicht, H., D.W. McComb, and N.P. Padture, *Interaction of ytterbium pyrosilicate environmental-barrier-coating ceramics with molten calcia-magnesia-aluminosilicate glass: Part II, Interfaces.* Acta Materialia, 2022. **241**: p. 118359.
138. Sternlicht, H., D.W. McComb, and N.P. Padture, *Interaction of ytterbium pyrosilicate environmental-barrier-coating ceramics with molten calcia-magnesia-aluminosilicate glass: Part I, Microstructures.* Acta Materialia, 2022. **241**: p. 118360.
139. Inc., P.S.T., *Model SG-100 Plasma Spray Gun Operator's Manual*. 2011.
140. Epp, J., *4 - X-ray diffraction (XRD) techniques for materials characterization*, in *Materials Characterization Using Nondestructive Evaluation (NDE) Methods*, G. Hübschen, et al., Editors. 2016, Woodhead Publishing. p. 81-124.
141. Hill, R. and C. Howard, *Quantitative phase analysis from neutron powder diffraction data using the Rietveld method.* Journal of Applied Crystallography, 1987. **20**(6): p. 467-474.
142. McCusker, L., et al., *Rietveld refinement guidelines.* Journal of Applied Crystallography, 1999. **32**(1): p. 36-50.

143. Scardi, P., M. Leoni, and R. Delhez, *Line broadening analysis using integral breadth methods: a critical review.* Journal of Applied Crystallography, 2004. **37**(3): p. 381-390.
144. Giurlani, W., et al., *Measuring the Thickness of Metal Coatings: A Review of the Methods.* Coatings, 2020. **10**(12): p. 1211.
145. Vespucci, S., et al., *Digital direct electron imaging of energy-filtered electron backscatter diffraction patterns.* Physical Review B, 2015. **92**(20): p. 205301.
146. Leitner, J., et al., *Application of Neumann–Kopp rule for the estimation of heat capacity of mixed oxides.* Thermochimica Acta, 2010. **497**(1): p. 7-13.
147. DiCarlo, J., et al., *SiC/SiC composites for 1200 C and above*, in *Handbook of ceramic composites*. 2005, Springer. p. 77-98.
148. Lee, K.N., *Current status of environmental barrier coatings for Si-Based ceramics.* Surface and Coatings Technology, 2000. **133-134**: p. 1-7.
149. Jang, B.-K., et al., *Mechanical properties and microstructure of Yb2SiO5 environmental barrier coatings under isothermal heat treatment.* Journal of the European Ceramic Society, 2020. **40**(7): p. 2667-2673.
150. Richards, B.T. and H.N.G. Wadley, *Plasma spray deposition of tri-layer environmental barrier coatings.* Journal of the European Ceramic Society, 2014. **34**(12): p. 3069-3083.
151. Garcia, E., et al., *Crystallization behavior of air-plasma-sprayed ytterbium-silicate-based environmental barrier coatings.* Journal of the European Ceramic Society, 2021. **41**(6): p. 3696-3705.
152. Fauchais, P. and M. Vardelle, *Sensors in Spray Processes.* Journal of Thermal Spray Technology, 2010. **19**(4): p. 668-694.
153. Vardelle, M., A. Vardelle, and P. Fauchais, *Spray parameters and particle behavior relationships during plasma spraying.* Journal of Thermal Spray Technology, 1993. **2**(1): p. 79-91.
154. Felsche, J. *The crystal chemistry of the rare-earth silicates*. in *Rare Earths*. 1973. Berlin, Heidelberg: Springer Berlin Heidelberg.
155. Sarikaya, O., *Effect of some parameters on microstructure and hardness of alumina coatings prepared by the air plasma spraying process.* Surface and Coatings Technology, 2005. **190**(2): p. 388-393.
156. Thirumalaikumarasamy, D., K.S. Kamalamoorthy, and V.B. Visvalingam, *Effect of experimental parameters on the micro hardness of plasma sprayed alumina coatings on AZ31B magnesium alloy.* Journal of Magnesium and Alloys, 2015. **3**(3): p. 237-246.
157. Chadha, S., R. Jefferson-Loveday, and T. Hussain, *Modelling Knudsen number effects in suspension high velocity oxy fuel thermal spray.* International Journal of Heat and Mass Transfer, 2020. **152**: p. 119454.
158. Cui, Y., et al., *Evolution of the residual stress in porous ceramic abradable coatings under thermal exposure.* Surface and Coatings Technology, 2020. **394**: p. 125915.
159. Watson, M. and M. Marshall, *Wear mechanisms at the blade tip seal interface.* Wear, 2018. **404-405**: p. 176-193.
160. Lima, R.S. and B.R. Marple, *Thermal Spray Coatings Engineered from Nanostructured Ceramic Agglomerated Powders for Structural, Thermal Barrier and Biomedical Applications: A Review.* Journal of Thermal Spray Technology, 2007. **16**(1): p. 40-63.
161. Laverty, W.F., *Rub energetics of compressor blade tip seals.* Wear, 1982. **75**(1): p. 1-20.
162. Padova, C., et al., *Development of an Experimental Capability to Produce Controlled Blade Tip/Shroud Rubs at Engine Speed.* Journal of Turbomachinery, 2004. **127**(4): p. 726-735.
163. Nitschke, S., et al., *An advanced experimental method and test rig concept for investigating the dynamic blade-tip/casing interactions under engine-like mechanical conditions.* Wear, 2019. **422-423**: p. 161-166.
164. Maozhong, Y., H. Baiyun, and H. Jiawen, *Erosion wear behaviour and model of abradable seal coating.* Wear, 2002. **252**(1-2): p. 9-15.

165. Lynam, A., et al., *Atmospheric plasma spraying of ytterbium disilicate for abradable and environmental barrier coatings: A story of processing-microstructure relationships.* Ceramics International, 2023. **49**(13): p. 22232-22243.
166. Tian, Z., et al., *Exploration of the low thermal conductivities of γ-Y2Si2O7, β-Y2Si2O7, β-Yb2Si2O7, and β-Lu2Si2O7 as novel environmental barrier coating candidates.* Journal of the European Ceramic Society, 2016. **36**(11): p. 2813-2823.
167. Zhou, Y.-C., et al., *Theoretical Prediction and Experimental Investigation on the Thermal and Mechanical Properties of Bulk β-Yb2Si2O7.* Journal of the American Ceramic Society, 2013. **96**(12): p. 3891-3900.
168. Kubaschewski, O. and C.B. Alcock, *Metallurgical Thermochemistry*. 5th Edition ed. 1979: Pergamon Press.
169. Ku, H.H., *Notes on the use of propagation of error formulas.* Journal of Research of the National Bureau of Standards, 1966. **70**(4).
170. *ASTM G76-13 Standard Test Method for Conducting Erosion Tests by Solid Particle Impingement Using Gas Jets*. 2013, ASTM International: West Conshohoken, PA, USA.
171. Eaton, H.E. and R.C. Novak, *Particulate erosion of plasma-sprayed porous ceramic.* Surface and Coatings Technology, 1987. **30**(1): p. 41-50.
172. Nicholls, J.R., M.J. Deakin, and D.S. Rickerby, *A comparison between the erosion behaviour of thermal spray and electron beam physical vapour deposition thermal barrier coatings.* Wear, 1999. **233-235**: p. 352-361.
173. Presby, M.J., et al., *High-Temperature Solid Particle Erosion of Environmental and Thermal Barrier Coatings.* Coatings, 2023. **13**(5): p. 902.
174. Presby, M.J. and B.J. Harder, *Solid particle erosion of a plasma spray – physical vapor deposition environmental barrier coating in a combustion environment.* Ceramics International, 2021. **47**(17): p. 24403-24411.
175. Fiala, P., et al. *New high temperature titanium compatible abradable seals*. in *Proceedings of 22nd heat treatment society conference and second international surface engineering conference, Seo15-17, Indianapolis, Indiana, USA, ASM international, Materials park, Ohio*. 2003.
176. Straffelini, G., *Friction and wear.* Methodologies for Design and Control. Switzerland: Springer International Publishing AG Switzerland, 2015.
177. Antwi, E.K., K. Liu, and H. Wang, *A review on ductile mode cutting of brittle materials.* Frontiers of Mechanical Engineering, 2018. **13**(2): p. 251-263.
178. Presby, M.J., J.L. Stokes, and B.J. Harder, *Solid particle erosion in ceramic matrix composites and environmental barrier coatings: A perspective.* Journal of the American Ceramic Society, 2023.
179. Lynam, A., et al., *An investigation into the erosion and wear mechanisms observed in abradable ytterbium disilicate environmental barrier coatings.* Journal of the European Ceramic Society, 2024. **44**(12): p. 7310-7327.
180. Ctibor, P., R. Lechnerová, and V. Beneš, *Quantitative analysis of pores of two types in a plasma-sprayed coating.* Materials Characterization, 2006. **56**(4): p. 297-304.
181. Armstrong, R., *The influence of polycrystal grain size on several mechanical properties of materials.* Metallurgical and Materials Transactions B, 1970. **1**: p. 1169-1176.
182. Stokes, J.L., *Thermal expansion coefficients of Ca2Y8 (SiO4) 6O2 and Ca2Yb8 (SiO4) 6O2 apatite-type silicates*. 2021.
183. Harmer, M.P., H.M. Chan, and G.A. Miller, *Unique opportunities for microstructural engineering with duplex and laminar ceramic composites.* Journal of the American Ceramic Society, 1992. **75**(7): p. 1715-1728.
184. Kane, K., et al., *Accelerated oxidation during 1350°C cycling of ytterbium silicate environmental barrier coatings.* Journal of the American Ceramic Society, 2021.

185. Wiesner, V.L. and N.P. Bansal, *Mechanical and thermal properties of calcium–magnesium aluminosilicate (CMAS) glass.* Journal of the European Ceramic Society, 2015. **35**(10): p. 2907-2914.
186. Webster, R.I. and E.J. Opila, *Viscosity of CaO-MgO-Al2O3-SiO2 (CMAS) melts: Experimental measurements and comparison to model calculations.* Journal of Non-Crystalline Solids, 2022. **584**: p. 121508.
187. Kumar, R., et al., *Effect of CMAS viscosity on the infiltration depth in thermal barrier coatings of different microstructures.* Surface and Coatings Technology, 2022. **432**: p. 128039.
188. Stolper, E., *Water in silicate glasses: An infrared spectroscopic study.* Contributions to Mineralogy and Petrology, 1982. **81**(1): p. 1-17.
189. Klemm, H., *Silicon Nitride for High-Temperature Applications.* Journal of the American Ceramic Society, 2010. **93**(6): p. 1501-1522.